Development and Characterisation of SGLT2 Monoclonal Antibodies

Dr. Nada Hassan Alzahrani

A thesis submitted in partial fulfilment of the requirements for the degree of Doctor of Philosophy

The University of Sheffield

Faculty of Health

School of Medicine and Population Health

Division of Clinical Medicine

October 2024

Acknowledgements

First and foremost, all praise and thanks are due to Almighty Allah for granting me the strength, determination, and patience to complete this journey.

This thesis would not have been possible without the invaluable guidance and support of my supervisor, Dr Philip Watson. I am deeply grateful for his continuous supervision throughout my PhD. His expertise, understanding, and immense knowledge were instrumental in teaching me the laboratory techniques necessary for my research and helping me shape this thesis.

I am also profoundly thankful to my second supervisor, Dr. Helen Kemp, for her unwavering professional and personal support during the final year of my PhD. Her insightful feedback and careful corrections have been vital in bringing this thesis to completion.

I want to express my sincere gratitude to the government of Saudi Arabia for granting me this incredible opportunity and for funding my research.

I want to express my gratitude to Timothy Winks and Susan Justice for their professional assistance and expertise in tissue culture, which was essential to the success of my experimental work.

Words cannot adequately express my gratitude to my parents, Hasan and Nora, whose endless inspiration, support, and encouragement have been my anchor throughout this journey.

To my father, Hasan, your unwavering belief in me has been a source of great strength. Your wisdom, patience, and guidance have shaped my perseverance, and I am forever grateful for your presence in my life.

To my mother, Norah, your boundless love and prayers have been my constant source of comfort and motivation. Your sacrifices and encouragement have lifted me during the most challenging moments, and I owe so much to your enduring support.

I also sincerely appreciate my brothers and sisters, who have always supported, encouraged, and reminded me to believe in myself.

To my beloved husband, Saqer, I offer my heartfelt thanks. You have shared in both my successes and setbacks, and your unwavering support, patience, and belief in me were the pillars of my strength during the most challenging times.

Finally, to my little ones, Naif, Sultan, and Talal, thank you for your love, motivation, and patience. You have witnessed every step of this journey, and your words of encouragement and tolerance during the problematic days have meant more than I can say.

Declaration

I hereby confirm that this thesis is my own original work and has not been submitted or accepted for any other academic degree or publication. I conducted all research and work presented within this thesis, except where specific contributions are noted. All sources of information have been properly cited and referenced throughout the text.

Nada Hassan Alzahrani

October 2024

Summary

Background: Chronic kidney disease (CKD) often leads to renal fibrosis, a condition marked by excessive extracellular matrix (ECM) deposition that disrupts kidney function and can result in end-stage renal disease (ESRD). The sodium-glucose cotransporter 2 (SGLT2), highly expressed in renal tubules, contributes to glucose reabsorption and is associated with CKD through its role in metabolic dysregulation and renal fibrosis. Targeting SGLT2 offers a tissue-specific approach for delivering therapeutic agents to reduce fibrosis. Current treatments lack tissue specificity and can cause systemic side effects, highlighting the need for targeted therapeutic strategies.

Aims: To generate and characterise an SGLT2-targeting monoclonal antibody for reducing renal fibrosis in CKD and explore its therapeutic mechanism.

Methods: Mice were immunised with an SGLT2-diphtheria toxin A (DTA) fusion protein. DTA was used to break immune tolerance against the self-protein SGLT2 by eliciting a stronger immune response. Spleen cells were harvested, RNA extracted, and cDNA created to generate a phage display library of fragment antigen-binding (Fab) antibody regions. Biopanning isolated high-affinity antibodies, followed by competitive ELISA to determine the binding epitopes. Full-length SGLT2 was transiently transfected into mammalian cells for validating antibody specificity through western blotting, while immunohistochemistry (IHC) on mouse kidney sections confirmed tissue-specific binding.

Results: Several SGLT2-targeting Fab fragments were identified through phage display. Competitive ELISA and western blotting confirmed antibody specificity with minimal cross-reactivity. IHC demonstrated kidney-specific binding, while biotinylated Fab fragments exhibited high affinity and stability. The monoclonal antibody could be further developed to deliver anti-fibrotic agents to SGLT2-expressing renal tissues, potentially reducing ECM deposition and preserving kidney function.

Conclusions: Monoclonal antibody fragments specifically targeting SGLT2 were successfully generated, suggesting a potential therapeutic approach for treating renal fibrosis in CKD. Further, *in vivo* studies are needed to explore their efficacy.

Table of Contents

List of Figures

List of Tables

List of Abbreviations

Abbreviation	The full version of the word
ADCs	Antibody-Drug Conjugates
APS	Ammonium Persulfate
ASOs	Antisense oligonucleotides
BSA	Bovine Serum Albumin
cDNA	Complementary Deoxyribose Nucleic Acid
CDRs	Complementarity-Determining Regions
CHO	Chinese Hamster Ovary
CKD	Chronic Kidney Disease
CMV	Cytomegalovirus
DNA	Deoxyribose nucleic acid
DTA	Diphtheria toxin A
DTT	Dithiothreitol
ECACC	European Collection of Authenticated Cell Cultures
ECM	Extracellular Matrix
ELISA	Enzyme-Linked Immunosorbent Assay
ESRD	End-Stage Renal Disease
Fab	Fragment Antigen-Binding
Fc	Fragment Constant
FITC	Fluorescein Isothiocyanate
FRs	Framework Regions
GFR	Glomerular Filtration Rate
GFP	Green Fluorescent Protein
IHC	Immunohistochemistry
IMAC	Immobilised Metal Ion Affinity Chromatography
IPTG	Isopropyl ß-D-1-thiogalactopyranoside
LB	Luria Bertani Medium
LOX	Lysyl Oxidase

mAbs	Monoclonal Antibodies
MMPs	Matrix Metalloproteinases
NPs	Nanoparticles
PAI-1	Plasminogen Activator Inhibitor 1
PBS	Phosphate Buffered Saline
PCR	Polymerase Chain Reaction
PDGF	Platelet-Derived Growth Factor
pfu/ml	Plaque-Forming Units per Millilitre
PVDF	Polyvinylidene Difluoride
RIPA	Radioimmunoprecipitation Assay
RNA	Ribose Nucleic Acid
RNAi	RNA interference
SB	Super Broth
scFv	Single-Chain Variable Fragments
SDS-PAGE	Sodium Dodecyl Sulphate-Polyacrylamide Gel Electrophoresis
SGLT2	Sodium-Glucose co-Transporter 2
SNx	Subtotal Nephrectomy
SOC	Super Optimal Broth with Catabolic Repression
SRCR	Scavenger Receptor Cysteine-Rich
TB	Terrific broth medium
TBST	Tris-Buffered Saline with Tween 20
TEMED	Tetramethyl Ethylene Diamine
TIMPs	Tissue Inhibitor Metalloproteinases
TG2	Transglutaminase 2
TGF-β	Transforming Growth Factor Beta
UUO	Unilateral Ureteral Obstruction
V	Variable Regions
VH	Heavy Chain
VK	Light Chain

Chapter 1: Introduction

1.1 Kidney Structure

The kidneys are a complicated organ located in the retroperitoneal part of the spine's sides in the abdominal cavity. Each adult human kidney weighs about 150 g and has a length of approximately 11 cm. The principal function of the kidneys is to maintain homeostatic body fluid levels and electrolytes. They achieve this through a complex filtering process, reabsorption, and excretion. The kidneys filter minerals, metabolism products, and toxins such as creatinine, uric acid, and urea from the blood and water, such as urine, preserving the body's internal environment. The kidneys also play a crucial role in the production and secretion of erythropoietin (a hormone), 1,25-dihydroxy vitamin D3 (the active form of vitamin D), and renin (an enzyme), as well as in the regulation of serum osmolality and extracellular fluid volume (George and Gounden, 2019).

This chapter begins with an overview of kidney structure and function, providing essential context for understanding kidney health and disease. It then introduces chronic kidney disease (CKD), highlighting its pathophysiology, common causes, and the underlying processes leading to renal scarring. The discussion extends to the use of animal models and biochemical mechanisms that drive fibrosis, setting the foundation for therapeutic interventions targeting renal scarring. Emerging strategies, such as targeting mediators of fibrosis and advanced drug delivery systems, are explored, with a specific focus on monoclonal antibodies and engineered approaches for precise therapy. The chapter concludes by presenting the potential of SGLT2-targeted antibody conjugates in addressing kidney diseases and outlines the hypothesis, aims, and objectives of this research.

The kidney comprises various highly specialised cells contributing to its complex anatomy and function. The nephron serves as the primary structural and functional unit of the kidney, filtering blood and managing fluid balance. Each kidney contains over a million nephrons, which are densely packed (Fig.1.1). The nephron includes the glomerulus, a specialised capillary network that performs the initial filtration of blood, followed by a tubular system lined with a single layer of epithelial cells. This tubule is subdivided into sections, including the proximal tubule, the Loop of Henle, the distal tubule, and the collecting duct, each with distinct cellular structures and functional roles that support the kidney's ability to regulate waste, electrolytes, and fluid balance (Rose, 2001).

Nephrons are closely packed together to shape the kidney parenchyma and divide into three main sections. The external section of the kidneys is called the cortex. In the cortex, the renal corpuscle contains glomeruli enclosed in a Bowman's capsule and convoluted tubules (proximal and distal). The middle section, called the medulla, comprises the Loops of Henle and the collecting ducts. In about eight cone-shaped regions, called pyramids, the medulla is formed and extends into the renal pelvis. The papillae are the tips of the pyramids in the medulla. The cortex and medulla connect to the internal section, the renal pelvis, covered by transitional epithelial cells. In the renal pelvis, urine flows into the ureter (Fenton and Praetorius, 2016).

The glomerular capillary tuft produces urine by creating an ultra-filtrate of blood plasma, which helps remove excess electrolytes and metabolic end-products. Bowman's capsule collects the ultra-filtered fluid, which then flows into the proximal convoluted tubule. As the fluid moves along its circular route, the epithelial cells in the proximal tubule reabsorb proteins. Next, the fluid enters the Loop of Henle, where cells reabsorb essential nutrients like glucose, amino acids, and water. The remaining filtrate continues to the distal convoluted tubule and eventually reaches the collecting duct, where H+ ions and electrolytes undergo further reabsorption. The nephron reabsorbs different amounts of ions at each stage: about 70% of filtered sodium is reabsorbed in the proximal tubule, 20% in the Loop of Henle, 8% in the distal tubule, and 2% in the collecting duct, with aldosterone influencing this process. Finally, the urine passes through the renal pelvis, enters the ureter, and collects in the bladder before being excreted from the body (Lote, 2000).

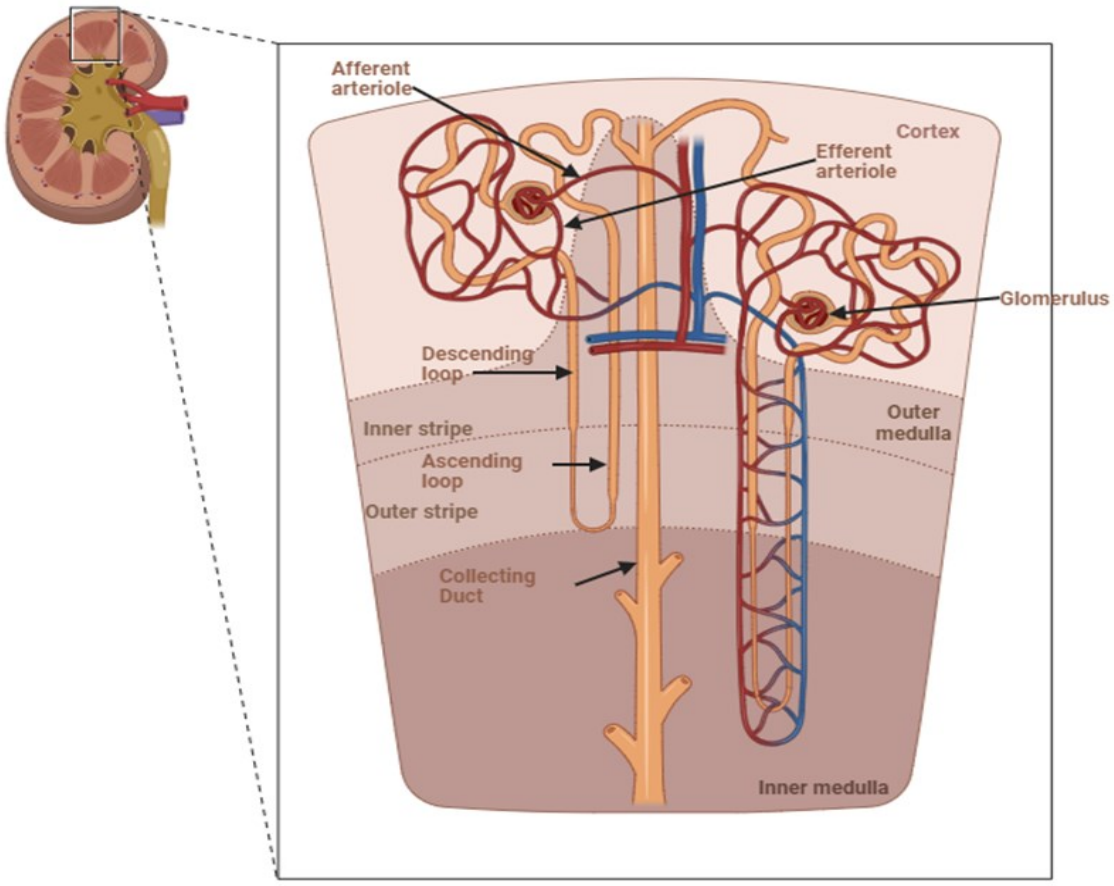

Figure 1.1: Structure of the Nephron.

Blood flows via the renal artery into the kidneys. Afferent arterioles supply blood to the glomerulus, where filtration takes place. The efferent arterioles feed into a branching capillary bed that surrounds the tubules and re-absorbs components from the glomerular filtrate. The capillary bed drains in the renal vein. The glomeruli and tubules are embedded in the tubular interstitial.

1.2 Kidney Function

The kidneys are vital excretory organs responsible for filtering and eliminating metabolic waste from the body by producing urine. The glomeruli, a network of capillaries, facilitate this process by allowing blood to pass through and removing waste and excess substances from the bloodstream (Smith, 1951). The glomerular filtration rate (GFR) measures how effectively the kidneys filter blood and remove waste, making it the most reliable indicator of kidney health. Clinicians use GFR to assess kidney function, manage the progression of kidney disease, and adjust medication dosages, particularly in populations with altered drug clearance, such as the elderly or those with renal impairment (Musso et al., 2016).

In addition to filtration, the kidneys perform essential functions to maintain homeostasis. The kidneys recover essential substances, such as electrolytes, glucose, and water, through the process of renal tubular reabsorption. At the same time, they eliminate waste by secreting hydrogen ions and certain drugs into the tubular fluid for excretion (Koeppen and Stanton, 2018). The kidneys also regulate blood pressure by secreting renin and supporting red blood cell production through erythropoietin release. Additionally, they regulate acid-base balance and activate vitamin D, which is critical for calcium metabolism and bone health (Moe et al., 2007).

1.3 Chronic Kidney Disease (CKD)

The persistent changes in kidney structure characterise CKD, including cysts, malformations, tumours, and atrophy, or progressive reduction in kidney function of at least three months, regardless of the underlying cause (Romagnani et al., 2017, Webster et al., 2017). If the GFR is less than 15 ml/min/1.73 m^2, the patient has attained end-stage renal disease (ESRD), in which case the kidney cannot perform its functions. The options available to these patients are renal replacement therapies, such as haemodialysis, peritoneal dialysis, kidney transplantation, or non-dialytic care, also called conservative care.

The Kidney Disease: Improving Global Outcomes (KDIGO) is an internationally recognised organisation that develops clinical practice guidelines for the management of kidney diseases. It classifies CKD into five stages based on the glomerular filtration rate (GFR) and markers of kidney damage, helping clinicians assess disease severity and guide treatment strategies (KDIGO, 2012). (Table 1.1) determined by the severity, cause, and duration of the condition.

This classification is primarily based on the GFR and the level of proteinuria, with serum albumin levels serving as a critical indicator of protein leakage into the urine (albuminuria). GFR is a widely recognised marker of renal excretory function, while albuminuria reflects damage to the renal filtration barrier, both critical factors in assessing kidney function (Romagnani et al., 2017).

The burden of CKD is significant with the public health problem and the high economic cost to healthcare systems. The incidence, prevalence of CKD, its risk factors, and mortality continue to increase worldwide, and there is a globally rising need for the effective treatment of ESRD (Yang et al., 2020). The prevalence of all CKD stages is shown to vary between 7 and 12% in several regions of the world. CKD G3-G5 prevalence varies worldwide, with values such as 3.1% in Canada, 5.8% in Australia, 6.7% in the United States, and 5.2% in England (Romagnani et al., 2017). The prevalence of renal replacement therapies in England in 2015 was 913 per million people, while the cost of renal replacement was estimated at £780 million for 2009/2010 by the National Health Service. The total cost of chronic kidney disease was more than £ 1.4 billion, an increase of almost three times the estimated cost for 2002 (Kerr et al., 2012). In addition, CKD patients are susceptible to a variety of other adverse outcomes; there exists a significant risk of acute kidney injury, cardiovascular disease, infection, death, and hospitalisation (Romagnani et al., 2017). Furthermore, according to the World Health Organization, approximately 1.5% of the global population died from this adverse health condition in 2012. Among the top fourteen leading causes of death, CKD accounted for 12.2 deaths per 100,000 people (Webster et al., 2017). Hypertension, diabetes mellitus, obesity, and infectious diseases such as glomerulonephritis are the most common diseases associated with CKD (Romagnani et al., 2017).

Adding to the influence of CKD, the financial burden of renal replacement therapies represents one of the most significant expenditures in hospital-based healthcare systems. The need for ongoing treatments, specialised equipment, and continuous medical supervision drives the high cost. For instance, dialysis requires regular sessions multiple times weekly, each involving complex machinery and skilled healthcare professionals. Similarly, kidney transplantation, while potentially curative, involves substantial costs for surgery, postoperative care, immunosuppressive medications, and long-term monitoring. These expenses strain healthcare resources and impose significant economic burdens on patients

and their families. In 2018, the United States had one of the highest rates of ESRD globally, with more than 2,200 cases per million people. The kidney transplantation rate for dialysis patients increased to 3.6/100 person-years, continuing an upward trend that began in 2014 after a decline. By the end of 2018, there were 554,038 dialysis patients and 229,887 individuals with a functioning kidney transplant in the United States. However, these figures do not include patients with ESRD who opted for conservative management instead of dialysis or transplantation, a choice that has been gaining more attention recently. Approximately 20% of traditional Medicare spending, amounting to $114 billion annually, is dedicated to Americans with kidney disease. Each year, over 100,000 Americans start dialysis for ESRD. Nevertheless, one in five of these patients will die within the first year (CMS, 2020).

Due to the profound impact of chronic kidney disease on patients' health and overall quality of life—manifesting in severe symptoms, chronic pain, frequent hospitalisations, and the need for invasive treatments such as nephrectomy, kidney transplantation, and haemodialysis, all of which contribute to considerable financial burdens and increased mortality rates—it becomes imperative to thoroughly understand and investigate the underlying mechanisms and etiological factors driving this disease.

Table 1.1: The Kidney Disease Improving Global Outcomes classification of CKD (Romagnani et al., 2017).

GFR categories (ml/min/ 1.73 m^2) Description and range				Persistent albuminuria categories Description and range		
				A1	A2	A3
				Normal to mildly increased	Moderately increased	Severely increased
				<30 mg/g <3 mg/mmol	30-300 mg/g 3-30 mg/mmol	>300 mg/g >30 mg/mmol
	G1	Normal or high	≥90			
	G2	Mildly decreased	60-89			
	G3a	Mildly to moderately decreased	45-59			
	G3b	Moderately to severely decreased	30-44			
	G4	Severely decreased	15-29			
	G5	Kidney failure	<15			

Low risk
Moderately increased risk
High risk
Very high risk

1.4 Renal Scarring

Renal scarring is the gradual degradation of kidney tissue, primarily due to excessive extracellular matrix deposition and fibroblast proliferation, which disrupts the kidney's cellular architecture. This scarring can affect both the glomeruli (glomerulosclerosis) and tubular structures. The condition is driven by chronic inflammation and an abnormal wound-healing process triggered by factors such as hypertension, diabetes mellitus, chronic infection, and toxic chemical exposures (Reiss et al., 2024). As the disease progresses, renal function deteriorates, eventually leading to renal failure, which requires significant medical intervention, including dialysis or transplantation.

Renal failure presents severe health challenges and imposes substantial financial burdens on patients. Dialysis, which mimics kidney function by removing waste products and excess fluid from the blood, is both costly and time-consuming, severely impacting patients' quality of life. Kidney transplantation, though offering a potential long-term solution, entails high costs associated with surgery, postoperative care, and lifelong immunosuppressive medication to prevent organ rejection. Consequently, the economic and personal toll of renal scarring and its progression to renal failure highlights the urgent need for early detection and the development of effective therapeutic strategies to prevent or mitigate this condition. (Lote, 1994).

1.4.1 Causes of Renal Scarring

1.4.1.1 Diabetes Mellitus

Hyperglycaemia is the primary cause of ESRD, requiring renal replacement therapies, and is associated with increased cardiovascular disease. A high blood sugar level leads to glomerular injury and a change in the kidney structure (Yamazaki et al., 2018).

Type 2 diabetes mellitus leads to glomerular hypertension by decreasing afferent arteriolar resistance and stimulating the efferent arterioles. As a result, the glomerular capillary’s raised pressure is a significant factor in renal sclerosis development (Nogueira et al., 2017). Diabetes and hypertension lead to glomerular expansion progressively, causing endothelial dysfunction and haemodynamic changes: loss of electric charge and thickening of the glomerular basement membrane, decreased number of podocytes, and mesangial distension

are shown to underlie the initial glomerular injury, which is likely to lead to glomerulosclerosis (López-Novoa et al., 2010).

Bramlage et al. (2020) conducted a study on patients with a mean age of 66.3 years, of whom 52.6% were male, with a mean body mass index of 31.7 kg/m^2. The mean GFR was 78.4±21.4 ml/min/1.73 m^2. The results indicated that the prevalence of impaired kidney function was significant at 53.0% in patients with type 2 diabetes mellitus. The 1-year incidence of CKD was as high as 6.6%. However, serial determinations of GFR were rare, occurring in only 7.8% of all patients. These patients were characterised by a high risk of CKD, with 88.1% having hypertension and 66.1% having dyslipidaemia.

Over three years, 30.9% of patients experienced a decrease in GFR of -12 ml/min/1.73 m^2 or more. In addition, there was a significant increase in the proportion of patients with GFR less than 30 ml/min/1.73 m^2, rising from 1.8% to 3.8%. Hypertension and albuminuria were identified as contributing factors to decreased renal function, while dyslipidaemia had no adverse effect on the slope of GFR (Bramlage et al., 2020).

1.4.1.2 Hypertension

High blood pressure plays a principal role in the cause of ESRD worldwide and is the second leading cause of ESRD after diabetes in the United States (Van Buren and Toto, 2011). The formation of systemic hypertension leads to glomerular hypertension in the glomerular capillary beds, which further contributes to the progression of glomerulosclerosis.

A study supporting this conducted by Joo et al. (2020) found that participants with an increasing systolic blood pressure trajectory, where systolic blood pressure rose from 105 to 124 mm Hg, had higher rates of incident CKD during a median follow-up of 7.7 years. Specifically, CKD incidence rates were 17.8 cases per 1000 person-years for those with high BP, compared to 8.9 and 9.6 cases for those with low or stable blood pressure trajectories, respectively. An increased blood pressure trajectory was associated with a 1.57-fold higher risk of CKD after adjusting for baseline factors. This risk was particularly significant in participants with baseline systolic BP below 120 mm Hg. Additionally, the course of increased BP trajectory has been linked to an increased risk of developing early-onset albuminuria (Joo et al., 2020).

1.4.1.3 Obesity

Obesity is linked to the excess high amount of protein in the urine (proteinuria) and is considered a potential risk factor for the development of ESRD. Research by Iseki et al. (2004) demonstrated that a higher body mass index was related to an increased risk of ESRD amongst men in the general population of Okinawa. This finding suggests that maintaining an optimal body weight may help reduce the risk of developing ESRD. A further study carried out by Ejerblad et al. (2006) , shows that obesity significantly contributes to the rising incidence of chronic renal failure in both men and women. While the elevated risk of chronic renal failure in obese individuals is primarily mediated through indirect effects, such as the high prevalence of type 2 diabetes and hypertension, direct effects may also contribute. These include glomerular hyperfiltration, increased renal pressure, and the deposition of ectopic fat in renal tissues. These studies underscore the importance of weight management in modifying the risk of renal diseases.

The global incidence of obesity, type 2 diabetes mellitus, and hypertension has significantly increased in recent decades. These conditions are key risk factors for CKD and ESRD. The rising prevalence of these conditions contributes directly to the growing burden of kidney disease. For instance, obesity not only elevates the risk of developing diabetes and hypertension, but it also independently contributes to kidney disease through mechanisms such as glomerular hyperfiltration and proteinuria (Iseki et al., 2004, Ejerblad et al., 2006).

Current trends suggest that the frequency of kidney disease will continue to rise in the coming years. A projection study indicates that the global number of individuals with chronic kidney disease will rise to 850 million by 2030 due to the increasing prevalence of diabetes, hypertension, and obesity (Bikbov et al., 2020). According to some predictions, CKD will affect more than 16% of the population in the United States alone by 2030 (Tuttle et al., 2014).

The escalation of CKD underscores the urgent need for new and effective therapies to prevent and manage kidney disease. Novel treatment strategies targeting the early stages of CKD, as well as addressing obesity, type 2 diabetes mellitus, and hypertension, are essential to mitigate the impending burden of renal disease on healthcare systems globally.

1.4.1.4 Glomerulonephritis

Glomerulonephritis is a significant cause of renal scarring (Satoskar et al., 2020). It can be defined as inflammation of the glomerulus caused by an immune or autoimmune process. It is characterised by immune-mediated damage to the glomerular basement membrane, the mesangial cells, or the capillary endothelial cells, resulting in proteinuria and haematuria (Kazi and Hashmi, 2023).

1.4.1.5 Pyelonephritis

The primary cause of chronic renal scarring in childhood is pyelonephritis, leading to hypertension, CKD, and progression to ESRD in a small but significant fraction of patients. Acute pyelonephritis can be defined as an infection caused by bacteria such as *Escherichia coli, Proteus, Klebsiella,* and *Enterobacter* that causes kidney inflammation. It is a complication of an ascending urinary tract infection that spreads to the kidneys and their collecting systems from the bladder (Belyayeva and Jeong, 2023). Consequently, the long-term deterioration in kidney function can be caused by pyelonephritis, and the risk of ESRD being treated significantly increases, particularly with renal scarring or reduced kidney function. In addition, potential pyelonephritis complications include sepsis, renal scarring, acute renal failure, and renal transplant pyelonephritis (Belyayeva and Jeong, 2023).

1.4.1.6 Polycystic Kidney Disease

Polycystic Kidney Disease is a significant cause of ESRD in both children and adults. This genetic disorder is characterised by the development of numerous fluid-filled cysts in the kidneys and other epithelial organs. It is inherited in two forms: autosomal dominant polycystic kidney disease and autosomal recessive polycystic kidney disease. Patients with this disease often experience advanced renal cyst formation and kidney enlargement, which can lead to severe renal insufficiency and, ultimately, ESRD. These patients typically require renal replacement therapy, such as dialysis or kidney transplantation, to manage the disease's progression (Bergmann et al., 2018).

1.4.1.7 Tubulointerstitial Nephropathies

Tubulointerstitial nephropaties is a recurrent cause of acute renal failure, described by an immune-mediated infiltration and accumulation of inflammatory cells in the interstitial kidneys (Joyce et al., 2017, Ulinski et al., 2012). The interstitial inflammation may lead to

chronic changes with the ongoing progression of CKD. Numerous aetiologies can contribute to the development of tubulointerstitial nephritis, including genetic and environmental factors, such as drug exposure, systemic autoimmune, infectious, genetic, and idiopathic (Joyce et al., 2017).

Currently, Type 2 diabetes and hypertension are the two leading causes of CKD. Furthermore, CKD's development and progress have been associated with obesity and smoking and were affected by metabolic factors such as insulin resistance, dyslipidaemia and hyperuricemia. It can be determined by the loss of kidney cells and their replacement with the extracellular matrix (ECM).

1.5 Animal Models

The development of new and effective treatments for renal scarring depends on expanding our understanding of the biochemical pathways and molecular triggers involved in the scarring process. Animal models have played a vital role in advancing our knowledge of matrix turnover and have provided a theoretical framework for analysing the scarring response in renal disease. Various animal models have been developed to mimic the functional and histological changes seen in human kidney diseases to varying degrees of accuracy (Chevalier, 2016).

Several animal models have been developed that, to a greater or lesser extent, reflect the changes observed in kidney function and histochemical tissue profiles in human disease (Chevalier et al., 2009).

The two most common models used are the mouse unilateral ureteral obstruction (UUO) model and the rat subtotal nephrectomy (SNx) model. Both models have distinct features that make them valuable for studying the pathological mechanisms of renal fibrosis and scarring and the potential efficacy of novel therapeutic interventions. The UUO model is beneficial for exploring the early fibrotic response, as it induces progressive tubulointerstitial fibrosis (Cao et al., 2015). On the other hand, the SNx model is commonly employed to study chronic kidney disease progression, as it mirrors long-term structural and functional changes associated with glomerulosclerosis and tubulointerstitial fibrosis (Zhang and Kompa, 2014).

1.5.1 Subtotal Nephrectomy (SNx) Model

The SNx model involves the surgical removal of a significant portion of kidney tissue, leading to compensatory hypertrophy and hyperfiltration in the remaining nephrons. These compensatory mechanisms eventually fail, resulting in glomerulosclerosis, tubular atrophy, interstitial fibrosis, and, ultimately, renal failure. This model is particularly relevant for studying the progression of CKD because it mirrors the gradual development of fibrosis observed in human patients, making it an invaluable platform for testing therapeutic interventions aimed at slowing or reversing renal fibrosis (Lafayette et al., 1992).

For example, a study conducted by Lafayette et al. (1992) demonstrated the potential of angiotensin II receptor antagonists in the SNx model. The study found that treatment with these antagonists significantly reduced glomerulosclerosis and interstitial fibrosis,

highlighting the therapeutic promise of targeting the renin-angiotensin system in managing CKD (Lafayette et al., 1992). Additionally, in a study by Johnson et al. (2007), tissue transglutaminase 2 (TG2) inhibition significantly reduced fibrosis and preserved renal function in the SNx model, highlighting the potential therapeutic benefits of targeting TG2 in CKD treatment. This study demonstrated that TG2 inhibitors could effectively reduce extracellular matrix accumulation, thereby slowing the progression of renal fibrosis (Johnson et al., 2007).

1.5.2 Unilateral Ureteral Obstruction (UUO) Model

The UUO model is another well-established method for inducing renal fibrosis by obstructing the ureter of one kidney. This leads to increased intratubular pressure, inflammation, tubular atrophy, and rapid interstitial fibrosis. This model is particularly valuable for its reproducibility and the speed with which fibrosis develops, making it an ideal platform for evaluating the efficacy of anti-fibrotic therapies (Chevalier et al., 2009).

An example of using the UUO model is the study that demonstrated the role of Transforming Growth Factor Beta (TGF-β) in promoting fibrosis. Moreover, in this study, blocking TGF-β signalling in the UUO model significantly reduced fibrosis, providing strong evidence that TGF-β is a critical mediator of fibrotic changes in the kidney (Yang et al., 2005).

Both the SNx and UUO models have been instrumental in demonstrating the efficacy of various therapeutic approaches, including tissue transglutaminase 2 (TG2) inhibitors and TGF-β antibodies, which have shown promise in reducing fibrosis in these settings (Johnson et al., 2007, Yang et al., 2005).

1.6 Biochemical Mechanisms Leading to Renal Scarring

Renal scarring can be defined as the gradual depletion of typical tissue architecture and replacement with an abnormal extracellular matrix (ECM). The renal cellular loss and the excessive and inappropriate accumulates of collagen and other ECM components lead to scarring of both glomerular (glomerulosclerosis), the renal interstitial (tubulointerstitial sclerosis), and the thickening of blood vessel walls (vascular sclerosis) associated with declining renal function, which leads to end-stage renal disease (Meng et al., 2014). The pathophysiology of glomerulosclerosis is similar to the pathophysiology of tubulointerstitial fibrosis. Glomerulosclerosis and tubulointerstitial fibrosis may result from an imbalance between excessive synthesis and decreased breakdown of the extracellular matrix, resulting from a normal wound-healing response being deregulated, with the proliferation of myofibroblasts and an uncontrolled inflammatory response (Nogueira et al., 2017).

Major enzymatic pathways essential in regulating cell and ECM turnover are influenced by multiple mediators, including profibrotic growth factors such as transforming growth factor (TGF-β) and platelet-derived growth factor (PDGF), pro-inflammatory cytokines, and chemokines (Johnson et al., 2003). For instance, activation of the PDGF family is essential in renal fibrosis development; it regulates cell proliferation, migration, production and accumulation of ECM (Ostendorf et al., 2012, Klinkhammer et al., 2018). Moreover, TGF-β is the most crucial cytokine that promotes glomerulosclerosis and tubulointerstitial fibrosis, as it activates mesangial cells and possibly plays a pivotal role in epithelial-mesenchymal transition. Activation of TGF-β induces a self-maintaining cycle of matrix deposition by increasing the protein synthesis and decreasing the matrix protein degradation, leading to persistent tissue injury (Nogueira et al., 2017). TGF-β also works to prevent ECM degradation by inhibiting the synthesis of matrix metalloproteinases (MMPs) and stimulating the synthesis of tissue inhibitor metalloproteinases (TIMPs) (Isaka, 2018).

In addition, TGF-β is released in a latent form and activated through tissue transglutaminase 2, a Ca^{2+}-dependent enzyme, resulting in increased ECM deposition and promoting tissue fibrosis. TG2 is pro-fibrotic and can crosslink several ECM proteins, increase their resistance to protein breakdown, increase net deposition and accumulation, and enhance cross-linked ECM stability (Szondy et al., 2017, Collighan and Griffin, 2009). Furthermore, TG2 is also involved in the transcription, secretion, and activation of TGF-β, which contributes to the

formation of a higher self-amplification loop in the development of fibrosis (Szondy et al., 2017).

MMPs are a family of zinc-containing endopeptidases that play various roles in renal inflammation and fibrosis, are involved in ECM remodelling, and are critical for regulating tissue development and homeostasis (Provenzano et al., 2020). In addition, MMPs are responsible for the degradation of collagen and other ECM proteins during average tissue turnover (Tsuruda et al., 2004). For instance, MMP9 is essential for neutrophil infiltration and tissue fibrosis induction (Murugapoopathy et al., 2020). The activities of MMPs are generally inhibited by TIMPs, which, in turn, tissue re-modelling and regulate ECM turnover. Therefore, TIMPs maintain the balance between ECM formation and ECM breakdown (Zakiyanov et al., 2019).

In summary, renal scarring can be seen as an imbalance between the deposition and turnover of matrix components. Inflammation, resulting from various potential causes, including hypertension, hyperglycaemia, and infection, shifts the biochemical pathways controlling matrix turnover, resulting in chronic scarring. Identifying the key players in regulating this pathway can suggest potential points of therapeutic intervention.

1.7 Therapeutic Approaches to Renal Scarring

Renal scarring, a consequence of persistent pathological processes despite the treatment of initial insults such as hypertension, diabetes, inflammation, infection, and genetic diseases, often progresses to chronic renal scarring. This progression can ultimately lead to end-stage renal failure, necessitating replacement therapy or transplantation (Campanholle et al., 2013). Various therapeutic strategies have been developed to address the complex mechanisms underlying renal scarring, targeting both the causes and the biochemical pathways involved in scar formation.

1.7.1 Targeting mediators of renal scarring

Understanding the biochemical basis of scarring has revealed multiple potential points for therapeutic intervention. Therapeutic strategies can broadly be divided into two categories: those addressing the underlying causes of scarring and inflammation and those directed at the biochemical processes that lead to the aberrant deposition of extracellular matrix (ECM) and subsequent scar formation.

1.7.1.1 Suppression of TGF-β Action

Inhibition of the TGF-β or its signalling pathways significantly limits renal fibrosis by reducing fibroblast activation and ECM deposition, whereas increased expression of TGF-β1 promotes fibrotic processes (Meng et al., 2014). Several approaches have been applied to disrupt TGF-β mediated responses, directly targeting TGF-β using natural TGF-β-binding proteins (such as decorin), antibodies, and soluble receptors. Other strategies involve blocking TGF-β receptors using small molecule inhibitors, targeting microRNA regulation by TGF-β, activating inhibitory Smads (such as Smad7), and promoting bone morphogenetic protein signalling. Smad proteins, critical mediators of TGF-β signalling, either promote fibrosis through Smad2/3 or inhibit it via Smad7, which blocks receptor phosphorylation and suppresses downstream signalling (Chuang et al., 2013, Isaka, 2018). However, TGF-β also has anti-inflammatory properties as it is an immunosuppressive molecule in the immune system. As a result, TGF-β inhibition could have severe influences on the immune system (Isaka, 2018, Meng et al., 2014).

1.7.1.2 PAI-1 and MMPs Inhibition

The matrix metalloproteinases (MMPs) family and the plasminogen activation system play critical roles in the homeostasis and regulation of extracellular matrix (ECM) components. These protease systems are interconnected since plasmin boosts MMP activity (Ruiz-Ortega et al., 2020). Plasminogen activator inhibitor 1 (PAI-1), an elevated protein in acute kidney injury and CKD, prevents fibrinolysis and contributes to ECM accumulation**.**

PAI-1 could be used as a possible therapeutic target for renal fibrosis (Rerolle et al., 2000) and, for instance, (Gu et al., 2016) inhibited PAI-1 activity with neutralising antibodies for four weeks in a type 2 diabetes mouse model. They found that it significantly prevented the expression of renal fibrosis markers and glomerular fibrotic morphology. In contrast, Matsuo et al. (2005) in a study on the UUO murine model found that overexpression of PAI-1 is essential in promoting fibrosis.

In a mouse model of obstructive nephropathy, it was found that the lack of MMP-9 appeared to protect the kidneys from fibrosis (Wang et al., 2010), including reducing ECM expression, preservation of thin basement membrane integrity, and blockade of tubular epithelial-to-mesenchymal transition. They demonstrated that blockade alone of MMP-9 improves renal interstitial fibrosis after obstructive injury but did not change the TGF-β1 induction. In addition, in a rat model of autosomal-dominant polycystic kidney disease, treatment with Batimastat (metalloproteinase inhibitor) led to a considerable reduction in cysts. In contrast, in a study of the role of MMP-2 in renal fibrosis and its influence on interstitial macrophage infiltration in a UUO mouse model, it was reported that treatment with a selective MMP-2 inhibitor appeared to accelerate renal fibrosis (Schelling, 2009).

1.7.2 Collagen Biogenesis

Tissue fibroblasts are the primary source of extracellular matrix production, including collagens (Yamauchi et al., 2018, Komohara and Takeya, 2017). The initial stage of collagen synthesis is the expression of pro-collagens. These are produced in the form of chains and are subsequently processed to form mature collagen molecules. Most collagens possess a conserved glycine-proline motif (Gly-Pro-X), and variations in the position and nature of the amino acid X residue define 28 different molecular subtypes of collagen (Collagen I-XXVIII) (Ricard-Blum, 2011, Gelse et al., 2003). An essential step in collagen processing is the enzymic

hydroxylation of proline and lysine residues, forming hydroxyproline and hydroxylysine. These residues contribute to the thermal stability of collagen in the mature matrix (Rappu et al., 2019). Helical procollagen molecules are subsequently exported to the extracellular space, where maturation continues with the enzymic cleavage at the N-terminal and C-terminal domains by various proteases, including bone morphogenic protein 1 and matrix metalloproteinases. Collagens are commonly heterotrimeric helical polymers that are, in turn, bundled into fibrils that comprise a significant component of the extracellular matrix. Formation and stabilisation of fibrils require additional processing. Critical steps in this process are catalysed by the lysyl oxidase (LOX) family of enzymes and transglutaminase (Fig. 1.2). The overall balance of ECM deposition and removal is influenced by the action of pro-fibrotic growth factors and the enzymic stabilisation of ECM components and their resistance to turnover.

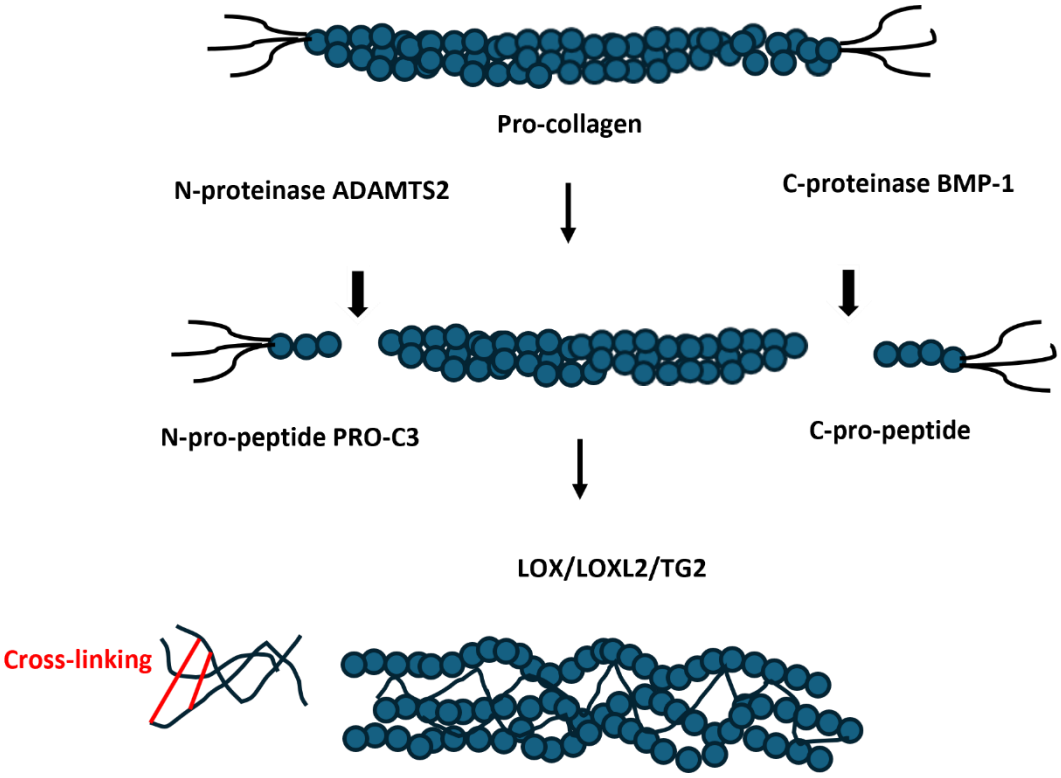

Figure 1.2: Synthesis and processing of collagen.

Pro-collagen is expressed and trimmed by the actions of ADAMTS2 and C-proteinase BMP-1. Mature collagen is then extensively crosslinked by the action of LOX and TG2.

1.7.2.1 Lysyl Oxidases (LOX)

Lysyl oxidase, also known as protein-lysine 6-oxidase, was first characterised by Pinnell and Martin in 1968 (Pinnell and Martin, 1968). The LOX family comprises LOX and four additional LOX-like (LOXL) 1-4 isoforms, which play crucial roles in the synthesis, maturation, and remodelling of the ECM. Different genes encode these isoforms (LOX, LOXL1, LOXL2, LOXL3, and LOXL4) and exhibit distinct, though sometimes overlapping, expression patterns and functions. Each gene contributes to the regulation of ECM homeostasis and tissue remodelling in various physiological and pathological contexts (Wang et al., 2021).

These enzymes are classified as copper-dependent and involved in the catalysis of ECM proteins, such as collagen and elastin, by forming aldehyde crosslinks. The oxidative deamination of the ε-amino groups of specific lysyl and hydroxylysine residues initiates the synthesis of these covalent crosslinks (Liburkin-Dan et al., 2022). The LOX enzymes stabilise bundles of mature collagen fibrils by oxidatively forming covalent inter-chain crosslinks between lysine residues, rendering them resistant to proteolytic cleavage. This ECM stabilisation significantly influences the ECM turnover and represents an essential factor in chronic scarring (Theocharis et al., 2016) .

A characteristic feature of the LOX family (Table 1.2) is a highly conserved catalytic domain at the carboxy terminus. This copper-binding domain comprises three conserved histidine residues (Fig.1.3). It catalyses the oxidation of tyrosine residue Tyr355, resulting in a conformation shift and the formation of a lysyl tyrosyl quinone intermediate and inter-chain bond formation (Chitty et al., 2019).

Table 1.2: The Key Features of Lysyl Oxidases.

Gene Name	Molecular Weight (kDa)	Protein size (Amino Acids)	Tissue expression	Localisation
LOX	~50	417	Wide distribution, including skin, lung, and aorta	ECM
LOXL1	~65	574	Eye, skin, heart, and kidney	ECM
LOXL2	~87	774	Liver, kidney, lung, placenta, and pancreas	ECM and nucleus
LOXL3	~82	729	Heart, skeletal muscle, and brain	ECM
LOXL4	~60	538	Wide distribution, including lung, heart, and kidney	ECM

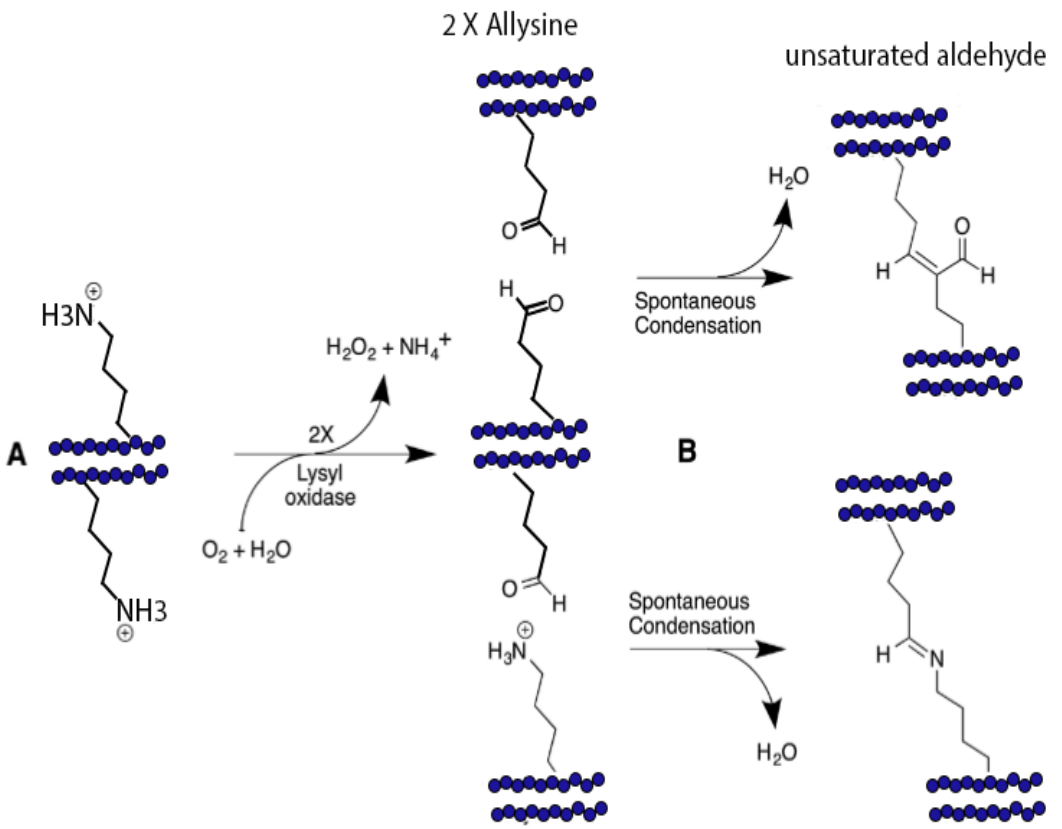

Figure 1.3: Crosslinking of collagen by LOX/LOXL.

LOX forms crosslinks through the oxidation of lysine. The aldehyde intermediate, allysine can condense in two ways to form a covalent bond with other amino acid residues in polypeptide chains.

1.7.2.2 LOX Structure

The LOX family members (Fig. 1.4) share a conserved overall structure, with some variations that contribute to their unique functional properties. At the N-terminus, these proteins possess a signal peptide that facilitates their secretion into the extracellular space. This peptide is cleaved upon secretion, ensuring the enzymes are correctly directed out of the cell (Trackman, 2016). This critical step enables their subsequent activity within the ECM.

The pro-peptide region follows the signal peptide and assists with the enzyme's correct folding, stabilisation, and secretion. Bone morphogenetic protein 1 or other proteases cleave the pro-peptide to generate the mature, active enzyme (Kagan and Trackman, 1991). This cleavage is a critical step, as it activates the enzyme, allowing it to perform its biological functions.

The core of the enzyme's activity resides in the lysyl oxidase domain, which contains the catalytic domain. This domain features a conserved copper-binding motif crucial for enzymatic function. It also contains a conserved lysine tyrosyl quinone cofactor formed by cross-linking a conserved lysine and a tyrosine residue essential for amine oxidase activity (Lucero and Kagan, 2006).

A distinctive feature of some LOX family members, specifically LOXL1, LOXL2, and LOXL3, is the presence of the Scavenger Receptor Cysteine-Rich (SRCR) domain. This domain is absent in LOX and LOXL4, suggesting functional diversification within the family. The SRCR domain is a structural foundation for interactions with other fibrosis regulators (Chen et al., 2020). The presence of this domain underscores the diverse roles played by different LOX enzymes in tissue remodelling and fibrosis.

Finally, the C-terminal region of these enzymes varies markedly in sequence and length between different LOX family members. For example, the C terminus of LOX is rich in basic amino acids, a feature essential for the oxidative deamination of peptidyl-lysine residues in target molecules (Lucero and Kagan, 2006). These differences in the C-terminal region also highlight the functional diversity of the LOX family, customising each enzyme to its specific biological role.

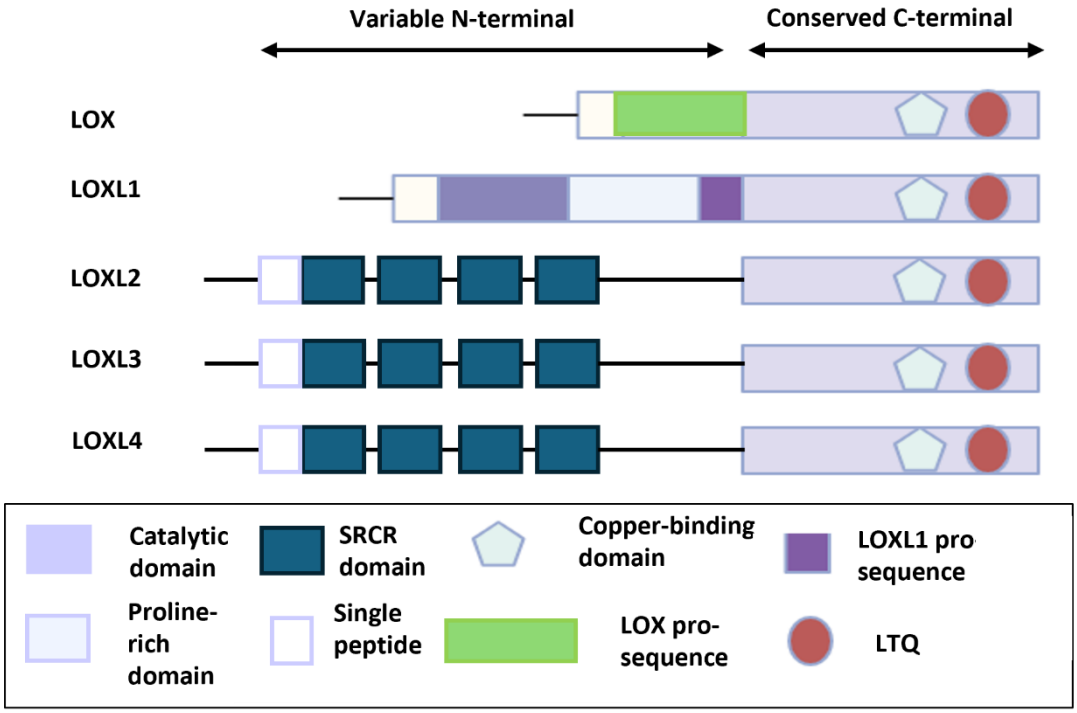

Figure 1.4: LOX family domain conservation and structural arrangements.

The LOX family members share a conserved overall structure, with some variations.

1.7.2.3 LOXL2 and LOXL4 Functions

LOXL2 and LOXL4 are pivotal members of the LOX family, which play crucial roles in cross-linking collagen and elastin within the ECM. This enzymatic activity is fundamental to maintaining tissue stability, elasticity, and remodelling. By facilitating the formation and stabilisation of collagen and elastin fibres, LOXL2 and LOXL4 significantly contribute to various tissues' structural integrity and resilience (Trackman, 2016).

These enzymes are integral to several physiological processes, including tissue development, fibrosis, and tissue repair. During tissue development, LOXL2 and LOXL4 help establish the ECM framework that supports cellular architecture and function. In the context of fibrosis, these enzymes contribute to the excessive accumulation and cross-linking of collagen, leading to tissue stiffening and scarring, characteristic of fibrotic diseases (Barker et al., 2012). Moreover, in tissue repair, LOXL2 and LOXL4 facilitate the remodelling of the ECM, aiding in restoring tissue integrity following injury.

In addition to their roles in normal physiological processes, LOXL2 and LOXL4 have been implicated in cancer progression. Their ability to modulate cell adhesion, migration, and invasion plays a significant role in the metastatic spread of cancer cells. By altering the ECM, these enzymes can create a microenvironment conducive to tumour cell dissemination, promoting metastasis (Peinado et al., 2008). This involvement in cancer progression highlights the potential of LOXL2 and LOXL4 as targets for therapeutic intervention in oncology.

Overall, LOXL2 and LOXL4 are essential for maintaining ECM integrity and functionality and influence various physiological and pathological processes. Their contributions to tissue development, repair, fibrosis, and cancer underscore their importance in health and disease.

1.7.2.4 The Role of LOXL2 and LOXL4 in Chronic Scarring and Fibrosis

LOXL2 and LOXL4 have been implicated in the development of chronic scarring due to their roles in the formation and stabilisation of the ECM through the crosslinking of collagen and elastin fibres. Chronic scarring, characterised by excessive deposition of ECM components, is a hallmark of various fibrotic disorders.

LOXL2 has been extensively studied and implicated in the progression of several fibrotic diseases, including liver, pulmonary, and kidney fibrosis. In these conditions, upregulation of LOXL2 has been observed, contributing to excessive ECM deposition and increased tissue

stiffness, ultimately leading to organ dysfunction (Barry-Hamilton et al., 2010, Tjin et al., 2017). The overexpression of LOXL2 in these pathological contexts underscores its critical role in the development and perpetuation of fibrosis.

In contrast, the direct involvement of LOXL4 in chronic scarring is less well-documented, although it remains an essential member of the LOX family. LOXL4 contributes to the stabilisation of the ECM through its ability to cross-link collagen and elastin fibres (Mäki et al., 2002). Despite the limited evidence of its direct role in chronic scarring, the fundamental functions of LOXL4 in matrix stabilisation suggest it could support fibrotic processes. Further research is required to elucidate the specific contributions of LOXL4 to chronic scarring and fibrotic diseases.

In summary, while the involvement of LOXL2 in chronic scarring and fibrotic diseases is well-documented, with significant evidence supporting its role in pathological ECM deposition, the role of LOXL4 in these conditions is unclear. Both enzymes are crucial for the formation and stabilisation of the ECM, which is a critical component of chronic scarring. Understanding the specific functions and regulatory mechanisms of LOXL2 and LOXL4 remains essential for developing targeted therapies for fibrotic diseases.

1.7.2.5 Therapeutic Potential of LOXL2 and LOXL4 Inhibition

Targeting LOXL2 and LOXL4 as therapeutic approaches to renal scarring is a promising strategy due to their involvement in ECM stabilisation and collagen and elastin crosslinking. Inhibiting these enzymes could reduce this fibrotic response and improve kidney function.

1.7.2.6 Small Molecule Inhibitors

Small molecules that selectively inhibit the enzymatic activity of LOXL2 and LOXL4 could help reduce excessive collagen and elastin cross-linking, alleviating renal scarring and fibrosis. For instance, a study conducted by Schilter et al. (2019) demonstrated that PXS-5153A, a small-molecule inhibitor targeting LOXL2/LOXL3 enzymes, reduced liver fibrosis in both carbon tetrachloride and streptozotocin/high-fat diet-induced models. Additionally, it improved cardiac output in a myocardial infarction murine model. The study concluded that PXS-5153A could reduce crosslinks and ameliorate fibrosis in liver and kidney models, providing a basis for further investigation into its therapeutic potential for fibrotic diseases.

1.7.2.7 Monoclonal Antibodies

Monoclonal antibodies explicitly targeting LOXL2 or LOXL4 can be developed to neutralise their activity in the ECM, thus reducing fibrosis and scarring. Developing monoclonal antibodies against LOXL2 has shown potential in preclinical studies for other fibrotic diseases (Rodriguez et al., 2010). Barry-Hamilton et al. (2010), they demonstrated that inhibition of LOXL2 using a monoclonal antibody, AB0023, reduced the development of a pathologic microenvironment, including the accumulation of collagen and the recruitment of immune cells, in animal models of fibrosis and cancer metastasis, such as the CCl4-induced liver fibrosis model and the bleomycin-induced lung fibrosis model.

Puente et al. (2019) evaluated the effects of the monoclonal antibody simtuzumab, which targets LOXL2, in preclinical and clinical studies. In preclinical models, LOXL2 inhibition using Simtuzumab showed promising results, reducing fibrosis and collagen crosslinking. However, in clinical trials, Simtuzumab did not demonstrate significant efficacy in patients with advanced liver fibrosis or non-alcoholic steatohepatitis (NASH).

The study concludes that, although Simtuzumab failed to show significant benefits in clinical trials, LOXL2 remains an exciting target for anti-fibrogenic therapy. The findings from these studies suggest that LOXL2 inhibition remains an exciting target for anti-fibrogenic therapy. Further research is needed to understand the role of LOXL2 in fibrosis better and develop novel therapeutic strategies targeting LOXL2 for treating fibrotic diseases.

The lack of research on monoclonal antibodies that inhibit LOXL4 suggests a pressing need for further investigation to explore their potential benefits and limitations in treating fibrosis and other LOXL4-related diseases.

1.7.2.8 Antisense oligonucleotides (ASOs) or RNA interference (RNAi)

Utilising ASOs or RNAi to silence LOXL2 and LOXL4 gene expression can reduce enzyme production, decreasing their impact on ECM remodelling and renal scarring. Cosgrove et al. (2018) studied the effects of LOXL2 in Col4α3/Alport mice, a model of Alport syndrome characterised by mutations in the Col4α3 gene encoding type IV collagen. These mice develop kidney fibrosis and progressive renal failure, making them ideal for studying renal scarring. The researchers found that LOXL2 was upregulated in the kidneys of these mice and that LOXL2 knockout led to reduced renal fibrosis, improved renal function, and increased survival

rates. Additionally, LOXL2 knockout diminished the expression of fibrotic markers such as collagen and alpha-smooth muscle actin and inhibited the activation of myofibroblasts, which are key drivers of fibrosis.

In contrast, there is limited research on LOXL4 knockdown as a therapeutic approach for fibrosis and related diseases. Further investigation is required to understand how LOXL4 contributes to these conditions and assess the efficacy and safety of LOXL4 inhibition. This research is crucial to determine optimal dosages, delivery methods, potential side effects, and the long-term effects of LOXL4 inhibition, aiming to develop new therapies that enhance clinical outcomes and elevate the overall quality of life for patients.

1.7.2.9 Tissue Transglutaminase

Transglutaminase was first described as a hepatic enzyme that catalysed the transfer of carboxamide groups of glutamine residues and accepter primary amine groups (Mycek et al., 1959). Subsequently, it was demonstrated that the transglutaminase catalysed the formation of an isopeptide crosslinking bond between glutamine and lysine residues in fibrin and that protein crosslinking was a central characteristic activity of the TG family of enzymes (Pisano et al., 1968).

These ε-(γ-glutamyl) lysine covalent bonds are very stable and resistant to proteolysis, and this crosslinking activity plays a critical role in a range of biological processes, including blood clotting, epidermis development, and fibrosis (Griffin et al., 2002). Transglutaminases are a superfamily of structurally similar enzymes, and nine members have been identified (Griffin et al., 2002) in humans.

The most important family members include factor XIIIa (clot stabilisation), TG1, which is essential for keratinocyte differentiation, and TG2, or tissue transglutaminase, which is expressed in all tissues and is the primary mediator of ECM homeostasis and wound healing (Griffin et al., 2002).

The catalytic domain of these enzymes (Fig. 1.5) is relatively conserved and features an invariant cysteine residue that acts as a transient reaction centre in a nucleophilic double displacement process (Groenen et al., 1994).

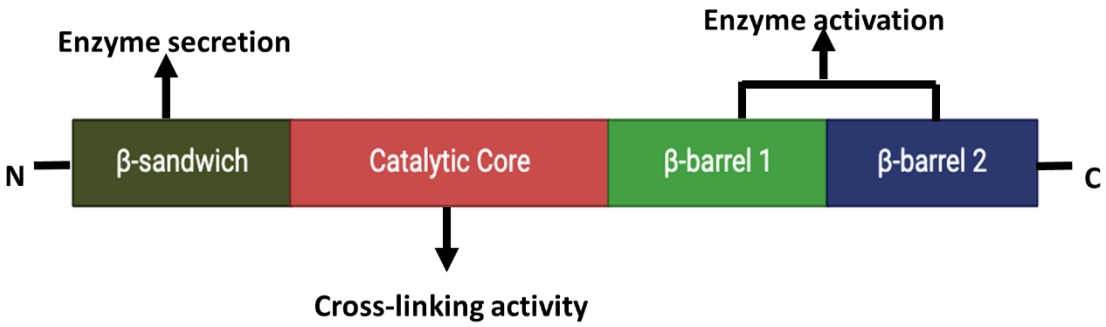

Figure 1.5: TG2 Domain Structure.

The TG2 domain structure includes a β-sandwich domain (amino acids 1–138) at the amino terminus, which mediates enzyme secretion. The catalytic core (amino acids 139–472) is responsible for the enzyme's cross-linking activity. Two β-barrel domains (β-barrel 1: amino acids 473–584, β-barrel 2: amino acids 585–687) play a role in enzyme activation. The protein has an overall size of 687 amino acids.

1.7.2.10 TG2 and Fibrosis

TG2 plays a central role in the stabilisation of ECM. Catalytic crosslinking collagens and other components of ECM, including fibronectin, stabilise the matrix and render it resistant to degradation by matrix metalloproteinases and other proteolytic enzymes. TG2 expression and activity are increased by the action of pro-fibrotic stimuli such as TGF-β and PDGF, and TG2 protein levels have been shown to correlate with fibrotic disease progression in a range of patient studies and experimental models including skin, liver, lung, and chronic renal scarring (Nardacci et al., 2003, Mirza et al., 1997, Grenard et al., 2001, Johnson et al., 1997).

Evidence suggests that dysregulation of TG2 activity in various pathological settings may be an essential driver of the chronic scarring process (Skill et al., 2001). In humans and animals, TG2 crosslinking activity is significantly increased in renal scarring, and the activity level correlates well with disease severity (Verderio et al., 2005).

Ikee et al. (2007) highlighted how elevated TG2 activity is related to renal disease progression, particularly in conditions like CKD and diabetic nephropathy. Another study demonstrated that TG2 plays a critical role in the development of renal fibrosis by promoting the accumulation of fibrillar collagen through TGF-β activation and enhancing inflammatory cell infiltration. These findings suggest that therapeutic strategies targeting TG2 inhibition could effectively reduce renal fibrosis and improve outcomes for patients with chronic kidney disease (Shweke et al., 2008).

Linge et al. (2005) found that hypertrophic scar cells resist a specific form of apoptosis, typically triggered by contractile collagen. This resistance is linked to the activity of TG2, which suggests that TG2 plays a crucial role in the persistence of hypertrophic scars by preventing the normal apoptotic process in these cells. Targeting TG2 may represent a potential therapeutic approach to reduce or prevent hypertrophic scarring.

1.7.2.11 TG2 as a Therapeutic Target

Given the multiple functions of TG2 related to chronic renal diseases, including cell adhesion and migration, insulin secretion, wound healing, and apoptosis, this enzyme may represent a valuable therapeutic target in situations of fibrous proliferation, including CKD (Schelling, 2009). For instance, administering two different TG2 inhibitors reduced scarring in rat models of renal fibrosis (Johnson et al., 2007). It was found that both inhibitors could ameliorate the

decline in renal function and reduce the progression of glomerulosclerosis by up to 77% and tubulointerstitial fibrosis by up to 99%. Inhibition of TG2 activity reduced the accumulation of collagen I and collagen III by directly inhibiting the crosslinking of ECM. Thus, it was demonstrated that transglutaminase inhibition offers a possible therapeutic option for kidney disease and other conditions caused by tissue fibrosis. In addition, TG2-knockout mice showed that abrogation of TG2 activity reduced the effects of experimental renal fibrosis, and the lack of TG2 expression did not produce an unhealthy phenotype (Furini et al., 2018). These results and other studies suggest that inhibiting extracellular TG2 activity may represent a proper therapeutic strategy for treating fibrotic diseases.

One major obstacle in developing anti-TG2 treatments has been the difficulty in producing specific inhibitors. Many early small molecule compounds were pan-TG blockers, exhibiting activity against multiple members of the TG enzyme family. Given the importance of TG enzymes in physiological processes such as blood clotting and maintaining skin structure, the use of these inhibitors often resulted in side effects in patients, limiting their suitability for systemic treatments (Siegel and Khosla, 2007). Some studies looked at the local delivery of the agents so that dosage could be kept to a minimum; targeted delivery of TG2 inhibitors remains one possible strategy for future applications (Johnson et al., 1997).

Recent developments have seen the development of more specific TG2 inhibitors (Schaertl et al., 2010) including the ZDON family of compounds(McConoughey et al., 2010). This compound family is derived from synthetic peptide TG2 substrates modified to form chemical bonds with the TG2 active site and act as irreversible enzyme inhibitors. These improvements in enzyme specificity and advances in tissue-targeted delivery will see TG2 inhibitors come to the forefront of anti-scarring therapeutics.

1.7.2.12 TG2-Inhibitory Monoclonal Antibody Zampilimab

Our research group has developed a novel monoclonal antibody targeting TG2, as detailed in the published study titled *"The Effect of TG2-Inhibitory Monoclonal Antibody Zampilimab on Tissue Fibrosis in Human In Vitro and Primate In Vivo Models of Chronic Kidney Disease"*. This study investigates the therapeutic potential of Zampilimab, a TG2-inhibitory monoclonal antibody, in combating fibrosis related to CKD.

The research emphasises the pivotal role of TG2 in the progression of renal fibrosis, a common complication of CKD that significantly contributes to kidney function decline. TG2 is implicated in the cross-linking of ECM proteins, which results in the excessive accumulation of fibrotic tissue within the kidneys.

Zampilimab was explicitly designed to inhibit TG2 activity, and its efficacy was evaluated in both human in vitro kidney cell models and *in vivo* primate models of CKD. In vitro, Zampilimab significantly demonstrated a reduction in TG2 activity in cultured human kidney cells. This inhibition correlated with a marked decrease in the deposition of fibrotic markers such as collagen, which are characteristically elevated in fibrotic kidney conditions.

In the *in vivo* primate models, Zampilimab treatment led to a notable reduction in renal fibrosis, as evidenced by decreased accumulation of collagen and other fibrotic components in the kidneys. Furthermore, the treated primates showed improved renal function compared to untreated controls. The mechanism of action of Zampilimab involves binding to TG2, thereby preventing its enzymatic activity. This inhibition disturbs the crosslinking of ECM proteins, a crucial process in fibrosis development, consequently reducing fibrotic tissue formation and aiding in preserving kidney function.

The findings suggest that Zampilimab holds promise as a novel therapeutic agent for managing fibrosis in CKD. By targeting TG2, Zampilimab introduces a new strategy for slowing or potentially reversing renal fibrosis, a significant driver of CKD progression. The study concludes that Zampilimab exhibits substantial potential as an antifibrotic therapy, with positive outcomes observed in both in vitro and *in vivo* models (Huang et al., 2024). Further clinical trials are required to assess its safety and efficacy in human patients; however, these preliminary results offer a promising outlook for developing TG2 inhibitors as a new class of antifibrotic therapies.

1.8 Drug Delivery System

Traditional drug delivery methods, which introduce therapeutic drugs or medicines into the body through formulations or devices, aim to enhance safety and effectiveness by controlling the rate, time, and place of release of drugs in the body (Jain, 2008). However, drug delivery systems, such as oral, intravenous, or intramuscular administration, often suffer from limitations, including rapid systemic clearance, poor bioavailability, and accidental off-target effects. These drawbacks can reduce the treatment efficacy and increase the risk of adverse reactions. Consequently, developing sophisticated drug delivery systems has become a focal point in pharmaceutical research. These systems are designed to optimise the delivery of therapeutic drugs by precisely controlling the timing, rate, and location of drug release within the body, thereby enhancing therapeutic outcomes and minimising side effects (Allen and Cullis, 2013).

Various pharmaceutical particles, including different shapes and sizes, have been employed in the drug delivery systems, ranging from conventional tablets to the most recent formulations of nanoparticles. One of the significant challenges for many disease treatments is delivering the therapeutic compound to the target site. Traditional delivery methods can be limited in their effectiveness, showing poor distribution in the body and requiring systemic dosing, which leads to higher drug concentrations outside the target tissue and increases the probability of off-target side effects (Wilczewska et al., 2012).

The effective administration of therapeutic drugs remains one of the biggest challenges in modern medicine. Controlling drug delivery can overcome these limitations and drawbacks. In controlled drug delivery systems, the drug is transported to the target site, thus minimising its impact on vital tissues and reducing unwanted side effects. Furthermore, these systems can safeguard the drug from rapid degradation or clearance, which means lower doses of medication are required (Morishita et al., 2015, Ma et al., 2020, Mitchell et al., 2021, Wilczewska et al., 2012).

1.8.1 Targeted Drug Delivery

Targeted drug delivery represents an unconventional therapeutic approach aimed at optimising the delivery of therapeutic agents directly to specific sites within the body, such as particular organs, tissues, or cells. This method significantly enhances the drug concentration

at the target site, thereby increasing treatment efficacy and minimising the systemic side effects typically associated with drug administration. Essentially, the purpose of targeted drug delivery is to ensure that the drug reaches the intended site of action preferentially. The vital advantage of this technique is that it allows for administering lower doses of the drug, which can substantially reduce adverse effects. This benefit has positioned targeted drug delivery as a cornerstone in clinical research and pharmaceutical development, underscoring its pivotal role in advancing therapeutic and diagnostic applications. Various drug carriers are employed in these advanced delivery systems, including monoclonal antibodies and fragments, soluble polymers, liposomes, lipoproteins, and nanoparticles. The primary objective of a targeted drug delivery system is to extend the duration of drug action, localise the drug to specific sites, target the diseased tissue, and protect the drug from premature interactions, thus ensuring a more effective and safer drug interaction with the target tissue (Rani and Paliwal, 2014).

1.8.1.1 Nanoparticles

Nanoparticles are conventionally described as particles or molecular assemblies with a diameter within the 1-100 nanometre range. They arise in nature, though recent studies have focused on developing synthetic molecular constructs that possess valuable functions in various fields, from technology to medicine. Clinical applications of nanoparticles have centred on their use as drug-delivery vehicles (Mitchell et al., 2021).

Specific cells or tissues can be targeted using nanoparticles allocated to be sized, charged, shaped, and dense with the relevant ligands. The size of nanoparticles impacts cell uptake, circulatory circulation half-life, and targeting (Ma et al., 2020). It is necessary to consider the physical characteristics of nanoparticles, such as size, surface charge, shape, and density, when attempting to overcome a biological barrier and reach their designated cellular target. The great potential of nanoparticles for drug delivery is shown by their capacity to reduce drug accumulation in renal tubules, decreasing renal tubular toxicity (Zhou et al., 2014).

Morishita et al. (2015) used polyethyleneimine nanoparticles that contain miR-146a, which were then injected into the mouse's tail vein and demonstrated that miR-146a was delivered to and overexpressed in the obstructed kidney induced by-UUO (Morishita et al., 2015). The activation of the TGF-β1-Smad and nuclear factor kappa B signalling pathways was reduced

by miR-146a, which minimised renal fibrosis. Delivering miR-146a, which inhibits profibrotic and inflammatory signalling pathways, appears to prevent renal fibrosis. Thus, providing appropriate miRs could be a therapeutic option for preventing renal fibrosis *in vivo* (Morishita et al., 2015).

In addition, it has been shown that polycyclic nanoparticles can be used to siRNA to glomerular mesangial in mice (Zuckerman et al., 2015), which can be used to deliver siRNA against particular targets. Furthermore, (Yu et al., 2019) demonstrated that 100 nm diameter poly (lactic-glycolic acid) nanoparticles could selectively accumulate in affected mice kidneys in correlation with the degree of kidney injury. Consequently, the result showed a significant reduction in tubular necrosis, better renal function in the initial stage, less collagen deposition, and improved renal fibrosis in the healing phase.

Using peptide and protein conjugates can also be a helpful strategy for improving nanoparticle targeting. Different conjugates can enhance chemical and biological stability and deliver particles' tissue and cellular distribution (Spicer et al., 2018).

Antibodies feature superlative affinity and specificity for their corresponding antigen, and accordingly, the use of antibody-nanoparticle conjugates is an increasing area of therapeutic research (Richards et al., 2017, Cardoso et al., 2012, Shargh et al., 2016). If the target tissue expresses a specific antigen, antibody-targeted nanoparticle treatment is possible.

Kidney tubules express a specific glucose transporter, SGLT2, with mRNA levels approximately 15 times higher than any other tissue (Rahmoune et al., 2005). SGLT2 is expressed mainly by the tubular epithelium and represents an abundant target protein in the kidney. The availability of a high-affinity monoclonal antibody directed against SGLT2 would allow the possibility of an engineered antibody-nanoparticle conjugate for enhanced drug delivery.

1.8.1.2 Engineering Antibodies for Targeted Delivery

The engineering of antibodies for targeted drug delivery has emerged as a crucial improvement in modern therapeutics, particularly in treating complex diseases such as cancer, autoimmune disorders, infectious diseases, and chronic inflammation. Antibodies are naturally occurring proteins with high antigen specificity, making them ideal candidates for targeted therapy. By engineering antibodies to recognise and bind to specific antigens expressed on the surface of diseased cells, it is possible to deliver therapeutic agents directly

to the disease site while sparing healthy tissues. This targeted approach enhances the treatment's efficacy and significantly reduces systemic toxicity and other side effects commonly associated with conventional therapies (Carter and Lazar, 2018).

Modern advancements in genetic and protein engineering have enabled the development of monoclonal antibodies (mAbs) with improved binding affinities, enhanced stability, and extended half-lives, making them more effective in clinical applications (Carter and Lazar, 2018). These engineered antibodies can be conjugated with various therapeutic agents, such as cytotoxic drugs, radioisotopes, or even small interfering RNA (siRNA), allowing for the precise delivery of these agents to the target cells. Furthermore, developing bispecific antibodies, which can bind to two different antigens simultaneously, represents a significant innovation in this field, offering even greater targeting specificity and therapeutic potential (Beck et al., 2017).

Antibody-drug conjugates (ADCs) are one of the most promising applications of engineered antibodies in targeted drug delivery. ADCs combine the high specificity of antibodies with the potent cytotoxic effects of chemotherapeutic agents, allowing for the direct targeting of cancer cells while minimising damage to healthy cells. This approach has shown considerable success in clinical trials, leading to the approval of several ADCs for the treatment of various cancers (Beck et al., 2017).

The field of antibody-mediated drug delivery has advanced significantly beyond early-generation antibody-drug conjugates (ADCs) that featured random conjugation and partially humanised antibodies. Modern approaches emphasise fully humanised or human-derived antibodies, site-specific conjugation techniques, next-generation linker chemistries, and innovative payloads. Such improvements aim to optimise drug-to-antibody ratios, enhance tumour penetration, improve pharmacokinetics, and minimise immunogenicity (Beck et al., 2017, Raeeszadeh-Sarmazdeh & Boder, 2022).

For example, HER2-targeted ADCs like trastuzumab deruxtecan (Enhertu®) employ a cleavable linker paired with a potent topoisomerase I inhibitor, achieving high internalisation efficiency and a bystander effect that extends cell killing beyond those directly targeted (Modi et al., 2020). Similarly, sacituzumab govitecan-hziy (Trodelvy®), which targets Trop-2, demonstrates how refined linkers and stable, highly potent payloads can improve outcomes

in difficult-to-treat conditions like metastatic triple-negative breast cancer (Bardia et al., 2019). Meanwhile, polatuzumab vedotin-piiq (Polivy®) shows how site-specific conjugation enhances ADC stability and efficacy in haematological malignancies (Tilly et al., 2022).

Beyond canonical IgG formats, engineered antibody fragments, bispecific antibodies, and nanobody-based conjugates are being explored. These designs can deliver cytotoxic payloads, immune effectors, or even nucleic acids directly to target cells and are often more amenable to tissue penetration, improving tumour selectivity while minimising off-target toxicity (Labrijn et al., 2019, Van Audenhove & Gettemans, 2016). Efforts are also underway to address the complexities of solid tumours—such as heterogeneous antigen expression and limited drug penetration—through careful target selection, improved payload potency, and the development of modular, adaptable platforms.

Collectively, these advances underscore a vibrant, rapidly evolving field. As antibody engineering, conjugation chemistry, and payload optimisation continue to progress, antibody-mediated drug delivery systems will likely offer safer, more effective, and more versatile treatments across a broad range of diseases.

1.9 Monoclonal Antibodies (mAbs)

1.9.1 General Structure and Function of Antibodies

Antibodies, or immunoglobulins (Ig), are essential glycoprotein molecules that play a pivotal role in the immune system's defence mechanisms by identifying and neutralising foreign pathogens such as bacteria and viruses. B-lymphocytes produce them in response to foreign antigens, which can be either protein or polysaccharide molecules that may be unfamiliar to the body, known as antigens. Furthermore, antibodies primarily bind to antigens or foreign cells, thus facilitating their recognition and subsequent destruction by phagocytes, including macrophage and complement proteins (Abbas et al., 2002).

The specific region of the foreign antigen to which an antibody binds is known as the epitope or antigen determinant (Fig. 1.6). Typically, this epitope consists of a short sequence of amino acids that the antibody identifies and binds to. Consequently, mAbs represent highly purified and specific antibodies targeted against a singular epitope. Importantly, each antibody produced is tailored with high specificity to the unique antigen that triggered its production. This remarkable specificity allows antibodies to selectively recognise and target the specific antigens they were designed to combat, contributing significantly to the body's ability to mount a highly targeted immune response (Talreja et al., 2020).

Structurally, antibodies are Y-shaped molecules consisting of two identical heavy chains and two identical light chains connected by disulphide bonds (Murphy and Weaver, 2017, Maibom-Thomsen et al., 2019). Each antibody molecule possesses two essential functional regions: a constant (Fc) region and a variable antigen-binding fragment (Fab) region. The Fc region is responsible for interacting with immune effector cells and mediating functions such as antibody-dependent cellular cytotoxicity and complement activation, which drives the functional activities of the antibody (Janeway et al., 2001, Lu et al., 2018, Abbas et al., 2021). The Fab region, conversely, is crucial for antigen binding and is highly variable, allowing for the vast diversity of antibodies that the immune system can produce (Lu et al., 2018, Schroeder Jr and Cavacini, 2010). This antibody can exist as a monomer or, in the cases of IgM and IgA, can form multimers (Lu et al., 2018).

The heavy chains encompass various classes, including μ (corresponding to IgM), δ (IgD), α (IgA), γ (IgG), and ε (IgE). In contrast, the light chains may belong to either κ or λ types. The N-

terminal variable domains of both light and heavy chains collectively shape two distinct antigen-binding sites, which, when combined with the CH1 and constant light domains, form the (Fab) arms. Conversely, the CH2 and CH3 domains (or CH2-4 in the case of IgM and IgE) come together to constitute an Fc region (Maibom-Thomsen et al., 2019).

The specificity of an antibody's binding to its antigen is determined by the unique structure of the variable region, particularly the complementarity-determining regions (CDRs) within the Fab region. These CDRs interact with specific epitopes on antigens, enabling precise recognition and binding (Abbas et al., 2021, Schroeder Jr and Cavacini, 2010). This high specificity underpins the therapeutic potential of antibodies, particularly in targeted therapies where minimising off-target effects is crucial (Nelson et al., 2010).

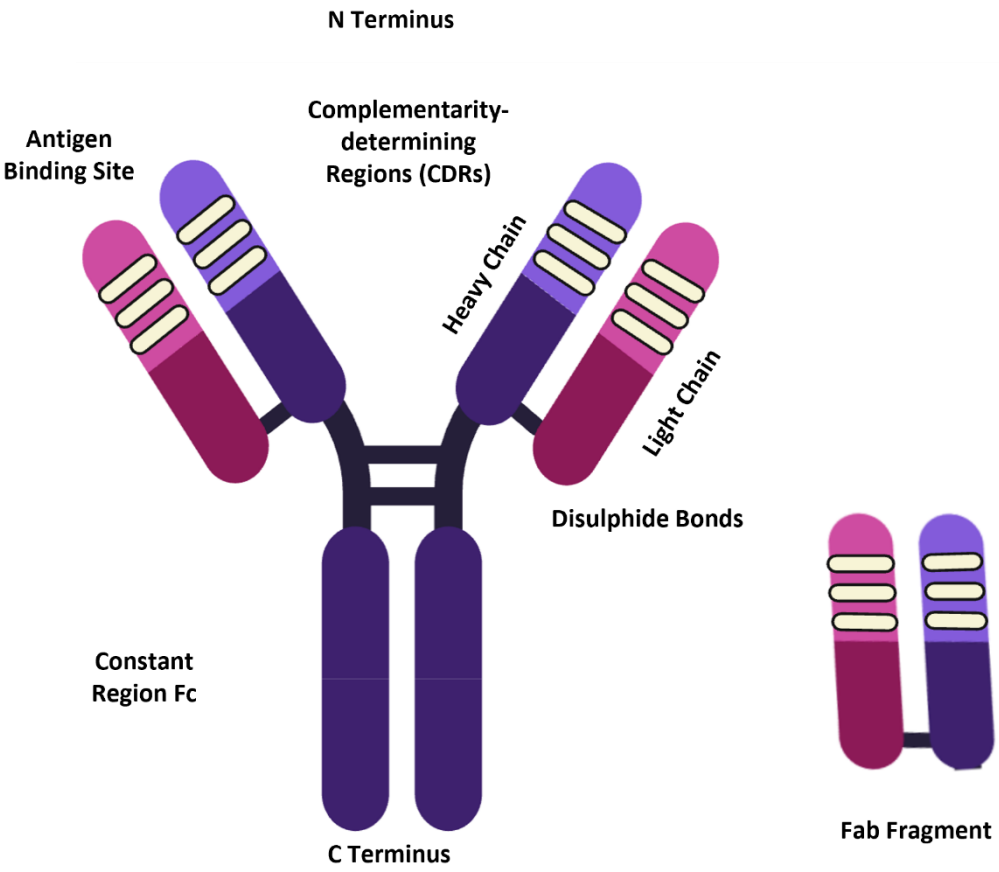

Figure 1.6: Diagram of IgG antibody structure.

The diagram illustrates the Y-shaped structure of the IgG antibody, composed of two identical heavy chains and two identical light chains. The Fab regions (top arms of the Y) contain the variable domains that are heavy and light chains responsible for antigen binding. The antigen-binding sites formed by the CDRs are highly specific for particular ligands (antigens). The Fc region interacts with Fc receptors on immune cells, triggering immune responses.

1.9.2 Antigen Binding and Specificity of the Variable Region

The variable domains of the heavy and light chains are the key determinants of an antibody's antigen-binding specificity and affinity. These domains contain three hypervariable regions, known as complementarity-determining regions (CDRs), interspersed with more conserved framework regions (FRs) that provide structural stability to the antibody. CDRs form the antigen-binding site responsible for antibodies' ability to recognise and bind to specific antigens (Schroeder Jr and Cavacini, 2010, Abbas et al., 2002, Abbas et al., 2021). The interaction between the CDRs and an antigen's epitope is the fundamental mechanism through which antibodies exert their effects, from neutralising pathogens to marking cells for destruction by other immune cells (Schroeder Jr and Cavacini, 2010).

The CDRs, specifically CDR1, CDR2, and CDR3, are the most variable parts of the antibody molecule and are directly involved in binding to the antigen's epitope. CDR3, particularly in the heavy chain, is the most variable part of the antibody and plays a vital role in precisely recognising antigens. The specific amino acid sequences and structures of the CDRs enable them to fit closely with an antigen's epitope, ensuring high specificity and strong binding affinity. This interaction is the foundation of the antibody's ability to neutralise pathogens, mark them for destruction by other immune cells or block the activity of toxins and other harmful molecules (Schroeder Jr and Cavacini, 2010, Murphy and Weaver, 2017, Altshuler et al., 2010).

The structure of the CDRs determines how an antibody will interact with its corresponding antigen. X-ray crystallography and other structural biology techniques have revealed that CDRs form a unique surface that complements the shape and charge of the antigen's epitope (Stanfield et al., 2004). This surface may be flat, convex, or concave, depending on the nature of the antigen and the corresponding CDR sequences. The precise fit between the CDRs and the antigen's epitope determines the antibody's binding affinity and specificity (Henry and MacKenzie, 2018).

Moreover, the framework regions of the variable domains, although less variable, play an essential role in supporting the proper orientation and conformation of the CDRs, ensuring that they can effectively engage the antigen. Any mutation or modification in the framework

regions can affect the overall stability and function of the antibody, which is an essential consideration in antibody engineering (Almagro and Fransson, 2008).

This understanding of the CDRs has also led to developing techniques, such as CDR grafting, to humanise non-human antibodies for therapeutic use in humans, thereby reducing immunogenicity while retaining antigen specificity (Almagro and Fransson, 2008, Jones et al., 1986).

1.9.3 Mechanisms of Antibody Diversity

The extraordinary diversity of antibodies, which enables the immune system to recognise and neutralise an immense variety of pathogens, is primarily generated through the process of V(D)J recombination. This mechanism is unique to developing B cells and involves the random joining of gene segments: variable (V), diversity (D), and joining (J) segments. These segments encode the variable regions of antibodies' heavy and light chains, which are crucial for antigen recognition (Tonegawa, 1983). The random combination of these gene segments generates many possible antigen-binding sites, contributing to the remarkable diversity observed in the antibody repertoire.

In addition to the combinatorial diversity provided by V(D)J recombination, further diversity is introduced through junctional diversity. During joining V, D, and J segments, the enzyme terminal deoxynucleotidyl transferase randomly adds or deletes nucleotides at the junctions, creating additional variation in the amino acid sequences of the antigen-binding sites (Jung et al., 2006). This process significantly increases the potential diversity of antibodies, allowing for a more effective immune response to a broader range of antigens.

Following antigen exposure, somatic hypermutation further enhances antibody diversity by introducing point mutations into the variable region genes of activated B cells. This process occurs in the germinal centres of lymphoid tissues and is facilitated by the enzyme activation-induced cytidine deaminase (Muramatsu et al., 2000). Somatic hypermutation allows for selecting B cells that produce antibodies with higher affinity for the antigen, known as affinity maturation. This selection process generates increasingly effective antibodies binding to and neutralising specific pathogens throughout an immune response (Schatz and Swanson, 2011).

Class switch recombination is another critical mechanism contributing to antibody diversity and functionality. It enables a B cell to change the isotype of the antibody it produces from

IgM to IgG, IgA, or IgE while retaining the same antigen specificity (Stavnezer et al., 2008). This process involves recombination between switch regions upstream of the constant region genes in the immunoglobulin heavy chain locus. Class switch recombination allows the immune system to adapt its effector functions to different stages of an immune response, enhancing the ability to clear pathogens or mediate different types of immune reactions, such as mucosal immunity (IgA) or allergic responses (IgE) (Kinoshita and Honjo, 2001).

These complex processes of generating and refining antibody diversity, encompassing V(D)J recombination, junctional diversity, somatic hypermutation, and class switch recombination, are fundamental to the immune system's capacity to recognise a vast array of pathogens. Understanding these mechanisms not only illuminates natural immunity but also provides valuable strategies for engineering synthetic antibodies with tailored specificity, affinity, and effector functions. By leveraging these genetic processes, researchers can design antibodies that bind with high precision to disease-relevant targets, thereby enabling the creation of more effective, safer therapeutic agents (Almagro & Fransson, 2008, Ecker et al., 2015).

Recent therapeutic successes exemplify the impact of these strategies. Teplizumab, an anti-CD3 monoclonal antibody, was engineered based on insights into antibody diversity and has been shown to delay the onset of type 1 diabetes in high-risk individuals, representing a milestone in autoimmune disease intervention (Herold et al., 2019).

In ophthalmology, the bispecific antibody faricimab targets both VEGF-A and Ang-2, two key factors in neovascular age-related macular degeneration (nAMD). Engineered from foundational knowledge of antibody structure and binding, faricimab improves visual outcomes and reduces treatment burden compared to current therapies (Heier et al., 2022).

In infectious disease, the antibodies tixagevimab and cilgavimab (Evusheld™) were derived from human monoclonal antibodies against SARS-CoV-2 and then optimised through *in vitro* engineering. These modifications improved their affinity and extended half-life, providing pre-exposure prophylaxis against COVID-19 in patients who respond poorly to vaccines (Levin et al., 2022).

Oncology has also benefited greatly from advanced antibody engineering. Antibody-drug conjugates, such as trastuzumab deruxtecan and sacituzumab govitecan, leverage finely tuned antibody frameworks for precise tumour targeting and efficient internalisation of

cytotoxic drugs. These ADCs have shown robust efficacy in HER2-positive and triple-negative breast cancers, respectively, improving outcomes for patients with otherwise limited therapeutic options (Modi et al., 2020, Bardia et al., 2019).

Taken together, these current and clinically impactful examples illustrate how understanding and directing antibody diversity informs the development of next-generation therapeutic antibodies. Ongoing research continues to refine these strategies, promising more effective and safer antibody-based treatments across diverse clinical applications.

1.10 Antibody Engineering

Antibody engineering is a field that focuses on designing, modifying, and producing antibodies to enhance their therapeutic potential. This field has grown significantly since the discovery of monoclonal antibodies, which are highly specific to particular antigens and have become essential tools in diagnostics and therapeutics. Traditionally, producing antibodies was a labour-intensive process that involved immunising animals and generating hybridomas, a technique that, while effective, was time-consuming and limited in its scope (Köhler and Milstein, 1975). The advent of recombinant DNA technology, however, has transformed antibody production, allowing for the creation of engineered antibodies with enhanced properties tailored for specific medical applications (Ecker et al., 2015, Carter, 2006).

One of the significant advancements in antibody engineering is the development of humanised and fully human antibodies. Early therapeutic antibodies were often derived from non-human species, such as mice, which could trigger immune responses in human patients, reducing their effectiveness and safety. To overcome this challenge, researchers developed techniques to humanise these antibodies by replacing most of the non-human antibody's structure with human components, leaving only the antigen-binding regions intact (Jones et al., 1986). This significantly reduced the immunogenicity of the antibodies. Further advancements led to the creation of fully human antibodies using techniques like phage display and transgenic animals, where the entire antibody is derived from human sequences, eliminating the risk of immune rejection (Hoogenboom, 2005).

Antibody engineering is also performed to improve antibody production through bacterial expression systems, which allow for more efficient and scalable production. The development of expression systems, such as those using *E. coli*, has facilitated the rapid and cost-effective production of recombinant antibodies, making them more accessible for various applications (Better et al., 1988). Additionally, engineering efforts are directed at enhancing the pharmacokinetic profiles of antibodies, such as improving their half-life in the bloodstream and modifying them for novel effector functions, such as targeting multiple antigens simultaneously (Carter and Lazar, 2018).

Phage display technology, developed in the 1980s, has been pivotal in advancing antibody engineering (Smith, 1985). This technique involves displaying large combinatorial libraries of

human antibody fragments on the surface of bacteriophage, enabling the direct selection of antigen-binding clones. Phage display has significantly expanded the possibilities of antibody engineering, allowing for the creation of antibodies that are difficult to obtain through traditional immunisation methods, particularly for unstable or autoantigens (Hoogenboom et al., 1998).

Moreover, antibody engineering has led to the development of antibody-drug conjugates, where cytotoxic drugs are linked to antibodies targeting cancer cells. Thus, the drug is delivered directly to the tumour while sparing healthy tissue (Beck et al., 2017).

Recombinant antibody technologies have made it possible to generate smaller antibody fragments, such as single-chain variable fragments (scFvs) and single-domain antibodies (VHHs or nanobodies), that retain their antigen-binding capabilities while offering several key advantages. These smaller formats typically exhibit enhanced tissue penetration, faster systemic clearance where desired, and reduced immunogenicity compared to full-length antibodies. They can be easily modified with labels for structural studies, enabling high-resolution imaging of antigen-antibody interactions. For example, single-domain nanobodies derived from camelid antibodies are increasingly used as molecular imaging probes in cancer diagnostics, as they can penetrate solid tumours more effectively and be conjugated to imaging agents for real-time tumour visualisation (Debie et al., 2020, Jovčevska & Muyldermans, 2020).

In addition to these size reductions, next-generation antibody engineering techniques are refining key characteristics like affinity, stability, half-life, and effector functions. Modern approaches use directed evolution, computational protein design, and high-throughput screening methods to optimise antibodies for specific therapeutic applications. For instance, the development of half-life extended Fc-engineered antibodies has led to treatments with reduced dosing frequency. An example is efgartigimod alfa, an engineered Fc fragment that increases IgG clearance, now approved for the treatment of generalised myasthenia gravis (Howard et al., 2021).

In oncology, engineering antibodies to produce bispecific formats has allowed simultaneous targeting of two different antigens, improving tumour cell killing and reducing resistance. Faricimab, a bispecific antibody approved for neovascular age-related macular degeneration

and diabetic macular oedema, exemplifies how careful engineering of the fragment antigen-binding (Fab) regions can yield a molecule that targets both VEGF-A and Ang-2, leading to sustained treatment effects with potentially fewer injections (Heier et al., 2022).

For infectious diseases, antibodies engineered for broader neutralisation have been pivotal in rapidly responding to emerging pathogens. The engineering of broadly neutralising antibodies against SARS-CoV-2 variants demonstrates how rational mutagenesis and affinity maturation methods can maintain or enhance efficacy against evolving viral antigens (Copin et al., 2021).

As technology continues to progress, glycoengineering of Fc regions—altering the carbohydrate moieties attached to the antibody Fc—offers another layer of refinement. By modulating Fc glycosylation patterns, researchers can fine-tune antibody-dependent cellular cytotoxicity (ADCC) and other immune effector functions. For instance, an improved understanding of Fc glycan modifications has led to the development of afucosylated antibodies, such as obinutuzumab, which have enhanced ADCC and improved clinical performance compared to earlier-generation antibodies (Sehn et al., 2016).

Collectively, these advancements demonstrate the potential of antibody engineering to create potent, safe, and highly targeted therapies. As researchers continue to enhance antibody design and understand the interplay between antibody structure and function, new and more effective treatments for challenging conditions, ranging from cancer and autoimmune disorders to infectious diseases, will become increasingly attainable.

1.10.1 Combinatorial Antibody Library Technology

Combinatorial antibody library technology was an essential advancement in the field of antibody engineering, allowing for the creation of large libraries of antibody variants that could be screened for specific binding properties. This method initially involved expressing antibody genes obtained from hybridomas in various expression systems, including mammalian cells, bacteria, and yeast (Neuberger, 1983, Cabilly et al., 1984). The technique provided a foundation for later developing more sophisticated approaches, such as phage display, by enabling the functional assembly of antibody fragments in bacteria and rapidly cloning antibody genes using polymerase chain reaction (PCR) (Skerra and Plückthun, 1988, Orlandi et al., 1989).

While combinatorial libraries were crucial in advancing antibody engineering, they had limitations, including the need for large amounts of purified antigen and extensive screening efforts to identify specific antibody clones. These challenges were addressed mainly by developing an antibody phage display, which became the preferred method for generating high-affinity antibodies with greater efficiency and flexibility (Almagro et al., 2019).

1.11 Phage Display

1.11.1 Filamentous Phage

Phage display is a powerful and commonly used technique in molecular biology and biotechnology, particularly for developing and selecting peptides, proteins, and antibodies with high affinity and specificity. At the heart of this technology is the M13 filamentous phage, a bacteriophage extensively utilised as a vector for displaying peptides and proteins on its surface (Smith, 1985, Winter et al., 1994).

The M13 filamentous phage belongs to the Inoviridae family and is characterised by its long, filamentous structure, typically about 6.5 nm in diameter and approximately 900 nm in length. The M13 phage infects *Escherichia coli* (*E. coli*) bacteria by binding to the F pilus, a structure involved in bacterial conjugation. The phage genome is a single-stranded DNA molecule, approximately 6.4 kilobases in length, encoding 11 genes. These genes are responsible for encoding the structural proteins of the phage and for the processes involved in phage replication and assembly (Russel, 1991, Smith and Petrenko, 1997) (Fig. 1.7).

The life cycle of the M13 phage is non-lytic, meaning that it does not kill the host cell upon replication. Instead, the phage is assembled and extruded through the bacterial membrane, allowing the host cell to grow and divide. This property is particularly advantageous for phage display, enabling continuous phage production without disrupting the host cell population. The non-lytic nature of M13 also facilitates the generation of large libraries of phage particles displaying diverse peptides or proteins, which can be screened for specific binding interactions (Smith and Petrenko, 1997).

M13 filamentous phage is the most commonly used vector in phage display due to its well-characterised genetics, ease of manipulation, and ability to display various peptides and proteins on its surface. The display of foreign peptides or proteins on the phage surface is typically achieved by fusing the gene encoding the peptide or protein of interest to one of the phage coat protein genes. The most commonly used coat proteins for this purpose are pIII and pVIII (Smith, 1985, Winter et al., 1994).

The pIII protein is located at one end of the phage particle and is involved in the phage's attachment to the bacterial F pilus during infection. The pIII protein is often used to display larger peptides or proteins, as it allows the insertion of relatively large sequences without

disrupting the phage's infectivity. The pVIII protein is the major coat protein, with about 2,700 copies per phage particle. It is suitable for displaying smaller peptides, and its abundance allows for a high-density display of the peptide on the phage surface, which can enhance binding interactions during the selection (Smith, 1985, Smith and Petrenko, 1997).

The fundamental principle behind phage display is the ability to fuse foreign genes to these coat proteins and express them on the phage surface. The phage display process involves the creation of a library of phage particles, each displaying a different peptide or protein on its surface. This library can then be screened, or "panned," against a target antigen to identify phages that bind specifically to the target. The DNA encodes the displayed peptide or protein within the phage particle, allowing for easy identification and amplification of the binding sequences (Smith, 1985, Winter et al., 1994) (Fig. 1.8).

The M13 filamentous phage offers several advantages that make it particularly well-suited for phage display applications. These include its stability and flexibility, non-lytic life cycle, high display capacity, and ease of genetic manipulation. These characteristics have made M13 an invaluable tool in molecular biology, facilitating the selection and optimisation of high-affinity binders from large combinatorial libraries (Smith and Petrenko, 1997, Russel, 1991).

M13 filamentous phage has been used extensively in many applications, from identifying high-affinity peptides and antibodies to developing novel therapeutic agents. M13-based phage display has produced monoclonal antibodies for therapeutic use in antibody engineering. The technology allows for the rapid selection and optimisation of antibodies with desired binding properties, making it a vital tool in drug discovery and development (Winter et al., 1994).

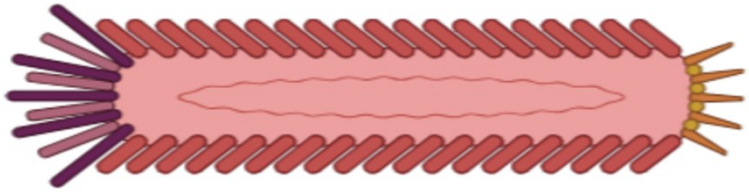

	pIII	pVI	pVIII	pVII	pIX
aa:	406	112	50	33	32
kDa:	42.5	12.4	5.2	3.6	3.7
Copies/virion:	~5	~5	2,700	~5	~5

Figure 1.7: Schematic of M13 Filamentous Phage.

A schematic diagram illustrating the length of the M13 filamentous phage, the arrangement of its coat proteins (pVIII, pIII, pVI, pVII, and pIX), and the single-stranded DNA genome enclosed within.

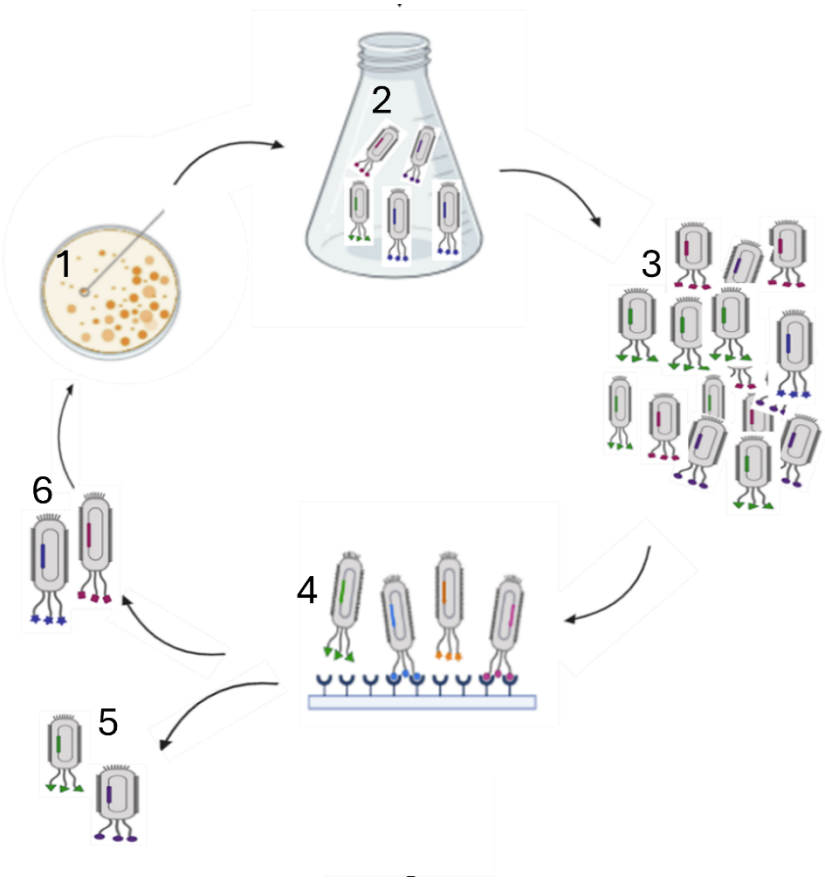

Figure 1.8: Schematic of the Phage Display Panning Cycle.

1. *E. coli* cells are transformed with phagemid and plated; **2.** Colonies are cultured in liquid media to amplify phage; **3.** A diverse population of phage displaying different peptides is generated; **4.** Phage binds to an immobilised target; **5.** Non-binders are washed away, and high-affinity phage are eluted and amplified for further rounds of selection.

1.11.2 Antibody Phage Display

Antibody phage display is an innovative technique that involves the presentation of antibody fragments on the surface of bacteriophage, notably M13 filamentous phage. This method has revolutionised the field of antibody engineering by enabling the rapid selection and optimisation of antibodies with high specificity and affinity for a wide variety of antigens. The process of displaying antibodies on M13 phage and selecting those with desired characteristics offer significant advantages over traditional antibody production methods, such as hybridoma technology (Winter et al., 1994, Smith, 1985).

In antibody phage display, the genes encoding the variable regions of antibodies (which determine antigen specificity) are fused to the genes encoding one of the coat proteins of the M13 phage, typically the pIII or pVIII protein. The pIII protein is often preferred for displaying larger antibody fragments, such as Fab fragments, because it can accommodate more giant insertions without disrupting the phage's ability to infect *Escherichia coli* (*E. coli*). The pVIII protein, the most abundant coat protein, is usually employed to display smaller peptides or antibody fragments, allowing for high-density display on the phage surface (Smith, 1985, Smith and Petrenko, 1997).

Once the antibody gene is fused to the coat protein gene, the recombinant phage is propagated in *E. coli*. As the phage is assembled within the bacterial host, the antibody fragments are expressed on the surface of the phage particles. This creates a phage library, each displaying a unique antibody fragment on its surface, with the corresponding genetic information encoded within the phage particle. This direct linkage between the indicated antibody and its genetic material allows for the rapid identification and amplification of antibodies with desired properties (Smith, 1985, Winter et al., 1994).

Antibody phage display offers several critical advantages over traditional methods such as hybridoma technology. One of the primary advantages is the ability to generate extensive libraries containing millions to billions of different antibody variants. This considerable diversity increases the likelihood of identifying antibodies with high affinity and specificity for a given antigen, even those rare or difficult to produce through traditional methods (Hoogenboom, 2005). Additionally, the phage display process is significantly faster than traditional hybridoma techniques, which require the immunisation of animals, fusion of B

cells with myeloma cells, and extensive screening to identify desirable clones. Phage display avoids these steps, allowing for the direct selection of high-affinity binders from a pre-existing library (Winter et al., 1994).

Another significant advantage of phage display is the ability to select fully human antibodies directly. This reduces the need for subsequent humanisation steps often required for therapeutic antibodies derived from non-human sources. This minimises the risk of immunogenicity in patients, making phage display a preferred method for generating therapeutic antibodies (Hoogenboom, 2005). Additionally, phage display is versatile and can select antibodies against various antigens, including small molecules, peptides, proteins, and complex structures like cells or tissues. It also allows for the engineering of antibodies with enhanced properties, such as increased affinity or altered specificity, through processes like affinity maturation (Smith and Petrenko, 1997).

Phage display is particularly advantageous when working with poorly immunogenic or toxic antigens, as it does not require using live animals for antibody generation. This makes it possible to generate antibodies against a broader range of targets that might be challenging to produce through traditional immunisation methods (Winter et al., 1994).

1.11.3 Phage Display Antibody Techniques

Phage display is a highly adaptable and powerful technology that enables the selection and optimisation of antibodies with high specificity and affinity for a wide range of targets. The techniques used in phage display involve several critical steps: the creation of phage libraries, the selection of antibodies through biopanning, and the expression of large libraries, including specific antibody formats such as Fab fragments.

The first step in phage display is creating a phage library, which involves generating an extensive collection of bacteriophages, each displaying a unique antibody fragment on its surface. Typically, these libraries are constructed by isolating the variable regions of immunoglobulin genes from a diverse population of B cells, often derived from immunised animals or human donors. The variable regions, which determine the antigen-binding specificity of the antibody, are then amplified using PCR and inserted into the phage genome. This is usually done by fusing the variable region genes with the genes encoding one of the

phage coat proteins, such as pIII or pVIII, enabling the display of the antibody fragment on the phage surface (Hoogenboom, 2005, Smith, 1985).

The production of recombinant filamentous phages displaying antibody fragments often requires the use of a helper phage, such as VCSM13. The helper phage supplies the replication and packaging machinery needed to assemble filamentous phages, while allowing the phage display system to encode and display foreign peptides or proteins on the phage surface.

One of the remarkable aspects of phage display is the ability to generate huge libraries, often containing up to 10^8 or more unique antibody variants. These libraries provide a vast diversity, significantly increasing the likelihood of identifying high-affinity antibodies against a specific antigen. The size and diversity of the library are crucial for the success of the selection process, as they allow for the exploration of vast sequence space and the identification of rare, high-affinity binders that might be missed in smaller libraries. Synthetic or semi-synthetic approaches can further enhance the diversity of these libraries by introducing artificial diversity through random mutagenesis or using degenerate primers during PCR (Hoogenboom, 2005).

Within phage display, Fab fragments (fragment antigen-binding) are a standard format for antibody display. Fab fragments consist of one constant and one variable domain from each of the antibody's heavy and light chains, forming a bivalent antigen-binding site. Fab fragments retain the antigen-binding specificity of the whole antibody but are smaller and more stable, making them ideal for expression in phage display systems.

Fab fragments' expression on the phage's surface is typically achieved by inserting the genes encoding the heavy and light chain variable regions into the phage genome, fused to the gene encoding the pIII or pVIII coat proteins. The use of the pIII protein is common for Fab display, as it allows for the presentation of larger fragments without compromising the phage's infectivity (Hoogenboom, 2005, Winter et al., 1994).

Fab fragments offer several advantages in phage display. They are more stable than single-chain variable fragments (scFv), particularly under physiological conditions. This stability is advantageous for downstream applications, such as therapeutic development (Hoogenboom, 2005). The bivalent nature of Fab fragments, which allows for two points of contact with the antigen, can lead to stronger binding interactions compared to monovalent formats like scFv

(Smith and Petrenko, 1997). Fab fragments can be easily converted into full-length antibodies by adding the Fc region, making them highly versatile for further development into therapeutic antibodies (Winter et al., 1994).

Once the phage library has been created and expressed, the next step is to select phage-displaying antibody fragments with high affinity for the target antigen, a process known as biopanning. This selection process typically involves incubating the phage library with the immobilised target antigen, allowing phage with specific binding affinity to adhere to the antigen. Unbound or weakly bound phages are washed away, and the bound phages are eluted and amplified in *E. coli* to produce a new enriched phage population. This process is repeated over several rounds, with each round or panning increasing the stringency of the selection by using higher washing stringency or lower antigen concentrations, thus enriching the library for phage with higher affinity for the target (Smith and Petrenko, 1997).

The biopanning technique is highly versatile and can be adapted to select antibodies against various targets, including small molecules, peptides, proteins, cells, and even whole organisms. Different panning strategies can be employed to enhance the selection process, such as subtractive panning, where phages that bind to non-target structures are removed, or competitive panning, where phage must compete with a known ligand or inhibitor to bind to the target (Winter et al., 1994).

1.11.4 Applications of Antibody Phage Display

Antibody phage display is a foundational technology in biotechnology, especially for developing therapeutic antibodies, diagnostics, and research tools. Its versatility and robustness make it invaluable for drug discovery, exploring protein-protein interactions, and creating targeted therapies for complex diseases.

Developing therapeutic antibodies is one of the most significant applications of antibody phage display. By rapidly identifying and optimising antibodies with high specificity and affinity for disease-associated antigens, phage display enables the creation of powerful therapeutics that can neutralise pathogens, modulate immune responses, or deliver cytotoxic agents to cancer cells. A prominent example is adalimumab (Humira®), an anti-TNF-α antibody developed through phage display technology, which has transformed the treatment landscape for rheumatoid arthritis and other autoimmune disorders (Voulgari & Drosos,

2014). Likewise, belimumab (Benlysta®), another phage display–derived antibody, targets the B-lymphocyte stimulator (BLyS) and is approved for patients with systemic lupus erythematosus (Kim et al., 2012).

In oncology, phage display-engineered antibodies also show promise. Panitumumab (Vectibix®), an EGFR-targeting antibody identified using phage display, is indicated for metastatic colorectal cancer (Vaughan et al., 2013). This approach extends to next-generation antibody formats, such as antibody-drug conjugates and bispecific antibodies, which are currently being explored for more precise and effective cancer therapies (Carter & Lazar, 2018). Moreover, phage display libraries have been instrumental in discovering potent binders against emerging pathogens, including SARS-CoV-2, as evidenced by the isolation of nanobodies capable of neutralising multiple variants of concern (Wu et al., 2023).

The flexibility of phage display in generating fully human or humanised antibodies is particularly advantageous, reducing immunogenicity risks associated with non-human antibodies. In parallel, phage display facilitates the engineering of antibodies to improve half-life, stability, and effector functions—key factors for developing best-in-class therapeutics (Hoogenboom, 2005, Carter and Lazar, 2018).

Phage display is equally prominent in diagnostic applications. By selecting high-affinity binders for specific biomarkers, researchers can build highly sensitive assays for early disease detection. For instance, single-domain antibodies (nanobodies) isolated via phage display have proven effective at detecting coronaviruses, as demonstrated by the successful generation and characterisation of nanobodies against SARS-CoV (Li et al., 2021). Phage display–derived antibodies also underpin various diagnostic platforms, including enzyme-linked immunosorbent assays (ELISAs) and lateral flow tests, offering the specificity needed to detect low-abundance markers (Smith and Petrenko, 1997).

In research, antibody phage display helps map protein–protein interactions, identify novel binding partners, and explore mechanisms of disease pathogenesis. Because high-affinity antibodies can be raised against virtually any target, phage display has become a powerful method for dissecting complex cellular pathways and discovering new drug targets. Finally, phage display has accelerated the development of advanced therapeutics, such as antibody-

drug conjugates and bispecific antibodies, paving the way for innovative treatments that combine precise targeting with potent clinical efficacy (Smith and Petrenko, 1997).

Overall, these examples highlight the broad impact of phage display in modern biomedicine—from blockbuster therapeutic antibodies to next-generation diagnostics and cutting-edge research applications.

1.12 SGLT2 Antibody as a Target for Kidney Diseases

Sodium-glucose co-transporter 2 (SGLT2) is a membrane protein predominantly expressed in the proximal convoluted tubules of the kidney, which plays a vital role in glucose reabsorption. SGLT2 is responsible for reclaiming approximately 90% of glucose from the glomerular filtrate, preventing its loss in urine and maintaining glucose homeostasis (Wright et al., 2011). This transporter is highly expressed in the kidney, with mRNA levels reported to be approximately 15 times higher than in any other tissue (Rahmoune et al., 2005). This significant expression in the kidney, particularly in the tubular epithelium, makes SGLT2 an abundant target for drug-delivery strategies for treating kidney diseases.

While SGLT2 inhibitors are widely used in managing type 2 diabetes by reducing glucose reabsorption, this approach diverges by focusing on the potential of SGLT2 as a vehicle for targeted drug delivery rather than inhibiting its function. This strategy capitalises on the localised expression of SGLT2, allowing for precise drug delivery to renal tissues, which is especially valuable in treating chronic kidney diseases where localised intervention is critical (Vallon & Thomson, 2017).

Developing an SGLT2-targeted monoclonal antibody leverages this specificity, not to inhibit glucose reabsorption but to deliver therapeutic agents directly to the kidney. By focusing on SGLT2 as a target, the delivery of drugs to renal tissues can be enhanced, which is especially valuable in conditions like CKD, where targeted intervention is crucial.

1.12.1 Potential Application of SGLT2 Antibody Conjugates in Kidney Diseases

The availability of a high-affinity monoclonal antibody directed against SGLT2 provides a unique opportunity for developing antibody-drug conjugates (ADCs) designed to deliver therapeutic agents specifically to the kidneys. Since SGLT2 is expressed predominantly by the tubular epithelium, it represents an ideal target protein for such therapeutic strategies.

Conjugating a specific drug to this antibody would enable enhanced drug delivery directly to the kidney, thus increasing the local concentration of the therapeutic agent in the renal tissue while minimising systemic exposure (Rajasekeran et al., 2017).

This approach is particularly promising in addressing the progression of fibrosis in CKD. By delivering anti-fibrotic or anti-inflammatory agents directly to the site of SGLT2 expression, the progression of fibrosis can potentially be slowed or even reversed, preserving kidney function and improving patient outcomes. This targeting strategy's specificity enhances therapeutic efficacy and reduces the risk of off-target effects, which are common in systemic drug delivery methods.

1.12.2 Advanced Drug Delivery Strategies

Covalent Drug-Antibody Conjugation

The covalent conjugation of therapeutic agents to an SGLT2-specific monoclonal antibody offers a stable and targeted drug delivery system. This strategy ensures the drug is delivered precisely to the kidney, leveraging the antibody's specificity to SGLT2. The stability of the covalent bond between the drug and the antibody is crucial, preventing premature release and ensuring that the therapeutic agent reaches the intended site within the kidney.

This method is particularly effective for delivering drugs aimed at reducing renal fibrosis. The high affinity of the monoclonal antibody for SGLT2, combined with the precise localisation of the transporter in the kidney, ensures that the therapeutic agent is concentrated where it is most needed, thereby maximising its effectiveness and reducing potential side effects associated with systemic distribution (Flygare et al., 2013). Similar strategies have shown promise in treating renal cancer, as discussed by Sganga et al. (2023), where ADCs have been explored for their ability to target specific antigens in renal cell carcinoma (Sganga et al., 2023). These approaches highlight the potential for ADCs to deliver therapeutic agents directly to renal tissues, effectively targeting pathological processes while minimising systemic toxicity.

Liposomal Drug Delivery

Liposomal drug delivery systems offer an advanced and flexible strategy for encapsulating therapeutic agents within a liposome, which is then conjugated to the SGLT2 antibody.

Liposomes are versatile carriers that can encapsulate a wide range of drugs, protecting them from degradation and ensuring their release at the target site (Allen and Cullis, 2013). Conjugating liposomes to an SGLT2-targeting antibody further enhances the specificity of drug delivery, ensuring that the therapeutic agent is delivered directly to the renal tissues.

This method is particularly advantageous in delivering drugs sensitive to degradation or requiring controlled release. The ability to engineer liposomes to respond to specific stimuli within the renal environment, such as pH changes or the presence of certain enzymes, allows for precise drug release at the site of SGLT2 expression. This controlled release further refines the precision of drug delivery, making achieving high therapeutic efficacy with minimal side effects possible (Sercombe et al., 2015).

Developing an SGLT2-targeted monoclonal antibody conjugated with specific therapeutic agents such as TG2 or LOXL4 represents a significant advancement in treating kidney diseases. This approach enables highly targeted drug delivery by capitalising on the high specificity of SGLT2 expression in the proximal tubules, particularly in the tubular epithelium where mRNA levels are significantly elevated. Advanced drug delivery strategies, such as covalent conjugation and liposomal encapsulation, further enhance this approach, offering a highly effective means of delivering therapeutics to the kidneys with precision and efficacy.

1.13 Hypothesis of Research

The central hypothesis of this research is that a monoclonal antibody specifically targeting SGLT2 can be developed and engineered to deliver therapeutic agents directly to the kidneys. This approach is expected to effectively address pathological processes such as fibrosis and inflammation in kidney diseases, particularly CKD. By leveraging the high specificity and localised expression of SGLT2 in the renal proximal tubules, it is hypothesised that this targeted strategy will enhance drug delivery efficacy, minimise systemic side effects, and provide a novel therapeutic avenue for renal conditions. It is hypothesised that breaking immune tolerance through SGLT2 loops fused with Diphtheria toxin A (DTA) will generate high-affinity antibodies capable of specifically binding to and delivering therapeutic agents to SGLT2 in renal tissues.

1.13.1 Overview of Research

The research focuses on developing an SGLT2-targeted monoclonal antibody for precise drug delivery to the kidneys, specifically aimed at addressing CKD, that can be used for therapeutic interventions in kidney diseases. The primary objective is to leverage the specific expression of SGLT2 in the renal proximal tubules to deliver therapeutic agents that target the underlying mechanisms of renal scarring. The research is structured around several key objectives and aims, each designed to address critical aspects of antibody development, from antigen design to functional validation.

1.13.2 Aims and Objectives

The primary goal of this study was the development of a mouse autoantibody directed against the extracellular domain of the SGLT2 glucose transporter. This approach was chosen because the study focuses on establishing a model system in mice to investigate the role of SGLT2 in renal scarring. A humanised antibody, while relevant for eventual clinical translation, was not suitable for the initial development phase due to cross-species immune responses that would preclude long-term studies in mice. Instead, a mouse "self" antibody allowed the breaking of immune tolerance to generate an antibody that could be tested in mouse models without eliciting an immune response against the antibody itself. The project objectives were to:

- Design a DNA sequence encoding the extracellular loops of SGLT2 fused with Diphtheria Toxin A (DTA) to break immunological tolerance. DTA, a non-toxic immunogenic fragment of the diphtheria toxin, serves as an immune adjuvant by eliciting a stronger immune response against the extracellular domains of the SGLT2 protein. These domains are considered "self" antigens in mice and would typically be ignored by the immune system. The inclusion of DTA is critical for overcoming immune tolerance and enabling the generation of antibodies against SGLT2 in mouse models.
- Design a DNA sequence encoding the extracellular loops of SGLT2 without DTA for subsequent immunisations. This version allows for boosting the immune response in mice after tolerance has been overcome, facilitating the development of highly specific antibodies against the extracellular loops of SGLT2.
- Clone and express recombinant extracellular domains of mouse SGLT2 fused with diphtheria toxin A (DTA) in *E. coli* using the pET21a vector to break immunological tolerance.

- Clone and express recombinant extracellular domains of mouse SGLT2 protein without a tag in *E. coli* using the pET21a vector to boost the immune response, thereby enhancing specificity against the native protein
- Immunise wild-type mice with SGLT2-Loops recombinant protein, followed by boosting with SGLT2-Loops-No-Tag protein.
- Construct an antibody library from splenocytes of immunised mice, followed by phage display for high-affinity antibody selection.
- Generate a fragment library for epitope mapping to identify antibody-binding regions of SGLT2.
- Functionally validate the selected antibodies using western blotting and by transiently transfecting full-length SGLT2 in CHO-K1 cells.
- Evaluate antibody binding and characterisation by staining kidney tissue sections with immunohistochemistry (IHC).

This research represents a comprehensive approach to developing a targeted therapeutic strategy for kidney diseases by engineering an SGLT2-specific monoclonal antibody. Each objective is carefully designed to ensure the successful development and validation of antibodies that can deliver therapeutic agents directly to the kidney. Integrating innovative techniques, such as Diphtheria Toxin A (DTA) fusion to break immune tolerance, phage display for antibody selection, and epitope mapping, ensures that the antibodies developed will have high specificity and efficacy.

DTA was used in this study as an immune adjuvant due to its strong immunogenic properties. Importantly, the toxic fragment of the diphtheria toxin was removed, and only the non-toxic immunogenic fragment A was used. This ensured the safety of the experimental procedures while effectively eliciting an immune response to break tolerance against the "self" SGLT2 protein during immunisation.

The final steps of functional validation through western blot and tissue staining are crucial for confirming that these antibodies target the kidney for therapeutic potential, positioning this research at the forefront of kidney disease treatment strategies.

Chapter 2: Materials and General Methods

2.1 Materials

Most reagents, including chemicals, buffers, acids, and solvents, were sourced from Sigma-Aldrich (Poole, UK), Fisher Scientific UK Ltd. (Loughborough, UK), or Melford Laboratories (Ipswich, UK). The reagents were analytical grade or molecular biology. The suppliers of more specialised reagents are detailed in the methods section.

Plasticware was obtained from various suppliers: Starlab (UK) Ltd. (Milton Keynes, UK), Corning Incorporated (Corning, NY, USA), Bibby Sterilin Ltd. (Bargoed, UK) and Nalgene Nunc International (Rochester, NY, USA). This included 0.5-ml and 1.5-ml Eppendorf tubes, 6-well plates, 96-well plates, 25-ml universal tubes, pipettes, pipette tips, cell culture flasks, and 15-ml and 50-ml centrifuge tubes.

2.1.1 Bacterial Strains, Helper Phage and Mammalian Cells

This study utilised several *E. coli* derivatives for specific purposes:

Table 2.1: Bacterial Strains, Helper Phage and Mammalian Cell Used in This Study.

Organism/Cell Line	Source
JM109	L2005, Promega
XL1-Blue	200228, Agilent
BL-21(DE3)-pLysS	L1195, Promega
VCSM13 helper phage	200251, Stratagene
CHO-K1	European Collection of Authenticated Cell Cultures

- **JM109 Chemically Competent Cells**

JM109 cells were chosen for their high efficiency in plasmid DNA transformation. They were used for routine cloning, transformation, and DNA preparation tasks. They are sensitive to commonly used antibiotics like ampicillin and have a robust growth rate.

- **XL1-Blue Super-Competent Cells**

XL1-Blue cells were employed for electroporation due to their exceptional DNA plasmid transformation efficiency, rapid growth rate, and susceptibility to antibiotics like ampicillin.

- **BL21 (DE3) pLys-S Cells**

These cells were selected for high-level protein expression using the T7 system. The target genes are regulated by the T7 promoter, which is not recognised by *E. coli* RNA polymerase. This results in minimal protein expression until T7 RNA polymerase becomes available. BL21 cells are stably transfected with Isopropyl ß-D-1-thiogalactopyranoside (IPTG)-inducible T7 RNA polymerase, facilitating controlled protein expression.

- **VCSM13 Helper Phage**

This phage is favoured in phage display experiments due to its low background noise, high phage titer, compatibility with the M13 bacteriophage system, and versatility with pIII and pVIII display systems.

- **Chinese Hamster Ovary (CHO) Cells**

Chinese hamster ovary (CHO) cells, specifically CHO-K1 cells, were obtained from the European Collection of Authenticated Cell Cultures (ECACC). CHO-K1 cells have well-established capabilities for efficient protein production, making them an attractive choice for recombinant protein manufacturing. Different expression vectors and transfection protocols are optimised for CHO-K1 cells, offering flexibility for tailoring the expression system to your needs.

2.1.2 Plasmids

Table 2.2: The Plasmids Used Throughout the Project.

Plasmid	Source
pcDNA3.1	V79020, Invitrogen
pMax-GFP	V014332, NovoPro
pET21a	V011023, NovoPro
pComb3	VPT4010, Creative Biogene

- **pcDNA3.1**

The pcDNA3.1 vector, designed for mammalian expression, facilitates functional protein expression. It incorporates a Cytomegalovirus (CMV) enhancer-promoter to ensure robust expression levels. It contains an ampicillin resistance gene for selection in *E. coli*. Additionally, the vector offers hygromycin B resistance for establishing stably transfected mammalian cell lines.

- **pMAX-GFP**

The pMax-GFP is a mammalian expression vector used as a positive control for transient transfection due to its inclusion of the green fluorescent protein (GFP) gene. This allows for easy visualisation and confirmation of successful transfection through the GFP expression.

- **pET21a**

The pET21a is a bacterial expression plasmid that utilises the T7 promoter-driven system for robust protein expression (Pan and Malcolm, 2000, Studier and Moffatt, 1986). It contains all essential elements for protein production, including the pBR322 origin of replication, ampicillin resistance gene, F1 origin of replication, poly-linker, *lac* operator, *lac* repressor gene, T7 promoter, T7 terminator, and ribosome binding site.

The system relies on a tightly regulated mechanism to control protein expression. In the presence of T7 RNA polymerase, which is encoded by the BL21 (DE3) pLysS host cells, the T7 promoter drives strong transcription of the gene of interest. However, under uninduced conditions, the *lac* repressor binds to the *lac* operator, preventing the activation of T7 RNA polymerase and subsequent transcription. This ensures that expression of the target protein remains suppressed during bacterial growth, reducing the metabolic burden on the cells.

Induction mechanism:

- The *lac* operon is inducible by either lactose or isopropyl β-D-1-thiogalactopyranoside (IPTG). When IPTG is added to the culture, it binds to the *lac* repressor protein, causing a conformational change that releases the repressor from the *lac* operator. This derepression enables the T7 RNA polymerase to bind to the T7 promoter and initiate transcription of the inserted gene at a high rate.
- The use of IPTG as an inducer is advantageous because it is not metabolised by the bacteria, ensuring consistent induction levels throughout the culture. This inducible system allows for high-density bacterial growth before controlled induction of protein production, maximising protein yield and minimising potential toxicity associated with premature expression.

This tightly regulated and robust induction mechanism makes the pET21a system ideal for the high-yield production of recombinant proteins in bacterial systems.

- **pComb3**

The pComb3 vector facilitates cloning and FAB antibody expression for phage display. It enables independent expression of immunoglobulin heavy and light chains in Fab fragments using separate *lacZ* promoters. Each chain precedes a pelB leader sequence for periplasmic localisation and disulphide bond formation. The heavy chain is expressed as an N-terminal cpIII fusion, facilitating its incorporation onto the phage surface.

2.1.3 Bacterial Culture Media

The following bacterial culture media were used:

- **Luria Bertani (LB) medium:** Prepared by dissolving 10 g tryptone (Millipore, 16922), 10 g sodium chloride (NaCl) (Sigma, S9888), and 5 g yeast extract (Sigma, Y1626) in 1 L of DI H_2O. The medium was then autoclaved for 20 min at 121°C.
- **Super Optimal broth with Catabolic repression (SOC) medium (Sigma, S1797):** Used during the final stages of competent cell transformation (JM109 and XL-1 Blue) transformation.
- **Terrific broth (TB) medium (Millipore, T0918):** Prepared by suspending 47.6 g of TB powder and 4 ml of glycerol in 1 L of DI H_2O and autoclaving.

- **Super Broth (SB) medium:** Composed of 30 g tryptone, 20 g yeast extract, and 10 g 3-[N-morpholino]-propane sulfonic acid (MOPS). The final volume was adjusted to 1 L with DI H_2O, mixed until dissolved, and the pH was adjusted to 7.0. Sterilisation was achieved by autoclaving for 20 min at 121°C.
- **LB Agar (Sigma, L3027)**: This was prepared by mixing 40 g/L of LB agar and autoclaving. After cooling, appropriate antibiotics were added before pouring plates.
- **2 x YT medium (Sigma, Y1003):** Prepared by suspending 16 g Bacto-tryptone, 10 g Bacto yeast extract and 5 g NaCl in 1L of DI H_2O and the pH was adjusted to 7.0. For solid media, 15 g of Bacto-agar was added.

2.1.4 Antibiotics for Bacterial and Mammalian Cell Culture

Antibiotics were utilised at 1000-fold concentrated stocks, prepared in sterile deionised water (DI H_2O) for bacterial culture media and in Dulbecco's Modified Eagle's Medium (DMEM-F12) (Lonza; 12-719F) for mammalian cell culture. Stocks were aliquoted in 1 ml volumes and stored at -20°C until required. Filter sterilisation was performed using 0.2-micron filter units (Millipore, UK). Specific antibiotic stocks and their applications:

- Ampicillin 100 mg/ml in DI H_2O, selection for plasmids with ampicillin resistance genes.
- Kanamycin 50 mg/ml in DI H_2O, selection for plasmids with kanamycin resistance genes.
- Carbenicillin 50 mg/ml in DI H_2O, selection for plasmids with carbenicillin resistance genes.
- Tetracycline 5mg/ml in 70% Ethanol, selection for plasmids with tetracycline resistance genes.

Mammalian Cell Culture

- Penicillin: Used in combination with streptomycin for broad-spectrum bacterial control. The specific concentration depends on the cell line and medium composition.
- Streptomycin: Used in combination with penicillin for broad-spectrum bacterial control. The specific concentration depends on the cell line and medium composition.

2.2 Methods

2.2.1 Mammalian Cell Culture

2.2.1.1 Cell Culture

CHO-K1 cells were removed from a liquid nitrogen tank and thawed in a water bath at 37°C. The cell suspensions were resuspended in medium, centrifuged at 300 × *g* for 5 minutes, and cultured in DMEM-F12 with 10% foetal bovine serum (Labtech; FCS-SA), 1% L-glutamine (Sigma-Aldrich; G7513), and 1% penicillin/streptomycin (Sigma-Aldrich; P4333) to ensure healthy cell growth.

When the cell lines cover 80% of the growth surface area, the nutrients in the medium are depleted, or the lactate levels in the medium are raised, the cells are passaged or subcultured to maintain their viability and prevent cell death. Cell culture ensures that cells are viable and prevents them from dying. In a 37°C water bath, medium, Dulbecco's Phosphate Buffered Saline (PBS) (Lonza; 17-512F), and Trypsin-EDTA (Sigma-Aldrich; T3924) were all pre-warmed for at least 30 min. The cells are commonly grown in T75 cm^2 flasks (Corning, UK); these cells were divided by removing the consumed medium from the flask and washing it with 5 ml of sterile PBS to remove any dead cells. Then, add 4 ml of Trypsin-EDTA to the adherent cells in the culture flask, and trypsin should be discarded as it is a proteolytic enzyme and should not be incubated with cells for an extended time. The flask was incubated at 37°C for 4 min to dissociate the cells from the surface. The cells were examined under a microscope to ensure they were separated from the surface of the flask; trypsin-EDTA was then inactivated by adding 10 ml of medium. The harvested cells were then transferred to a 25 ml universal tube and centrifuge for 5 min at 100 x *g* using a Sorvall RT 6000D centrifuge (Thermo Fisher Scientific Inc., Waltham, MA, USA). The media was discarded after spinning, the cell pellet was re-suspended in 5 ml of medium, and 500 µl of the cell's suspension was dispensed into a sterile flask containing 15 ml of media. All cultures were kept at 37°C in an incubator (Sanyo, Japan) with a humidified atmosphere containing 5% CO2.

2.2.1.2 Cell Counting

The cells were stained with an equal amount of Trypan blue solution Cell counting was performed both manually and automatically. Manual counting of cells was conducted using a haemocytometer (Neubauer chamber), which has a grid etched into its surface. A specialised

glass coverslip is placed over the chamber, and the chamber's depth is precisely 0.1 mm. The haemocytometer counting grid has a total surface area of 9 mm^2, resulting in a volume of 0.9 mm^3 per chamber. The cells were mixed with an equal volume of 0.4% Trypan blue solution (Sigma-Aldrich; T8154), used as a marker for dead cells to determine the number of living/dead cells. The cell suspension was placed gently beneath the coverslip so capillary action draws the suspension out. The number of cells within the four corner squares was tallied with an inverted light microscope. Cells positioned inside the grid and those in contact with the bottom and left lines of each square were included in the count, whereas cells touching the upper and right lines of the square were excluded. The live (unstained) and dead (stained) cells in the four outer squares are counted.

The average number of cells per square was calculated by employing this formula:

Average number of cells per ml = Average cell count (n/4) × Dilution factor × 10^4

So, if 69 cells were counted after a 1:2 dilution, the average number of cells would be 69 x 2 x 10^4=138 x 10^4 cells/ml. Cell viability was calculated using this equation: 100 X (live cells) / (live cells + Dead cells).

Automated cell count using a TC20™ automated cell counter (Bio-Rad, UK) with disposable count slides. The cells were mixed with an equal amount of Trypan blue solution. Next, the cell suspension was placed on the slide. The slide was inserted into a TC20 cell counter; counting starts automatically. The total number of cells (without Trypan Blue) or live cells (with Trypan Blue) was obtained in 30 seconds.

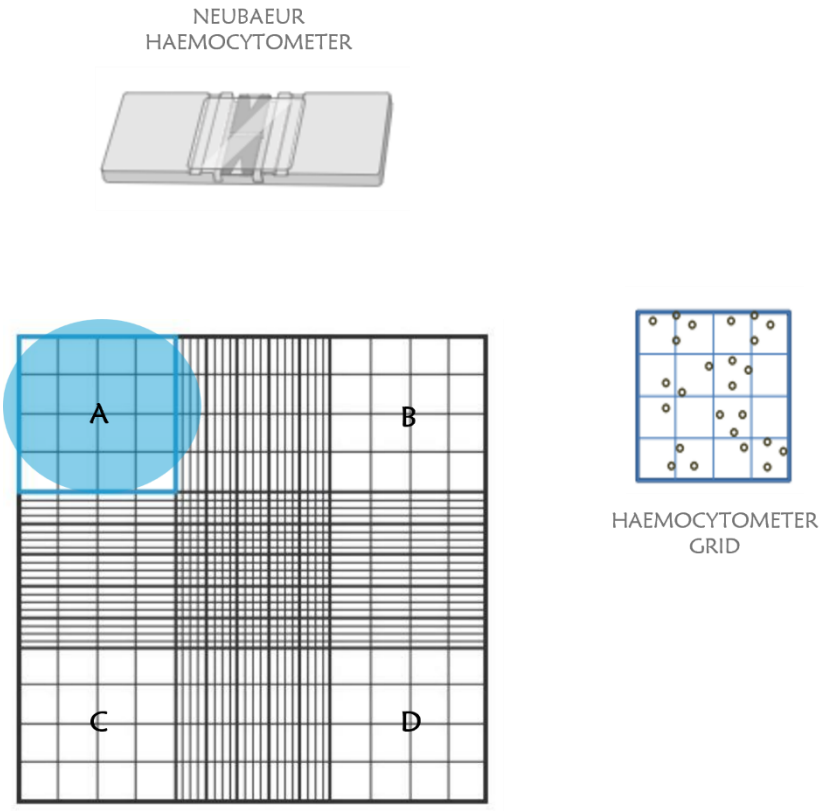

Figure 2.1: The haemocytometer is four-chamber, as seen under the microscope.

2.2.1.3 Cell Freezing

Freezing cell lines is a tissue culture technique that allows cells to be used later. Since continuous cell growth can alter the cell genotype and genetic change, cells were stored in liquid nitrogen to conserve the cell line. They were frozen at low passage numbers in a freezing mixture of 90% FBS and 10% dimethyl sulfoxide liquid (Fisher Scientific; 67-68-5), which serves as a cryoprotective agent. To freeze, cells were separated from a T75 flask with Trypsin-EDTA solution and placed in 10 ml of culture medium. Cells were centrifuged at 1000 rpm for 5 min and cells pellet was resuspended in a freezing mixture. The suspension has been divided into 1 ml aliquots in Sarstedt cryovials and stored at -80°C overnight in a Mr. Frosty freezing container. The cryovials were placed in liquid nitrogen the next day for long-term storage.

2.2.1.4 Transfection of CHO-K1 cells

The transfection was carried out in 6-well plates. First, cells were seeded to achieve 60–70% confluence at transfection. Specifically, 0.25-1 × 10^6 adherent cells were seeded per well in 2 ml of DMEM-F12 medium. On the day of transfection, the medium was removed, the wells were washed with 1X PBS, and 2 ml of fresh DMEM-F12 medium was added to each well.

Lipofectamine 2000 Reagent (Invitrogen, #11668019) was prepared by diluting 12 µl in 150 µl of Opti-MEM Medium. Concurrently, 14 µg of DNA was diluted in 700 µl of Opti-MEM Medium. To form the DNA-lipid complexes, 150 µl of the diluted DNA was mixed with 150 µl of the diluted Lipofectamine 2000 Reagent in a 1:1 ratio. This mixture was then incubated for 10 min at room temperature to allow the DNA-lipid complexes to form.

Following the incubation, 250 µl of the DNA-lipid complex was added to each well-containing cells, resulting in a final concentration of 1.25 ng/µl DNA and 0.6% (v/v) Lipofectamine 2000 Reagent per well. The cells were incubated for two days at 37°C to allow for the expression of the transfected DNA. A further well of non-transfected cells was included as a negative control, and another well transfected with a GFP plasmid was included as a positive control.

After incubation, the transfected cells were analysed using the Zeiss Cell Discoverer 7 Automated Microscope. This advanced imaging system features an automated stage, high-resolution objectives, and integrated fluorescence imaging capabilities. It utilises specific

fluorescence filters to detect the emission spectrum of GFP (excitation at ~488 nm and emission at ~509 nm), enabling accurate identification of transfected cells.

The microscope is equipped with; high-sensitivity cameras for capturing fluorescence signals with minimal photobleaching; and environmental control units to maintain optimal temperature (37°C), CO_2 levels, and humidity, ensuring that live cells remain viable during imaging. Automated focus and stage for precise, reproducible imaging across multiple wells or regions of interest in a multi-well plate.

The analysis was performed using ZEN imaging software, which allowed the segmentation of fluorescence signals, quantification of GFP-positive cells, and measurement of fluorescence intensity. These parameters provided insights into transfection efficiency, protein expression levels, and cellular localisation of the expressed proteins. GFP fluorescence was compared with non-transfected controls to ensure the specificity of the analysis.

After being visualised with a Zeiss Cell Discoverer 7 Automated Microscope, the transfected cells were lysed using RIPA buffer (Radioimmunoprecipitation Assay Buffer), a widely used lysis solution with a pH of 7.4. This buffer disrupts cell membranes and solubilises proteins.

2.2.1.5 Preparation of Mammalian Cell Protein Extracts

Proteins expressed in transfected cells were extracted using Radioimmunoprecipitation assay lysis buffer (RIPA) supplemented with one complete™ Protease Inhibitor Cocktail (Roche, #11697498001). Following incubation for 48 hours, the culture medium was initially aspirated from cells cultured in a 6-well plate. Subsequently, the cells underwent two gentle washes with ice-cold PBS to remove the residual medium with careful aspiration of PBS after each wash. Each well was treated with 200–300 µl of ice-cold RIPA buffer, ensuring the entire well surface coverage. The plate was incubated on ice for 5 min to allow the buffer to permeate the cells and initiate lysis.

Following incubation, cells were detached from the plate using a cell scraper, ensuring a complete collection of lysates into a designated well area. The collected lysate was then transferred into pre-chilled microcentrifuge tubes. To complete lysis, the lysate underwent brief sonication (3–5 pulses of 1 second each). Subsequently, the lysate was centrifuged at 12,000–14,000 x *g* for 15 min at 4°C to pellet cell debris. The resulting supernatant, containing solubilised proteins, was carefully transferred to a new microcentrifuge tube.

The supernatant was either immediately utilised for further investigations, such as western blotting or Coomassie staining, or stored at -80°C for subsequent analysis. This protocol was meticulously followed under controlled temperature conditions to ensure the integrity and quality of extracted proteins for downstream experimental procedures.

2.2.2 Molecular Biology Techniques

2.2.2.1 Heat Shock DNA Transformation

DNA transformation is a procedure in which cells absorb DNA from their surrounding context and integrate it into their genetic material (Johnston et al., 2014). The plasmid DNA was transformed using commercially available, chemically competent JM109 cells (Promega). Generally, 20–50 ng of purified plasmid (with a maximum volume of less than 5 µl) was carefully added to 50 µl of competent cells and incubated on ice for 25 min. The bacterial suspension was immediately transferred to ice after being heat-shocked for 1 min at 42°C. Following a 10 min incubation on ice, 250 µl of SOC medium was added. The culture was then incubated at 37°C for 45 min, shaking at 200 rpm, to allow the bacteria to express the resistance protein associated with the plasmid. Subsequently, 50 µl of the bacterial culture was spread on LB agar plates supplemented with the appropriate selection antibiotic (ampicillin). The plates were incubated inverted overnight at 37°C to allow the growth of transformed colonies.

2.2.2.2 Electroporation Transformation

Electroporation, a precise and careful process, was conducted using pre-chilled 1 mm cuvettes and electrocompetent *E. coli* cells. A pUC plasmid was used as a positive control. The electroporation parameters were set to 1.7 kV, 200 ohms resistance, and 25 µF capacitance, with a target time constant of 4.5-4.7 ms. Electrocompetent cells were thawed on ice and mixed gently. A 1-3 µl volume of plasmid DNA (<100 ng) was added to 50 µl of cells in a pre-chilled microcentrifuge tube, mixed gently, and transferred to a cuvette. Care was taken to avoid air bubbles, and the mixture was evenly distributed at the bottom of the cuvette. The cuvette was placed in the electroporator, and a single pulse was applied. Following electroporation, 1000 µl of SOC medium was added to the cuvette, and the contents were transferred to a bijou tube. The cells were recovered by shaking incubation at 37°C for 30-60 minutes. Finally, 2-5 µl of the recovered cells were plated on LB agar plates containing the appropriate antibiotic and incubated overnight at 37°C.

Finally, 2–5 µl of the recovered cells were mixed with 95 µl of SOC medium and plated on LB agar plates containing the appropriate antibiotic. The plates were then incubated overnight at 37°C. The addition of SOC medium ensured even distribution and provided sufficient nutrients for colony growth, compensating for the small volume of recovered cells used.

2.2.2.3 Subculture and Confirmation of Transformed Colonies

After overnight incubation, five individual colonies from each LB agar plate containing ampicillin were chosen for further analysis. Each colony was inoculated into 5 ml LB broth cultures containing 100 µg/ml ampicillin for antibiotic selection. These cultures were incubated at 37°C with shaking at 200 rpm for 16-18 hours.

For long-term storage, 750 µl aliquots from each overnight culture were mixed with an equal volume of sterile glycerol, aliquoted into cryovials, and stored at -80°C. This cryopreservation technique ensures viable bacterial stocks for future experiments.

To verify successful plasmid transformation, small-scale plasmid DNA preparations were performed using the miniprep method on the remaining culture volumes. Extracted DNA from each culture was analysed by agarose gel electrophoresis to confirm plasmid presence and size. Additionally, restriction enzyme digestion was employed to assess the proper integration of the target gene within the plasmid backbone. This multi-step approach provided robust confirmation of successful transformation and plasmid integrity.

2.2.2.4 Preparation of Plasmid DNA

Small-Scale Plasmid DNA Purification Using Monarch Mini-Prep Kit

A Monarch mini-prep kit (New England Biolabs) was employed to isolate plasmid DNA from 5 ml overnight cultures of transformed *E. coli* grown in an LB medium. The procedure followed the manufacturer's instructions with minor modifications. Briefly, 1-5 ml of bacterial culture was centrifuged at 16,000 x *g* for 1 min. The supernatant was discarded, and the cell pellet was resuspended in 200 µl of plasmid resuspension buffer (B1) containing RNase. Subsequently, 200 µl of lysis buffer (B2) was added to induce cell lysis, followed by gentle inversion until a colour change was observed. The lysate was neutralised with 400 µl of plasmid neutralisation buffer (B3), resulting in a uniform yellow colour and precipitate formation. Clarification was achieved by centrifugation at 16,000 x *g* for 10 min. Enriched with DNA, the supernatant was carefully transferred to a mini column with a top filter inserted into

a manifold. Vacuum application facilitated the passage of the liquid through the filter while the DNA was retained on the column resin. Washing steps were performed: first with 200 µl of plasmid wash buffer, then 400 µl of Plasmid Wash Buffer 2 containing ethanol. To eliminate residual ethanol, which could impede subsequent enzymatic reactions, the column was centrifuged for 1 min. Finally, the filter was transferred to a new microfuge tube, and elution of the DNA was achieved by adding 50 µl of DNA elution buffer to the matrix, incubating for 2 min, and spinning at 16,000 x *g* for 5 min.

Large-Scale Plasmid Purification Using Qiagen Maxi-Prep Kit

Large-scale plasmid DNA purification, often called maxi-prep, is a technique to isolate significant quantities of plasmid DNA from bacterial cultures. This DNA is valuable for subsequent applications such as transfection experiments or large-scale cloning. A maxi-prep kit (Qiagen) was employed per the manufacturer's instructions on 400-500 ml overnight cultures of transformed *E. coli* grown in an LB medium for large-scale plasmid DNA isolation. Following centrifugation at 6,000 x *g* for 15 min at 4°C, the cell pellet was resuspended in RNase-containing buffer P1. Subsequent lysis with buffer P2 and incubation at room temperature for 5 min generated a viscous lysate. Neutralisation with buffer P3 and ice incubation for 15 min yielded a colourless, less viscous suspension. The cleared lysate was then subjected to a vacuum manifold. Transferring the lysate to a pure yield clearing column allowed the supernatant to pass through while the DNA bound to the binding membrane in the pure yield binding column. After removing the clearing column, the binding column was washed with an ethanol-containing solution under vacuum, followed by an additional vacuum drying step. The purified DNA was eluted with nuclease-free water and centrifugation, with final verification and concentration determination performed using restriction enzyme digestion and a Nanodrop 1000 spectrophotometer, respectively.

2.2.2.5 Restriction Enzyme Digestion of Plasmid DNA

Restriction enzyme digestion is a well-established technique to cleave plasmid DNA at defined recognition sequences. This enables scientists to easily manipulate and analyse the DNA for various purposes, including cloning, vector construction, and mutation analysis. High-fidelity restriction enzymes purchased from New England Biolabs were utilised for these experiments, ensuring accurate and efficient DNA cleavage. The selection of specific enzymes

was tailored based on the individual requirements of each experiment, strategically targeting specific restriction sites within the plasmid DNA sequence (Table 2.3). Restriction digest reactions were carried out for 1-5 hours at 37°C.

Table 2.3: Shows the Procedure for Setting Up a Typical Digest to Validate DNA or Prepare Inserts and Vectors for Ligations.

Preparing the insert and vector	**Volume**
DNA Plasmid (Typically ~ 5 µg)	x µl
10 x Reaction Buffer	7 µl
Restriction Enzyme 1	3 µl (X U, enzyme activity depends on the specific restriction enzyme used)
Restriction Enzyme 2	3 µl (X U, enzyme activity depends on the specific restriction enzyme used)
Sterile H_2O	Qsp 70µl

2.2.2.6 Agarose Gel Electrophoresis for DNA Fragment Analysis

Agarose gel electrophoresis, a well-established technique, was employed to separate and size-fractionate DNA fragments following enzymatic digestion. This analysis verified the presence and integrity of the target plasmid DNA. Specifically, high-quality, low-melting-point agarose was utilised for its optimal gel formation and resolving power. Before gel loading, DNA digests were mixed with Midori green direct (Geneflow, UK) at a 10:1 volume ratio or with 2 µl of ethidium bromide to facilitate the visualisation of bands within the gel. Subsequently, the DNA samples and the Quick-Load Purple 1 kb DNA ladder or Quick-Load 100 bp DNA Ladder (New England Biolabs, USA) were loaded onto the agarose gel. The ladders serve as size references, allowing us to estimate the sizes of the DNA fragments in the samples based on their relative positions within the gel after electrophoresis.

For standard analysis, electrophoresis was performed at 100 V for approximately 45 minutes, corresponding to an electric field strength of 5–10 V/cm. This setup facilitated the rapid separation of larger DNA fragments. Conversely, lower voltages (10-30 V) were applied for DNA fragment purification over extended durations (6-15 hours), enabling better resolution and extraction of smaller bands. DNA bands were visualised using SynGene's GeneSnap software (G: Box, Cambridge, UK) under UV light. Precise band excision from the gel matrix was then performed using LED illumination.

2.2.2.7 Plasmid DNA Gel Purification

Following agarose gel electrophoresis, a gel extraction technique was employed to isolate the desired plasmid DNA fragment. This method, often called gel purification, facilitated the removal of the fragment from the agarose matrix while minimising contamination. To ensure a successful outcome, DNA fragments were meticulously excised from the gel under LED light with precise control, aiming to minimise the inclusion of excess gel that could hinder subsequent enzymatic reactions.

For purification, a commercially available Monarch® DNA Gel Extraction Kit (New England Biolabs, UK) was utilised, adhering to the manufacturer's instructions. Four volumes of Monarch Gel Dissolving Buffer were added to the tube containing the excised gel slice. This mixture was incubated at 37-55°C with periodic inversion until complete gel dissolution. The resulting solution was then passed through a column inserted into a manifold using a vacuum.

Subsequently, 500 µl of DNA Wash Buffer was applied, and the vacuum was reapplied to facilitate buffer flow through the column. Finally, elution of the purified DNA was achieved with 50 µl of elution buffer, which was then directly utilised for downstream ligation reactions.

2.2.2.8 Enzyme-Mediated DNA Ligation

Enzymatic DNA ligation was employed to join two DNA molecules covalently. This process, catalysed by DNA ligase, involves the formation of a phosphodiester bond between the 3'-hydroxyl group of one DNA fragment and the 5'-phosphate group of another. Each ligation reaction was performed in a total volume of 20 µl, maintaining a 3:1 insert-to-vector ratio to optimise product yield. The concentrations of both insert and vector were determined using agarose gel electrophoresis, with fluorescent intensity comparisons of the respective bands guiding the calculation. All T4 DNA ligase enzymes and their accompanying reaction buffers were purchased from New England Biolabs, ensuring consistent and reliable performance. Notably, high-fidelity enzymes were utilised for cloning purposes to minimise the risk of unwanted mutations. The setup of a typical ligation of DNA is outlined in Table 2.4. Each ligation should incorporate a negative control, consisting of the vector with ligase enzyme. The ligations were incubated overnight at 16°C, after which the ligase enzyme was inactivated by heating for 10 min at 65°C. High-efficiency JM109 competent cells in single-use vials were employed to transform 5 µl of the ligation.

Table 2.4: Typical Composition of the Ligation Reaction.

Component	Amount	Notes
DNA Vector	2 µg (x µl)	Corresponds to X pmol based on a vector size of X kb
DNA Insert	25 ng x µl	Corresponds to Y pmol based on an insert size of Y bp. Vector-to-insert ratio: 1:3
10x DNA ligase buffer	2 µl	Contains ATP required for ligation
T4 DNA Ligase	1 µl (5 U)	5 U of T4 DNA ligase was added to catalyse ligation
Sterile H_2O	To 20 µl	Adjusted to a final volume of 20 µl

2.2.2.9 Ethanol Precipitation of DNA

Ethanol precipitation was performed in a few simple steps to purify and concentrate the DNA after ligation. First, two volumes of cold 100% ethanol were added directly to the ligation reaction mixture. The solution was gently mixed to encourage the DNA to precipitate, allowing the ethanol to interact with the DNA molecules effectively.

The mixture was then centrifuged at 13,000 x *g* for 15 minutes at 4°C, causing the DNA to form a compact pellet at the bottom of the tube. Carefully, the supernatant was removed, and the pellet was washed with 1 ml of cold 70% ethanol. This step helped to remove any remaining salts or impurities while keeping the DNA intact.

After another quick spin at 13,000 x *g* for 5 minutes, the ethanol was discarded, and the pellet was left to air-dry for a short time to ensure all traces of ethanol evaporated. Finally, the clean DNA was dissolved in 50 µl of buffer, ready for use in downstream applications.

2.2.3 RNA methods

2.2.3.1 RNA Extraction

RNA extraction, or RNA isolation, is a procedure to isolate and purify RNA from biological samples. All procedures involving RNA took stringent precautions to avoid contamination. Surfaces underwent thorough cleansing with RNaseZap, and all glassware was baked at 110°C. Plastics and gloves also underwent meticulous treatment, and they were subjected to RNaseZap or UV light to ensure cleanliness and prevent contamination. To maintain the highest levels of integrity, reagents were either brand new or sourced from designated RNA stocks. Total RNA was extracted from the spleen of a mouse or frozen kidney tissues of mice or rats using the Trizol reagent method. Approximately 1 ml of Trizol reagent was introduced to the spleen, followed by vigorous homogenisation until complete disintegration. The homogenised samples were then incubated for 5 min at room temperature. Subsequently, 0.2 ml of chloroform was added, followed by a vigorous 15-second vortex. The mixture was then centrifuged at 13,400 x *g* for 15 min at 4°C using a C-18k centrifuge (Sigma, UK).

The transparent, upper aqueous layer containing the nucleic acids was carefully transferred into a new endonuclease-free tube. The lower phenol layer, containing dissolved protein and fat, was discarded. 0.4 ml of propan-2-ol was added to the aqueous layer to precipitate the RNA, followed by a 15 min incubation on ice. Afterwards, the sample was centrifuged again at 13,400 x *g* for 10 min. The resulting supernatant was discarded, leaving behind the RNA pellet, which was then washed with 1ml of 75% ethanol. After another round of centrifugation, the remaining liquid was removed, and the sample was air-dried to eliminate residual ethanol. The RNA pellet was dissolved in 100 µl of DEPC-treated, RNA-free H_2O. Finally, the concentration of the extracted RNA was determined using a nanodrop 1000 device. The RNA was screened through agarose gel electrophoresis for further validation, facilitating a check of the band patterns and brightness.

2.2.3.2 Reverse Transcription

The total extracted RNA was reverse transcribed to produce complementary DNA (cDNA). This process was performed using SMART Moloney Murine Leukaemia Virus Reverse Transcriptase (MMLV RT) (Clontech, California, USA). Due to its capability to synthesise a more substantial proportion of full-length cDNAs, SMART MMLV RT is the preferred enzyme for tasks such as cDNA synthesis, real-time RT-PCR, and library construction. This process

utilised random primers that covered all RNA regions to produce a cDNA pool containing a variety of cDNA lengths.

A microfuge tube combined 1–2 µg of RNA, 1 µl of 50 µM random primer, and RNase-free H_2O to a final volume of 10 µl. The mixture was then heated at 65°C for 3 minutes, immediately followed by cooling on ice. Subsequently, 1 µl of 10 mM dNTP mix, 2 µl of 100 mM DTT, and 4 µl of 5× First Strand Buffer were added to the mixture and gently mixed by pipetting. Finally, 1 µl of SMART MMLV RT enzyme was added, and the reaction volume was adjusted to 20 µl with RNase-free H_2O.

The tube was first incubated at room temperature for 10 minutes to allow primer annealing, followed by a 60-minute incubation at 42°C for cDNA synthesis. The reaction mix was then incubated at 70°C for 15 minutes to inactivate the reverse transcriptase enzyme. After completion, the cDNA sample was stored at -20°C for subsequent use.

2.2.3.3 Standard Polymerase Chain Reaction (PCR)

Standard PCR techniques were employed to amplify cDNA templates derived from kidney tissues of immunised mouse spleens with a target protein. All necessary equipment, including gloves, pipettes, and racks, underwent sterilisation through irradiation using short wavelength UV for 10 min. Working primers were prepared by combining 10 µl each of sense and antisense primers with 80 µl of RNA-free H_2O. Each 50 µl reaction held the following components (Promega, UK) (Table 2.5).

A negative control without cDNA was included in each reaction to confirm no contamination in the PCR reactants. Table 2.7 provides detailed PCR cycling settings. All PCR reactions were carried out by a PCR amplification thermal cycler (Proteus II Helena Bioscience, UK).

PCR involves four key steps: initialisation, denaturation, annealing, and extension (Table 2.6). During the initialisation phase, the reaction mixture is heated to 95°C for 3 min, activating the DNA polymerase. The denaturation step involves heating the reaction to 94°C for 45 seconds, breaking the hydrogen bonds between the double-stranded DNA. Following this, the temperature is lowered to 55°C during the annealing phase, enabling the primers to bind to complementary sequences in the DNA template, guiding DNA polymerase replication. In the final extension phase, DNA polymerase integrates the dNTPs in a 5’ to 3’ direction,

synthesising a new DNA strand. The amplified PCR products were subjected to agarose gel electrophoresis to visualise and analyse the resultant DNA bands.

Table 2.5: Master Mix Reaction Solution Constituents for PCR.

Master Mix	**Volume**
GoTaq® Hot Start Master Mixes	25 µl
cDNA	2 µl
Working Primers	1 µl (6 µM)
RNA-free H_2O	22 µl
Total volume	50 µl

Table 2.6: Displays the PCR Cycling Parameters.

Step	**Temperature**	**Time**	**Cycle**
Initialisation	95 °C	3 min	1 cycle
Denaturation Annealing DNA extension	94 °C 55 °C 72 °C	45 sec 1 min 1 min	30-35 cycles
Final extension	72 °C	5 min	1 cycle
Final hold	4 °C	As required	cycle

2.2.4 Protein Methods

2.2.4.1 Recombinant Protein Expression

2.2.4.2 Small-Scale Recombinant Protein Expression in a T7 System

To investigate the preliminary expression of recombinant proteins, suitable pET21a expression vectors containing the gene of interest were transformed into the T7 expression host strain BL21 (DE3) pLysS. (Novagen, UK). Competent cells at a concentration of approximately 1 x 10^8 cells/ml were transformed with 50 ng of plasmid DNA and plated on LB agar plates containing selective antibiotics (100 µg/ml ampicillin) containing 1% glucose. After overnight incubation at 37°C, a single colony was selected to inoculate 10 ml of fresh LB medium containing 100 µg/ml ampicillin and 1% glucose. The next day, 1.5 ml of this culture was transferred to 10 ml LB media containing 1% glucose and 100 µg/ml ampicillin. This culture was grown under controlled conditions (around 5 hours in a 37°C shaking incubator set at 200 rpm) until reaching a desired optical density OD_{600nm} of around 0.4. Subsequently, protein expression was induced by adding IPTG to a final concentration of 1 mM.

Cells were incubated at 37°C for 3 hours post-induction, harvested by centrifugation at 2300 x *g* for 10 min, and the pellets were stored at -20°C. To optimise protein expression, conditions such as induction temperature (25°C and 37°C), IPTG concentration (0.1–1 mM), and post-induction incubation times (3–6 hours) were systematically tested. The optimised condition (37°C, 3 hours, 0.5 mM IPTG) yielded the highest soluble protein levels. Harvested cells were thawed and resuspended in lysis buffer containing 20 mM sodium phosphate, 500 mM NaCl pH 7.4, 1% sodium deoxycholate (Sigma Aldrich, UK), and a complete protease inhibitor cocktail tablet, EDTA free (Roche Diagnostics, UK), followed by sonication using an ultrasonic processor, VCX500 (Jencons, UK), with 4 × 10 sec bursts on ice. The cell lysate was centrifuged at 4472–6708 × *g* for 20 minutes, and the supernatant was collected as Soluble Protein Fraction 1 (SPF1). The previous step was repeated to obtain a second supernatant, saved as Soluble Protein Fraction 2 (SPF2). The remaining pellet was resuspended and washed with 250 µl of deionised water to extract the Insoluble Protein Fraction (IPF). Protein fractions (SPF1, SPF2, and IPF) were analysed using Coomassie staining and western blotting on SDS-PAGE gels to evaluate protein content and solubility.

2.2.4.3 Large-Scale Expression of Recombinant Proteins

Following successful plasmid transformation and preliminary expression assessment, large-scale recombinant protein production was scaled up to 1 L culture volumes. To optimise protein yield and solubility, expression parameters were adjusted based on observations from the initial trials. Using the same transformation protocol as previously described, 10 ml of the pre-grown starter culture containing transformed BL21 (DE3) pLysS cells were inoculated into 1 L of fresh TB medium supplemented with 1% glucose and 100 µg/ml ampicillin. This culture was grown in 2.5 L baffled flasks to ensure adequate aeration during shaking at 200 rpm and a constant temperature of 37°C.

Cell growth was monitored by measuring the optical density at 600 nm (OD_{600}). Once the culture reached an OD_{600} between 0.4 and 0.6, protein expression was induced by adding IPTG to a final concentration of 1 mM. This differed from the initial trials, where alternative induction conditions (e.g., lower IPTG concentrations or delayed induction) were tested. Induction at OD_{600} 0.4–0.6 was selected to optimise cell density and avoid overgrowth, which had previously led to reduced protein solubility due to metabolic stress and the formation of inclusion bodies. Similarly, 1 mM IPTG was chosen based on trial results showing that this concentration effectively balanced robust protein induction with minimal metabolic burden on cells.

The culture was then incubated for an additional 8 hours at 37°C with continued shaking to allow sufficient protein production. Extending the post-induction incubation time from shorter periods used during trials (e.g., 4 hours) resulted in improved protein yield, while further extending it beyond 8 hours did not provide additional benefits. Cells were harvested by centrifugation at 6,000 × *g* for 20 minutes. The resulting cell pellets, enriched with the expressed recombinant protein, were collected and stored at -80°C for further processing and purification.

These adjustments to the induction conditions during scale-up ensured improved recombinant protein yield and solubility while maintaining scalability. Preliminary results from the scaled-up production confirmed that the changes were effective, although further fine-tuning of parameters such as post-induction temperatures or medium composition could further enhance production.

2.2.4.4 Subcellular Fractionation of Proteins from Bacterial Cultures

Bacterial pellets from 1 L cultures were resuspended in 50 ml of lysis buffer containing 20 mM $NaPO_4$ (pH 7.4), 500 mM NaCl, 1% sodium deoxycholate, and a complete, EDTA-free protease inhibitor cocktail tablet (Roach, UK). Following a 30-minute incubation on ice, cell lysis was performed using an ultrasonic processor as previously described for small-scale cultures (section 2.2.4.2). The lysate was centrifuged at 40,000 × *g* for 30 min to separate the soluble fraction from the insoluble pellet, and the supernatant was collected as soluble protein fraction 1 (SPF1). The centrifugation step was repeated to obtain soluble protein fraction 2 (SPF2).

To process the insoluble fraction, the pellet was resuspended in 250 ml of deionised water, sonicated on ice, and centrifuged at 40,000 × *g* for 30 minutes. This washing step was repeated three additional times, following the same method used in (section 2.2.4.2), with adjustments for larger volumes. The insoluble protein fraction (IPF) was then further processed by resuspending and sonicating briefly on ice to isolate inclusion bodies (IB). All protein fractions (SPF1, SPF2, IPF, and IB) were stored at -80°C for subsequent analysis.

2.2.4.5 Solubilisation of Recombinant Proteins from Inclusion Bodies

Recombinant proteins expressed in *E. coli* were isolated as insoluble inclusion bodies (IBs) through centrifugation. The pellets were then resuspended and solubilised using denaturing buffers to disrupt protein-protein and protein-solvent interactions. These buffers typically contain a combination of chaotropic agents (e.g., urea, guanidine hydrochloride), reducing agents (e.g., dithiothreitol, β-mercaptoethanol), and detergents (e.g., Triton X-100, sodium deoxycholate).

This protocol used a solubilisation buffer containing 20 mM $NaPO_4$ (pH 7.0), 500 mM NaCl, and 8 M urea. The buffer was freshly prepared on the day of use and filtered through a 0.45 µm membrane to remove any particulate matter. While the urea was not deionised, high-purity molecular biology-grade urea was used, which is widely accepted for protein solubilisation protocols. According to the manufacturer's specifications, this grade of urea is free from significant ionic contaminants and suitable for use without additional deionisation. The IB pellets were resuspended in the solubilisation buffer at a defined protein

concentration (e.g., 10 mg/ml) and incubated with gentle agitation at room temperature or 4°C in the dark for a specified time (e.g., 2 hours). The extent of solubilisation was monitored by measuring the decrease in light scattering or by SDS-PAGE analysis.

Following incubation, the sample was centrifuged at 9,000 x *g* for 5 min to remove insoluble material, including cellular debris and undissolved protein aggregates. The solubilised protein supernatant was collected, and the protein concentration was determined using Nanodrop spectrophotometry.

2.2.4.6 Purification of His-Tagged Recombinant Proteins using IMAC

Solubilised His-tagged proteins were purified using a pre-packed HisTrap HP column (Cytiva, USA) on a BioLogic LP chromatography system (BioRad, UK). This column employs immobilised metal ion affinity chromatography (IMAC) with nickel ions chelated to the resin, precisely capturing proteins containing histidine tags (Table 2.7). The binding buffer (20 mM sodium phosphate, 500 mM NaCl, 8 M urea, and 20 mM imidazole, pH 7.4) equilibrated the column with five column volumes before sample loading. Samples were diluted 1:1 with binding buffer and loaded onto the column at a 1 ml/min flow rate. The unbound fraction (flow-through, FT) was collected and stored at -80°C. Subsequently, the column was washed with 10 column volumes of binding buffer to remove non-specifically bound proteins.

A washing buffer containing 20 mM Na_2PO_4, 500 mM NaCl, 8 M urea, and 40 mM imidazole (pH 7.4) further enhanced elution specificity by competitively disrupting weaker His-tag interactions with the nickel ions. The washes were collected separately (fractions W1 and W2) and stored at -80°C. Finally, the His-tagged proteins were eluted with elution buffer (20 mM Na_2PO_4, 500 mM NaCl, 8 M urea, and 500 mM imidazole, pH 7.4) at a 1 ml/min flow rate, collecting 0.5 ml fractions.

A gradient elution method was not used in this protocol as the goal was to elute all His-tagged proteins simultaneously by competing nickel ions with a high concentration of imidazole (500 mM). This approach simplifies the process and ensures complete recovery of the target protein in a single step while minimising the time required for the optimisation of a gradient. While gradient elution may provide finer separation of contaminants, the step elution method used here was effective for achieving high purity and yield of the desired protein.

The protein concentration in each fraction was determined using the Bradford assay, and all fractions were stored at -80°C. To assess the oligomeric state of the purified protein, peak fractions were analysed by non-reduced SDS-PAGE on 12% or 15% Coomassie-stained gels to determine the oligomeric state of the purified protein.

The protein concentration in each fraction was determined using the Bradford assay, and all fractions were stored at -80°C. To gain insights into the protein's structural properties and functional potential, peak fractions were analysed by non-reduced SDS-PAGE on 12% or 15% Coomassie-stained gels to assess the oligomeric state of the purified protein. Determining the oligomeric state was essential for understanding whether the purified protein forms monomers, dimers, or higher-order oligomers, as oligomerisation can significantly influence its biological activity and stability. This analysis provided critical information about the protein's behaviour during expression, solubilisation, and purification, which could inform downstream applications.

Purified protein was dialysed at 4°C against 5 L of dialysis buffer (300 mM NaCl, 20 mM Na_2PO_4, pH 7.4) using Bio-Design dialysis tubing with a 10 kDa molecular weight cut-off. The buffer was exchanged twice over 24 hours to ensure the thorough removal of small molecules and contaminants such as urea, imidazole, and salts introduced during purification. Dialysis allows the protein to equilibrate with the dialysis buffer, reducing potential interference from these small molecules in downstream assays.

During dialysis, small molecules and salts below the 10 kDa cutoff diffused out of the tubing, while the purified protein remained inside due to its larger molecular size. This process helped restore the protein to a more physiological environment, improving its stability and preparing it for subsequent analyses. Following dialysis, the purified protein concentration was re-quantified using the Bradford assay and Nanodrop 1000 spectrophotometry to ensure accuracy and account for potential protein loss during dialysis.

Table 2.7: Shows the Specifications of HisTrap HP Columns.

Ligand	**Histidine Tag Column**
Based matrix	cross-linked spherical agarose, 6%
Average bead diameter	34 µm
Dynamic binding capacity	Not less than 40 mg His-tagged protein/ml medium
Flow rate	1 ml/min
Storage	20% Ethanol
Storage temperature	4°C to 30°C

2.2.4.7 Protein Quantification by Bradford Assay

The Bradford assay, established by M.M. Bradford (1976), is a widely used colourimetric method for rapid and accurate protein quantification (Bradford, 1976). This assay relies on the interaction between Coomassie Brilliant Blue G-250 dye and protein molecules. The dye undergoes a conformational change upon binding, shifting its colour to blue with a maximum absorbance of 595 nm. The intensity of the blue colour is directly proportional to the amount of protein-bound, allowing for protein quantification through spectrophotometric measurement at 595 nm.

The Bradford assay utilises a calibration curve generated using known protein concentrations as standards to ensure accuracy. In this experiment, bovine serum albumin (BSA) served as the standard protein, with concentrations of 0.05, 0.1, 0.2, 0.4, 0.6, 0.8, and 1.0 mg/ml prepared in phosphate-buffered saline (PBS).

Sample lysates and standards (5 µl each) were dispensed in duplicate into a 96-well plate. Subsequently, 250 µl of Bradford reagent (Bio-Rad) was added to each well. The plate was then incubated for 5 min at room temperature. Finally, the optical density at 595 nm was measured for all samples and standards. Protein concentrations were subsequently calculated using GraphPad Prism software.

2.2.4.8 Protein Analysis by SDS-PAGE

The protein samples were separated using sodium dodecyl sulphate-polyacrylamide gel electrophoresis (SDS-PAGE). The SDS-PAGE analysis was performed using the Protean II and Mini-Protean II apparatus (Biorad, Hemel Hempstead, UK). All reagents were obtained from National Diagnostics UK.

The choice of gel percentage for SDS-PAGE depends on the size of the protein being analysed. Lower molecular weight proteins are best resolved on higher percentage gels, while larger proteins require lower percentage gels for optimal resolution. For instance, a 15% SDS-PAGE gel is used for proteins under 10 kDa, a 12% gel for proteins between 10-30 kDa, a 10% gel for proteins between 30-100 kDa, and an 8% gel for proteins over 100 kDa.

For the analysis of a 15 kDa protein, a 12% SDS-PAGE gel was prepared using the ProtoGel® 40% kit from National Diagnostics. The gel solution was composed of 30 ml of ProtoGel 40% (acrylamide: bis-acrylamide at a 37.5:1 ratio), 25 ml of 4× resolving buffer (1.5 M Tris-HCl, pH

8.8, with 0.4% SDS), and 43.9 ml of deionised water. To initiate polymerisation, 1 ml of 10% ammonium persulfate (APS) and 0.1 ml of TEMED were added under a fume hood. The mixture was gently swirled, poured into the gel casting cassette, and allowed to polymerise for 10–20 min.

Following the polymerisation of the resolving gel, a 4% stacking gel was prepared by mixing 1 ml of ProtoGel 40%, 2.5 ml of 4× stacking buffer (0.5 M Tris-HCl, pH 6.8, with 0.4% SDS), and 6.44 ml of deionised water. Polymerisation was initiated by adding 0.05 ml of 10% APS and 0.01 ml of TEMED. This mixture was poured over the polymerised resolving gel, and a comb was inserted to form wells. The stacking gel was allowed to be set for 20 minutes before use.

This protocol follows the manufacturer's guidelines for preparing SDS-PAGE gels using the ProtoGel® 40% kit.

2.2.4.9 Sample Preparation and Electrophoresis

Samples were prepared by combining 20 µg of protein, quantified using the Bradford assay, with an equivalent volume of a mixture consisting of 180 µl of 4× Laemmli loading buffer (Bio-Rad, #1610747) and 20 µl of β-mercaptoethanol. The final concentration of β-mercaptoethanol in the mixture was 5% (v/v), as recommended for reducing SDS-PAGE.

The protein samples were initially reduced using potent reducing agents such as β-mercaptoethanol to break down disulphide bonds (S-S) into sulfhydryl groups. This was followed by denaturation through heating at 100°C for 5 min. After cooling to room temperature and brief centrifugation to settle contents at the tube bottom, the comb was removed from the stacking gel. Wells were filled with Tris-Glycine SDS-PAGE buffer (National Diagnostics, #EC-870, UK). Subsequently, 10 µl of Precision Plus Protein All Blue Pre-Stained Protein Standards Marker (Bio-Rad, #1610373, UK) was immediately loaded with the samples. Gels were run at 100-150 V for 120 min to separate proteins until the bromophenol blue loading dye front reached approximately 1 cm from the end of the gel.

2.2.4.10 Staining SDS-PAGE Gel with Coomassie Brilliant Blue

After completing the SDS-PAGE gel electrophoresis, the gel was transferred into a clean staining container. Coomassie Brilliant Blue staining solution, composed of 0.1% (w/v) Coomassie Brilliant Blue R-250, 45% (v/v) methanol, and 10% (v/v) acetic acid in distilled water, was added to submerge the gel completely. The gel was incubated at room

temperature for 1–2 hours with gentle shaking to ensure thorough staining of the proteins. After the incubation period, the staining solution was removed, and the gel was briefly rinsed with distilled water.

Next, the gel was immersed in a de-staining solution of 40% methanol, 10% glacial acetic acid, and 50% distilled water and incubated with gentle shaking. The de-staining solution was replaced multiple times until the transparent background and the protein bands were distinctly visible.

2.2.4.11 Western Blotting

After completing the SDS-PAGE gel electrophoresis, the protein bands were transferred to a polyvinylidene difluoride (PVDF) membrane using a semi-dry electroblotting technique. The PVDF membrane was first activated by wetting it in methanol for 30 seconds, then soaking it briefly in distilled water, and equilibrating it in 1× Trans-Blot Turbo Transfer Buffer. The transfer buffer used was commercially sourced from Bio-Rad as part of the Trans-Blot Turbo Transfer Pack (Bio-Rad, 1704272). Simultaneously, the transfer packs were soaked in the same buffer to ensure uniform transfer conditions.

The transfer packs were then assembled into the cassette, and a roller was used to remove any air bubbles that might interfere with the transfer. The Trans-Blot Turbo System was activated, and the transfer process was carried out for approximately 7 min.

Following the transfer, the membrane was removed from the cassette and washed thrice in 1× TBST (Tris-buffered saline with Tween 20). The 1× TBST buffer was prepared by mixing 20 mM Tris-HCl (pH 7.6), 150 mM NaCl, and 0.1% (v/v) Tween 20 in distilled water. The membrane was then incubated in a blocking buffer consisting of 3% (w/v) bovine serum albumin (BSA) dissolved in 1× TBST for one hour at room temperature to prevent non-specific binding. After blocking, the membrane was washed thrice with 1× TBST, with each wash lasting 20 minutes.

For the primary antibody incubation, the membrane was placed in a mixture of the primary antibody diluted in 5 ml of 1% BSA in TBST and incubated overnight in a cold room on a rolling machine. The following day, the membrane was washed three times for 30 min each at room temperature on a shaker using 1× TBST to remove any excess primary antibodies. The membrane was then incubated with the secondary antibody and diluted in 5 ml of 1% BSA in

TBST for one hour at room temperature on a rolling machine. This was followed by three washes, each lasting 30 min, with 1× TBST to eliminate any excess secondary antibody.

To detect the antibody binding, the membrane was developed using the ECL Western Blotting Substrate (Promega, W1015). Equal volumes of Reagent 1 and 2, approximately 1.5 ml each, were mixed and spread evenly over the membrane surface to ensure it remained wet during the incubation period of 1-3 min. Finally, the results were visualised using the Bio-Rad ChemiDoc™ MP Imaging System. This thorough procedure ensured precise protein transfer and detection, providing clear and reliable results for the analysis.

2.2.5 Immunisation

Animal immunisation was carried out following standard procedures established by BioservUK (Selden Way, Rotherham). Four BALB/c mice, aged 8 to 10 weeks, were immunised on day 0 via subcutaneous injection with 200 µg (50 µg per mouse) of the recombinant SGLT2-Loops fusion protein. At 14 days post-immunisation, mice received a booster dose of SGLT2-Loops-No-Tag without adjuvant, administered subcutaneously at 50 µg per mouse.

Ten days following the booster, immune sera were collected from each mouse. Approximately 100 µl of serum was obtained per mouse and tested by ELISA for reactivity against the SGLT2-Loops and SGLT2-Loops-No-Tag proteins.

On day 28, the mice were administered a booster dose of 30 µg of SGLT2-Loops-No-Tag antigen per mouse via intraperitoneal injection without adjuvant. 5 days later, the mice were euthanised, and their spleens were collected for further analysis.

2.2.6 Enzyme-linked Immunosorbent Assay (ELISA)

The ELISA 96-well plate (Costar) was coated with a diluted target protein in carbonate coating buffer (ThermoFisher, 62610. AP, pH 9.6). A total of 50 µl of the diluted solution was dispensed into each well. The plate was incubated overnight at 4°C to ensure proper coating. For controls, some wells were coated with 3% BSA in coating buffer as negative controls, while other wells were coated with a positive control protein. After the coating step, the plate was washed five times with 400 µl of 1x TBST. The wells were then blocked with 400 µl of 3% BSA in 1x TBST for 1 hour at room temperature to prevent nonspecific binding. After blocking, the wells were washed five times with 400 µl of 1x TBST to remove excess blocking solution.

Various concentrations of sample cultures or purified antibodies were prepared and added to the wells in duplicates, with 100 µl per well, following a pre-determined timetable. This incubation was carried out for 2 hours at room temperature to allow the antibodies to bind to the target protein. The wells were then washed five times with 400 µl of 1x TBST to remove unbound antibodies. Detection of bound antibodies was performed using a secondary antibody conjugated to HRP, which was incubated for 1 hour at room temperature. Following this incubation, the wells were washed five times with 400 µl of 1x TBST. To develop the colourimetric signal, 100 µl of TMB substrate (ThermoFisher, 34018) was added to each well and incubated for 10 min at room temperature.

The reaction was stopped by adding 50 µl of 2.5M sulphuric acid (H_2SO_4) to each well. The absorbance was measured at 450 nm to quantify the bound antibodies. This protocol ensures accurate detection and quantification of antibodies in the samples, with appropriate negative and positive controls to validate the assay.

2.2.7 Phage Library Enrichment (Biopanning)

Biopanning was employed to enrich the phage library for antibodies with high affinity to the target antigen. This process involved multiple rounds of selection, progressively increasing stringency to isolate phages displaying specific antibody fragments.

In the first round, 5–10 µg of purified target antigen was immobilised by coating onto a 96-well plate or other surfaces, such as magnetic beads, and incubating overnight at 4°C. Following immobilisation, the wells were blocked with 3% BSA in PBS for 1 hour at room temperature to minimise non-specific phage binding. After blocking, the wells were washed three times with TBS-T (TBS containing 0.1% Tween-20) to remove excess blocking reagent and unbound antigen.

The phage library, diluted in blocking buffer, was added to the antigen-coated wells and incubated at room temperature for 1 hour to allow binding. Unbound and weakly bound phages were removed through a series of washes with TBS-T. In subsequent rounds, the stringency of the washes was increased by raising the Tween-20 concentration or the number of wash cycles to eliminate non-specific binders. Bound phages were eluted by adding 100 µl of 0.1 M glycine-HCl (pH 2.7) to each well and incubating for 10 minutes at room temperature. The eluate was neutralised by the immediate addition of 15 µl of 1 M Tris-HCl (pH 9.0).

The eluted phages were used to infect mid-log phase *E. coli* XL1-Blue cells and cultured in SB medium supplemented with ampicillin to propagate the phage library. To facilitate the production of filamentous phages, VCSM13 helper phage was added to the culture, providing the replication machinery and coat proteins required for packaging recombinant phages. The culture was incubated at 37°C with shaking for 16–18 hours to ensure sufficient phage production.

The amplified phage population was harvested by centrifugation to pellet the bacterial cells, and the supernatant containing the amplified phage was filtered through a 0.45 µm filter to remove any remaining bacterial debris. The enriched phage population underwent additional rounds of biopanning, with increasing stringency at each step to enrich for phages displaying high-affinity antibody fragments. Typically, three to five rounds of panning were performed, with enrichment monitored by measuring phage binding to the target antigen through phage ELISA assays.

After the final round of selection, individual phage clones were isolated, sequenced, and further characterised for their binding specificity and affinity to the target antigen.

The phage-containing supernatant was collected and mixed with 1/5 volume of 20% PEG 8000 (w/v) and 2.5 M NaCl to precipitate the phages. Polyethylene glycol (PEG) is a high-molecular-weight polymer that facilitates the precipitation of phages by reducing their solubility in solution, while NaCl enhances the aggregation process. The mixture was incubated on ice for 1 hour, followed by centrifugation at 12,000 x *g* for 30 minutes at 4°C to pellet the phages. The resulting pellet was resuspended in 1 ml of PBS or another suitable buffer.

The enriched phage population underwent additional rounds of biopanning, with increased washing stringency in each round to progressively select for high-affinity binders. Typically, three to five rounds of biopanning were performed, and the enrichment was monitored through phage ELISA to evaluate the binding of phages to the target antigen. After the final round, individual phage clones were isolated by plating on ampicillin-containing LB agar plates. Selected positive clones were sequenced and further characterized for their binding specificity and affinity to the target antigen.

2.2.8 Phage Titration (Plaque-Forming Assay)

To determine the concentration of phage particles in the prepared library, a plaque-forming assay was performed. The procedure began with the preparation of a tenfold serial dilution of the phage suspension in 1X TBST, typically ranging from 10^{-1} to 10^{-6}. These dilutions ensured a suitable range for plaque counting, critical for accurately determining the phage concentration.

Next, 200 µl of an overnight culture of XL1-Blue cells grown to an OD_{600nm} of approximately 0.5 was mixed with 10 µl of each phage dilution. The mixture was incubated at 37°C for 15 minutes to allow the phage to infect the bacteria. After this incubation, the infected cells were mixed with 3 ml of molten soft agar (0.7% agar in LB medium containing 100 µg/ml ampicillin), maintained at 42°C, to avoid premature solidification. The mixture was then poured onto pre-warmed LB agar plates (1.5% agar) containing 100 µg/ml ampicillin and spread evenly across the surface.

The plates were incubated overnight at 37°C, during which clear zones (plaques) formed on the bacterial lawn, representing individual phage infections. The plaques were counted the following day, and the concentration of phage particles in the original suspension was calculated using the formula:

$$\text{Phage concentration (pfu/ml)} = \frac{\text{Number of plaques} \times \text{Dilution factor}}{\text{Volume of phage suspension (ml)}}$$

This assay provided an accurate measurement of the phage titer, expressed as plaque-forming units per milliliter (pfu/ml), essential for standardising phage library concentrations for downstream experiments.

2.2.9 Purification of IgG Antibodies Using Protein G Column

IgG antibodies derived from phage display were purified from culture supernatants using affinity chromatography on a Protein G Sepharose column (Cytiva, USA). Before loading the sample, the packed resin was equilibrated with 10 column volumes of phosphate buffer (10 mM sodium phosphate, pH 7.25). The supernatant was centrifuged at 6,000 x *g* for 30 minutes to remove particulates and filtered through a 0.45 µm filter. The clarified supernatant was gently loaded onto the column using a Biologic LP system at an optimised flow rate of 1 ml/min.

The column was then washed with 10 column volumes of phosphate buffer until the UV absorbance returned to baseline. Bound IgG was eluted by applying 5 ml of 0.1 M glycine (pH 2.7) at a flow rate of 1 ml/min. The peak elution fractions, detected via UV absorbance, were immediately neutralised with 20% of 1 M Tris/HCl (pH 8) to prevent IgG aggregation.

The eluted samples were dialysed (using Snakeskin dialysis tubing with a 10,000 Da MWCO) against 5 L of 1X Tris buffer at 4°C, with two buffer exchanges over a 24-hour period. The Protein G column was re-equilibrated with 10 column volumes of phosphate buffer before subsequent sample applications. After each use, the column was washed with 5 column volumes of phosphate buffer and stored in 20% ethanol.

Protein concentration in the collected fractions was measured using either the NanoDrop 1000 spectrophotometer or the Bradford assay. For NanoDrop measurements, 2 µl of each sample was loaded onto the pedestal, and the absorbance at 280 nm was recorded. Protein concentration was calculated automatically by the NanoDrop software using the protein extinction coefficient and path length (0.1 cm). This method allowed for rapid, accurate quantification of protein concentration without requiring additional reagents or dilutions. All purified IgG samples were aliquoted and stored at -80°C.

2.2.10 Fab Biotinylation

Biotinylation on FAB was performed using EZ-Link Sulfo-NHS-LC-Biotin (Thermo Scientific, A39257). The biotinylating process attaches biotin molecules to proteins and antibodies due to its strong binding to the proteins avidin and streptavidin. Due to its small size (244 Da), biotin can bind to various proteins without changing their biological functions. To determine the volume of biotin reagent required for a reaction involving a 20-fold molar excess, the following calculation is performed:

mmol biotin = ml protein x (mg protein/ml protein) x (mmol protein/ mg protein)

After calculating the amount of biotin reagent, the volume of a 10 mM biotin solution to add to the reaction is determined by:

µl Biotin = mmol Biotin x (1,000,000 µl / L) x (L /10 mmol)

After that, the calculated volume of the 10 mM biotin reagent solution is added to the protein solution. The reaction mixture is then incubated on ice for two hours or at room temperature for 30 min. The reaction is stopped by adding 10 µl of 1 M Tris-HCl.

2.2.11 Immunohistochemistry

Immunohistochemistry (IHC) is essential for visualising specific antigens in tissue sections. A critical initial step in IHC involves dewaxing tissue sections, which removes the paraffin wax to facilitate the penetration of aqueous solutions into fixed tissues.

First, tissue sections were dewaxed using xylene, and the sections were usually immersed in xylene for 10 min, ensuring complete paraffin removal. Subsequently, the tissue sections were subjected to a series of ethanol washes at decreasing concentrations (100%, 90%, 75%, and 50%) to dehydrate the tissue and prepare it for rehydration in distilled water and PBS for 10 min each.

Following dewaxing and rehydration, the tissue sections were subjected to antigen retrieval. In this step, slides were boiled in sodium citrate buffer (10 mM sodium citrate, pH 6.0) to expose antigens that may have been masked or cross-linked during fixation. The buffer was prepared by dissolving 2.94 g of trisodium citrate dihydrate in 1 L of distilled water and adjusting the pH to 6.0 using 1 M HCl. Then, the tissue sections were washed with PBS to remove any remaining buffer and treated with trypsin. Trypsin digestion helps further expose antigens by breaking down protein cross-links in the tissue. Subsequent washing with PBS ensures the tissue is adequately prepared for antibody incubation.

To block non-specific binding, tissue sections were treated with blocking solutions such as 5% BSA, 5% donkey serum or 10% goat serum, depending on the experimental requirements. This step prevents antibodies from binding to irrelevant sites on the tissue sections, thus enhancing the specificity of the staining. Then, tissue sections were incubated overnight at 4°C with primary antibodies specific to the target antigen. Primary antibodies bind specifically to their target antigens in the tissue sections, facilitating their detection in subsequent steps.

After overnight incubation, tissue sections undergo a series of washes with PBS to remove unbound primary antibodies and prepare them for secondary antibody staining. Secondary antibodies, conjugated to fluorophores such as Alexa Fluor or fluorescein isothiocyanate (FITC), secondary antibodies were then applied to the tissue sections. These antibodies bind

to the primary antibodies already attached to the target antigens, allowing the visualisation of specific antigen-antibody complexes.

Finally, tissue sections were washed with PBS to remove excess secondary antibodies and mounted using fluorescence mounting media. Coverslips were carefully applied to the slides to protect the tissue sections and reduce fluorescence quenching. Once mounted, slides were sealed with nail polish and stored in a dark environment to prevent photobleaching of fluorophores.

Chapter 3: Generation of Recombinant SGLT2

3.1 Introduction

Sodium-glucose cotransporter 2 (SGLT2) is a notable member among the six subtypes comprising the sodium-glucose cotransporter family (Wicik et al., 2022). Within the kidney tubules, a remarkable specificity exists in expressing the glucose transporter SGLT-2 at mRNA levels approximately 15 times higher than in any other tissue (Rahmoune et al., 2005). SGLT2 is primarily expressed by the tubular epithelium, making it a significant target protein within the kidney. Overexpression of SGLT2 was observed in the proximal tubular epithelial cells of patients with type 2 diabetes mellitus, and SGLT2 inhibitors, which enhance glucose secretion, are commonly used to treat patients with type 2 diabetes (Katsurada et al., 2021).

The availability of a high-affinity monoclonal antibody against SGLT2 presents the opportunity for developing an engineered antibody conjugate, thereby enhancing drug delivery strategies. The development of SGLT2 inhibitors has been implicated in various human diseases, focusing on chronic kidney diseases and diabetes mellitus, notably diabetic kidney disease.

Generating an antibody against a self-antigen-like mouse SGLT2 poses a unique challenge. Traditional immunisation protocols using the full-length protein from a heterologous species might induce antibodies targeting regions of the co-transporter that were intra-cellular and thus not helpful in targeting the protein *in vivo*. A second issue was that regions with secondary structure would be unlikely to fold correctly when expressed in a bacterial host. This could result in the development of antibodies that would only recognise denatured antigens and would thus be ineffective against native proteins in an *in vivo* setting. To overcome these obstacles, we implemented a two-pronged strategy. Firstly, we targeted regions known to be extracellular, and secondly, we identified extracellular loops that lacked secondary structure and were also predicted to be immunogenic. By focusing on these regions, antibodies can be developed with good selectivity for the desired epitopes on mSGLT2 and able to bind extracellular portions of the molecule. The immune system naturally shows tolerance towards self-antigens to prevent autoimmune reactions. In the context of mSGLT2, this tolerance can disturb the development of a robust antibody response. To overcome this difficulty, various strategies can be employed. These may include using adjuvant molecules that enhance the immune response, adopting novel immunisation techniques such as DNA vaccination, or using fusion proteins.

The rationale behind our immunisation protocol is to enhance the probability of obtaining a monoclonal antibody that is specific to mouse SGLT2 and effective in tissue targeting within mouse models of renal scarring. While mouse, rat, and human SGLT2 share structural conservation (Fig. 3.1), immunising mice with SGLT2 from a different species might lead to the selection of antibodies targeting more divergent epitopes, potentially diminishing their reactivity with mouse SGLT2.

Recent studies have invented a promising pathway to overcome immune tolerance using fusion proteins derived from highly immunogenic polypeptides like tetanus toxin or diphtheria toxin A (DTA) to stimulate robust immune responses in immunised mice (Percival-Alwyn et al., 2015). In our project, we employed multiple combined tags. First, we strategically employed a region of diphtheria toxin A containing numerous immunogenic T-cell epitopes. This region was fused to the carboxy terminus of mouse SGLT2-Loops. This contemporary fusion approach addresses the challenges posed by immune tolerance and holds promise for yielding a diverse array of self-reactive antibodies. In addition, the incorporation of diphtheria-toxin A epitopes strategically fused to mSGLT2-Loops adds a layer of complexity to the immunisation process, enhancing the potential for generating monoclonal antibodies with superior efficacy in targeting mouse SGLT2 in the context of renal scarring models. This expression construct was engineered to incorporate codon optimisation and a C-terminal 6-histidine tag to achieve high-throughput purification of the recombinant protein (Fig. 3.2).

Simultaneously, we encountered a challenge in developing antibodies against specific linear determinants produced by mammalian cells that fold at the end, such as peptides. The concern is that these generating antibodies may not always recognise the same region in the native, folded protein due to differences in amino acid positioning. Moreover, there is a concern regarding the specificity of antibody targeting towards the intracellular side of the SGLT2 transporter.

To address this, we examined the structural characteristics of SGLT2, particularly the exposed segments, specifically the extracellular loops (EL1, EL2, EL3) (Niu et al., 2022) (Fig. 3.3). These loops are not structured as alpha-helices or beta-sheets; instead, they are linear. These linear sequences from extracellular SGLT2 loops (EL1, EL2, EL3) were codon-optimised, synthesised, and fused with a commercially synthesised DTA. Incorporating a C-terminal 6-histidine tag facilitates efficient protein purification, and the sequence includes *Nhe*I and *Xho*I restriction

sites (Fig. 3.2) for seamless cloning into the modified pET-21a expression vector (Fig. 3.4). This design is implemented to ensure that the resulting antibodies can effectively reach and interact with the SGLT2 transporter. This complexity of methodology aims to enhance the precision and efficacy of our antibody development strategy. The cornerstone of recombinant protein production lies in cloning the gene of interest into a suitable expression vector that incorporates flanking regions for restriction enzyme digestion.

Bacterial systems are a strategic choice for efficient production, especially applicable to fragments not reliant on glycosylation. Glycosylation, a post-translational modification, can significantly influence proteins' structural and functional attributes, including antibodies and their fragments. This approach simplifies the production process by utilising the pET vector, which contains a strong, regulated promoter, ensuring efficient and cost-effective protein expression. In contrast, while offering benefits such as proper folding and post-translational modifications, a mammalian expression system tends to yield lower quantities, limiting its suitability for large-scale production due to associated cost and efficiency considerations (Verma et al., 1998).

E. coli remains the preferred choice for recombinant protein production due to its well-established genetic tools and ease of manipulation. Decades of research have yielded numerous optimised protocols for every step involved in utilising *E. coli* as a protein expression host (Baneyx, 1999, Makrides, 1996).

Despite its advantages, *E. coli* can present challenges in obtaining functional recombinant proteins, particularly for those of eukaryotic origin. Improper protein folding is a frequent culprit behind the lack of functionality. Eukaryotic proteins may rely on disulphide bridges, which cannot form in the reducing cytoplasm of *E. coli*. Alternatively, they might require specific co-factors, be part of a multi-protein complex missing other components, or depend on chaperones that differ between prokaryotic and eukaryotic cells (Carrio and Villaverde, 2002). Post-translational modifications or polypeptide chain processing, both absent in *E. coli*, can also be essential for functionality (Villaverde and Carrio, 2003).

Furthermore, a significant challenge arises from the link between overexpression and improper folding. Even native *E. coli* proteins can become insoluble when overexpressed due to the high levels achievable with solid promoters. This often results in protein aggregation

and the formation of inclusion bodies (Carrio and Villaverde, 2002). In the context of my study, folding was a concern because the recombinant protein being expressed requires proper conformation to retain its functional properties. However, as inclusion bodies were anticipated due to overexpression in E. coli, strategies such as solubilisation using denaturants and refolding protocols were employed to recover functional protein. These steps mitigate the challenges posed by folding issues and ensure that the protein is suitable for downstream applications.

```
musSGLT         MEQHVEAG--SELGEQKVLIDNPADILVIAAYFLLVIGVGLWSMFRTNRGTVGGYFLAGR
huSGLT2         MEEHTEAGSAPEMGAQKALIDNPADILVIAAYFLLVIGVGLWSMCRTNRGTVGGYFLAGR
                **:*.***  .*:* **.************************ ***************

musSGLT         SMVWWPVGASLFASNIGSGHFVGLAGTGAASGLAVAGFEWNALFVVLLLGWLFVPVYLTA
huSGLT2         SMVWWPVGASLFASNIGSGHFVGLAGTGAASGLAVAGFEWNALFVVLLLGWLFAPVYLTA
                ****************************************************.******

musSGLT         GVITMPQYLRKRFGGHRIRLYLSVLSLFLYIFTKISVDMFSGAVFIQQALGWNIYASVIA
huSGLT2         GVITMPQYLRKRFGGRRIRLYLSVLSLFLYIFTKISVDMFSGAVFIQQALGWNIYASVIA
                ***************:************************************************

                                                                LOOP 1
musSGLT         LLGITMIYTVTGGLAALMYTDTVQTFVILAGAFILTGYAFHEVGGYSGLFDKYLGAMTSL
huSGLT2         LLGITMIYTVTGGLAALMYTDTVQTFVILGGACILMGYAFHEVGGYSGLFDKYLGAATSL
                ******************************.** ** ******************** ***

musSGLT         TVSKDPSVGNISSTCYQPRPDSYHLLRDPVTGDLPWPALLLGLTIVSGWYWCSDQVIVQR
huSGLT2         TVSEDPAVGNISSFCYRPRPDSYHLLRHPVTGDLPWPALLLGLTIVSGWYWCSDQVIVQR
                ***:**:****** **:**********.*********************************
                                                        LOOP 2
musSGLT         CLAGKNLTHIKAGCILCGYLKLMPMFLMVMPGMISRILYPDEVACVVPEVCKRVCGTEVG
huSGLT2         CLAGKSLTHIKAGCILCGYLKLTPMFLMVMPGMISRILYPDEVACVVPEVCRRVCGTEVG
                *****.*************** ****************************:*********

musSGLT         CSNIAYPRLVVKLMPNGLRGLMLAVMLAALMSSLASIFNSSSTLFTMDIYTRLRPRAGDK
huSGLT2         CSNIAYPRLVVKLMPNGLRGLMLAVMLAALMSSLASIFNSSSTLFTMDIYTRLRPRAGDR
                ************************************************************:
```

Figure 3.1: Alignment of Human/Mouse SGLT2.

Alignment of human and mouse SGLT2 proteins highlights significant structural conservation, particularly in the external loop regions selected for expression. Despite evolutionary divergence, these conserved regions suggest shared functional elements. Given this conservation, cross-reactivity of a mouse-derived antibody with human SGLT2 is possible but would depend on the sequence and structural similarity of the specific epitopes recognised by the antibody. Experimental validation would be required to confirm cross-reactivity.

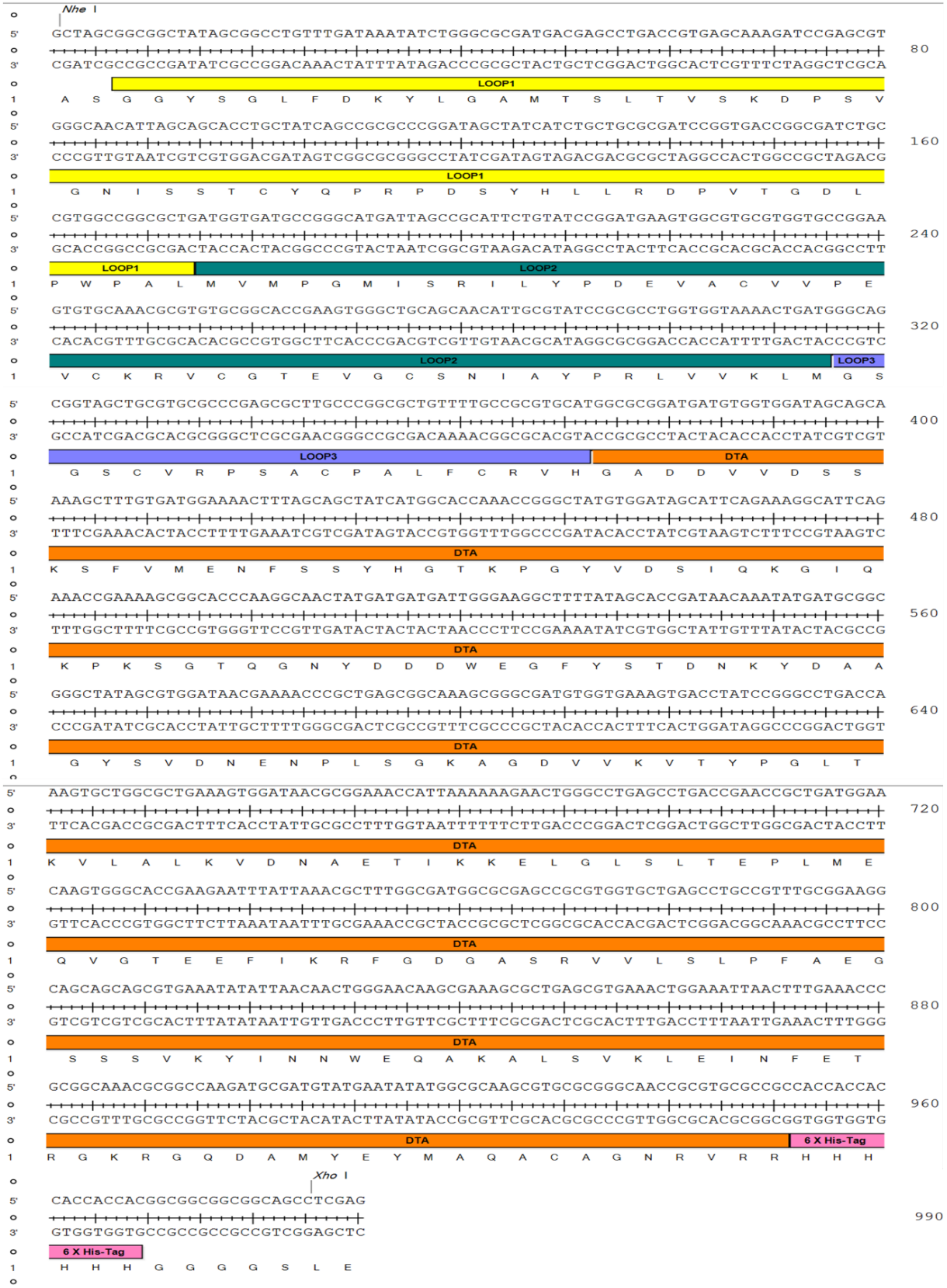

Figure 3.2: Sequence of Synthetic SGLT2-Loops Construct.

The SGLT cDNA was synthesised and fused at the C-terminus with an immunogenic segment of DTA. A 6xHis tag was incorporated at the C-terminus to facilitate purification and detection while minimising disruption to protein function.

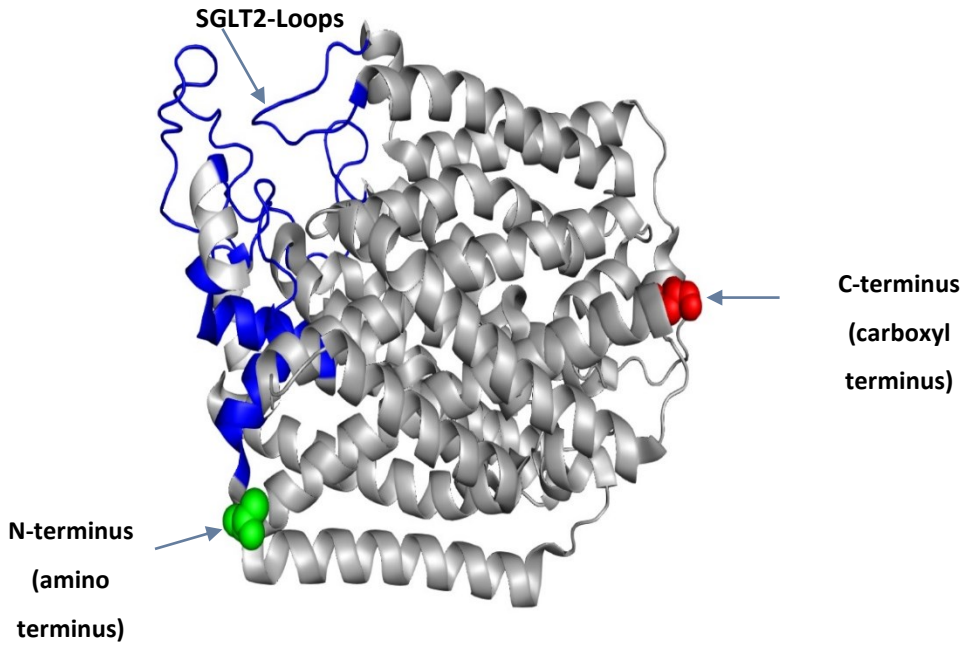

Figure 3.3: Structure of Mouse SGLT2.

The structure of mouse SGLT2 was visualised using PyMOL (Version 2.5, Schrödinger, LLC). The protein backbone is rendered in gray ribbons, and the extracellular loop residues are highlighted in blue.

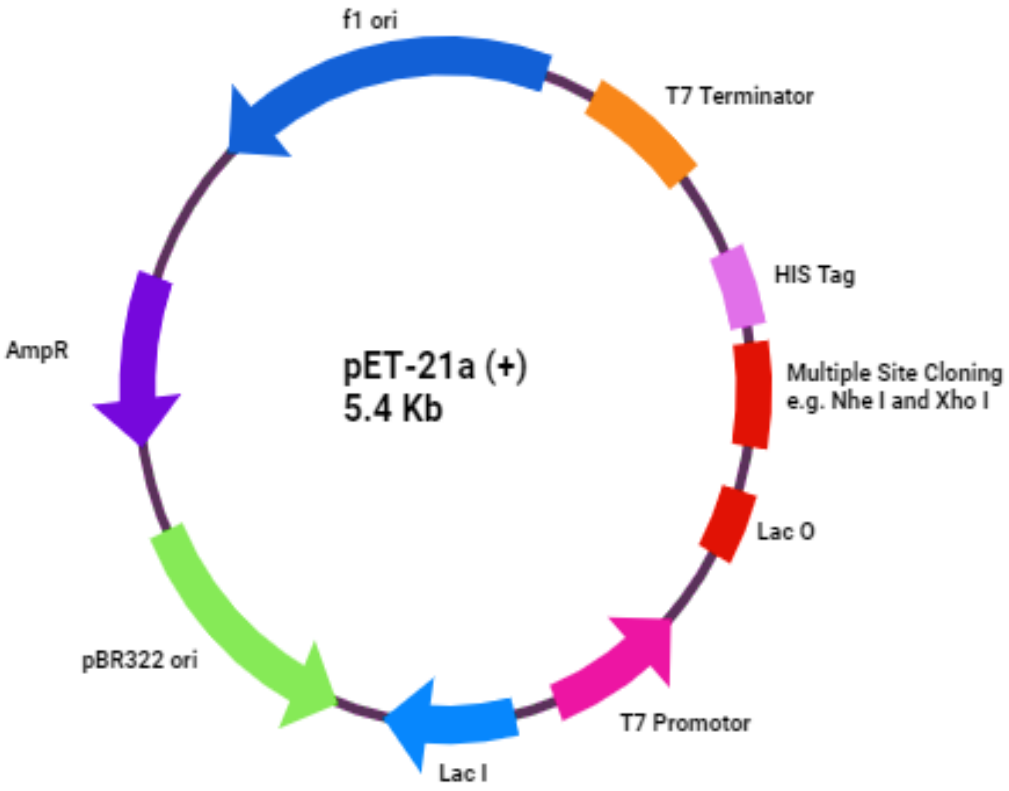

Figure 3.4: Bacterial Expression pET21a Vector Map

The pET21a vector is designed for high-level protein expression in bacterial cells, with a T7 promoter and a His tag for purification. An additional C-terminal 6×His tag was added to ensure efficient purification and detection of the expressed protein.

3.2 Aims and Objectives

The aim of the work in this chapter was to produce purified recombinant SGLT2 proteins, specifically the SGLT2-Loops and SGLT2-Loops-No-Tag domains in sufficient quantities for the immunisation of mice. The workflow scheme is shown in Fig. 3.5. The term "No-Tag" in the SGLT2-Loops-No-Tag refers to the absence of the DTA fusion tag but still includes the His6 tag for protein purification purposes. The specific objectives were to:

- Prepare SGLT2-Loops and SGLT2-Loops-No-Tag inserts for cloning into the pET21a expression vector.
- Perform ligation and transformation of the inserts into *E. coli* for protein expression.
- Induce recombinant protein expression in *E. coli*.
- Purify the expressed SGLT2 proteins and assess purity through SDS-PAGE and western blot.
- Optimise solubilisation and purification methods to ensure sufficient protein yield for immunisation.

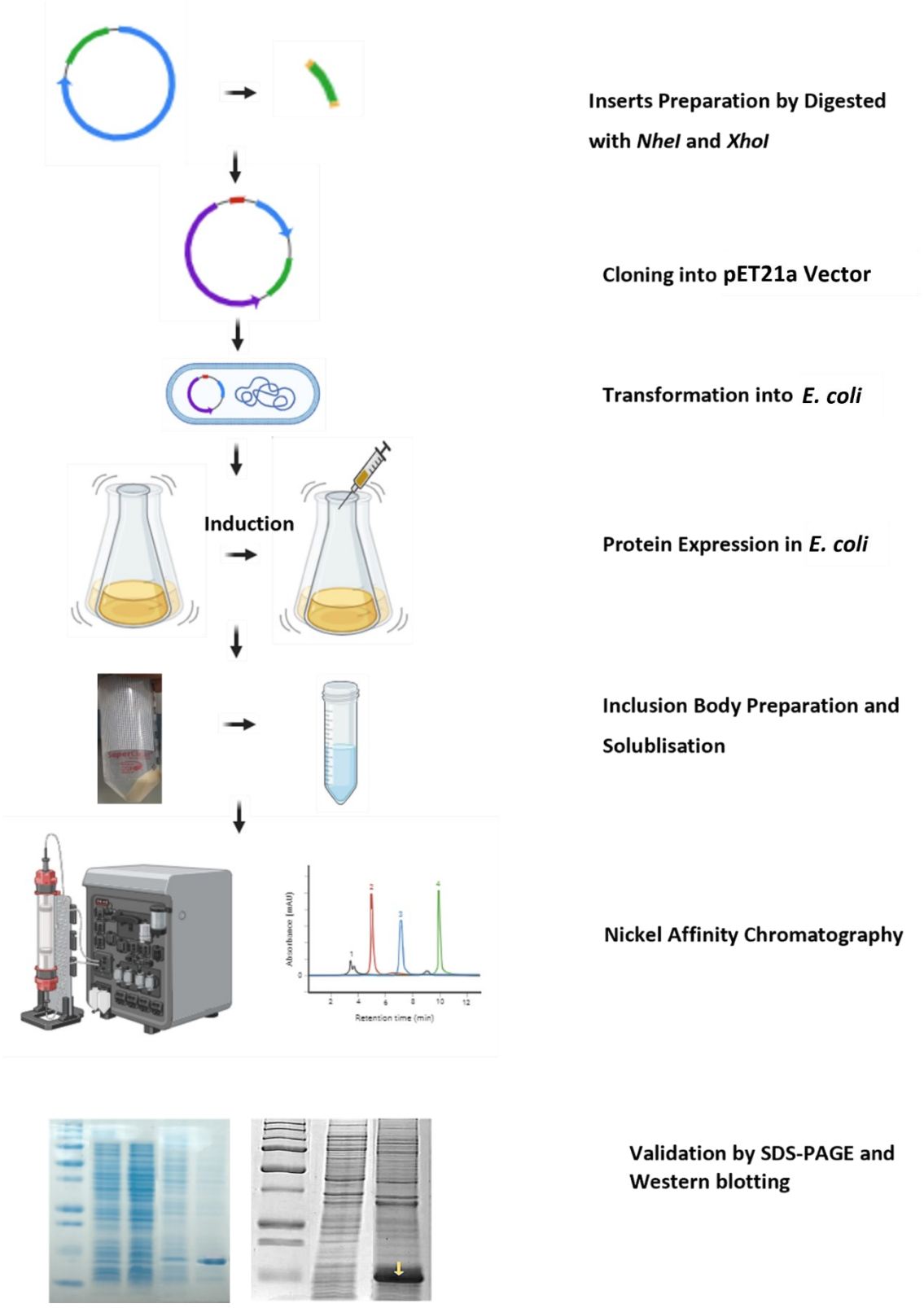

Figure 3.5: Scheme of Recombinant Protein Expression and Purification Workflow in *E. coli.*

3.3 Experiments and Results

3.3.1 Preparation of SGLT2-Loops, SGLT2-Loops-No-Tag and pET21a Plasmids

The mouse SGLT2-Loops and SGLT2-Loops-No-Tag inserts were excised from plasmid pUC-SGLT2-Loops and pUC-SGLT2-Loops-No-Tag by digestion with *Nhe*I and *Xho*I restriction enzymes (2.2.2.5). These sites flank the inserts within the plasmids, allowing for their precise excision as fragments measuring 1,744 bp and 378 bp, respectively, were visualised and recovered by gel electrophoresis (Figs. 3.6 and 3.7).

The expression vector backbone was recovered by digesting pET21a Rat Catalytic Core TG2 with *Nhe*I and *Xho*I, yielding a 5,443 bp fragment (Fig. 3.8). Although the insert in this plasmid (Rat Catalytic Core TG2) is irrelevant to this study, the plasmid was chosen because it allowed for reliable double digestion. Using a plasmid with an existing insert ensures that both restriction sites are functional, thereby reducing the risk of incomplete digestion and simplifying downstream ligation steps. After digestion, the vector backbone was separated and purified by gel electrophoresis (2.2.2.6).

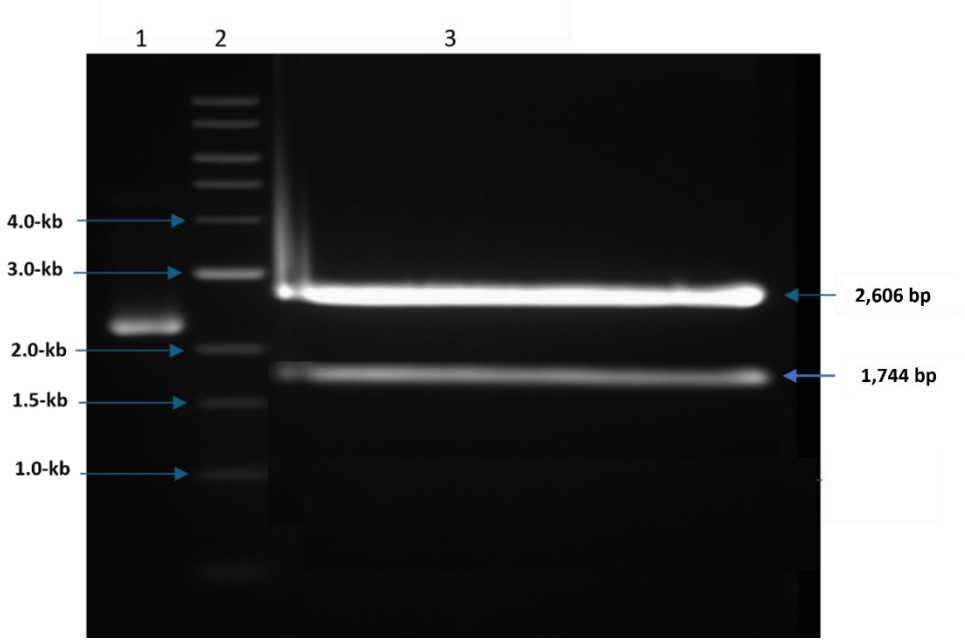

Figure 3.6: Gel Recovery of SGLT2-Loops Insert.

The synthetic SGLT2-Loops fusion coding sequence was isolated by digestion of pUC-SGLT2-Loops plasmid with *Nhe*I and *Xho*I. Digests were run on 0.8% (w/v) agarose gel. Lane 1: Undigested pUC-SGLT2-Loops plasmid; Lane 2: Molecular weight of 1 kb DNA ladder, bands starting at the bottom: 500, 1,000, 1,500, 2,000, 3,000, 4,000, 5,000, 6,000, 8,000, and 10,000; Lane 3: pUC- SGLT2-Loops plasmid was restricted to show 2,606 bp pUC (plasmid) and 1,744 bp SGLT2-Loops (insert).

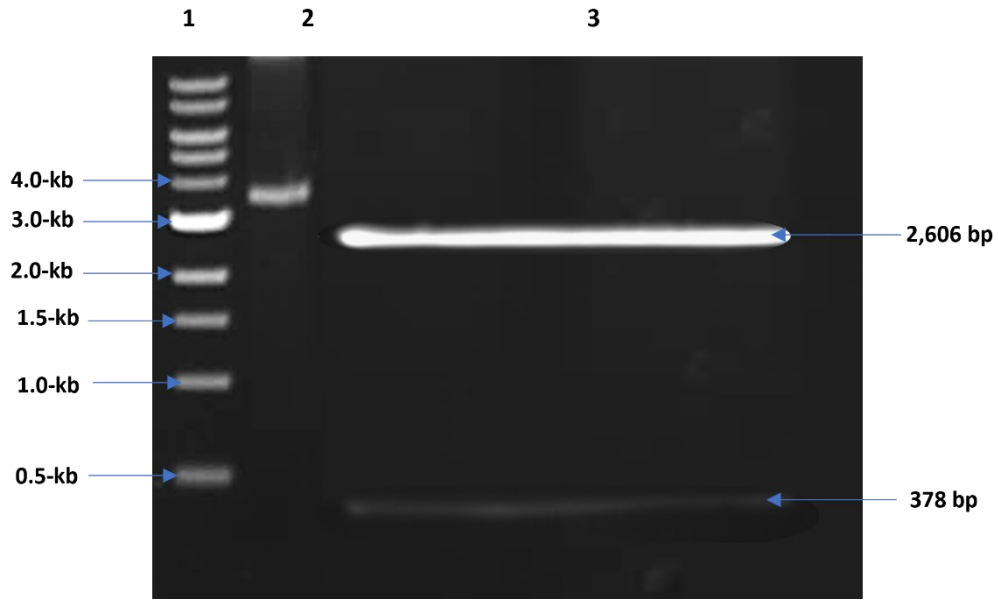

Figure 3.7: Gel Recovery of SGLT2-Loops-No-Tag Insert.

The synthetic SGLT2-Loops-No-Tag sequence was isolated by digesting the pUC-SGLT2-Loops-No-Tag plasmid with *Nhe*I and *Xho*I. The digests were run on 0.8% (w/v) agarose gel. Lane 1: Molecular weight of 1 kb DNA ladder, bands starting at the bottom: 500, 1,000, 1,500, 2,000, 3,000, 4,000, 5,000, 6,000, 8,000, and 10,000; Lane 2: pUC-SGLT2-Loops-No-Tag was restricted to show 2,606 bp pUC (plasmid) and 378 bp SGLT2-Loops-No-Tag (insert).

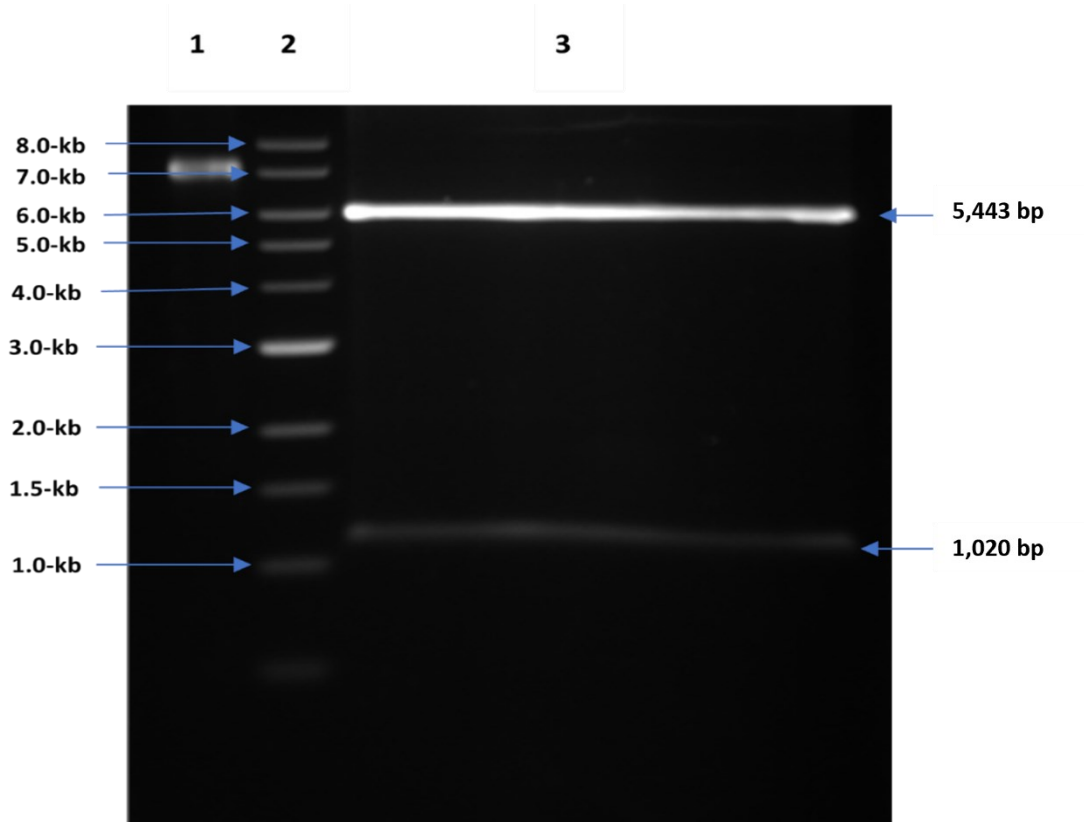

Figure 3.8: Digestion of pET21a Rat Catalytic Core TG2.

Expression vector pET21a Rat Catalytic Core TG2 was digested with *Nhe*I and *Xho*I. The vector backbone was resolved by running on 0.8% (w/v) Agarose gel. Lane 1: Undigested pET21a Catalytic Core TG2 plasmid; Lane 2: Molecular weight of 1 kb DNA ladder, bands starting at the bottom: 500, 1,000, 1,500, 2,000, 3,000, 4,000, 5,000, 6,000, 8,000, and 10,000; Lane 3: pET21a Rat Catalytic Core TG2 was restricted to show 5,443 bp pET21a (plasmid) and 1,020 bp Rat Catalytic Core TG2 (insert).

3.3.2 Cloning of SGLT2-Loops and SGLT2-Loops-No-Tag pET21a Plasmid.

The SGLT2-Loops and SGLT2-Loops-No-Tag inserts were ligated into pET21a, and then transformed into JM109 *E. coli* via heat shock at 42°C for 40 seconds (2.2.2.1). Following an overnight incubation plate at 37˚C, a single colony was picked for each sequence. The pET21a SGLT2-Loops and pET21a SGLT2-Loops-No-Tag plasmids minipreps were conducted, and the recovered plasmids restriction mapped with *Nhe*I and *Xho*I to validate successful incorporation (2.2.2.5) (Figs. 3.9 and 3.10). Plasmids were then subjected to sequencing to confirm the correct reading frames.

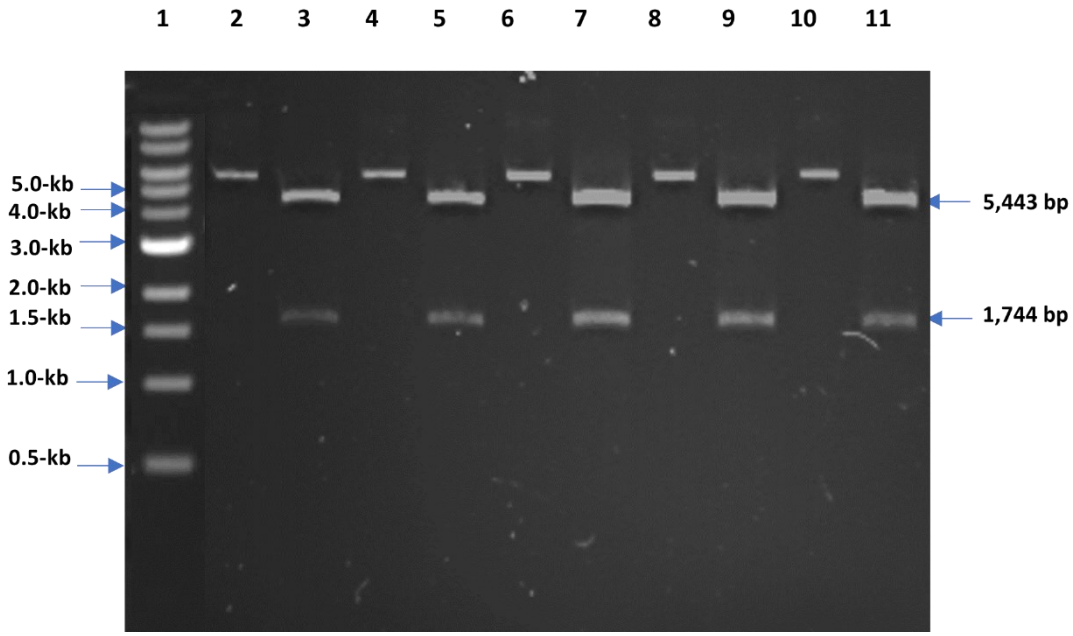

Figure 3.9: Screening of Mini preps pET21a SGLT2-Loops Ligation.

A series of mini preps were digested with *Nhe*I and *Xho*I. A 1,744-bp fragment was released, detecting positive clones. Lane 1: Molecular weight of 1 kb DNA ladder, bands starting at the bottom: 500, 1,000, 1,500, 2,000, 3,000, 4,000, 5,000, 6,000, 8,000, and 10,000; Lane 2,4,6,8, and 10: Undigested pET21a SGLT2-Loops plasmid mini preps; Lane 3,5,7,9, and 11: pET21a SGLT2-Loops plasmid mini preps were restricted to show 5,443 bp pET21a (plasmid) and 1,744 bp SGLT2-Loops (insert).

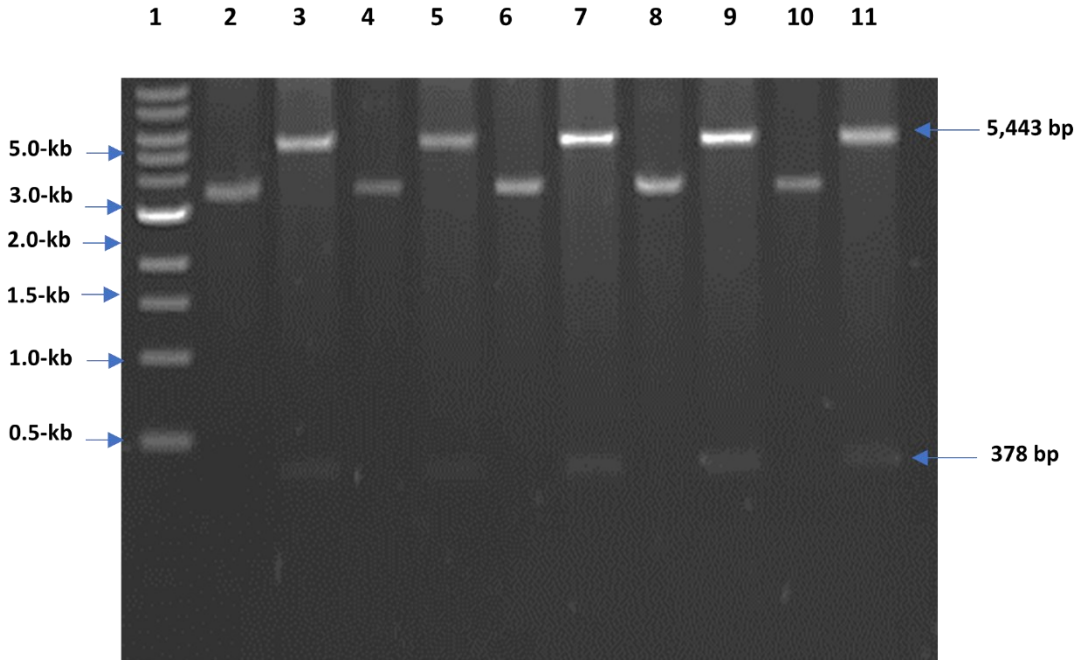

Figure 3.10: Screening of Mini preps from SGLT2-Loops-No-Tag pET21a Ligation.

A series of mini preps were digested with *Nhe*I and *Xho*I. A 378-bp fragment released detected positive clones. Lane 1: Molecular weight of 1 kb DNA ladder, bands starting at the bottom: 500, 1,000, 1,500, 2,000, 3,000, 4,000, 5,000, 6,000, 8,000, and 10,000. Lane 2,4,6,8, and 10: Undigested pET21a SGLT2-Loops-No-Tag plasmid minipreps. Lane 3,5,7,9 and 11: pET21a SGLT2-Loops-No-Tag plasmid minipreps were restricted to show 5,443 bp pET21a (plasmid) and 378 bp for the faint bands corresponding to the SGLT2-Loops-No-Tag (insert).

3.3.3 Small-Scale Expression of Recombinant Proteins in *E. coli*

The recombinant plasmids, pET21a SGLT2-Loops and the pET21a SGLT2-Loops-No-Tag (no-DTA) were transformed into *E. coli* BL21 (DE3) pLysS cells for the purpose of protein expression (2.2.2.1). Protein expression was induced by adding 1 mM IPTG to the LB medium, supplemented with 1% glucose and 100 µg/ml ampicillin, and incubating the cultures at 37°C. The expressed proteins were then analysed using SDS-PAGE (2.2.4.8), with 12% and 15% Coomassie blue-stained polyacrylamide gels (2.2.4.10). Distinct bands were observed at approximately 37 kDa and 15 kDa, corresponding to the molecular weights of SGLT2-Loops and SGLT2-Loops-No-Tag, respectively (Figs. 3.11 and 3.12).

To determine the cellular localisation of each expressed SGLT2 domain within *E. coli*, the cell lysate was subjected to sonication followed by centrifugation, separating the lysate into soluble and insoluble fractions. Subsequently, both fractions were analysed via SDS-PAGE. The SGLT2-Loops and SGLT2-Loops-No-Tag proteins were exclusively identified in the insoluble protein fraction (IPF), indicating that these proteins formed inclusion bodies.

Further confirmation of the SGLT2-Loops protein's identity, particularly its DTA-fusion component, was achieved through western blot analysis (2.2.4.11). The blot was probed with a rabbit anti-DTA antibody conjugated to HRP (Abcam, Ab151222) at a 1:2,000 dilution, followed by detection with a goat anti-rabbit secondary conjugated to HRP antibody at a 1:10,000 dilution (Invitrogen, 34160) (Fig. 3.13). This analysis successfully verified the presence of the DTA-fusion within the SGLT2-Loops proteins.

For the untagged (no-DTA) construct, however, western blotting using anti-DTA antibodies was not applicable, as the no-tag version lacks the DTA component. To address this limitation, future analyses could consider using anti-His6 antibodies for detection, as the His6 tag present in the tagged SGLT2-Loops construct would allow for its identification even in the absence of the DTA tag. This approach could provide a useful method for confirming the identity of the His-tagged SGLT2-Loops protein in experiments involving the no-tag construct.

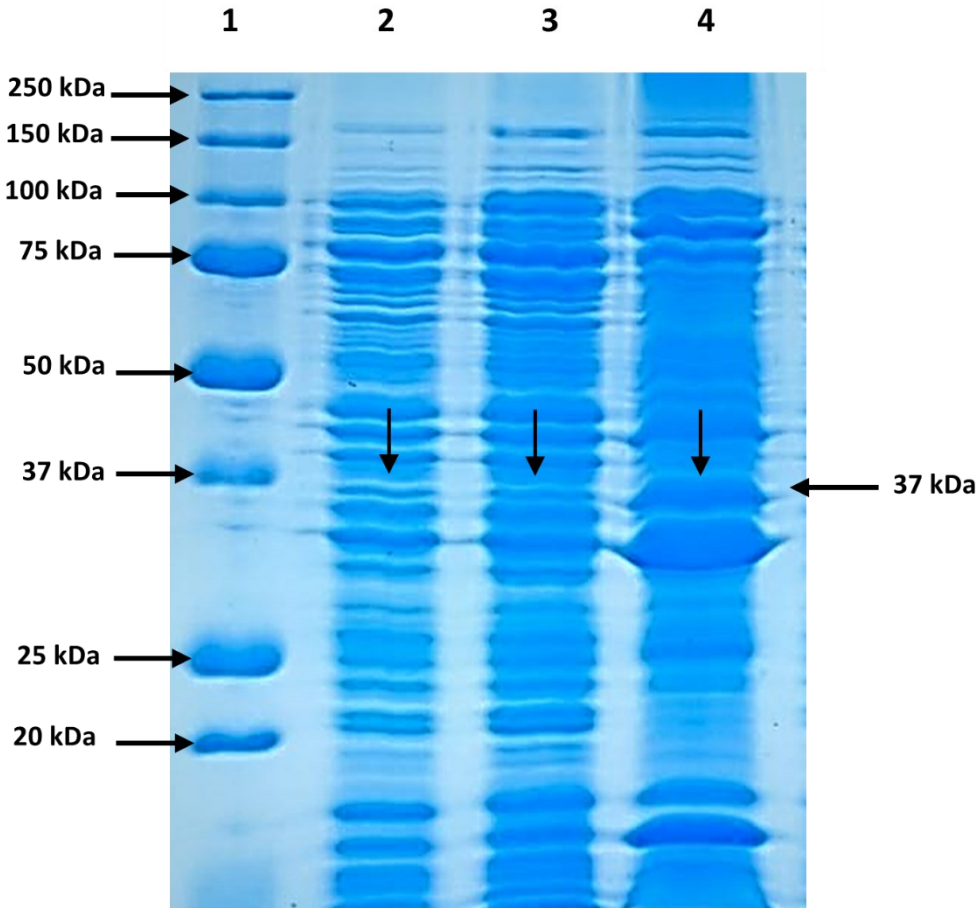

Figure 3.11: *E. coli* Expression of DTA-tagged SGLT2-Loops

A 12% SDS-PAGE reducing gel was Coomassie blue-stained, revealing the expression of mouse SGLT2-Loops (DTA-tagged version) in *E. coli.* Lane 1: Precision plus protein marker (all blue); Lane 2: Non-induced cells at 0 hours with an OD_{600} of 0.08; Lane 3: Non-induced cells after 2 hours at an OD_{600} of 0.2; Lane 4: IPTG-induced total cell extract after 3 hours of induction with 1 mM IPTG. A distinct 37-kDa band corresponding to the DTA-tagged mouse SGLT2-Loops was visible upon induction.

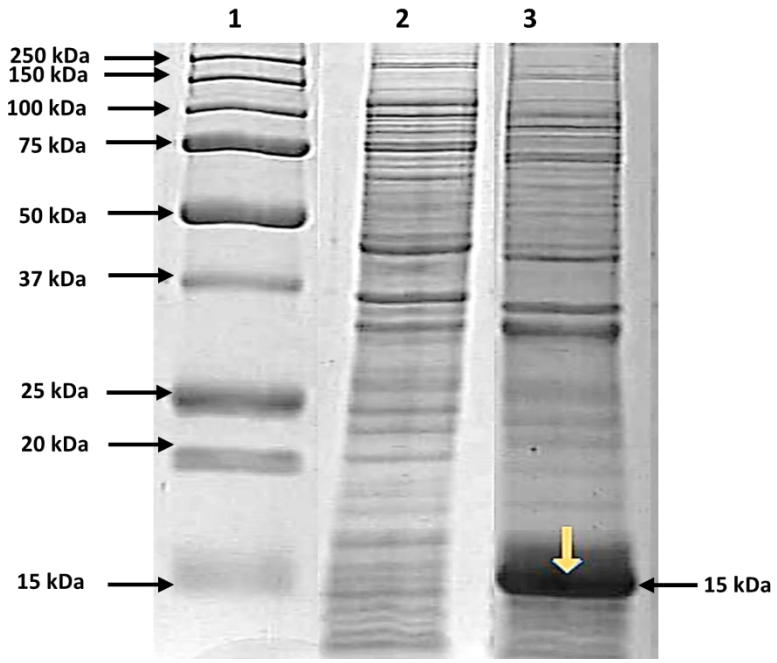

Figure 3.12: E. coli Expression of SGLT2-Loops-No-Tag.

A 15% SDS-PAGE reducing gel was Coomassie blue-stained, revealing the expression of mouse SGLT2-Loops-No-Tag in *E. coli*. Lane 1: Precision plus protein marker (all blue), featuring bands at 10, 15, 20, 25, 37, 50, 75, 100, 150, and 250 kDa from the bottom; Lane 2: Non-induced cells (control), collected prior to IPTG induction; Lane 3: IPTG-induced total cell extract, collected 3 hours post-induction with 1 mM IPTG. Upon induction, a distinct 15 kDa band corresponding to mouse SGLT2-Loops-No-Tag was observed. The gel image was processed by cropping and adjusting the contrast to enhance the visibility of the protein bands, with no other alterations made.

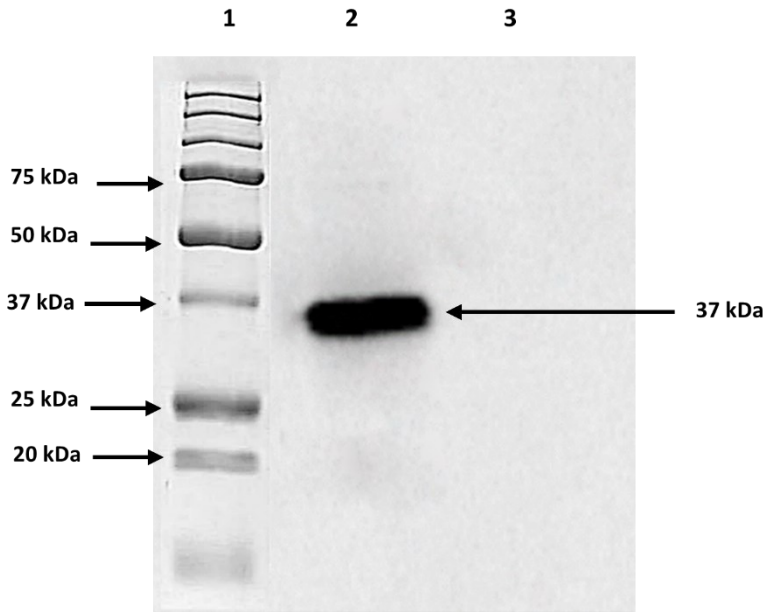

Figure 3.13: Western Blot Analysis of Inclusion Body from SGLT2-Loops Expression.

Western blot analysis of the inclusion body from SGLT2-Loops expression was performed on a PVDF membrane. The blot was probed with a rabbit anti-DTA antibody conjugated to HRP (Abcam, Ab151222) at a 1:2,000 dilution, followed by detection with a goat anti-rabbit secondary antibody conjugated to HRP. The protein bands were visualised after chemiluminescent detection. Lane 1: Precision plus protein marker (all blue), used to determine the size of the detected bands; Lane 2: Total protein from the inclusion body, showing a distinct band at 37 kDa corresponding to the DTA-tagged SGLT2-Loops protein.

3.3.3 Large-Scale *E. coli* Expression of SGLT2-Loops

pET21a vector containing the SGLT2-Loops was transformed into BL21 (DE3) pLysS cells (2.2.2.1), which were then used to inoculate a 1-litre of LB media supplemented with 1% glucose and 100 µg/µl ampicillin. The induction step of transfected BL21 cells involved using 1 mM IPTG stimulated the expression of a robust 37 kDa band on a 12% Coomassie blue-stained reducing polyacrylamide gel (2.2.4.10). This band corresponds precisely to the SGLT2-Loops domain (Fig. 3.11).

The extraction process was adjusted to include 20 mM sodium phosphate, 500 mM NaCl, pH 7.4, 1% sodium deoxycholate, and a complete protease inhibitor cocktail tablet, EDTA free in 200 ml cell lysis buffer (2.2.4.5), as shown in (Fig. 3.14), to facilitate the breakdown of cells for optimal extraction. To determine the presence of the SGLT2-Loops protein in the insoluble fraction, additional washing steps using DI H_2O were implemented. This involved thorough rinsing to remove any residual contaminants and accurately determine the protein's localisation within the insoluble fraction. Subsequently, each fraction experienced loading onto an SDS-PAGE (2.2.4.10) (Fig. 3.15). Analysis of subcellular fractions revealed that SGLT2-Loops protein primarily resided within the insoluble fraction, identified as the inclusion body.

3.3.4 Large-Scale *E. coli* Expression of SGLT2-Loops-No-Tag

pET21a vector, containing the SGLT2-Loops-No-Tag, was transformed into BL21 (DE3) pLysS cells (2.2.2.1) and induced as above. Cell fractions were analysed on a 15% Coomassie blue-stained reducing polyacrylamide gel (2.2.4.10), revealing a distinct 15 kDa band corresponding to the SGLT2-Loops-No-Tag domain. Proteins were extracted as above. As before, the resulting fractions were further fractionated on an SDS-PAGE (Fig. 3.16). Analysis of subcellular fractions demonstrated that SGLT2-Loops-No-Tag was in the insoluble fraction.

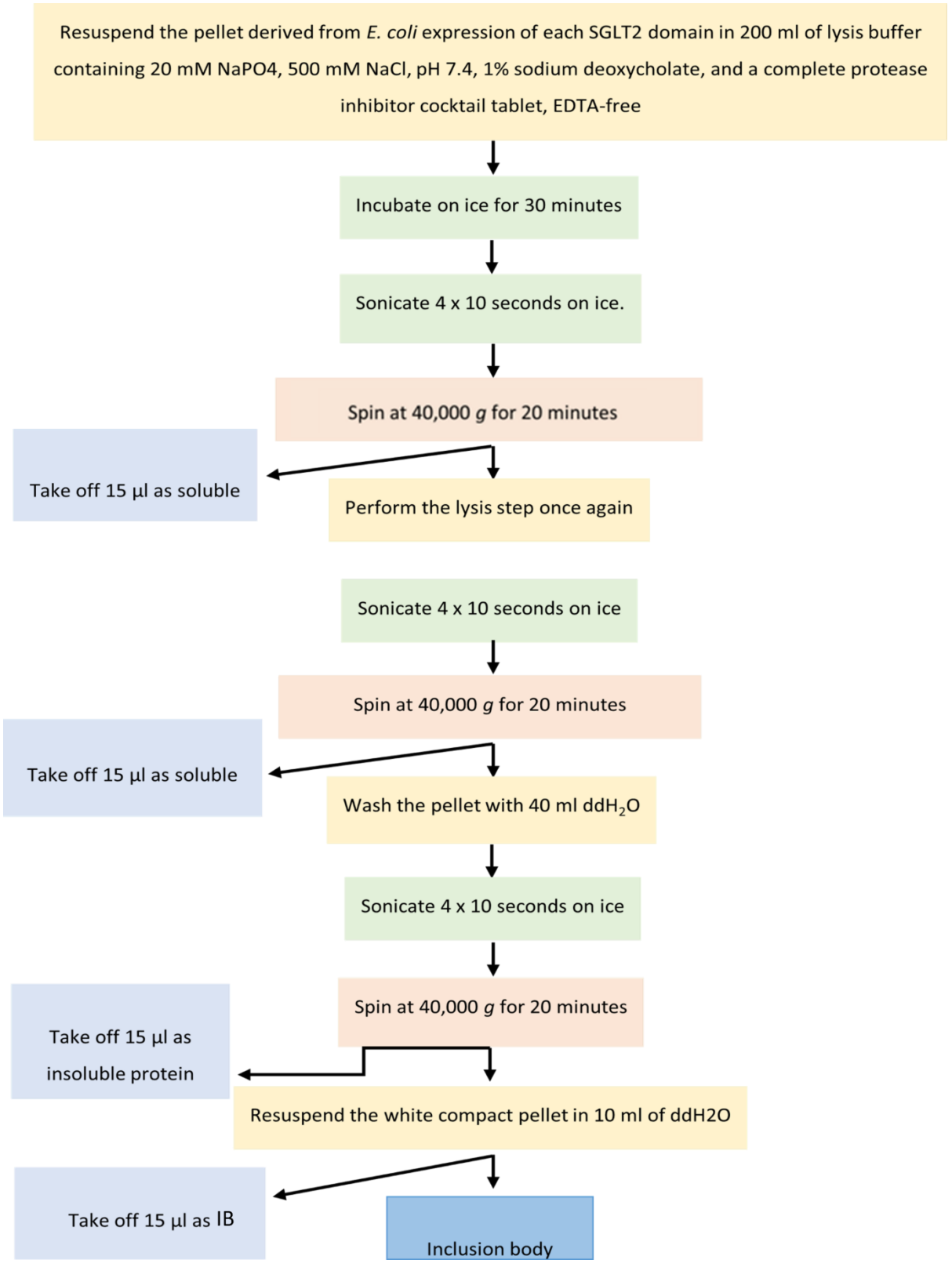

Figure 3.14: Process of Cell Fractionation and Isolation of Inclusion Bodies.

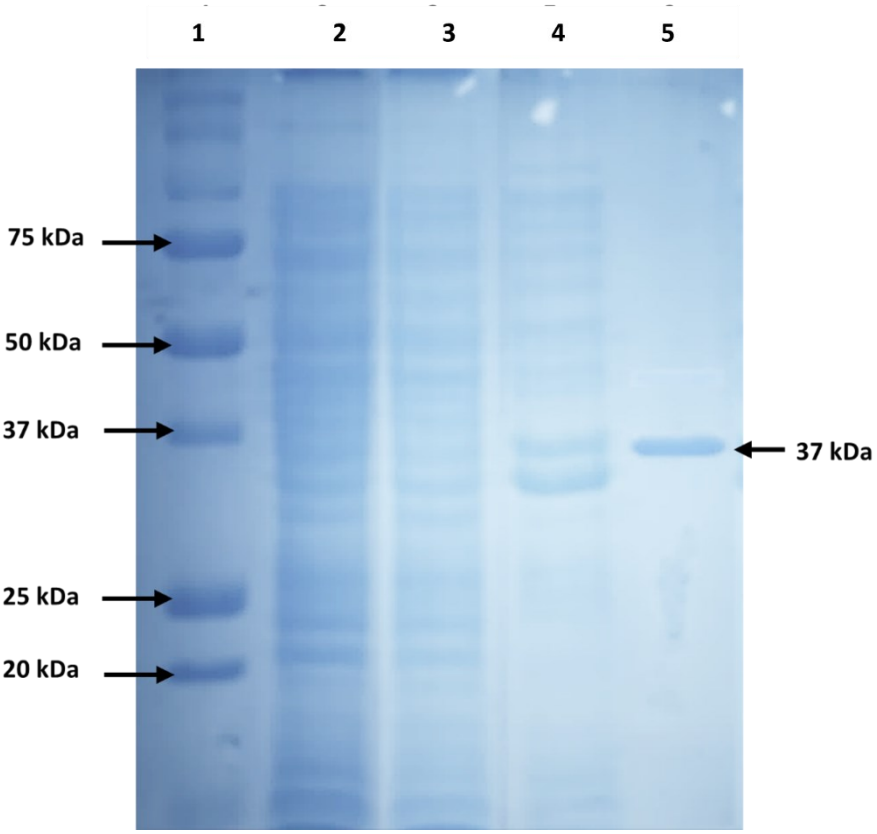

Figure 3.15: Fractionation of Recombinant SGLT2-Loops.

Protein fractions and washes were applied to a 12% reducing gel and subjected to SDS-PAGE. The gel was then Coomassie blue-stained, revealing the expression of mouse SGLT2-Loops in *E. coli.* Lane 1: Precision plus protein marker (all blue), featuring bands at 10, 15, 20, 25, 37, 50, 75, 100, 150, and 250 kDa from the bottom; Lane 2: Soluble Protein Fraction 1 (SPF1); Lane 3: Soluble Protein Fraction 2 (SPF2); Lane 4: Water extraction fraction wash; Lane 5: Inclusion body. Lane 4 shows two distinct bands: one at approximately 37 kDa corresponding to the SGLT2-Loops protein, and a second band at a higher molecular weight, likely representing a non-specific or aggregated protein. The distinct 37 kDa band in Lane 5 was confirmed as SGLT2-Loops.

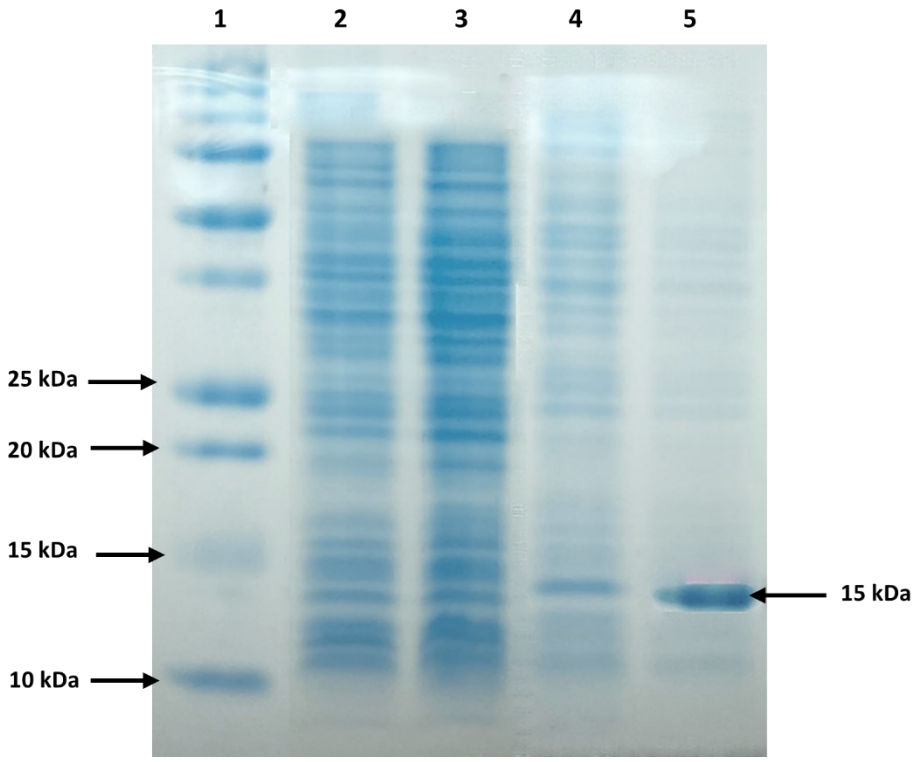

Figure 3.16: Fractionation of Recombinant SGLT2-Loops-No-Tag.

Protein fractions and washes were applied to a 15% reducing gel and subjected to SDS-PAGE. The gel was then Coomassie blue-stained, revealing the expression of SGLT2-Loops-No-Tag.Lane 1 The precision plus protein marker all blue, featuring bands at 10, 15, 20, 25, 37, 50, 75, 100, 150, and 250 kDa from the bottom; Lane 2: Soluble Protein Fraction 1 (SPF1); Lane 3 Soluble Protein Fraction 2 (SPF2); Lane 4; Water extraction fraction wash; Lane 5; Inclusion Body. A 15 kDa band corresponding to SGLT2-Loops-No-Tag was observed upon induction with 1 mM IPTG as the inclusion body.

3.3.5 Solubilisation of SGLT2 Insoluble Domains

The SGLT2-Loops and SGLT2-Loops-No-Tag domains were predominantly located within inclusion bodies in *E. coli*, necessitating subsequent solubilisation in an appropriate buffer. Semi-pure protein aggregates of each SGLT2 domain, accompanied by contaminants, were subjected to solubilisation in 20 mM $NaPO_4$ and 500 mM NaCl with the addition of varying concentrations (2M and 8M) of different chaotropic reagents such as urea or guanidine hydrochloride. Dithiothreitol (DTT), a reducing agent, was also employed to investigate its role in facilitating the solubilisation of inclusion body proteins.

Optimisation trials were carried out to enhance the efficiency of protein solubilisation. Solubilisation was significantly improved in the presence of 6M guanidine hydrochloride. Urea, particularly at 8M concentration, gave comparable results to guanidine hydrochloride for the solubilisation of the inclusion body.

Only 40% of the protein from SGLT2 inclusion bodies exhibited solubility in the presence of 2M urea in buffer composed of 20 mM $NaPO_4$, 500 mM NaCl, and 10 mM DTT at pH 8 compared to approximately 80% solubility achieved with 8M urea. Increasing the pH to 10 in the buffer (20 mM $NaPO_4$, 500 mM NaCl and 10 mM DTT) with 8M urea did not help dissolve a higher amount of SGLT2. Additionally, increasing the DTT concentration from 10 to 20 mM in 20 mM $NaPO_4$ and 500 mM NaCl, with 8 M urea, had minimal impact on solubilisation. Notably, dissolving SGLT2 in a buffer consisting of 20 mM $NaPO_4$ and 500 mM NaCl, pH 7.4 without DTT, did not yield significantly different results. Therefore, the optimal conditions for SGLT2 solubilisation were determined to be in a buffer of 20 mM $NaPO_4$ and 500 mM NaCl at pH 7.4, supplemented with 8 M urea.

Furthermore, our investigation revealed that employing lower temperatures (4°C) had a beneficial effect on the solubilisation of SGLT2 domain inclusion bodies compared to the process at room temperature. However, the solubilised SGLT2 domain proteins appeared to form a clear solution in the supernatant, whereas other impurities, such as aggregated proteins, remained insoluble and were separated out during centrifugation. This observation allowed for an early purification step by removing these insoluble contaminants. These established protocols were selected for large-scale solubilisation of both SGLT2 domains, to generate sufficient material for subsequent refolding processes.

3.3.6 Purification of SGLT2-Loops

The solubilised SGLT2-Loops were purified using a HisTrap HP column, a ready-to-use system specifically designed to purify proteins with six histidine tags at the C-terminus using immobilised metal affinity chromatography (IMAC) (2.2.4.6). The purification process was carried out on a Biologic LP chromatography system. After extensive washing of the nickel column, the protein was eluted with 500 mM imidazole (Fig. 3.17). Two elution pools were collected separately, with the first pool containing the protein eluted at a lower imidazole concentration and the second pool collected at a higher concentration of imidazole. The protein content in each fraction was determined using the Bradford assay, and fractions with concentrations exceeding 0.2 mg/ml were combined for further processing.

The final volume of the combined pools was 7m ml, and the protein was dialysed using Snakeskin dialysis tubing (10,000 Da MWCO) against 5 L of dialysis buffer (150 mM NaCl, 40 mM $NaPO_4$ pH 7.4) at 4°C to remove imidazole and urea and to facilitate protein refolding. No aggregation of the eluted SGLT2-Loops was observed during dialysis, suggesting that the protein remained soluble under the dialysis conditions. The dialysis process effectively removed imidazole, which had initially been added to a concentration of 500 mM in the elution buffer, resulting in a final concentration of imidazole near zero in the dialysed sample. Similarly, urea, which had been used in the solubilisation buffer at a concentration of 8 M, was also removed during dialysis, resulting in a final urea concentration that was negligible in the purified protein.

Purification was further assessed using the Bradford assay (2.2.4.7) and confirmed by SDS-PAGE (Fig. 3.18) comparing the purified SGLT2-Loops with a BSA standard curve. The concentration of the purified SGLT2-Loops was measured using a Nanodrop 1000, with the first sample producing a concentration of 0.582 mg/ml and the second sample measuring 0.463 mg/ml. The final concentration of the purified protein was 0.522 mg/ml in 5 ml, giving a total yield of 2.61 mg.

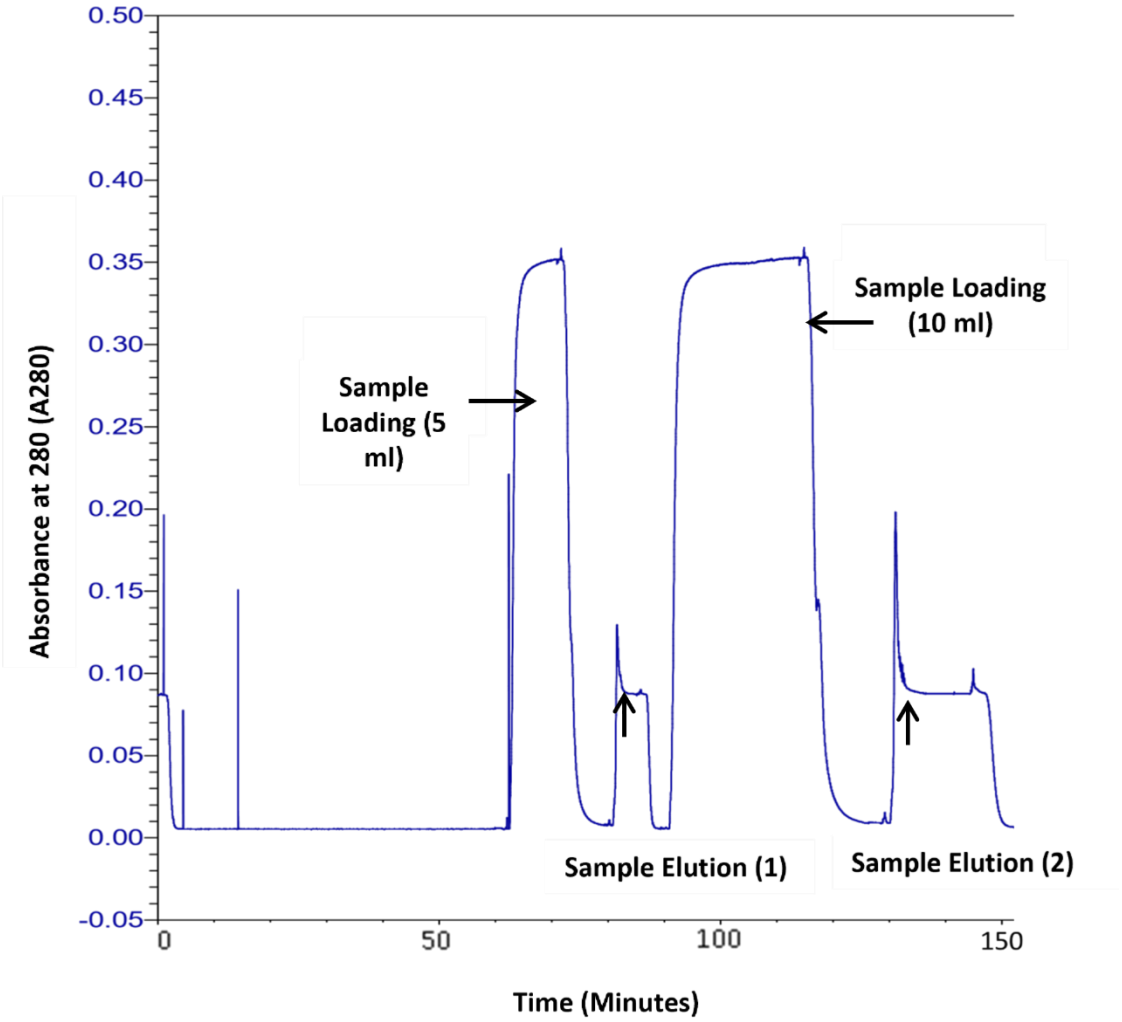

Figure 3.17: Elution Profile of SGLT2-Loops from the Nickel Column.

The elution profile shows protein absorbance at 280 nm versus elution time (in minutes) for SGLT2-Loops. The low absorbance values observed during elution suggest that the concentration of protein is below 1 mg/ml, potentially correlating to a concentration of approximately 0.5 mg/ml, as determined by the Bradford assay. The flow rate during the chromatography process was 1 mL/min, allowing for the estimation of volumes at each point in the profile. Two distinct elution pools were collected. The concentration of the purified SGLT2-Loops was measured using a Nanodrop 1000, with the first sample producing a concentration of 0.582 mg/ml and the second sample measuring 0.463 mg/ml. The final concentration of the purified protein was 0.522 mg/ml in 5 ml.

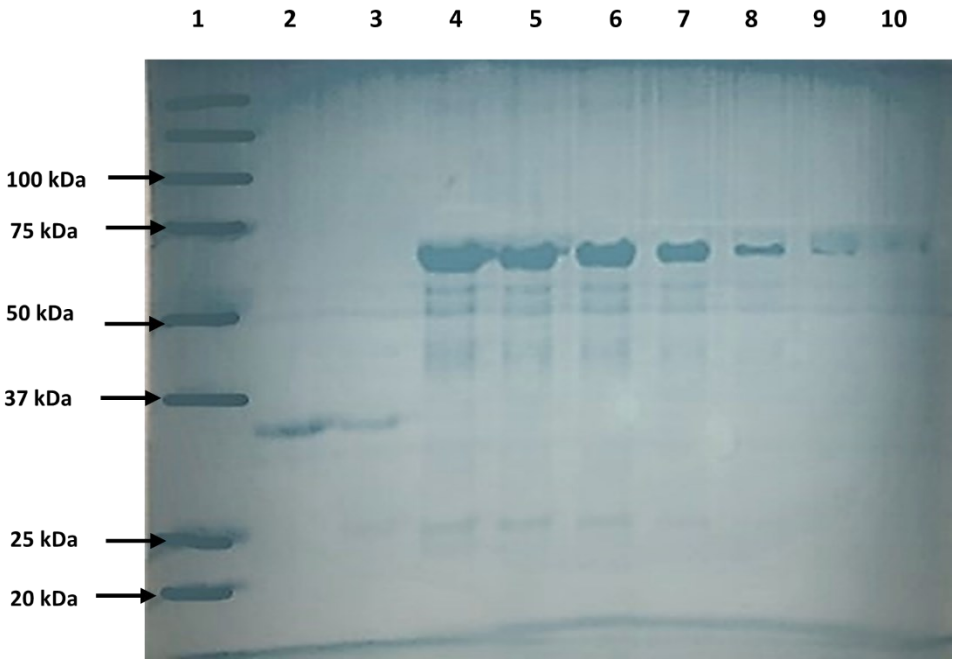

Figure 3.18: SDS–PAGE of Purified SGLT2-Loops and BSA Standard Curved.

A 12% SDS-PAGE gel stained with Coomassie blue displaying purified SGLT2-Loops proteins post-dialysis against 150 mM NaCl, 40 mM $NaPO_4$, pH 7.4. Lane 1: Precision plus protein marker (all blue); Lane 2: Pure SGLT2-Loops sample 1 with a concentration of 0.582 mg/ml; Lane 3: Pure SGLT2-Loops sample 2 with a concentration of 0.463 mg/ml; Lanes 4 to 10: BSA standard curve at concentrations of 1, 0.8, 0.6, 0.4, 0.2, 0.1, and 0.05 mg/ml, respectively. The amount of protein loaded in each lane was 20 µg for both the SGLT2-Loops samples and the BSA standards, based on Bradford assay quantification.

3.3.7 Purification of SGLT2-Loops-No-Tag

The purification of soluble SGLT2-Loops-No-Tag via nickel column chromatography followed the same procedure outlined above (2.2.4.6). The elution profile of SGLT2-Loops-No-Tag from the Ni-column (Fig. 3.19) exhibited clear resolution. The concentration of the harvested SGLT2-Loops-No-Tag was determined to be 1.5 mg/ml. The total yield of the protein was calculated by multiplying the concentration by the total volume of the eluted pool. The volume of the eluted protein pool was 5 ml, giving a total yield of 7.5 mg. Subsequently, the eluted SGLT2-Loops-No-Tag was dialysed as previously described to eliminate imidazole. Notably, no aggregation was observed during the dialysis process.

The efficacy of the purification process was evaluated through SDS-PAGE (Fig. 3.20), revealing the presence of SGLT2-Loops-No-Tag as a distinct band, indicating its high purity.

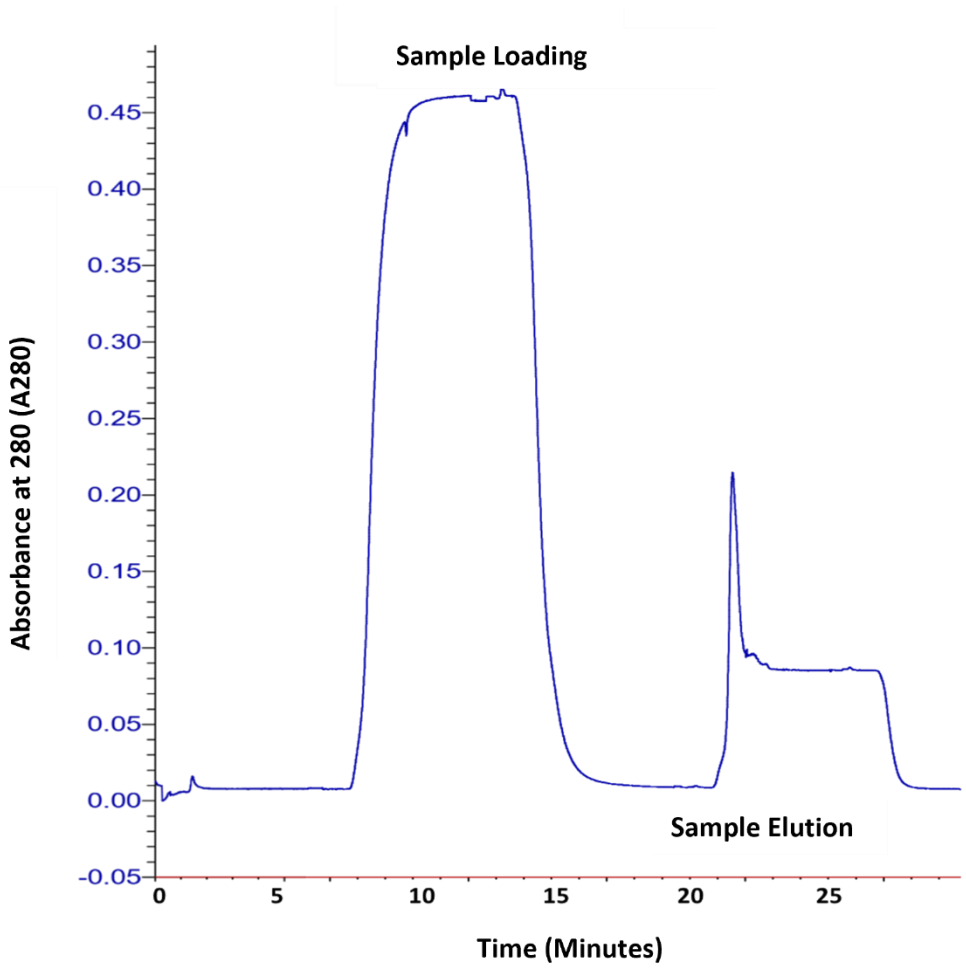

Figure 3.19: Elution Profile of SGLT2-Loops-No-Tag from Nickel Column.

Elution profile showing the protein absorbance at 280 nm versus elution time in minutes for SGLT2-Loops-No-Tag.

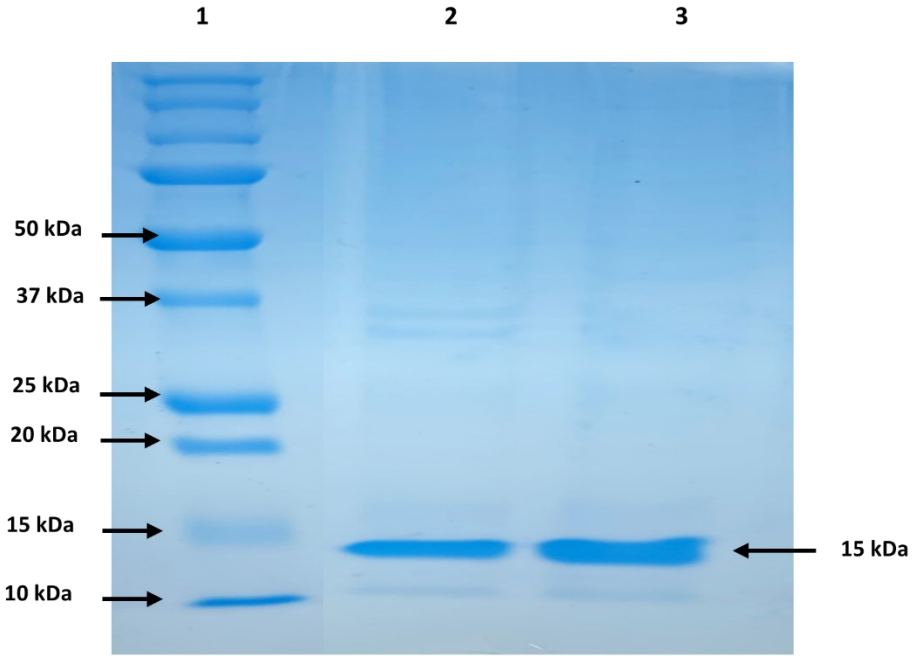

Figure 3.20: PAGE of Purified SGLT2-Loops-No-Tag.

A 15% SDS-PAGE gel stained with Coomassie blue was used to display purified SGLT2-Loops-No-Tag post-dialysis against 150 mM NaCl and 40 mM $NaPO_4$ at pH 7.4. Lane 1: Precision Plus protein marker (all blue), featuring bands at 10, 15, 20, 25, 37, 50, 75, 100, 150, and 250 kDa from the bottom; Lane 2: Pure SGLT2-Loops-No-Tag before dialysis; Lane 3: Pure SGLT2-Loops-No-Tag after dialysis. The amount of protein loaded in each lane was 20 µg, based on Bradford assay quantification.

3.4 Discussion

The successful production, solubilisation, and purification of mouse SGLT2 protein expressed in *E. coli* mark a significant milestone in our pursuit. Additionally, incorporating diphtheria toxin A into the fusion protein represents an innovative approach to overcoming immune tolerance and enhancing antibody diversity. Our objective was to target specific linear determinants in the extracellular loops of SGLT2 to generate monoclonal antibodies with high specificity and efficacy in tissue targeting, particularly within mouse models of renal scarring. The structural analysis of SGLT2, particularly the extracellular loops, guided the development of the fusion protein, facilitating antibody development. Through meticulous preparation, cloning, and induction of recombinant protein expression, we demonstrated the feasibility of producing SGLT2 domains within bacterial systems.

Following the preparation and cloning of SGLT2 inserts into the expression vector, recombinant protein expression was induced in *E. coli* cells. Large-scale expression was conducted, and cellular localisation analysis revealed the presence of SGLT2 proteins primarily in insoluble fractions.

Efficient solubilisation of inclusion bodies containing SGLT2 domains was achieved through optimisation trials with various chaotropic reagents and reducing agents. The optimal conditions for solubilisation were determined, providing a foundation for large-scale solubilisation processes.

Purification of SGLT2 domains was accomplished through nickel column chromatography, followed by dialysis to remove imidazole and the chaotropic agent (urea). The removal of urea during dialysis suggests that this process was also intended to aid in protein refolding. The efficacy of the purification and refolding was confirmed through SDS-PAGE and concentration measurement. The final concentration of urea was negligible after dialysis, as the dialysis buffer did not contain urea, and the chaotropic agent was effectively removed during the process.

In conclusion, the successful generation of recombinant SGLT2-Loops and SGLT2-Loops-No-Tag proteins in *E. coli* bacteria has been achieved, accompanied by the development of a robust purification protocol from the bacterial lysate. Both proteins demonstrated the capability to be recovered in an insoluble form, inclusion body, and were effectively

solubilised in a solution composed of $NaPO_4$, NaCl, and urea at pH 7.4. Further, the purified proteins underwent successful purification through nickel column chromatography. These proteins were demonstrated to be suitable for immunisation purposes. This successful purification represented a significant step forward in our efforts to generate monoclonal antibodies of SGLT2.

Chapter 4: Immunisation of Mice with Recombinant SGLT2

4.1 Introduction

The generation of monoclonal antibodies (mAbs) represents a promising approach for developing targeted therapies against specific proteins involved in disease processes (Köhler and Milstein, 1975). This study explores the hypothesis that monoclonal antibodies targeting the SGLT2 can be used for therapeutic purposes. SGLT2 is predominantly expressed in the renal proximal tubules, where its expression level is approximately 15 times higher than in any other tissue. This unique expression pattern makes SGLT2 an attractive target for therapeutic intervention, particularly in kidney-related diseases.

The primary objective of this study is to recover a high-affinity monoclonal antibody directed against mouse SGLT2. Achieving this goal necessitates overcoming immune tolerance to the SGLT2 antigen. To facilitate this, we employed a strategy involving protein fusions, where the SGLT2 antigen was fused with an antigenic domain of Diphtheria Toxin (DTA). This approach has been previously shown to be able to break tolerance in mouse immunisation (Percival-Alwyn et al., 2015). The powerful stimulus of the diphtheria toxin antigen is capable of overwhelming the humoral tolerising mechanisms and producing an immune response to the fusion protein and the individual fusion partners. Accordingly, we designed a construct in which three external peptide loops of SGLT2 were fused to an antigenic domain of DTA.

This chapter focuses on the immunisation of BALB/c mice, selected for their robust immune responses and proven efficacy in hybridoma generation. The immunisation strategy initially administered the SGLT2-Loops-DTA fusion protein, followed by booster doses with the SGLT2-Loops-No-Tag protein, where the DTA fusion partner was not present. This sequential approach was designed to enhance and refine the immune response, with the aim of targeting the native, untagged form of the SGLT2 loops, which would be critical for the development of therapeutically relevant monoclonal antibodies (mAbs).

The success of the immunisation was assessed by using ELISA to provide quantitative data on the antibody response in the sera of the immunised mice. ELISA analysis allowed for the evaluation of both the magnitude and specificity of the immune response. The initial goal was to recover spleens from the immunised mice and generate hybridomas by fusing isolated B cells with an immortal myeloma cell line using the classical hybridoma technology. The fusion process, followed by the limiting dilution approach, is intended to create hybridomas that are

capable of producing monoclonal antibodies specific to the target antigen. These hybridomas will then be screened for their ability to produce antibodies against the antigen of interest.

4.2 Aims and Objectives

The work in this chapter aimed to generate monoclonal antibodies targeting the extracellular loops of SGLT2 through immunisation and subsequent antibody recovery. The specific objectives were to:

- Immunise BALB/c mice with the recombinant SGLT2-Loops protein to break immune tolerance.
- Boost the immune response with SGLT2-Loops-No-Tag antigen to enhance specificity against the native protein.
- Measure antibody responses in the sera of immunised mice using ELISA.

4.3 Experiments and Results

4.3.1 Immunisation

Four BALB/c mice were immunised with the recombinant SGLT2-Loops-DTA protein following the protocol described in section 2.2.5. The immunisation regimen consisted of an initial priming dose, followed by booster immunisations at regular intervals to enhance the specificity and magnitude of the immune response. The SGLT2-Loops fusion protein, which included an antigenic domain of Diphtheria Toxin, was expressed, purified, and used for immunisation. Ten days after the final booster dose with SGLT2-Loops-No-Tag, sera were collected from each mouse via tail vein bleeds. The sera were then serially diluted and tested for reactivity against the SGLT2-Loops and SGLT2-Loops-No-Tag antigens using ELISA.

4.3.2 Antibody Response Analysis (ELISA)

The antibody responses were evaluated by ELISA (2.2.6), which measured the specific IgG levels in the sera of immunised mice. A single group of mice was initially immunised with the SGLT2-Loops-DTA fusion protein, designed to break tolerance. The analysis revealed a strong IgG response towards the SGLT2-Loops protein in all four mice, with ELISA signals remaining high even at serum dilutions up to 1:12,800 (Fig. 4.1), indicating that the initial immunisation successfully induced a robust immune response.

Following the primary immunisation, the mice were boosted with the untagged SGLT2-Loops-No-Tag construct. The IgG response against the SGLT2-Loops-No-Tag antigen was comparatively weaker. Among the four mice, only Mouse 3 exhibited significant reactivity, with detectable ELISA signals at dilutions up to 1:3,200 (Fig. 4.2). This weaker response was not unexpected, as the immune system had primarily recognised the immunodominant DTA fusion partner during the initial immunisation.

Following the ELISA analysis, all four immunised mice were euthanised, and their spleens were harvested for splenocyte isolation. The splenocytes were subsequently used for RNA extraction, laying the groundwork for generating an antibody library.

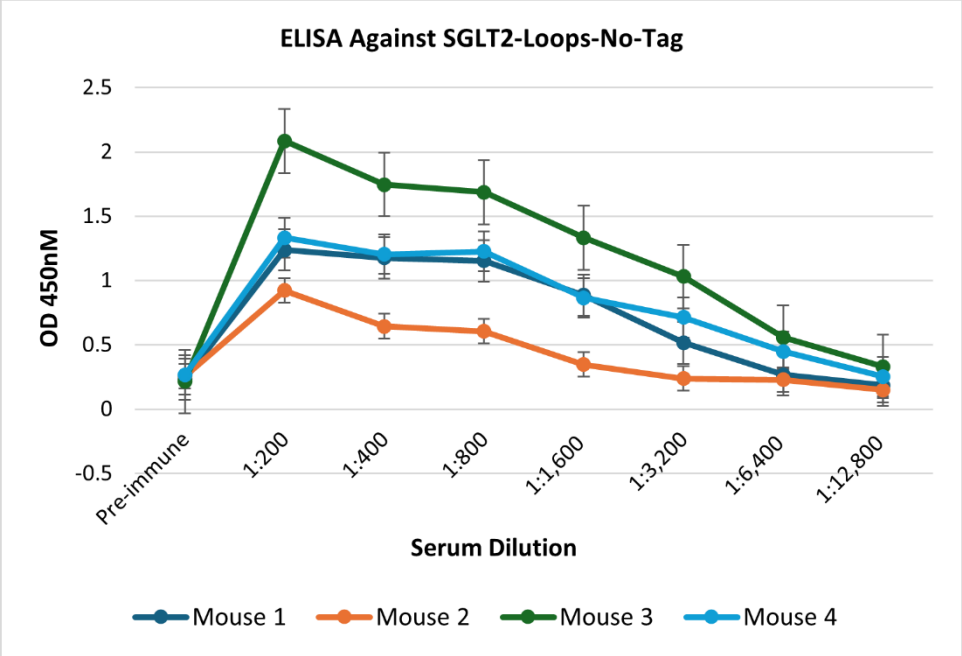

Figure 4.1: SGLT2-Loops ELISA of Pre- and Post-immune Sera from Immunisation.

Serum samples from immunised mice were serially diluted from 1:200 to 1:12,800 and evaluated using an enzyme-linked immunosorbent assay (ELISA). Wells were coated with recombinant SGLT2-Loops protein (1 µg/ml; 50 µl/well), and antibody detection was achieved using a goat anti-mouse IgG Fc secondary antibody conjugated to HRP.

The ELISA was conducted once in triplicate, following a standard immunisation protocol. This approach is not classified as a repeated experiment, as animal welfare regulations allow mice to be bled only once. Confidence in the measured antibody response was derived from the group size (n=4), with individual variability across data points being approximately ±10%. The pre-immune sera served as a baseline control, highlighting the specificity of the post-immune response to the SGLT2-Loops protein.

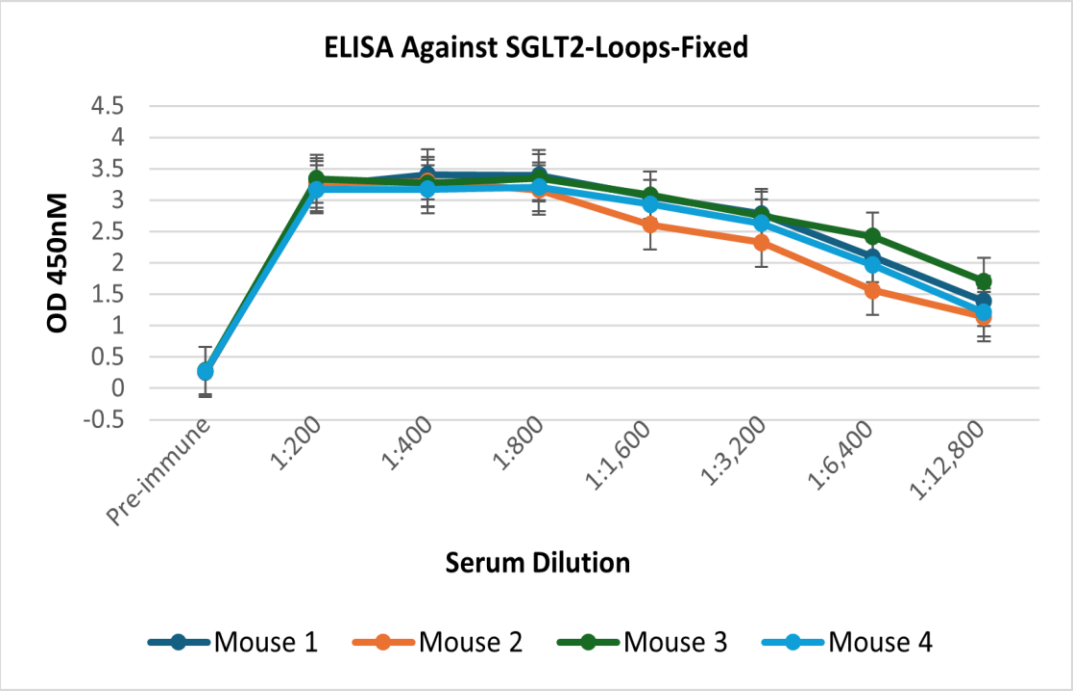

Figure 4.2: SGLT2-Loops-No-Tag ELISA of Pre- and Post-immune Sera from Immunisation.

Serum samples from immunised mice were serially diluted from 1:200 to 1:12,800 and analysed using an enzyme-linked immunosorbent assay (ELISA). Wells were coated with recombinant SGLT2-Loops-No-Tag protein (1 µg/ml; 50 µl/well), and antibody detection was achieved using a goat anti-mouse IgG Fc secondary antibody conjugated to HRP.

This ELISA was conducted once in triplicate, adhering to standard immunisation protocols. Due to animal welfare regulations restrict mice to a single bleeding event, so this is not classified as a repeated experiment. The confidence in measured responses was supported by the group size (n=4), with an individual error margin of approximately ±10%. Pre-immune sera were included as a control to establish baseline antibody levels, demonstrating a significant increase in post-immune antibody binding to the SGLT2-Loops-No-Tag protein.

Attempts to isolate specific hybridomas by limiting dilution were unsuccessful. While a number of ELISA-positive supernatants were initially obtained, all antibody production was subsequently lost in the resulting cell lines. This outcome may have been influenced by tolerising mechanisms in the immunised mice, which likely reduced the initial number of antigen-specific B-cell clones within the recovered splenocytes. A low frequency of antibody-producing B cells in the spleen would inherently diminish the efficiency of clonal expansion and hybridoma generation through limiting dilution.

The absence of hybridoma generation data from the Bioserve lab further limited the ability to establish hybridomas. Instead, ELISA results provided by the lab were repeated in triplicate using blood samples, confirming antibody responses in the immunised mice. Given the challenges associated with hybridoma generation, spleens provided by the lab were used to extract RNA for the construction of a phage display library as an alternative method to identify antigen-specific antibodies. This approach offered a viable pathway despite the low frequency of antigen-specific B cells within the recovered tissue and the technical challenges inherent in the phage display library preparation process.

Spleen tissue from the immunised mice has been retained in liquid nitrogen storage for potential future use. This preserved tissue could facilitate optimised refinement of phage display techniques, such as single-cell sorting and sequencing of antibody-producing B cells, to overcome the limitations encountered in this study.

4.4 Discussion

The immunisation of BALB/c mice with the SGLT2-Loops fusion protein, followed by boosting with SGLT2-Loops-No-Tag, aimed to generate monoclonal antibodies against the extracellular loops of SGLT2, a protein highly expressed in the renal proximal tubules. Compared to other tissues, the high expression level of SGLT2 in the kidney underscores its potential as a therapeutic target, particularly for kidney-related diseases.

The strong IgG response observed in ELISA assays against the SGLT2-Loops-DTA fusion protein suggested that the immunogen was able to elicit an immune response. Incorporating DTA into the immunisation strategy was intended to overcome the challenge of immune tolerance, which often arises when the immune system fails to recognise an antigen as foreign due to its similarity to endogenous proteins. DTA can enhance the immune response by inducing a mild inflammatory reaction, making it a valuable tool for generating high-affinity antibodies. The reaction against the SGLT2-Loops (without DTA) was somewhat less, and this was not surprising as this antigen was completely autologous in nature.

Despite efforts to generate hybridomas, the immunisation procedure did not yield any stable hybridoma lines. The immunisation protocol successfully elicited an immune response, as confirmed by ELISA, which detected antigen-specific antibodies in the sera of immunised mice. However, the subsequent hybridoma formation process, involving the fusion of splenocytes with myeloma cells, was unsuccessful.

This lack of hybridoma formation could be attributed to several factors. First, the rarity of specific antibody-producing B cells in the spleens may have reduced the efficiency of the fusion process. This scarcity might have been a result of tolerising mechanisms in the mice, which limited the expansion of antigen-specific B-cell clones. Additionally, technical limitations during the fusion process, such as suboptimal cell viability, fusion efficiency, or inadequate selection conditions for hybridomas, may have contributed to the failure to establish stable lines.

These observations underscore the challenges inherent in hybridoma generation and highlight the importance of optimising immunisation and fusion procedures to improve outcomes. Further refinement of the fusion protocol or exploration of alternative methods,

such as phage display library generation, could provide a pathway for isolating antigen-specific antibodies in future studies.

The challenges encountered in this study highlight the complexity of generating mAbs through hybridoma technology, mainly when targeting proteins with specific tissue expression profiles like SGLT2. While using the SGLT2-Loops fusion protein and DTA was an innovative approach to enhancing immunogenicity, further optimisation of the immunisation protocol may be necessary. Strategies such as including adjuvants, alternative antigen designs, or different immunisation schedules could improve the likelihood of generating hybridomas that produce high affinity mAbs against SGLT2.

The spleen tissues were retained, and the decision was made to attempt antibody isolation using a phage display approach. Phage display enables powerful selection methods to be employed and the recovery of relatively rare antibodies from splenocytes, lymphocytes, or blood samples (Smith, 1985).

Chapter 5: Isolation of Antibodies by Phage Display

5.1 Introduction

Monoclonal antibodies (mAbs) have emerged as pivotal tools in therapeutic and diagnostic applications due to their exceptional specificity and affinity for target antigens. Targeting specific protein domains, such as those in the SGLT2, has attracted considerable interest, especially in kidney-related disorders where SGLT2 is expressed at a high level in tubules. Small-molecule drugs have targeted SGLT2 as a treatment for diabetes. Blocking SGLT2 glucose transport reduced circulating glucose levels by increasing urinary excretion. Specific antibodies could represent a novel approach for this therapeutic strategy. A possible additional application for SGLT2 antibodies could be in the targeted delivery of drugs to kidney tissue and in the development of novel animal models of renal scarring. Phage display is a highly versatile and robust platform that facilitates the selection of high-affinity antibodies from extensive libraries (Smith, 1985, Barbas, 2001). This chapter focuses on preparing a recombinant Fab phage library from an immunised mouse spleen and enriching SGLT2-specific Fabs by biopanning on purified antigens. It also generates, purifies, and characterises Fab fragments that specifically target the loops of the SGLT2 protein devoid of affinity tags (SGLT2-Loops-No-Tag).

The phage display process involves several rounds of biopanning, where the phage library is incubated with purified SGLT2-Loops-No-Tag protein. This allows the phage-displayed Fab fragments to interact with the target antigen. Phages that do not bind to the antigen are washed away, while those that exhibit high-affinity interactions are selectively eluted and amplified. This iterative process enriches the phage population for Fab fragments that demonstrate solid and specific binding to the SGLT2-Loops-No-Tag, ultimately isolating high-affinity binders.

Following the selection process, individual phage clones were isolated, and their corresponding Fab fragments were expressed and purified for further characterisation. The binding specificity and affinity of these Fab fragments were evaluated using ELISA. The ELISA provides a quantitative measure of the interaction between the Fab fragments and the SGLT2-Loops-No-Tag protein, which is critical for identifying candidates with optimal binding characteristics (Barbas, 2001).

This approach capitalises on the advantages of Fab fragments, which maintain the antigen-binding capabilities of full-length antibodies while offering benefits such as reduced size and increased stability. These properties make Fab fragments particularly suitable for therapeutic applications where smaller antibody formats are advantageous. By specifically targeting the loops of the SGLT2 protein, these Fab fragments have significant potential in developing novel therapies aimed at modulating SGLT2 function in various pathological conditions.

A phage display strategy was then employed to isolate Fab fragments, explicitly targeting the loops of the SGLT2 protein. The pComb3 vector was utilised as the backbone for cloning and expressing the Fab fragments derived from the immunised mice. This vector facilitates the individual expression of the immunoglobulin heavy and light chains of the Fab fragment through the inclusion of two independent *lacZ* promoters. Each chain is preceded by a pelB leader sequence, which directs the secretion of the chains into the bacterial periplasm. The periplasm provides a reducing environment crucial for forming disulfide bonds, essential for adequately assembling functional Fab fragments (Fig. 5.1).

Furthermore, the pComb3 vector allows for incorporating functional Fab fragments onto the phage surface for selection purposes. This is achieved by cloning the heavy chain upstream of the gene encoding the phage coat protein (cpIII), resulting in its expression as an N-terminal cpIII fusion. This fusion facilitates the anchoring of the Fab fragment to the phage virion, enabling its display and subsequent interaction with target antigens. The pComb3 vector incorporates specific restriction enzyme recognition sites for efficient cloning of heavy chains, *Xho*I and *Spe*I, while the light chains are inserted into the *Sac*I and *Xba*I sites (Fig. 5.2).

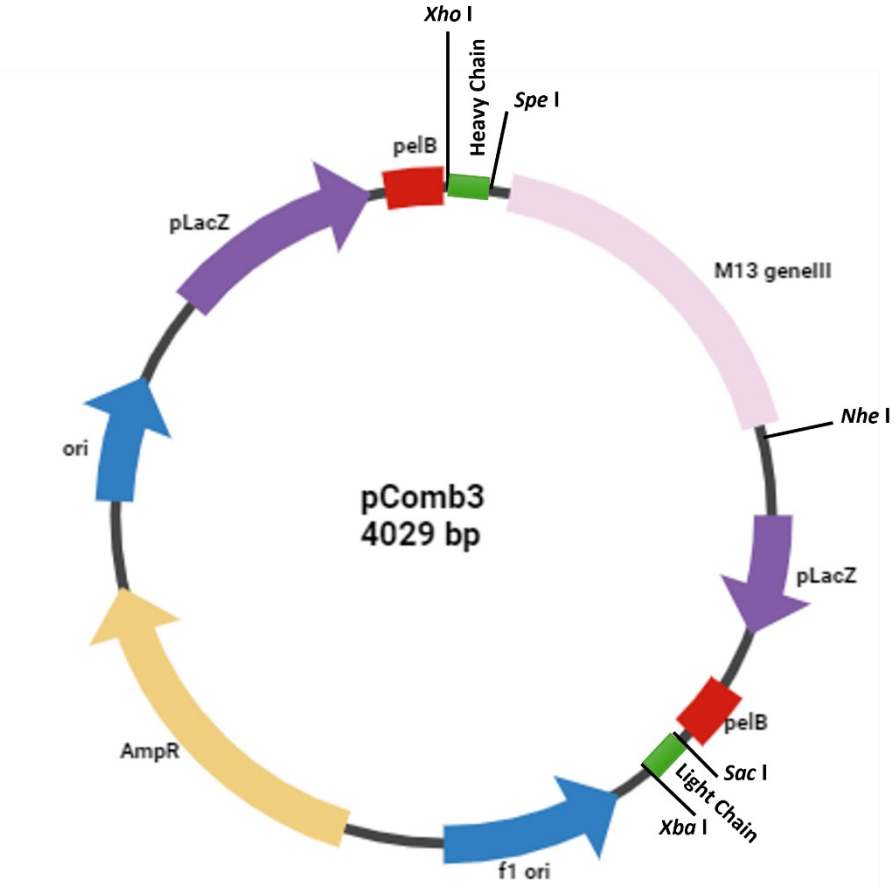

Figure 5.1: pComb3 Phagemid Vector Map.

The phagemid pComb3 vector is designed to facilitate the cloning and expression of immunoglobulins for phage display. This vector enables the display of antibody fragments on the surface of bacteriophages, which is helpful for antibody screening and selection.

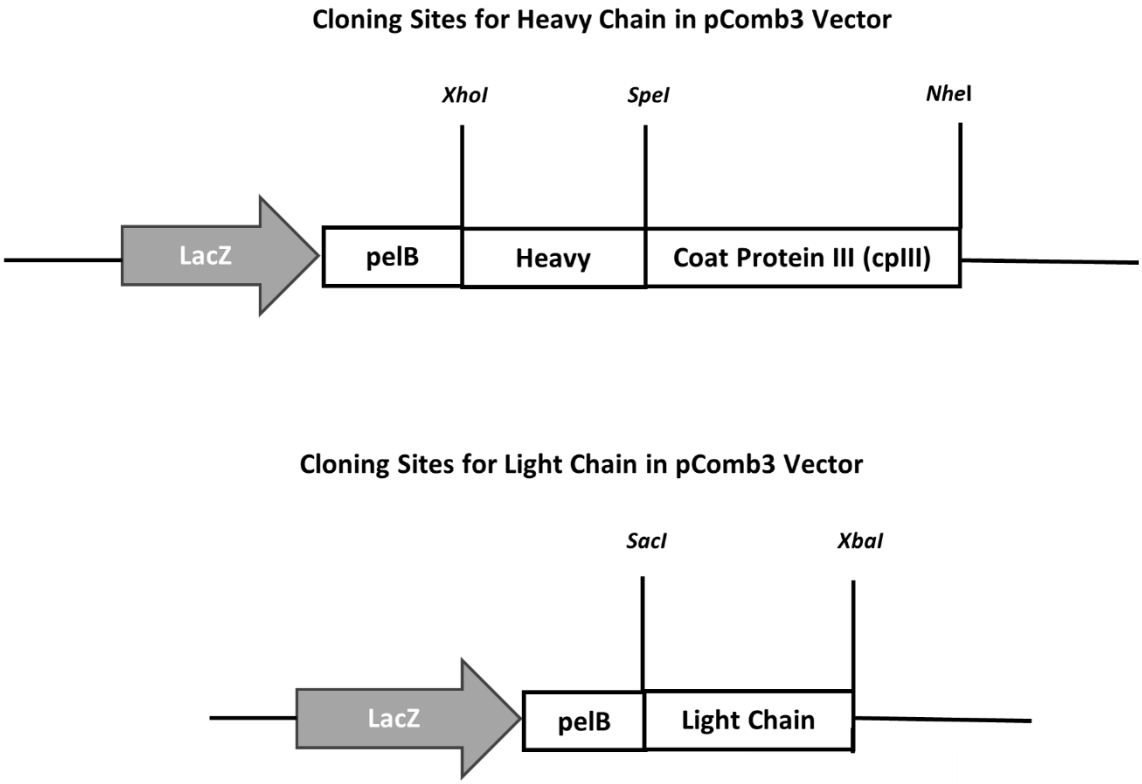

Figure 5.2: Cloning Sites of Heavy and Light Chains in the pComb3 Vector.

This figure illustrates the cloning sites for both the heavy and light chains within the pComb3 vector. The top section of the figure depicts the insertion of the heavy chain variable region (VH) into the pComb3 vector, showing the specific restriction enzyme sites (*Xho*I and *Spe*I) used for cloning. The bottom section illustrates the cloning of the light chain variable region (VK) into the same vector, highlighting the corresponding restriction sites (*Sac*I and *Xba*I). This diagram provides a visual overview of the strategic placement of the variable regions within the pComb3 vector.

5.2 Aims and Objectives

The primary aim of this chapter was to generate and isolate recombinant monoclonal antibodies specifically targeting the SGLT2-Loops domain, a key region involved in SGLT2's function. To achieve this, we utilised a phage display system to construct and express Fab (Fragment antigen-binding) fragments, which are composed of the variable regions of the heavy (VH) and light (VK) chains of immunoglobulins. The workflow, as depicted in Fig. 5.3, included the following objectives:

- Design specific primers to amplify the variable regions (VH and VK) of the immunoglobulin genes from the extracted RNA of immunised mice.
- Clone the amplified VH and VK genes into the pComb3 phagemid vector to generate a Fab antibody library for phage display.
- Perform biopanning rounds to enrich phage particles displaying Fab fragments with high specificity and affinity for the SGLT2-Loops-No-Tag protein.
- Express and purify selected Fab fragments in *E. coli* and evaluate their binding specificity and affinity using ELISA.

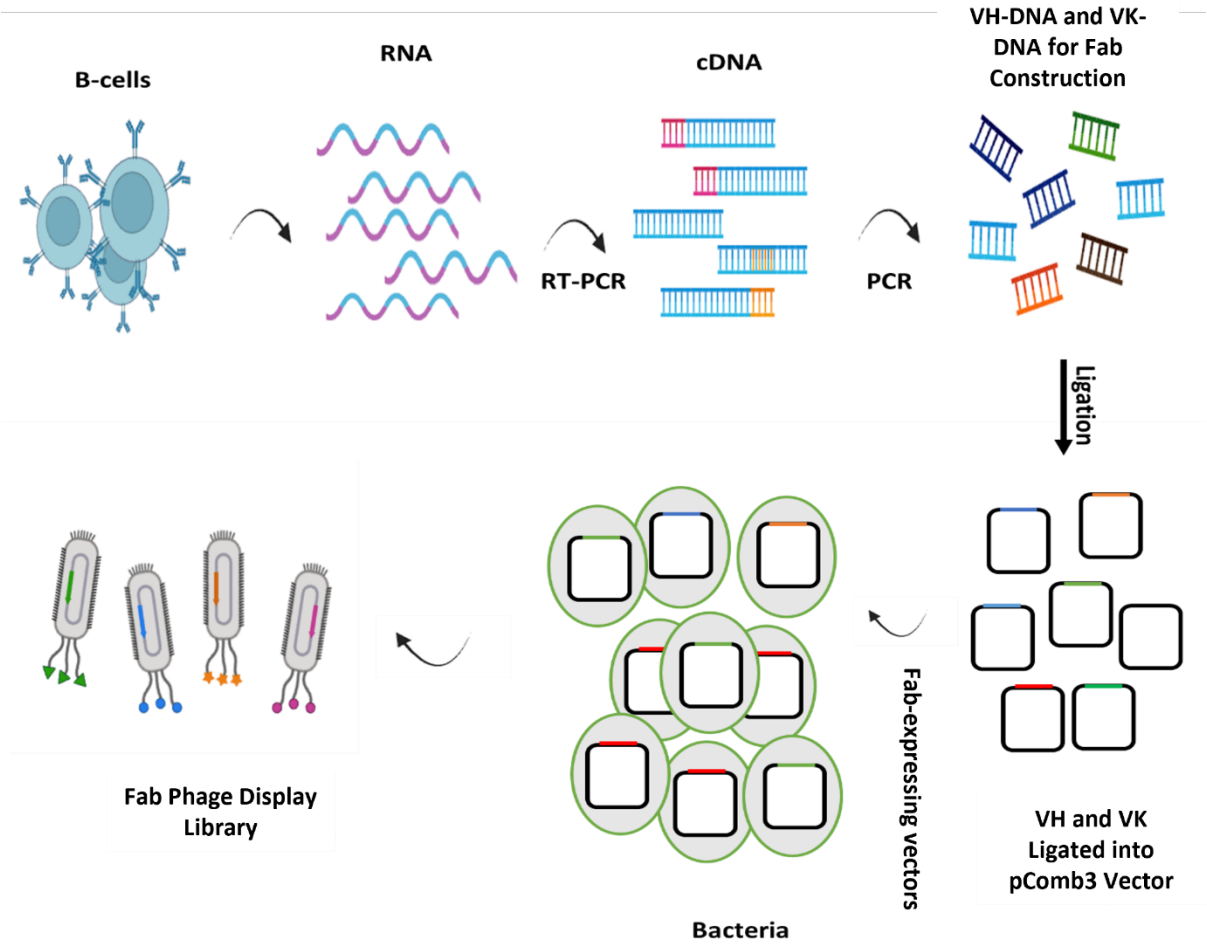

Figure 5.3: Schematic Representation of Phage Display Library Development for Fab Antibodies Targeting SGLT2-Loops.

This figure illustrates the process of constructing a recombinant Fab phage display library. The workflow begins with the isolation of RNA from immunised B-cells, which is reverse-transcribed to cDNA. The variable regions of the heavy (VH) and light (VK) chains are amplified via PCR and ligated into the pComb3 vector, enabling the co-expression of both chains as Fab fragments. The recombinant vectors are introduced into *E. coli* via transformation, which produces a phage display library. In this library, Fab fragments are displayed on the surface of filamentous phage particles, enabling subsequent biopanning to select high-affinity Fab fragments specific to the SGLT2-Loops.

5.3 Experiments and Results

5.3.1 Isolation of Splenocytes

Following the immunisation protocol, the mice were sacrificed according to ethical guidelines, and their spleens were harvested. The spleens were then processed to isolate immune cells, specifically B lymphocytes responsible for antibody production. These cells served as the source of the genetic material required for subsequent antibody library construction. The total RNA was extracted from the isolated spleens of immunised mice using the TRIzol-based method described in 2.2.8. The quality of the isolated RNA was assessed by 0.8% agarose gel electrophoresis (2.2.6) (Fig. 5.4). Analysis of the gel revealed the presence of two distinct bands corresponding to 28S and 18S ribosomal RNAs, indicating minimal RNA degradation. This confirms that the extracted RNA is sufficient for subsequent cDNA preparation.

5.3.2 cDNA Synthesis

The isolated total RNA was subjected to reverse transcription into cDNA using random primers and SMART Moloney Murine Leukaemia Virus Reverse Transcriptase (MMLV RT) following the manufacturer's instructions (2.2.3.2).

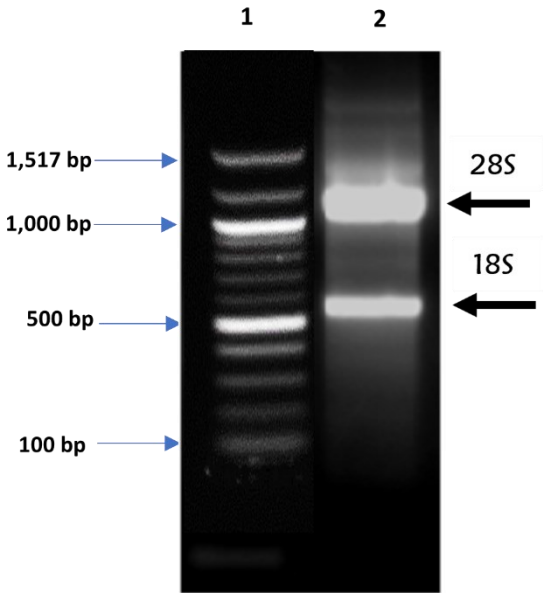

Figure 5.4: Total RNA of Mouse Spleen Post-Immunisation with SGLT2 Immunogen.

5.3.3 Amplification of SGLT2 Heavy Chain Variable Region

The cDNA obtained from the immunised mice was used as a template for PCR amplification of the antibody variable region (VH) sequences. These sequences correspond to the heavy chain variable regions of antibodies generated in response to immunisation with the SGLT2-Loops-No-Tag protein. Specific primer sequences were designed to amplify the variable regions (V) of the immunoglobulin genes using lasergene software and modified to incorporate restriction enzyme recognition sites with additional flanking sequences that are compatible with the cloning sites of the pComb3 vector. They were synthesised by Azenta Life Science (Genomics, UK) under the commercial service of Genewiz. Seven primers were used to target various variable regions of the heavy chain (VH), and seven primers targeted the variable regions of the kappa light chain (VK) (Table 5.1.). These primers were carefully selected to cover the diversity of the immunoglobulin repertoire. The IgG constant (C) region primers were specifically designed for the heavy and light chains, allowing for amplification across all four IgG subclasses.

First-strand cDNA was amplified in separate reactions, each utilising a distinct heavy chain variable region amplification primer paired with the appropriate constant region primer. PCR amplification was performed using GoTaq® Hot Start Master Mix x2, which contains Taq DNA polymerase and includes a hot-start mechanism to enhance specificity by reducing nonspecific amplification (2.2.3.3).

Each 50 µl PCR reaction consisted of the components listed in Table 5.2. The thermal cycling conditions were optimized for specific and efficient amplification, typically involving 30–35 cycles of denaturation at 94°C for 1 minute, annealing at 55°C for 30 seconds, and extension at 72°C for 1 minute.

Table 5.1: Primers Used for Amplifying Immunoglobulin Variable and Constant Regions.

This table lists the primers designed for amplifying the variable (VH and VK) and constant regions of immunoglobulin genes. The sequences include degenerate bases, and a key is provided below for interpreting the base codes.

Name	Sequences
VH1	SAKGTGCAGCTCGAGSAGTCAGGACCT
VH2	GAGGTYCAGCTCGAGCARTCTGGACCT
VH3	CAGGTCCAACTCGAGCAGYCTGGGKCT
VH4	GAGGTTCAGCTCGAGCAGTCTGGRGCWG
VH5	GARGTGAAGCTCGAGGAGWCTGGASGA
VH6	GAGGTGAAGCTTCTCGAGTCTGGAGGT
VH7	GAAGTGMAGCTCGAGGAGTCTGGGGGA
IGG-1	AGGCTTACTAGTACAATCCCTGGGCACAAT
IGG-2A	GTTCTGACTAGTGGGCACTCTGGGCTC
IGG-2B	CTCCTTACTAGTAGGACAGGGGTTGATTGT
IGG-3	GGGGGTACTAGTCTTGGGTATTCTAGGCTC
VK1	CCAGTTCCGAGCTCGTTGTGACTCAGGAATCT
VK2	CCAGTTCCGAGCTCGTGTTGACGCAGCCGCCC
VK3	CCAGTTCCGAGCTCGTGCTCACCCAGTCTCCA
VK4	CCAGTTCCGAGCTCCAGATGACCCAGTCTCCA
VK5	CCAGATGTGAGCTCGTGATGACCCAGACTCCA
VK6	CCAGATGTGAGCTCGTCATGACCCAGTCTCCA
VK7	CCAGTTCCGAGCTCGTGATGACACAGTCTCCA
KAP-CONST	GCGCCGTCTAGAATTAACACTCATTCCTGTTGAA

Key to Degenerate Bases in Primer Sequences:

S: G or C **R**: A or G **C**: C

Y: C or T **W**: A or T **G**: G

K: G or T **M**: A or C **A**: A

Table 5.2: Shows the Constituents of the PCR Reaction Mixture.

Master Mix	**Volume**
GoTaq® Hot Start Master Mix x2	25 µl
cDNA	1 µl
Each Primer with its Constant Primer 10 µM	1 µl
RNA-free H_2O	22 µl
Total volume	50 µl

The resulting PCR products were resolved on a 0.8% agarose gel (2.2.2.6) to visualise and verify the correct size of the amplification fragments. Gel electrophoresis confirmed successful amplification with an expected ~800 bp product in the presence of cDNA. Negative controls were routinely included to ensure that the reagents were contamination-free and showed no bands on the gel (Fig. 5.5). Following amplification, the reaction products were combined and precipitated using 100% ethanol for purification. PCR products amplified with identical VH region primers were further purified after electrophoresis on a slot agarose gel. The DNA from the slot gel was then extracted and purified with the Monarch PCR & DNA Cleanup kit (New England Biolabs, T1030L).

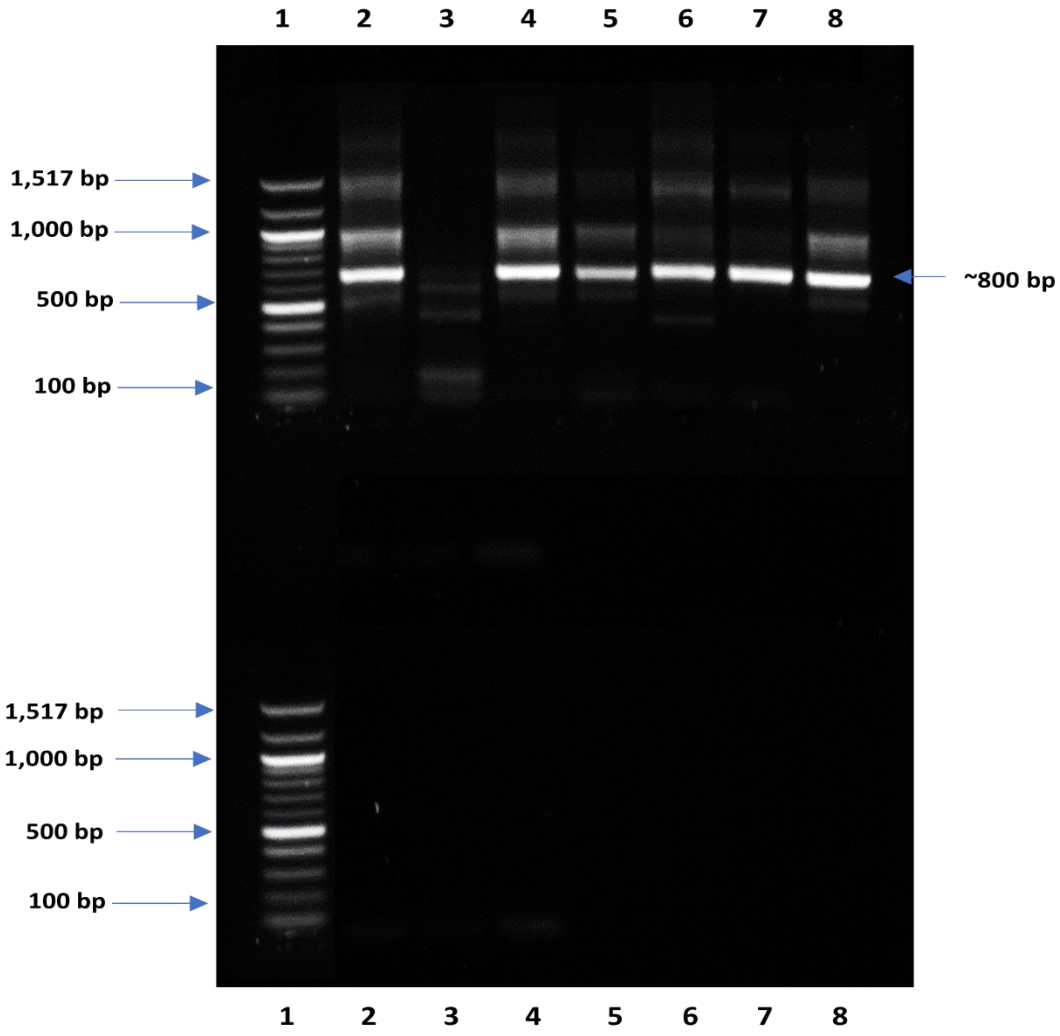

Figure 5.5: PCR Amplification of Heavy Chain Variable Regions.

This figure demonstrates the amplification of heavy chain variable region (VH) genes from splenocyte cDNA. The reactions were performed using seven different primers, each corresponding to a specific VH region, with amplification running for 30 cycles. Lane 1: 100 bp ladder, confirming the expected product size of approximately 700 bp. Lanes 2–8 (Upper Panel): PCR reactions using primers VH1–VH7. Specifically: Lane 2: VH1, shows a clear band. Lane 3: VH2, showing no amplification. Lane 4: VH3, showing a clear band. Lane 5: VH4, showing a clear band. Lane 6: VH5, showing a clear band. Lane 7: VH6, showing a clear band. Lane 8: VH7, showing a clear band. Despite repeating the reaction several times and troubleshooting (e.g., replacing primers, cDNA, and reagents, optimising PCR conditions), Lane 3 persistently fails to amplify. This could suggest that the cDNA template for this specific target may be absent or degraded, possibly due to low expression levels of the corresponding antibody sequence in the immunised mice or the primers designed for this specific reaction may not bind efficiently to the target sequence due to sequence variation. Lanes 2–8 (Lower Panel): Non-template negative controls for each reaction, showing no bands and confirming specificity.

5.3.4 Cloning of SGLT2 Immunoglobulin VH into pComb3 Vector

At this step, the goal was to clone the heavy chain variable region of the immunoglobulin into the pComb3 vector, a phagemid vector commonly used in phage display applications. This step was specifically focused on preparing the VH fragment for later pairing with the light chain variable region (VK) to ultimately generate functional Fab fragments.

The pComb3 vector and the PCR-amplified VH fragments were digested separately with the restriction enzymes *Xho*I and *Spe*I, which correspond to the flanking sequences added during PCR amplification (2.2.2.5). This ensured directional cloning of the VH fragment into the vector. Following digestion, the VH fragment was ligated into the vector to allow its expression in the phage display system.

After digestion, the vector backbone, with an expected size of approximately 4,000 bp, was purified from the gel (Fig. 5.6). The digested VH fragments were similarly purified and then ligated into the prepared pComb3 vector using T4 DNA ligase. The ligation reaction was incubated at 15°C overnight to ensure optimal insertion of the VH fragments into the vector. The reaction mixture was heated to 75°C for 15 min to terminate the ligase activity. The ligation product was then purified via ethanol precipitation (2.2.2.9) and dissolved in 50 µl buffer.

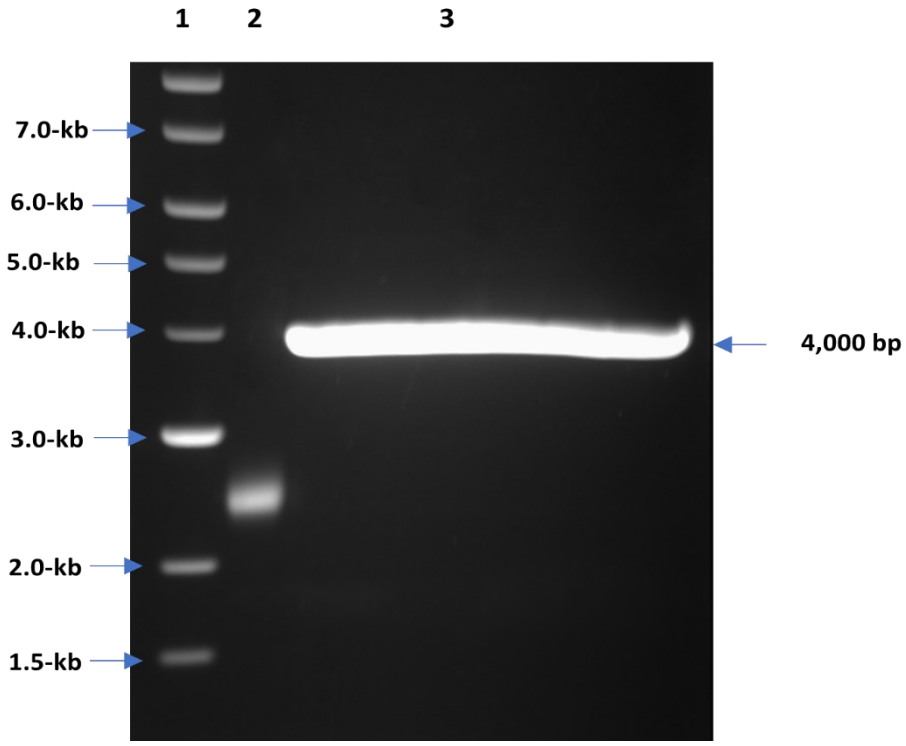

Figure 5.6: Digestion of pComb3 Vector for Heavy Chain Cloning.

Expression vector pComb3 was digested with *Spe*I and *Xho*I. The vector backbone was resolved by running on 0.8% agarose gel. Lane 1: Molecular weight of 1 kb DNA ladder, bands starting at the bottom: 500, 1,000, 1,500, 2,000, 3,000, 4,000, 5,000, 6,000, 8,000, and 10,000 bps; Lane 2 Undigested pComb3 plasmid; Lane 3 pComb3 was restricted to show 4,000 bp.

5.3.5 Transformation of VH Library

The ligated pComb3 vector containing the VH fragments was employed to transform XL1-Blue cells by electroporation (2.2.2.2). Electroporation was chosen for its high efficiency in transforming large DNA molecules, which is crucial for successful library construction in phage display applications. The transformed bacteria were plated on LB agar containing ampicillin to select for colonies that had successfully taken up the pComb3 vector, thereby enabling the evaluation of ligation efficiency. The remaining transformed cells were stored on ice overnight.

A threshold of at least 2 x 10^6 independent clones was established to ensure the library's success.

5.3.6 Amplification of the SGLT2 Light Chain Variable Region (VK)

The SGLT2 light chain variable region amplification was carried out using specific primers listed in Table 5.1 and cDNA as the template, following standard PCR protocols (2.2.3.3). Each PCR reaction was conducted for 30-35 cycles to ensure sufficient amplification of the target sequences. To maintain experimental integrity, a non-template negative control was included in each reaction set, confirming the absence of contamination and ensuring that any amplification observed was specific to the target cDNA.

Post-amplification, the PCR products were analysed by gel electrophoresis (2.2.2.6) (Fig. 5.7) and purified to remove any residual primers, nucleotides, and other impurities (2.2.2.7); the quality and quantity of the purified PCR products were verified through agarose gel electrophoresis to ensure that the amplification was successful. The products were of the expected size of ~700 bp.

5.3.7 Cloning of the SGLT2 Light Chain VK into the pComb3-VH Vector

The purified anti-SGLT2 light chain PCR products were digested with *Sac*I and *Xba*I restriction enzymes. These enzymes were selected based on the flanking restriction sites incorporated into the PCR primers, allowing seamless integration of the amplified VK region into the pComb3-VH vector. After digestion, the digested fragments were separated and purified using a 0.8% agarose gel to ensure that only the correctly digested fragments were used for subsequent ligation (2.2.2.6).

In parallel, the pComb3-VH expression vector, already containing the VH region, was digested with the same *Sac*I and *Xba*I restriction enzymes. This step ensured the vector was appropriately linearised and ready to accept the VK insert. The digested and gel-purified anti-SGLT2 light chain fragments were then ligated into the prepared pComb3-VH vector using T4 DNA ligase (2.2.2.8). The ligation reaction was incubated overnight at 15°C, allowing optimal conditions for inserting the light chain fragments into the vector.

After ligation, the mixture was heated to 75°C for 15 min to terminate the ligase activity. It was then precipitated using ethanol to concentrate the DNA and remove any remaining salts and enzymes from the ligation reaction (2.2.2.9). The purified ligation product was then dissolved in 50 µl of elution buffer, preparing it for transformation.

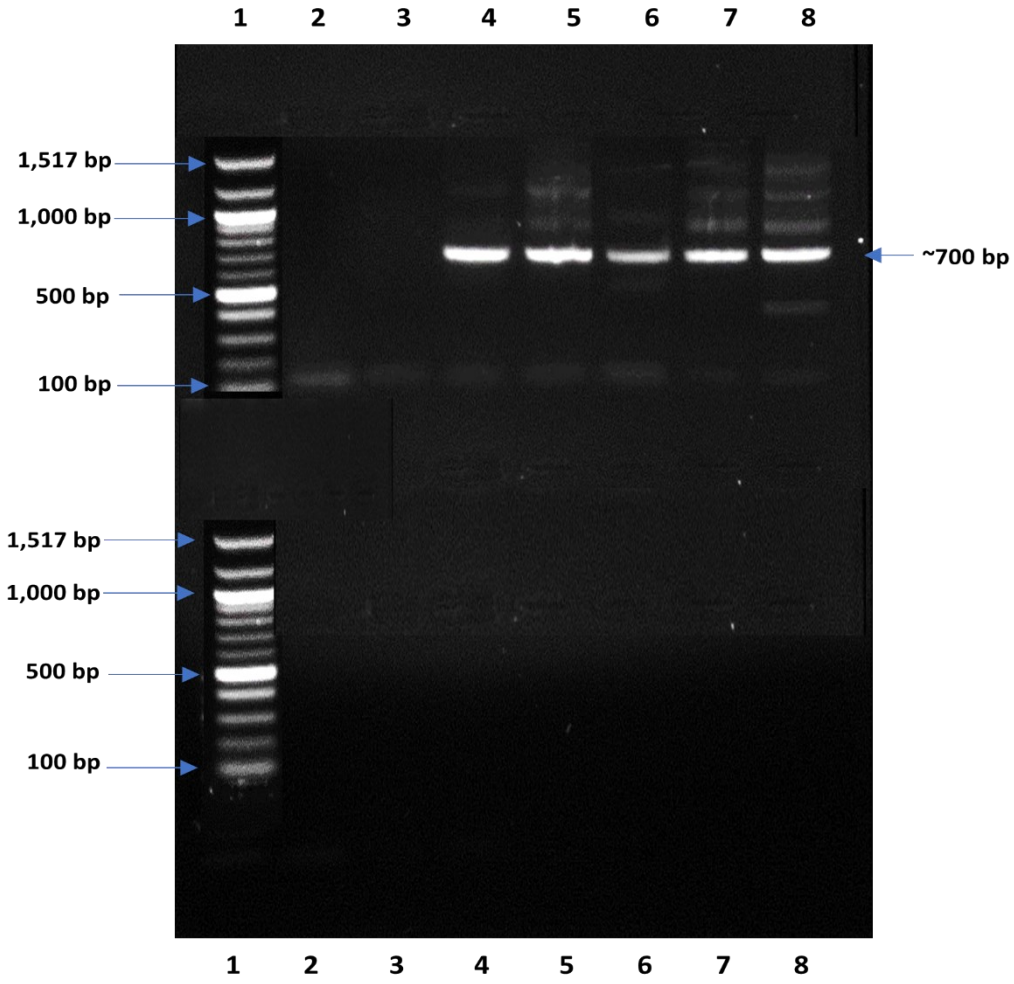

Figure 5.7: PCR Amplification of Light Chains from Splenocyte cDNA

This figure illustrates the amplification of light chain variable region (VK) genes from splenocyte cDNA. The reactions were performed using seven different primers, each corresponding to a specific VK region, with amplification running for 30 cycles. Lane 1: 100 bp ladder, confirming the expected product size of approximately 700 bp. Lanes 2–8 (Upper Panel): PCR reactions using primers VK1–VK7. Specifically: Lane 2: VK1, showing no amplification. Lane 3: VK2, showing no amplification. Lane 4: VK3, showing a clear band. Lane 5: VK4, showing a clear band. Lane 6: VK5, showing a clear band. Lane 7: VK6, showing a clear band. Lane 8: VK7, showing a clear band. Repeated attempts to amplify VK1 and VK2, including primer changes, reaction conditions, and template cDNA, consistently yielded no product. This suggests the absence of the corresponding sequences in the template or structural issues with these regions preventing efficient amplification. Lanes 2–8 (Lower Panel): Non-template negative controls for each reaction, showing no bands and confirming specificity. This figure highlights successful amplification for VK3–VK7 and consistently failed amplification for VK1 and VK2, likely due to inherent template limitations rather than technical errors.

5.3.8 Confirmation of Construct Integrity

All constructs were linearised with *Xho*I digestion and analysed by 0.8% gel electrophoresis (2.2.2.6) alongside the original pComb3 vector (Fig. 5.8). The presence of the anti-SGLT2 heavy chain in pComb3-VH was confirmed by an approximately 800 bp size increase compared to pComb3. Following the successful integration of the anti-SGLT2 light chain, the final construct, SGLT2-pComb3, exhibited a further size increase of approximately 700 bp compared to pComb3-VH, confirming the successful cloning process.

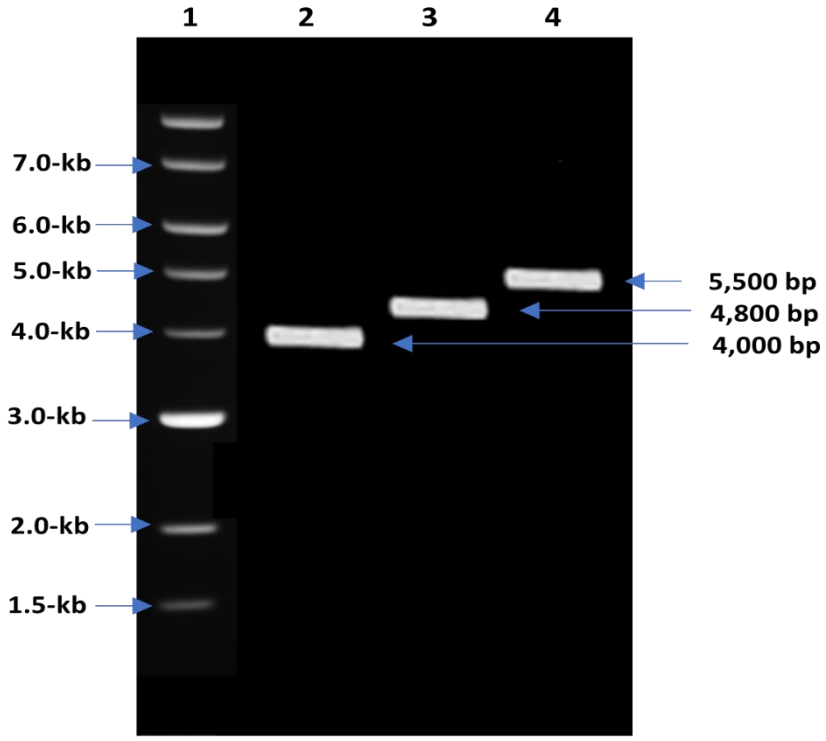

Figure 5.8 Size Comparison of pComb3, pComb3-VH, and pComb3-VH-VK Constructs.

Comparison of the sizes of pComb3, pComb3-VH, and pComb3-VH-VK constructs. DNA samples were linearised via *Xho*I digestion and analysed using agarose gel electrophoresis. Lane 1: Molecular weight of 1 kb DNA ladder, bands starting at the bottom: 500, 1,000, 1,500, 2,000, 3,000, 4,000, 5,000, 6,000, 8,000, and 10,000 bps.; Lane 2: pComb3 (4000 bp); Lane 3: pComb3-VH (4000 + 800 bp); Lane 4: pComb3-VH-VK (pComb3-SGLT2) (4000 + 800 + 700 bp).

5.3.9 Transformation and Expression of Fab Fragments

A total of 0.6 µg of recombinant DNA containing the VH and VK regions was transformed into 50 µl of XL1-Blue competent cells via electroporation (2.2.2.2). Following transformation, 1 ml of SOC medium was added, and the mixture was incubated in a shaker incubator at 37°C for 1 hour to allow recovery and initial expression of antibiotic resistance. The transformed cells were then plated onto LB agar plates containing ampicillin, ensuring that only cells successfully transformed with the pComb3-VH-VK construct would grow. After overnight incubation, individual colonies were selected and cultured in liquid media to test multiple clones for Fab expression. This step was essential to identify clones that successfully expressed functional Fab fragments for subsequent binding specificity and affinity analyses.

5.3.10 Anti-SGLT2 Library Rescue and Amplification

Following the electroporation of pComb3-VH-VK (pComb3-SGLT2) ligations, the transformed cells were immediately placed on ice to maintain viability while the transformation efficiency was determined. This was calculated by plating an aliquot of the transformed cells onto LB agar plates containing 100 µg/ml ampicillin and counting the number of colonies formed after overnight incubation. The total number of colonies was then extrapolated to the entire transformation volume, providing an estimate of the number of successful transformants.

Subsequently, the remaining cells were transferred to 10 ml of SB medium containing 100 µg/ml ampicillin and incubated at 37°C with shaking for 6 hours. The culture was then expanded into 100 ml of fresh SB medium supplemented with 100 µg/ml ampicillin. Ampicillin was used to maintain selection for the pComb3 vector, which carries the ampicillin resistance gene. Then, incubated at 250 rpm and 37°C for an additional 6 hours. The culture achieved an OD_{600}nm of approximately 0.4, indicating sufficient bacterial growth to commence superinfection with helper phage. The purpose of superinfection was to facilitate the assembly of phage virions and their secretion into the culture medium.

Next, the culture was superinfected with 50 µl of VCSM13 helper phage and supplemented with 10 µg/ml tetracycline, and kanamycin. Tetracycline was included to ensure the survival of the XL1-Blue host cells, which are naturally resistant to tetracycline. Kanamycin was added to select for the VCSM13 helper phage, which carries the kanamycin resistance gene. The

incubation was continued overnight at 37°C with shaking to allow for the rescue and packaging of the Fab-displaying phage particles.

On the following day, after superinfection by helper phage, the phage library was precipitated, harvested and purified using the protocol described in 2.2.7. The eluted phage particles were resuspended in 1 ml of 3% BSA and 2 ml 1X TBST and concentrated to a density of approximately 10^{11} plaque-forming units per millilitre (pfu/ml) (2.2.8).

On the following day, after superinfection with the helper phage, the phage library was precipitated, harvested, and purified. Specifically, the culture supernatant containing the phage particles was collected by centrifugation at 10,000 x *g* for 15 minutes at 4°C to remove bacterial cells. The supernatant was then mixed with 1/5 volume of the PEG/NaCl solution and incubated on ice for 1 hour. The mixture was centrifuged again at 12,000 x *g* for 30 minutes at 4°C to pellet the phages (2.2.7).

The resulting phage pellet was resuspended in 1 ml of 3% BSA and 2 ml of 1X TBST, stabilising the particles and preventing nonspecific binding in subsequent assays. The phage preparation was concentrated to a density of approximately 10^{11} plaque-forming units per milliliter (pfu/ml) for use in downstream applications (2.2.8).

5.3.11 Selective Enrichment of Anti-SGLT2 Fab Library

To selectively enrich the anti-SGLT2-Loops library for high-affinity binders, a biopanning process was conducted using ELISA wells coated with the purified SGLT2-Loops-No-Tag antigen. Initially, the wells were prepared by coating with 15 µg of purified SGLT2 antigen (1mg/ml) in 50 µl of Coating Buffer (pH 9.6) and incubated overnight at 4°C. The following day, the wells were blocked with 400 µl of 3% BSA in 1X TBST for 1 hour at room temperature to prevent non-specific binding. After blocking, the wells were washed five times with 1X TBST. Subsequently, 100 µl of the phage library was added to each well and incubated for 1 hour at room temperature for specific binding interactions.

During the first round of panning, the wells were washed five times with 1X TBST after incubation with the phage library to remove unbound phage. The adherent and bound phage were then eluted using 100 µl of glycine buffer (0.1 M glycine/HCl, pH 2.7), then neutralised with 6 µl of 2 M Tris-HCl, and incubated for 10 min at room temperature to recover the specifically bound phage.

In subsequent rounds of panning, the washing stringency was progressively increased to enhance the selection of high-affinity phage particles. Specifically, the number of washes was increased from five to ten in the later rounds, ensuring that only the phage with the most potent and specific binding to the SGLT2-Loops antigen remained. This incremental increase in washing stringency was crucial for enriching the library with high-affinity binders while eliminating phage with weaker interactions.

The eluted phages from each round were used to infect 1 ml of log-phase XL1-Blue host culture, facilitating the propagation of the enriched library. Infected cultures were serially diluted and plated onto LB agar plates, allowing for the quantification of enriched phage particles, with each round refining the library to yield the most specific and high-affinity anti-SGLT2-Loops clones. After overnight growth at 37°C, the resulting colonies were counted to calculate the number of phages that had been successfully selected. Uninfected XL1-Blue cells (host cells) were also plated as a negative control to confirm the absence of contamination.

Infected host cells were cultured in 10 ml of SB medium supplemented with 1% glucose and 100 µg/ml ampicillin for 6 hours at 37°C until the OD_{600nm} was approximately 0.4. This culture was then transferred to 100 ml of fresh SB medium containing helper phage, 100 µg/mL ampicillin, and 10 µg/ml tetracycline and incubated overnight at 37°C with shaking at 200 rpm.

The next day, the enriched phage library was harvested by centrifugation. The supernatant was collected, and 40 ml was precipitated with 10 ml of (40% PEG/5 M NaCl) for 2 hours on ice to precipitate phage particles. The precipitated phage was collected by centrifugation, re-suspended in 1 ml of 3% BSA and 2 ml TBST, and used for the subsequent enrichment round of panning. This phage was then used in the next round of panning in the same way as the original library.

This biopanning process using SGLT2-Loops antigen was performed on the anti-SGLT2-Loops phage library for a total of five rounds. Each panning experiment was repeated at least four times, with increasing washing stringency after the initial round to enhance enrichment specificity.

5.3.12 Phage Titration

Following the final round of biopanning, phage titration is crucial for accurately determining the concentration of phage particles in the sample. The process begins with preparing fresh host cells, specifically *E. coli* XL1-Blue, by adding 200 µl to 10 ml of LB and incubating at 37°C for a minimum of 4 hours to reach the log phase of growth. Meanwhile, a series of 10-fold serial dilutions of the phage stock from each round of biopanning was prepared in a sterile LB medium, typically at dilutions of 10^{-2}, 10^{-4} and 10^{-6}.

Next, 100 µl of the log-phase bacterial culture was combined with 100 µl of each phage dilution in separate sterile tubes. These phage-bacteria mixtures were incubated at room temperature for 5-10 min to allow efficient phage adsorption onto the bacterial cells. Following incubation, the mixtures were plated on LB agar plates supplemented with ampicillin and incubated overnight at 37°C. The resulting plaques were counted the following day, and the phage titer was calculated in plaque-forming units per millilitre (pfu/ml).

Table 5.3: Phage Titration Results Across Rounds (10^{-4} Dilution)

Round	Number of plaques	Calculated Titer (pfu/ml)
Round 1	72	5.4×10^6
Round 2	98	8.9×10^6
Round 3	165	1.43×10^7
Round 4	124	2.15×10^7
Round 5	211	1.75×10^7

Phage titration was conducted after each round of biopanning to quantify the concentration of phage particles. The number of plaques observed at the 10^{-4} dilution increased progressively with each round, indicating successful enrichment of phages with higher affinity for the target antigen. Based on the plaque counts at this dilution, the calculated phage titers demonstrated a clear trend of increasing concentration, consistent with the expected outcome of selective enrichment.

The increase in the number of plaques observed at the 10^{-4} dilution highlights the successful enrichment of the phage library for high-affinity clones targeting SGLT2-Loops. This trend demonstrates that the biopanning process effectively selected for specific binders while removing non-specific phages, resulting in a higher concentration of functional phages in the

eluted population. These results validate the effectiveness of the biopanning protocol and suggest that subsequent rounds will yield clones with even greater specificity and affinity.

5.3.13 Expression, Solubilisation and Purification of SGLT2 Fabs

Following the final round of biopanning with anti-SGLT2-Loops antibody against the SGLT2-Loops antigen, phage particles from round 5 were harvested using a maxi-prep protocol (2.2.2.3). To enable subsequent purification of the SGLT2-Loops Fab fragment, the SGLT2-pComb3 construct was digested with *Nhe*I and *Spe*I restriction enzymes (2.2.2.5), explicitly targeting the ~700 bp cpIII protein-coding regions for removal. Fig. 5.9 illustrates digestion, which separates the pComb3 vector, containing SGLT2 VH and VK genes, from the cpIII region.

This desired SGLT2-pComb3 fragment was then extracted and purified from the agarose gel using a commercial DNA extraction kit and eluted (2.2.2.7). The purified fragment was self-ligated using T4 DNA ligase and incubated overnight at 15°C (2.2.2.8). The ligation mixture was heat-inactivated at 75°C for 15 min before being transformed into chemically competent XL1-Blue cells. The transformed cells were plated onto LB agar plates for selection.

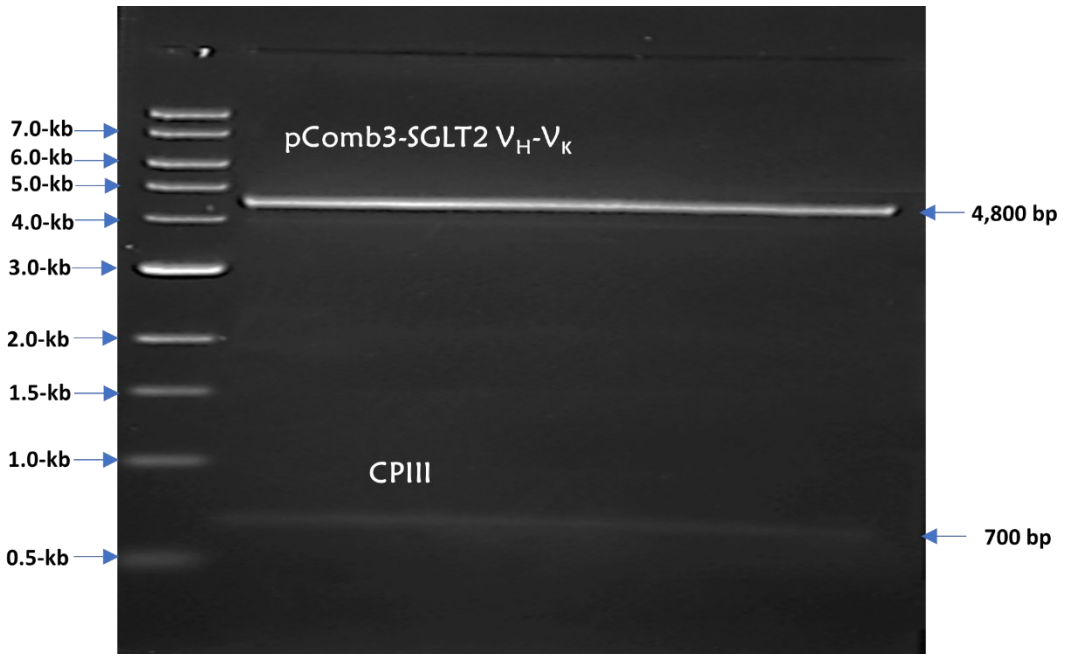

Figure 5.9: Digestion of Fab Library DNA for CPIII Removal.

The figure shows the results of an experiment where the SGLT2 VH-VK-pComb3 construct was digested with *Nhe*I and *Spe*I restriction enzymes to remove the cpIII protein. The digested DNA fragment was then separated by electrophoresis on a 0.8% agarose gel. Lane 1 contains a 1 kb DNA ladder. The bands start at 500 bp and increase in size up to 10,000 bp; Lane 2 contains the SGLT2 VH-VK-pComb3 construct after digestion with *Nhe*I and *Spe*I. This lane shows two bands: a large band at around 4800 bp and a smaller band at around 700 bp. The smaller fragment represents the DNA sequence for the cpIII protein, not the protein itself.

5.3.14 Identification of Anti-SGLT2 Fabs Using ELISA Screening

To identify individual clones that specifically bind to the SGLT2-Loops-No-Tag antigen and express high-affinity antibodies, 48 colonies were randomly selected from LB agar plates following the final round of biopanning. Each colony was inoculated into a separate culture containing 10 ml of SB medium supplemented with 1% glucose and 100 µg/ml ampicillin. The cultures were incubated for 6 hours at 37°C until an OD_{600}nm of approximately 0.4 was achieved. Subsequently, the cultures were induced with 1 mM IPTG and incubated overnight at 30°C to promote the expression of Fab.

The following day, the cultures were centrifuged to separate the bacterial cells (pellets) from the culture supernatants. The supernatants, containing secreted Fab fragments, were collected for ELISA screening, while the cell pellets were resuspended in glycerol and stored at -80°C for potential future use.

The Fab fragments make their way into the culture supernatant through the secretion pathway facilitated by the bacterial expression system. In the pComb3 vector system, Fab fragments are expressed with a pelB leader sequence, a signal peptide that directs the Fab fragments to the periplasmic space during synthesis. The oxidising environment of the periplasm ensures proper folding and formation of disulfide bonds, which are critical for Fab functionality.

From the periplasm, some Fab fragments naturally leak into the culture supernatant. This leakage can occur due to minor membrane disruption during overexpression or mechanical stress caused by shaking or aeration during bacterial culture. Additionally, some phagemid systems are designed to enhance the secretion of soluble Fab fragments into the supernatant, ensuring adequate yields for downstream applications such as ELISA.

By collecting the supernatant, the soluble Fab fragments are immediately available for screening assays, while the preserved cell pellets provide a resource for future experiments, such as additional protein production or further molecular analyses.

ELISA screening was conducted to identify clones expressing mAbs with high affinity for the SGLT2-Loops-No-Tag antigen (2.2.6). In brief, the ELISA plates were coated with purified recombinant SGLT2-Loops-No-Tag antigen and incubated at 4°C overnight. Following blocking and washing, each supernatant was tested in duplicate wells to ensure reliability. The supernatant was used neat, without dilution, to directly assess the presence and activity of the Fab fragments. This approach maximised the detection of antigen-binding activity, as it avoided the potential dilution of low-abundance Fab fragments in the supernatant.

To ensure the validity of the screening, both positive and negative controls were included. For the positive control, some wells were coated with a known positive antigen, human granzyme B, to confirm the effectiveness of the assay and the reactivity of the detection system. For the negative control, 48 wells were coated with 3% BSA in a coating buffer, which should not bind the phagemid-displayed antibodies, establishing the baseline for non-specific binding.

SGLT2-Loops-specific clones, negative and positive controls were detected using a goat anti-mouse IgG (Fab-specific) antibody conjugated to HRP. The detection process involved adding TMB substrate, and the enzymatic reaction was stopped after 10 min of incubation by adding sulfuric acid, resulting in a colour change. The intensity of the colour, measured as absorbance at 450 nm using a microplate reader, was directly proportional to the number of Fab fragments bound to the antigen, reflecting their binding affinity (Fig. 5.10).

Clones exhibiting high ELISA signals compared to both the 3% BSA-coated negative control wells and the baseline readings were identified as potential high-affinity mAbs. These clones were selected for further characterisation based on their strong binding to the SGLT2-Loops-No-Tag antigen compared to the controls, indicating their potential for high specificity and affinity.

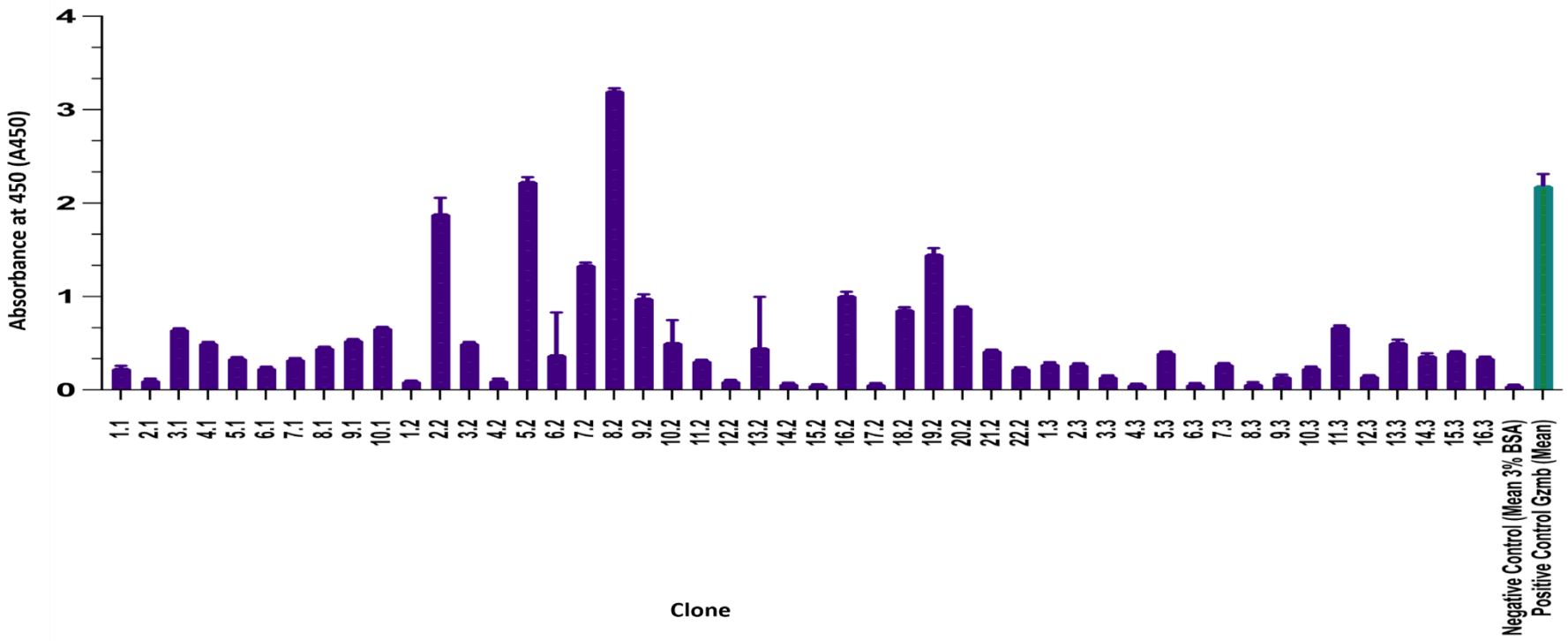

Figure 5.10: ELISA Screening of 48 Anti-SGLT2 Clones.

ELISA was performed to screen 48 individual phage-displayed antibody clones for their binding affinity to the SGLT2-Loops-No-Tag antigen. Each clone's absorbance at 450 nm (A_{450}) was measured to determine the relative binding strength. A single bar represents the mean absorbance of the negative control wells coated with 3% BSA, and a single green bar represents the mean absorbance of the positive control wells, which were coated with human granzyme B, confirming the assay's effectiveness. Clones exhibiting absorbance values significantly higher than the negative control were identified as potential high-affinity binders and selected for further characterisation. To control for variability in Fab concentration across the supernatants, the supernatant was not normalised for Fab concentration in this initial screening. Instead, the ELISA assay focused on detecting antigen binding under identical assay conditions for all samples. While Fab concentrations were not measured in this step, the selection criteria prioritised clones with robust binding signals, and further characterisation of selected clones included Fab quantification and activity assays to confirm their specificity and affinity.

5.3.15 Heavy and Light Chains Sequence

Following identifying high-affinity anti-SGLT2 clones through ELISA screening, the next step involved sequencing the variable regions of the heavy and light chains. This sequencing was essential to confirm the selected clones' identity and assess their diversity.

Plasmid DNA was extracted from the positive clones that exhibited significantly higher absorbance values compared to the negative control during ELISA screening. The extraction was performed using a standard plasmid miniprep procedure (2.2.2.4). The purified plasmid DNA from each positive clone was sent to Azenta Life Sciences (Genewiz) for sequencing. The sequencing was conducted using PC-Prim 1 or M13R. The heavy and light chain sequences were aligned using the VBASE2 database to identify the corresponding immunoglobulin gene segments and assess the diversity and specificity of the clones. The alignment allowed for identifying framework regions and complementarity-determining regions, along with the closest matching germline sequences. This analysis was used to investigate the diversity of the Fabs recovered. The sequencing results for the heavy and light chains are shown in Appendices AI and AIII.

The aligned sequences were compared against the mouse germline sequences. The alignment results, including framework regions and CDRs, are shown in Table 5.4. The multiple sequence alignments of the heavy and light chains, generated using Clustal, are displayed in Appendices AII and AIV.

The aligned sequences were compared against the mouse germline sequences to evaluate their similarity and identify diversity within the framework regions and CDRs. The alignment results, summarised in Table 5.4, and the multiple sequence alignments of the heavy and light chains, are displayed in Appendices AII and AIV, providing detailed insights into the selected clones' genetic makeup.

The analysis revealed that all heavy chain variable regions originated from the musIGHV655 germline, indicating a conserved framework across the clones. This conservation is crucial for maintaining the structural integrity and stability of the Fab fragments. However, variability was observed in the diversity (DH) and joining (JH) segments. For example, DSP2.7 and DSP2.8 were the most frequently utilised DH genes, while the JH segments varied primarily between

JH1 and JH4, suggesting diversity in the antigen-binding loops of the heavy chains, particularly within CDR3.

For the light chain variable regions, all clones shared the same germline V gene (IGKV16-104*01) from the musIGKV128 germline, indicating structural consistency. However, the J gene usage varied across clones, with IGKJ2*01 being the most common, while others, such as IGKJ4*01 and IGKJ5*01, appeared in specific clones. This variability contributes to differences in antigen-binding loops and highlights the functional diversity among the selected clones.

The multiple sequence alignments further supported these findings. Conserved framework regions were observed across both heavy and light chains, ensuring structural stability, while significant sequence diversity was detected in the CDRs. Notably, the heavy chain CDR3 regions displayed the highest variability, consistent with their critical role in determining antigen specificity and binding affinity. Similarly, diversity in the light chain CDR regions enhanced the specificity of the antigen-binding site.

These findings indicate that the selected clones represent a structurally stable yet diverse repertoire of Fabs with a high potential for specific binding to the SGLT2-Loops-No-Tag antigen. This balance of conservation and diversity confirms the success of the phage library selection process and provides a robust platform for further functional and structural characterisation.

Table 5.4: Summary of Variable Gene Usage of Heavy and Light Chains.

a. Heavy Chain Sequences Summary of VH, DH, and JH Gene Usage

Clone(s)	VH	DH	JH
FAB 1.3	musIGHV655	DSP2.8	JH1 mouse
FAB 2.3	musIGHV655	DSP2.7 (same score: DSP2.1, DSP2.5, DSP2.8)	JH4 mouse
FAB 3.3	musIGHV655	DSP2.7 (same score: DSP2.1, DSP2.5, DSP2.8)	JH4 mouse
FAB 5.3	musIGHV655	DSP2.8	JH1 mouse
FAB 5.2	musIGHV655	DSP2.8	JH1 mouse
FAB 7.2	musIGHV655	DSP2.7 (same score: DSP2.1, DSP2.5, DSP2.8)	JH4 mouse
FAB 7.3	musIGHV655	DSP2.8	JH1 mouse
FAB 9.2	musIGHV655	DSP2.7 (same score: DSP2.1, DSP2.5, DSP2.8)	JH4 mouse
FAB 3.2	musIGHV655	DSP2.7 (same score: DSP2.1, DSP2.5, DSP2.8)	JH4 mouse
FAB 10.2	musIGHV655	DSP2.7 (same score: DSP2.1, DSP2.5, DSP2.8)	JH1 mouse
FAB 8.2	musIGHV655	DSP2.8	JH1 mouse
FAB 19.2	musIGHV655	DSP2.8	JH4 mouse
FAB 23.2	musIGHV655	DSP2.8	JH1 mouse

b. Light Chain Sequences Summary of V and J Genes

Clone(s)	Germline (Light)	V	J
FAB 1.3	musIGKV128	IGKV16-104*01	IGKJ2*01
FAB 2.3	musIGKV128	IGKV16-104*01	IGKJ2*01
FAB 3.3	musIGKV128	IGKV16-104*01	IGKJ5*01
FAB 5.3	musIGKV128	IGKV16-104*01	IGKJ2*01
FAB 5.2	musIGKV128	IGKV16-104*01	IGKJ2*01
FAB 7.2	musIGKV128	IGKV16-104*01	IGKJ4*01
FAB 7.3	musIGKV128	IGKV16-104*01	IGKJ2*01
FAB 9.2	musIGKV128	IGKV16-104*01	IGKJ2*01
FAB 3.2	musIGKV128	IGKV16-104*01	IGKJ2*01
FAB 19.2	musIGKV128	IGKV16-104*01	IGKJ2*01

This table summarises the VH, DH, and JH gene segments for heavy chains and the V and J genes for light chains across the selected Fab clones. While all clones utilise the musIGHV655 germline for their VH regions and IGKV16-104*01 for the light chain V genes, variability in DH and JH segments for heavy chains and J genes for light chains reflects diversity in the antigen-binding regions. This diversity, especially in CDRs, suggests that the clones possess distinct antigen-binding surfaces, which are critical for specificity and affinity. These findings, combined with the sequence alignment results, confirm the library's robustness and its adaptation to bind the SGLT2-Loops-No-Tag antigen effectively.

5.3.16 Expression and Purification of Fab Fragments

To express the Fab fragments, clones that demonstrated the highest binding affinity to the SGLT2-Loops-No-Tag antigen during ELISA screening were selected. These clones were prioritised based on their absorbance values at 450 nm (A_{450}), significantly exceeding the negative controls, indicating strong antigen-binding specificity. The decision to choose these clones was guided by their potential for further functional and structural characterisation.

A small aliquot of the glycerol stock of the selected clones, prepared after the final round of biopanning and ELISA screening, was used to inoculate an initial culture. Specifically, 100 µl of the glycerol stock was added to 2 L of SB medium supplemented with 100 µg/ml ampicillin and 1% glucose to repress basal expression of the Fab fragments. The culture was incubated overnight at 37°C with shaking at 250 rpm to promote bacterial growth and reach the logarithmic phase.

The culture was monitored until the OD_{600} reached approximately 0.6–0.8, indicating that the cells had reached the mid-log phase, an ideal stage for the induction of protein expression. At this point, IPTG was added to the culture to a final concentration of 1 mM to induce Fab fragment expression. The culture was then incubated at 25°C with shaking at 200 rpm for 16–20 hours to allow optimal protein expression and folding, ensuring that the Fab fragments were produced in a soluble and functional form.

Following the induction period, the bacterial cells were harvested by centrifugation at 6,000 x *g* for 30 minutes at 4°C to separate the cells from the culture medium. The supernatant, which may contain soluble Fab fragments secreted into the medium, was carefully collected and filtered through a 0.45 µm filter to remove any remaining cellular debris. The filtered supernatant was then immediately processed for protein purification.

Following the expression of Fab fragments, purification was conducted using Protein G affinity chromatography (2.2.9). The purification process began with equilibrating the Protein G column using a buffer containing 20 mM sodium phosphate and 150 mM NaCl at pH 7.0. This step was essential to optimise conditions for the efficient binding of Fab fragments to the column. The clarified culture supernatant, containing the expressed Fab fragments, was then applied to the equilibrated Protein G column, allowing the target proteins to bind specifically to the Protein G resin.

Following the binding step, unbound proteins and non-specifically bound contaminants were removed by washing the column with 10–20 column volumes of the same buffer (20 mM sodium phosphate, 150 mM NaCl, pH 7.0). The washing process continued until baseline absorbance levels were achieved, indicating the effective removal of impurities.

The bound Fab fragments were eluted from the column using 0.1 M glycine-HCl, pH 2.7. To prevent denaturation caused by the acidic elution buffer, the eluted fractions were immediately neutralised with 1 M Tris-HCl, pH 8.0 (Fig. 5.11).

The eluted Fab fragments were dialysed using Snakeskin dialysis tubing with 10,000 Da MWCO against 5 L of dialysis buffer PBS (pH 7.4) at 4°C to remove the glycine-HCl, followed by ultrafiltration device concentration.

The purity and integrity of the purified Fab fragments were assessed using reducing SDS-PAGE. The analysis confirmed the successful purification of the Fab fragments with minimal contamination. Under reducing conditions, the expected molecular weight of the Fab fragments was approximately 25 kDa, consistent with the separation of the heavy and light chains of the Fab fragments after disulphide bond reduction (Fig. 5.12).

Following the purification and dialysis of the Fab fragment 19.2, its concentration was initially measured using a Nanodrop spectrophotometer at 280 nm, yielding a concentration of 0.3 mg/ml. To validate this measurement, the concentration was also estimated using the BSA standard curve method on an SDS-PAGE gel, which indicated a concentration of approximately 0.6 mg/ml.

Fab 19.2 was chosen for further analysis after attempts with other clones yielded lower concentrations or encountered challenges during purification. While Fab 19.2 did not demonstrate the strongest binding in ELISA results, it provided sufficient yield and purity for downstream analysis, making it a practical choice for further characterisation. Additionally, its unique sequence diversity suggested potential relevance for SGLT2 targeting, warranting further investigation despite its moderate ELISA performance.

A total volume of 1 ml of purified Fab fragment was obtained, resulting in an estimated yield of 0.3–0.6 mg, depending on the measurement method used. Both methods confirmed the

successful purification of Fab 19.2, as indicated by distinct bands at the expected molecular weight of approximately 25 kDa for the heavy and light chains under reducing conditions.

After confirming the concentration, the purified Fab fragments were aliquoted and stored at -80°C to preserve their stability and functionality for subsequent experimental applications.

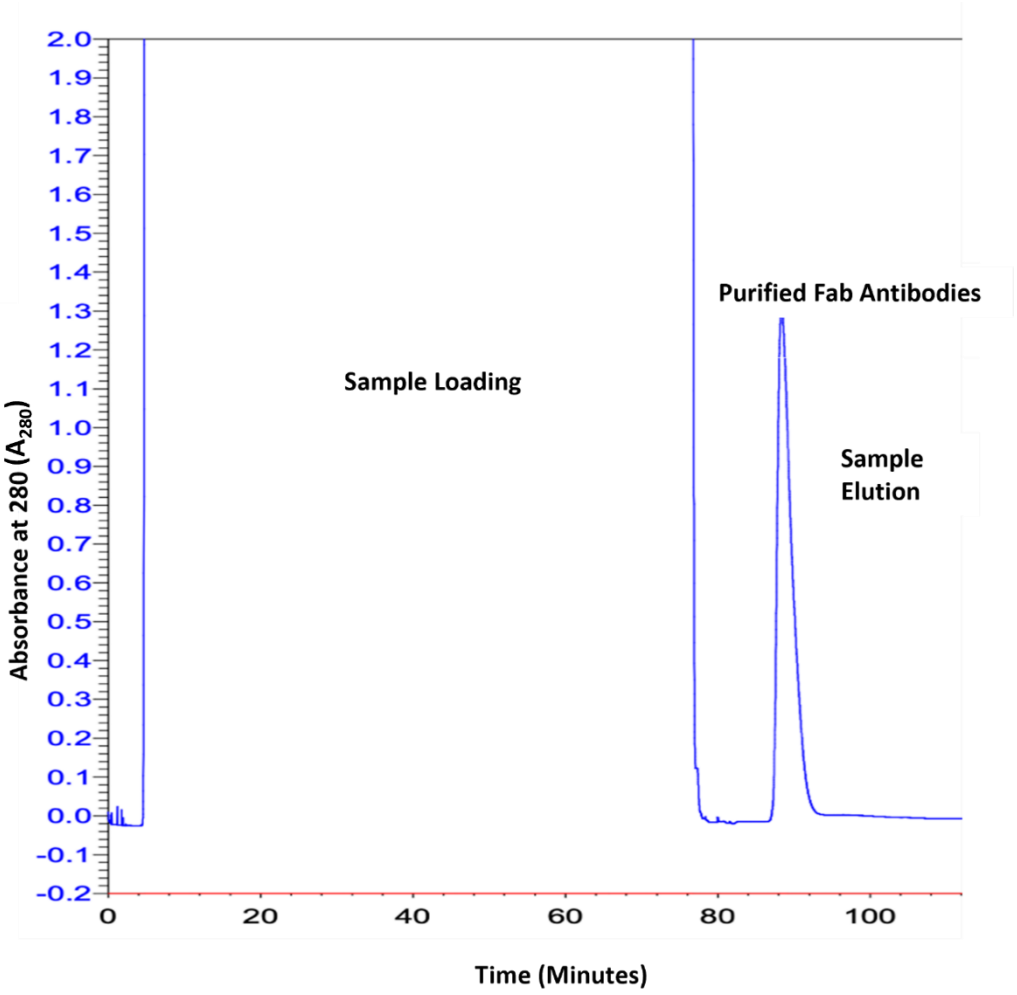

Figure 5.3: Purification Process of 19.2 Fab Antibodies.

This figure illustrates the purification steps of Fab antibodies. The process begins with sample loading onto the purification column, followed by washing and elution steps to isolate the desired Fab fragments. The chromatogram shows the different peaks corresponding to various stages of the purification, with the specific peak indicating the purified Fab antibodies highlighted.

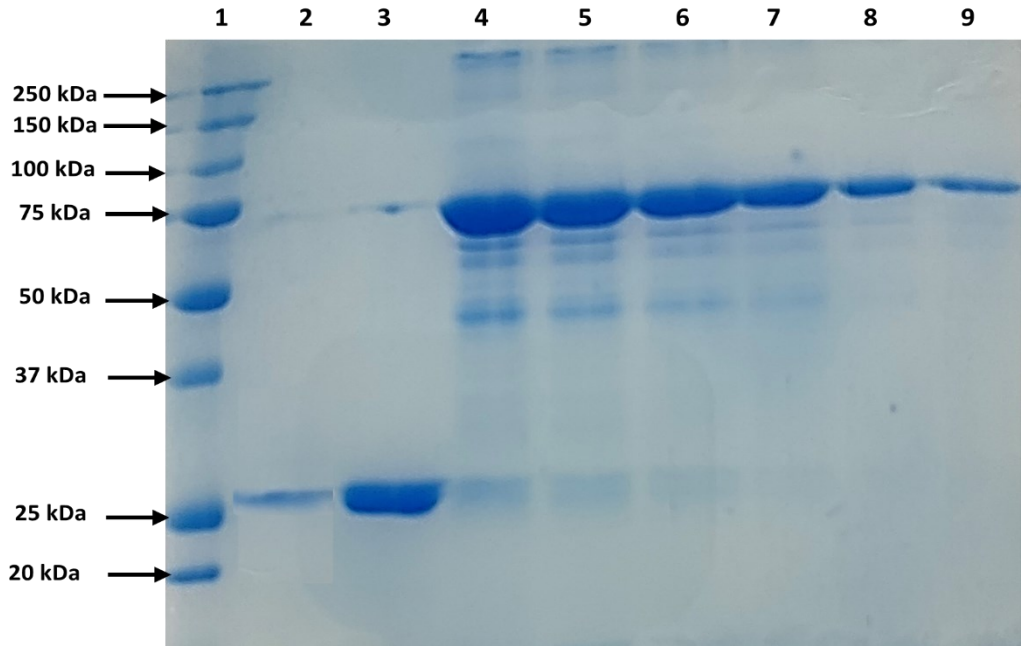

Figure 5.4: SDS-PAGE Analysis of Purified Fab Fragments.

The SDS-PAGE analysis was performed to assess the purity and estimate the concentration of the purified Fab fragments. Lane 1 contains the molecular weight marker. Lane 2 shows the Fab fragment named "13.3 Fab," and Lane 3 contains the Fab fragment named "19.2 Fab." Lanes 4 to 9 contain the BSA standard curve, which was used to estimate the concentration of the Fab fragments by comparing band intensities. Under reducing conditions, the Fab fragments separated into their heavy and light chains, each with an expected molecular weight of approximately 25 kDa. The analysis confirmed successful purification with minimal contamination, as indicated by the presence of distinct bands at the expected molecular weight.

5.3.17 ELISA to Assess the Specificity of Fab 19.2

A standard ELISA was conducted to evaluate the binding specificity and affinity of the purified Fab 19.2. This assay was designed to confirm the interaction of Fab 19.2 with its target antigen, the SGLT2-Loops (2.2.6). Two wells of the ELISA plate were coated with the SGLT2-Loops antigen and prepared by diluting the antigen in a carbonate coating buffer. For controls, two wells were coated with 3% BSA in carbonate coating buffer to serve as the negative control, and two wells were coated with human granzyme B antigen in the same buffer to serve as the positive control. A previously isolated anti-granzyme B Fab was used as a positive binder control for the granzyme B wells. The plate was incubated overnight at 4°C to ensure proper antigen binding.

Following the coating step, the wells were blocked with 3% BSA in PBS to prevent non-specific binding. The Fab 19.2 sample was added to the SGLT2-Loops-coated and negative control wells, while the granzyme B Fab was added to the corresponding positive control wells. The plate was incubated for 1 hour at room temperature to allow binding. After incubation, the wells were washed thoroughly with PBST to remove unbound Fab. A goat anti-mouse IgG (Fab-specific) antibody conjugated to HRP was then added to each well and incubated for an additional hour at room temperature. This secondary antibody specifically binds to the Fab fragment, allowing detection of the Fab-antigen interaction. TMB substrate was added to each well to visualise the binding, initiating a colourimetric reaction that was stopped by adding 1 M sulphuric acid. The absorbance was measured at 450 nm using a microplate reader.

The ELISA results (Fig. 5.13) demonstrate that the absorbance values for Fab 19.2 are nearly identical to those of the positive control (human granzyme B). This indicates that Fab 19.2 exhibits a strong and specific binding affinity for the SGLT2-Loops antigen. This close alignment in absorbance suggests that the binding activity of Fab 19.2 is comparable to that of the well-characterized positive control.

In contrast, the negative control (3% BSA) showed minimal absorbance, confirming no significant non-specific binding of Fab 19.2 to the wells. The lack of detectable binding in the negative control wells further validates the specificity of Fab 19.2 for its target antigen, with no background signal observed. Additional specificity testing through serial dilution

experiments (6.3.1.3) further supports these findings, demonstrating Fab 19.2's robust binding characteristics.

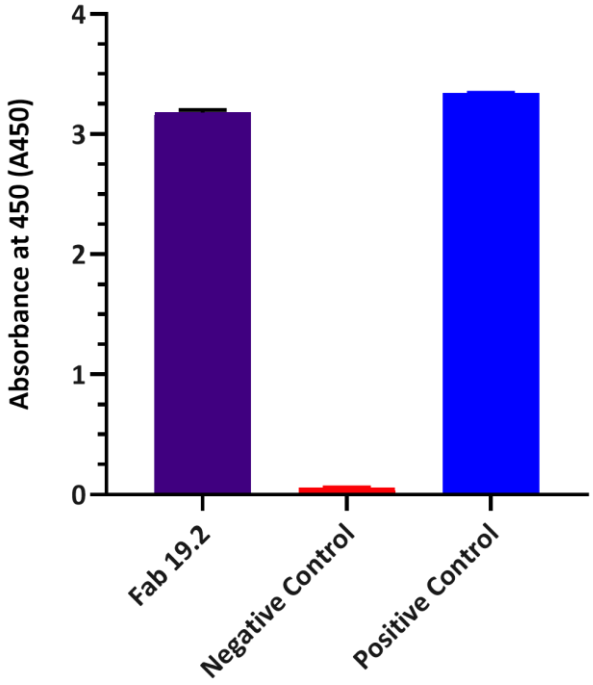

Figure 5.5: Comparative ELISA Absorbance of Fab 19.2, Negative Control, and Positive Control.

The column graph displays the ELISA absorbance values at 450 nm for Fab 19.2 (purple), the negative control (red, 3% BSA), and the positive control (anti-granzyme B Fab against granzyme B). The high absorbance values for Fab 19.2 indicate strong and specific binding to the SGLT2-Loops antigen, comparable to the binding observed with the positive control. The negative control exhibited minimal absorbance, confirming the absence of significant non-specific binding by Fab 19.2. The results validate the specificity and functionality of Fab 19.2, as further confirmed by serial dilution experiments conducted to evaluate binding behaviour across a range of concentrations (detailed in Section 6.3.1.3). The positive control demonstrated the effectiveness of the assay. Error bars represent the standard deviation of the measurements.

5.3.18 ELISA for Exclusion of His-Tag Binding

An additional ELISA was performed to validate the specificity of Fab 19.2 further and to exclude the possibility of non-specific binding to the His-tag present in the SGLT2-Loops antigen. In this experiment, Fab 19.2 was tested at two different concentrations (1:2,000 and 1:5,000) against three different antigens: SGLT2-Loops (target antigen), 3% BSA (negative control), and a COVID-19 antigen which is an irrelevant antigen included solely because it contains a His-tag, used to test for non-specific binding to the His-tag itself (positive control). Each antigen was coated in duplicate wells of the ELISA plate. The Fab 19.2 sample was then applied to each well, followed by detection with a goat anti-mouse IgG (Fab-specific) antibody conjugated to an HRP.

This ELISA aimed to determine whether Fab 19.2 specifically binds to the SGLT2-Loops antigen or interacts with the His-tag present in the recombinant COVID-19 antigen used as a positive control in this assay.

The ELISA results (Fig. 5.14) demonstrated that Fab 19.2 exhibited strong binding to the SGLT2-Loops antigen, consistent with previous findings. Notably, the absorbance values for the COVID-19 antigen wells were minimal and similar to the negative control (3% BSA), indicating no significant binding of Fab 19.2 to the irrelevant His-tagged antigen. This result strongly suggests that the binding of Fab 19.2 to the SGLT2-Loops antigen is mediated by specific interactions with the SGLT2-Loops domain itself, rather than by non-specific interactions with the His-tag.

The His-tags were not cleaved from the recombinant SGLT2-Loops antigen as the antigen design did not include a cleavage site for tag removal. While cleaving His-tags can further validate specificity, the experimental design addressed this by including a His-tagged irrelevant antigen (COVID-19 antigen) as a control. The inclusion of this control ensured that any observed binding was due to interactions with the SGLT2-Loops domain and not the His-tag. This approach avoided additional enzymatic digestion steps and ensured sufficient antigen availability for the experiments, without compromising the validity of the specificity assessment.

Table 5.5: ELISA Results for Fab 19.2 Binding Specificity at Different Concentrations.

Fab 19.2 Concentration	Antigen Coated on Wells	Absorbance (450 nm) 1	Absorbance (450 nm) 2	Mean Absorbance (450 nm)
1:2,000	SGLT2-Loops (Target)	1.361	1.258	1.2595
1:2,000	3% BSA (Negative Control)	0.0567	0.062	0.05935
1:2,000	COVID-19 Antigen His-tag (Positive Control)	0.068	0.076	0.072
1:5,000	SGLT2-Loops (Target)	0.587	0.594	0.5905
1:5,000	3% BSA (Negative Control)	0.057	0.054	0.0555
1:5,000	COVID-19 Antigen His-tag (Positive Control)	0.06	0.061	0.0605

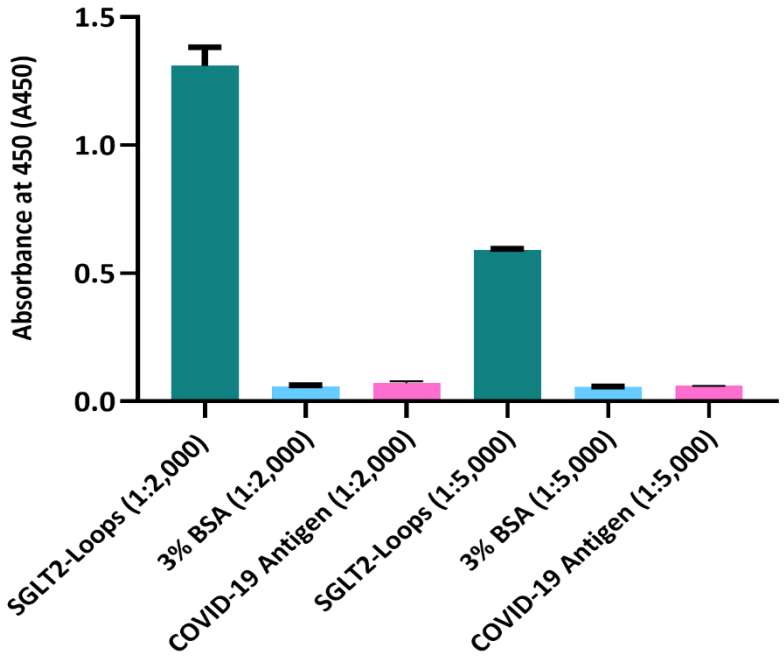

Figure 5.6: ELISA Analysis of Fab 19.2 Binding Specificity Across Different Antigens and Concentrations.

5.4 Discussion

The generation and characterisation of Fab fragments targeting the loops of the SGLT2 protein represent a significant achievement in this study. Fab fragments were successfully produced using phage display technology, which is a robust platform for selecting antibodies with high specificity and affinity from vast libraries. Fab 19.2 was isolated and shown to exhibit strong specificity for the SGLT2-Loops antigen. This specificity, demonstrated through a series of ELISA experiments, highlights the robustness of phage display as a tool for developing antibodies with precise binding capabilities.

Phage display technology has long been recognised as a powerful method for generating antibodies with high specificity. It enables the rapid screening of large libraries to identify candidates with the desired binding characteristics, a technique initially established by Smith (1985) and later refined by Barbas (2001). This approach has been instrumental in producing antibodies that selectively target specific antigens.

This study employed the iterative biopanning process to enrich the library for Fab fragments with a high affinity for the SGLT2-Loops antigen. This method is consistent with previous findings where antibodies were isolated with high affinity and specificity for various targets, including membrane proteins. It has been shown to effectively isolate antibodies with strong binding specificity, as demonstrated by Hoogenboom et al. (1991). A series of Fabs that bound the SGLT2 antigen were isolated. Sequence analysis showed that the Fabs were highly similar and most likely identical in their binding properties. One of these, 19.2, was selected for further analysis.

The specificity of Fab 19.2, evidenced by its strong binding to the SGLT2-Loops antigen and minimal interaction with the negative control (3% BSA), is in line with the results of similar studies. These studies have shown that phage display-derived antibodies exhibit high target specificity and minimal off-target effects (McCafferty et al., 1990).

Following its isolation, the variable regions of Fab 19.2 heavy and light chains were sequenced to confirm the identity and diversity of the selected Fab fragments. The sequencing analysis revealed distinct VH and VK sequences. The VH sequence was derived from the musIGHV655 germline, with variability in CDRs, particularly in CDR3, which is known to play a critical role in antigen binding and specificity. Similarly, the VK sequence was derived from the

musIGKV128 germline, with differences in the J gene segment contributing to binding diversity.

The presence of somatic hypermutation was observed in both the heavy and light chains, characterized by nucleotide substitutions in the CDRs. These mutations are indicative of affinity maturation, a process by which B-cells generate high-affinity antibodies during an immune response. The diversity observed in the CDR regions of Fab 19.2 underscores its potential as a high-affinity binder, while the relatively conserved framework regions ensure structural stability.

These findings provide a molecular basis for the high specificity of Fab 19.2, confirming that it is a strong candidate for further functional characterisation. A more detailed analysis of the sequence alignments and their implications is provided in Table 5.4 and Appendices AII and AIV.

It was important to confirm that Fab 19.2's binding to the SGLT2-Loops antigen is not influenced by non-specific interactions, particularly with the His-tag, which is commonly used in recombinant protein production. To address this, an additional ELISA was conducted, where Fab 19.2 was tested against three antigens: the SGLT2-Loops antigen, an irrelevant COVID-19 antigen with a His-tag, and 3% BSA as a negative control. The results demonstrated that Fab 19.2 showed strong binding to the SGLT2-Loops antigen, consistent with its intended specificity, with minimal binding to the COVID-19 antigen and 3% BSA. This confirms that the interaction between Fab 19.2 and the SGLT2-Loops antigen is highly specific and not mediated by non-specific binding to the His-tag, further validating the utility of Fab 19.2 as a highly selective targeting agent.

The next chapters will explore detailed epitope mapping and functional tests to further elucidate the interaction between Fab 19.2 and the SGLT2-Loops antigen, providing a deeper understanding of its specificity and functionality.

Chapter 6: Characterisation of SGLT2 Fab Antibodies

6.1 Introduction

The preceding chapter described the isolation of SGLT2-specific Fabs using phage display technology. Sequence analysis of the recovered Fabs showed that they were likely to be essentially identical and targeting the same epitope on SGLT2. The immunoglobulin heavy chains and light chains were highly similar. Accordingly, we selected the best binder, as assessed by ELISA, and the goal in this chapter was to analyse the binding properties of this Fab (19.2), attempt to identify the corresponding epitope and assess the specificity of this antibody in immunohistochemistry and western blotting. Characterising monoclonal antibodies is an essential process in antibody development, particularly when determining their specificity and mechanism of action. The characterisation of Fab 19.2 will be explored through advanced methods such as epitope mapping, western blotting, and immunohistochemistry. These methods will provide a comprehensive understanding of its binding properties and functionality.

Epitope mapping, the process of determining the specific binding sites, or epitopes, on an antigen recognised by a monoclonal antibody, is a cornerstone in characterising antibody reagents. This information is invaluable in understanding the mode of action of antibodies, as it provides insights into how the antibody interacts with its target antigen. Essentially, epitope mapping is like a roadmap that guides us through the intricate complex between antibodies and antigens. Additionally, it is essential to identify potential cross-reactivity with other antigens, which is fundamental for developing highly specific diagnostic and therapeutic tools. When working with a large number of antibodies, epitope mapping also allows for grouping antibodies based on their binding sites, thereby streamlining the analysis process and avoiding redundant testing. (He et al., 2012, Zhang, 1996).

To identify the exact epitopes of the full-length SGLT2 protein recognised by Fab 19.2 and understand the binding properties of this interaction. Advanced techniques, including biotinylation, competitive ELISA, and phage display, were used to achieve this goal. The biotinylation of Fab 19.2 was optimised to ensure that the modified antibody retained its binding affinity for the SGLT2-Loops antigen. Competitive ELISA was then used to assess the biotinylated antibody to compete with unbiotinylated Fab for binding sites.

Several approaches have been described for analysing antibody-antigen binding sites, which vary depending on whether the epitopes are linear or conformational. Linear epitopes consist of a contiguous sequence of amino acids preserved upon fragmentation of the target antigen. In contrast, conformational epitopes are formed by amino acid residues that are brought together in the native three-dimensional structure of the antigen. These conformational epitopes usually exist only in the native protein and are more challenging to map because they rely on the antigen's tertiary structure (Amit et al., 1986).

Traditional methods for mapping conformational epitopes, such as X-ray crystallography, are time-consuming, expensive, and require large quantities of antibodies and purified antigens (Amit et al., 1986). Alternatively, "large fragment" analysis, which involves fragmenting the target antigen through proteolysis or recombinant DNA techniques, can map both linear and conformational epitopes. However, this approach may disrupt the native structure of the antigen, leading to the loss of antibody binding, particularly in conformational epitopes (Fack et al., 1997). On the other hand, Linear epitope mapping is less technically challenging and often employs methods such as synthetic peptide arrays or phage display libraries (Nilvebrant and Rockberg, 2018).

Phage display can also be used for epitope mapping. The open reading frame (ORF) of the target antigen is fragmented, and random coding regions (approximately 100-200 bp) are cloned into a phage display vector. Small regions of the target antigen are expressed on the surface of phage virions. In a reverse procedure of Fab biopanning, an antibody is immobilised on a plastic surface and used to enrich the fragment library. After several rounds of enrichment, random clones are sequenced to determine if a consensus sequence is present corresponding to the target epitope (Fack et al., 1997, Nilvebrant and Rockberg, 2018).

In addition to epitope mapping, it is essential to validate the functionality of Fab 19.2 through other assays, such as western blotting and immunohistochemistry. To address that, the pcDNA3.1 vector was employed for transient transfection to express the full-length SGLT2 protein. This vector, driven by the strong CMV promoter, facilitates high-level expression of SGLT2 in mammalian cells (CHO-K1) (Fig. 6.1). The insertion of the SGLT2 gene into the pcDNA3.1 vector was achieved using *Nhe*I and *Hind*III restriction enzymes, ensuring directional cloning and maintaining the integrity of the protein. The expression of full-length SGLT2 in transiently transfected cells will be used for western blotting to confirm that Fab

19.2 can bind to the denatured form of SGLT2. This is critical for validating the antibody's ability to recognise its target in a simplified *in vitro* system. In parallel, immunohistochemistry will be conducted using mouse kidney tissue sections to assess Fab 19.2's ability to bind to the native conformational form of SGLT2 *in situ*. This dual approach comprehensively evaluates the antibody's binding properties across different experimental conditions.

The importance of this validation cannot be overstated, as proved by numerous studies that have used similar approaches to confirm the specificity and reliability of antibodies employed in both research and clinical diagnostics, thereby ensuring the accuracy of experimental results and diagnostic outcomes. For instance, Bordeaux et al. (2010) demonstrated standardised protocols to validate antibodies employed in immunohistochemistry, leading to reproducible and reliable results in cancer biomarker studies. Similarly, Baker (2015) highlighted the critical role of validation in reducing false-positive rates in western blot experiments, emphasising that rigorous testing is essential for ensuring antibody specificity in protein detection. Another example includes Uhlen et al. (2016), who employed a multi-platform approach to validate antibodies used in The Human Protein Atlas, improving the reliability of large-scale proteomic research. These studies underscore the importance of adopting robust validation methods to enhance the reproducibility and accuracy of both research findings and clinical applications.

Combining these techniques not only maps the precise epitopes recognised by Fab 19.2 but also confirms the antibody's specificity and binding efficiency.

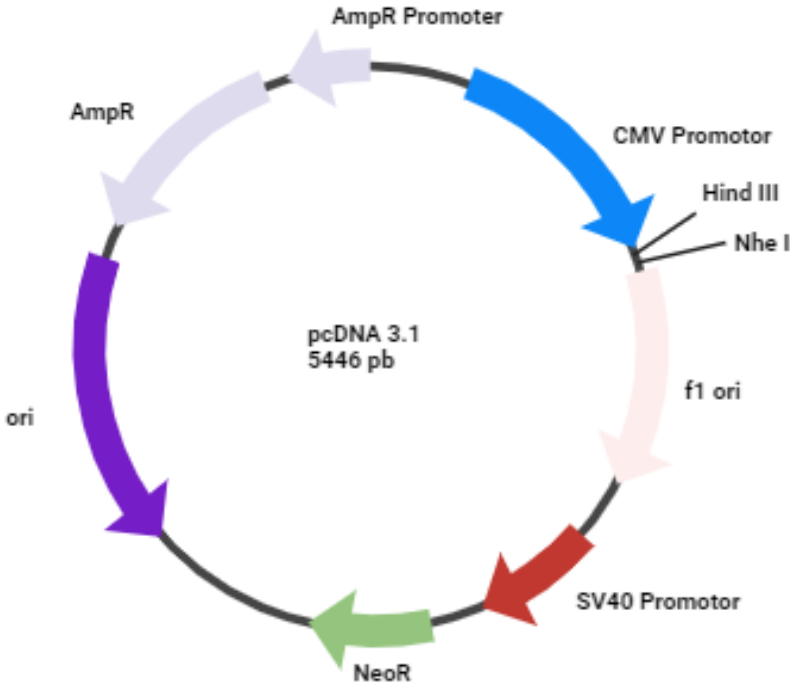

Figure 6.1: Mammalian Expression Vector pcDNA3.1.

Mammalian expression vector contains CMV enhancer-promoter and allows high-level stable and transient expression in mammalian cells.

6.2 Aims and Objectives

The primary aim of this chapter is to comprehensively characterise Fab 19.2 by combining epitope mapping, western blotting, and Immunohistochemistry. This will provide critical insights into the antibody's binding properties and specificity. The workflow scheme is shown in Fig. 6.2. The specific objectives were to:

- To identify the specific epitopes on the SGLT2 protein recognised by Fab 19.2 through phage display-based epitope mapping.
- To validate the binding efficiency of biotinylated Fab 19.2 using competitive ELISA.
- To assess the functionality of Fab 19.2 in binding to denatured SGLT2 *in vitro* through western blot analysis.
- To confirm Fab 19.2's specificity *in situ* by evaluating its binding to native SGLT2 in tissue sections using Immunohistochemistry.

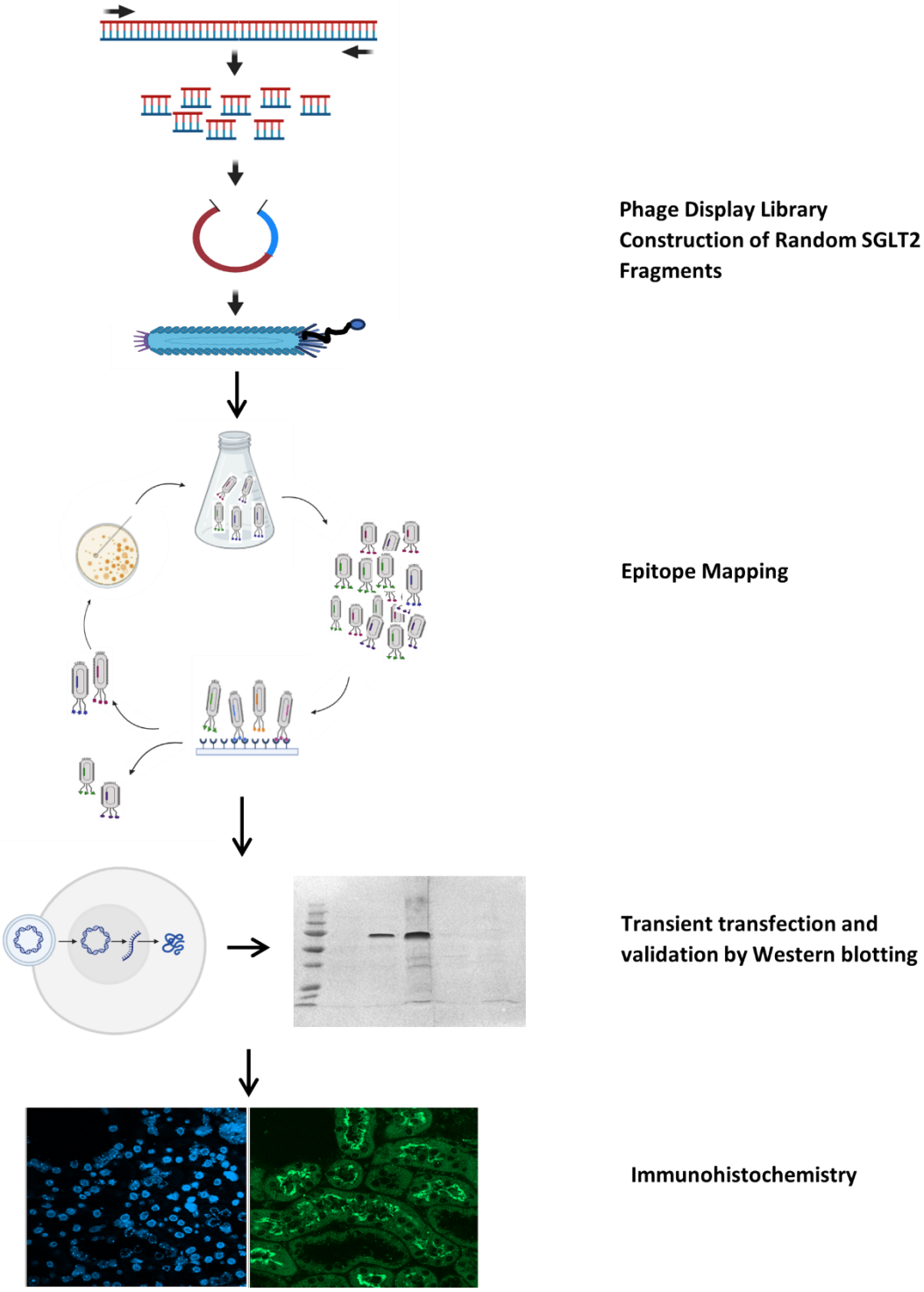

Figure 6.2: Schematic Representation of the Generation and Characterisation of SGLT2-Specific Fab Fragments.

6.3 Experiments and Results

6.3.1 Epitope Mapping

6.3.1.1 Biotinylating of Fab 19.2

The biotinylation of Fab 19.2 is crucial for enhancing the versatility and sensitivity of detection methods. Facilitating its interaction with avidin-conjugated labels allows the Fab to be efficiently used in downstream applications such as epitope mapping, western blotting, and immunohistochemistry.

The biotinylation of Fab 19.2 was carried out using EZ-Link Sulfo-NHS-LC-Biotin (Thermo Scientific, A39257), a reagent that attaches biotin molecules to proteins and antibodies through covalent bonds. Due to the size of biotin (244 Da), this reagent facilitates strong binding to avidin and streptavidin without significantly altering the biological functions of the proteins.

A 20-fold molar excess of the biotin reagent relative to the Fab protein was used to ensure effective biotinylation. The amount of biotin reagent required for the reaction was calculated using the following formula:

mmol biotin = ml protein x (mg protein/ml protein) x (mmol protein/ mg protein) x (20 mmol biotin/mmol protein).

I ml of Fab 19.2 (at a concentration of 0.3 mg/ml) was used for this reaction.

1 ml Fab 19.2 x (0.3 mg Fab 19.2 / 1 ml IgG) x (1 mmol Fab/50,000 mg Fab) x (20 mmol Biotin/1mmol Fab) = 0.00012 mmol Biotin.

The volume of 10 mM biotin reagent solution required was calculated by using this formula:

µl Biotin = mmol Biotin x (1,000,000 µl / L) x (1 L /10 mmol).

0.00012 mmol Biotin x (1,000,000 µl / L) x (1 L /10 mmol) =12 µl of biotin reagent.

Accordingly, 12 µl of the 10 mM biotin reagent solution was added to the 500 µl of the Fab 19.2 protein solution, which had a 0.3 mg/ml concentration. The reaction mixture was then incubated on ice for two hours or at room temperature for 30 min, allowing sufficient time for the biotin molecules to attach to the Fab fragments covalently. The biotinylation reaction

was halted by adding 10 µl of 1 M Tris-HCl (pH 7.5), which neutralises the reactive NHS ester groups in the biotin reagent.

The addition of Tris-HCl stops the reaction by providing free amine groups from the Tris base. These amine groups compete with the lysine residues on the Fab fragments for the remaining NHS ester groups on the biotin reagent. Once the NHS esters react with the amines from Tris, they are neutralised and no longer available for further biotinylation, effectively halting the reaction. This ensures that biotinylation is limited to the intended extent and avoids over-labeling, which could potentially affect the function or structure of the Fab fragments.

The biotinylated Fab 19.2 solution was subjected to dialysis to remove excess biotin. The solution was transferred to Snakeskin Dialysis Tubing (10,000 Da MWCO, ThermoFisher) and dialysed overnight against 2 L of PBS (pH 7.4) at 4°C with gentle stirring. After dialysis, the Fab 19.2 was collected, and its concentration was re-measured using a Nanodrop spectrophotometer at 280 nm, yielding a concentration of 200 ng/µl.

6.3.1.2 Competitive ELISA

The competitive ELISA was designed to evaluate the binding specificity and potential inhibitory effect of biotinylated Fab 19.2 when competing with its unbiotinylated counterpart for the SGLT2-Loops antigen. The experiment was carefully structured (Table 6.1) to include both experimental groups and appropriate negative controls to ensure the reliability of the results. In addition, the results were conducted in triplicate to ensure their reliability and reproducibility.

- **Group 1** wells were coated with the SGLT2-Loops antigen at 2 µg/mL concentration in carbonate buffer and incubated overnight at 4°C. After blocking with 3% BSA in 1X TBST to prevent non-specific binding, 100 µl of unlabelled Fab 19.2 supernatant was added to the wells. Based on prior measurements, the concentration of unlabelled Fab in the supernatant was estimated to be approximately 0.3 mg/ml.

  Subsequently, 100 µl of biotinylated Fab 19.2, diluted 1:5000 from a stock concentration of 0.2 mg/ml, was introduced to the wells. This corresponds to a final concentration of 0.04 µg/ml for the biotinylated Fab. The detection of bound Fab was facilitated by adding Streptavidin-HRP, followed by adding TMB substrate. After sufficient colour development, the reaction was stopped by adding 50 µl of 2 M H_2SO_4 to each well.

Absorbance was measured at 450 nm to quantify the binding. This group was duplicated to ensure the reproducibility of the results.

- **Negative Control 1** was established alongside Group 1 to confirm that any observed binding was specific to the SGLT2-Loops antigen. In these wells, 3% BSA was used as the coating instead of the SGLT2-Loops antigen, while all other steps, including the addition of Fab 19.2 supernatant and biotinylated Fab, remained consistent with Group 1. The low absorbance in these wells would indicate minimal non-specific binding, thus validating the specificity of Fab 19.2's interaction with the SGLT2-Loops antigen. This control was also duplicated for accuracy.
- **Group 2** wells were similarly coated with the SGLT2-Loops antigen and treated with 100 µl of unbiotinylated Fab 19.2. In this group, detection was performed using a goat anti-mouse IgG (Fab-specific) antibody conjugated to HRP, followed by the addition of TMB substrate**.** The reaction was halted by adding sulphuric acid**.** This group served as a comparison to assess whether the biotinylated Fab in Group 1 effectively competed with the unbiotinylated Fab for binding to the antigen. The duplication of this group ensured that the results were consistent and reliable.
- **Negative Control 2** mirrored the setup of Group 2 but used 3% BSA as the coating instead of the SGLT2-Loops antigen. This control was crucial for assessing non-specific interactions in the Group 2 setup. The detection method remained the same as in Group 2, with TMB and stopped by sulfuric acid. The low absorbance in these wells would confirm that the signals observed in Group 2 were specific to the interaction between Fab 19.2 and the SGLT2-Loops antigen. Like the other groups, this control was duplicated to enhance the robustness of the findings.

The competitive ELISA results (Fig. 6.3) suggest that the biotinylated Fab 19.2 can compete with the unbiotinylated Fab for binding to the SGLT2-Loops antigen. The reduced absorbance observed in Group 1, compared to Group 2, supports the conclusion that the biotinylated Fab retains its binding activity. However, the incomplete inhibition observed in Group 1 indicates that the concentration of unbiotinylated Fab in the supernatant may be too low to fully compete with the biotinylated Fab.

In a competitive ELISA, the extent of inhibition is directly related to the relative concentrations of the competing antibodies. If the unbiotinylated Fab is present at a lower concentration, it

may only partially compete, resulting in reduced but not complete inhibition. This partial inhibition suggests that while the unbiotinylated Fab is functional, its concentration is likely a limiting factor in achieving full competition.

Table 6.1: Competitive ELISA for Fab 19.2 Design.

Well Group	Coating Ag	Fab Added	Secondary antibody	Detection Method	Outcome
Group 1	SGLT2-Loops	100 µl Fab 19.2 Supernatant	1. Biotinylated Fab 19.2 (1-hour incubation, wash) 2. Streptavidin-HRP (1:5000)	TMB and sulfuric acid	Assess if biotinylated Fab competes
Negative Control 1	3% BSA	100 µl Fab 19.2 Supernatant	1. Biotinylated Fab 19.2 (1-hour incubation, wash) 2. Streptavidin-HRP (1:5000)	TMB and sulfuric acid	Control for non-specific binding in Group 1
Group 2	SGLT2-Loops	100 µl Unbiotinylated Fab 19.2	goat anti-mouse IgG (Fab-specific) antibody conjugated to HRP (1:10,000)	TMB and sulfuric acid	Comparison of binding efficiency
Negative Control 2	3% BSA	100 µl Unbiotinylated Fab 19.2	goat anti-mouse IgG (Fab-specific) antibody conjugated to HRP (1:10,000)	TMB and sulfuric acid	Control for non-specific binding in Group 2

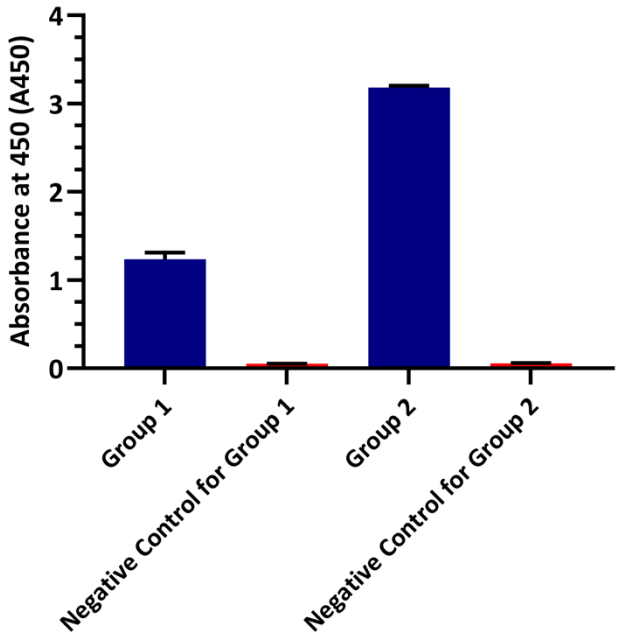

Figure 6.3: Competitive ELISA Results Between Biotinylated and Unbiotinylated Fab 19.2 Binding to SGLT2-Loops Antigen.

This figure shows the ELISA results. They indicate that in Group 1, where biotinylated Fab 19.2 competed with unbiotinylated Fab, there was reduced absorbance compared to Group 2, where only unbiotinylated Fab was present, suggesting partial competition. Negative controls confirmed the specificity of the binding.

6.3.1.3 Determination of Optimal Biotinylated Fab 19.2 Concentration

To determine the optimal concentration of biotinylated Fab 19.2 for binding to the SGLT2-Loops antigen, an ELISA was performed. Recombinant SGLT2-Loops protein was immobilised onto the ELISA plate at a fixed concentration of 1 mg/ml. Biotinylated Fab 19.2, prepared at an initial stock concentration of 100 ng/µl, was applied at four final concentrations: 50 ng/ml (1:2,000 dilution), 20 ng/ml (1:5,000 dilution), 10 ng/ml (1:10,000 dilution), and 5 ng/ml (1:20,000 dilution). These concentrations were prepared by serial dilutions of the stock solution.

After incubation and washing, Streptavidin conjugated to HRP was added to detect the biotin tag. The signal was quantified by measuring absorbance at 450 nm after adding TMB substrate and stopping the reaction with H_2SO_4. This assay was conducted in triplicate to ensure reliability and reproducibility.

The purpose of the experiment was to identify the minimum effective concentration of Fab 19.2 that maintains robust binding to the antigen, optimizing efficiency and sensitivity for future applications. Negative controls containing 3% BSA instead of antigen were included for each sample to account for non-specific binding, validating the specificity of Fab 19.2.

The ELISA results (Fig. 6.4) demonstrate that Fab 19.2 exhibits concentration-dependent binding to the SGLT2-Loops antigen. At the highest concentration tested (50 ng/ml, corresponding to a 1:2,000 dilution), the absorbance values indicate robust binding activity. As the concentration decreases to 20 ng/ml (1:5,000 dilution) and 10 ng/ml (1:10,000 dilution), the absorbance values progressively decrease, reflecting a reduction in binding intensity. However, even at the lowest concentration tested (5 ng/ml, corresponding to a 1:20,000 dilution), Fab 19.2 still produces a measurable signal, above the background levels observed in the negative controls.

The negative controls consistently show very low absorbance values across all concentrations, confirming the specificity of Fab 19.2 for the SGLT2-Loops antigen and ruling out non-specific interactions.

These findings suggest that higher concentrations of Fab 19.2 (e.g., 50 ng/ml or 20 ng/ml) are optimal for achieving strong binding signals. In contrast, lower concentrations, such as 5

ng/ml, may still be useful for experiments with limited antibody availability, provided sensitivity requirements are met.

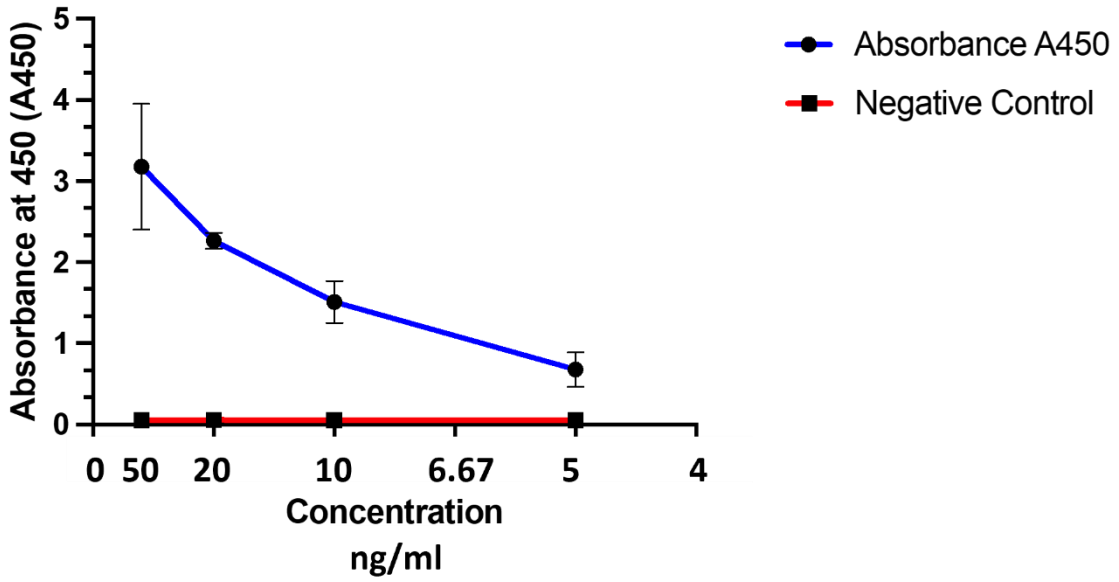

Figure 6.4: ELISA Analysis of Biotinylated Fab 19.2 Binding to SGLT2-Loops Antigen Across Different Concentrations.

The line graph illustrates the absorbance values at 450 nm for various dilutions of biotinylated Fab 19.2 (1:2,000, 1:5,000, 1:10,000, and 1:20,000) as measured by ELISA. The binding activity decreases with increasing dilution, while the negative control consistently shows minimal absorbance across all dilutions, confirming the specificity of Fab 19.2 for the SGLT2-Loops antigen.

6.3.1.4 Fragmentation of Full-Length SGLT2 DNA

The fragmentation of the full-length SGLT2 DNA was a critical step in creating a diverse library of smaller DNA fragments for epitope mapping. This approach aimed to produce a random assortment of DNA fragments that, when expressed, represented various regions of the SGLT2 protein (Fig. 6.5). By generating this library, the experiment sought to identify specific epitopes recognised by Fab 19.2. The full-length SGLT2 DNA was designed using Lasergene software and synthesised in the pUC plasmid by Azenta Life Sciences. The DNA was amplified in *E. coli* using the maxiprep method described in section 2.2.2.4, followed by purification as described in section 2.2.2.7, yielding a high-quality preparation with a concentration of 0.6 mg/ml. This concentration provided an adequate quantity of DNA for enzymatic digestion and downstream applications.

The full-length SGLT2 DNA in the pUC plasmid was subjected to enzymatic fragmentation using *DNase*I to generate a library of randomly digested DNA fragments suitable for downstream applications. An enzyme diluent was prepared by combining 5 µl of 1 M Tris-HCl, 10 µl of 1 mg/ml BSA stock, and 85 µl of nuclease-free water. To this mixture, 1 µl of *DNase*I enzyme was added, and the solution was gently mixed by flicking the tube, followed by a brief spin to ensure thorough mixing.

For the digestion reaction, a 10X reaction buffer was prepared by combining 50 µl of 1 M Tris, 10 µl of 1 M $MnCl_2$, 10 µl of 10 mg/ml BSA, and 30 µl of nuclease-free water. The full-length SGLT2 DNA (20 µL at a concentration of 0.6 mg/ml) was then mixed with 10 µl of the 10X reaction buffer and 70 µl of nuclease-free water. To initiate the digestion, 3 µl of the prepared enzyme diluent was added to the DNA mixture, and the reaction was incubated at 37°C for 15–20 minutes. The digestion was halted by placing the reaction on ice.

The digested DNA fragments were treated with T4 DNA Polymerase (Large Klenow Fragment) to ensure blunt ends for downstream applications. The reaction mixture included 40–50 µL of eluted DNA, 5 µl of T4 DNA Polymerase buffer, 1 µi of 10 mM dNTPs, and 1 µl of T4 DNA Polymerase (specific activity: 5 units/µl). This mixture was incubated at room temperature for 15 minutes, and the reaction was subsequently stopped by heating at 75°C for 20 minutes.

The extent of DNA digestion was assessed by running a 5 µl sample on an agarose gel alongside a 100-bp ladder. The goal was to obtain a smear with most DNA fragments in the

100–200 bp range. After electrophoresis, the smear corresponding to this size range was excised from the gel. Fragments larger than 200 bp were also included, while those smaller than 100 bp were excluded to maintain the desired size range (Fig. 6.6).

Finally, the DNA was purified from the gel using a DNA extraction kit, and the eluted DNA was collected in 40-50 µl of elution buffer. This purified DNA, consisting of randomly digested SGLT2 fragments, was then ready for cloning in the pComb3 vector and subsequent epitope mapping.

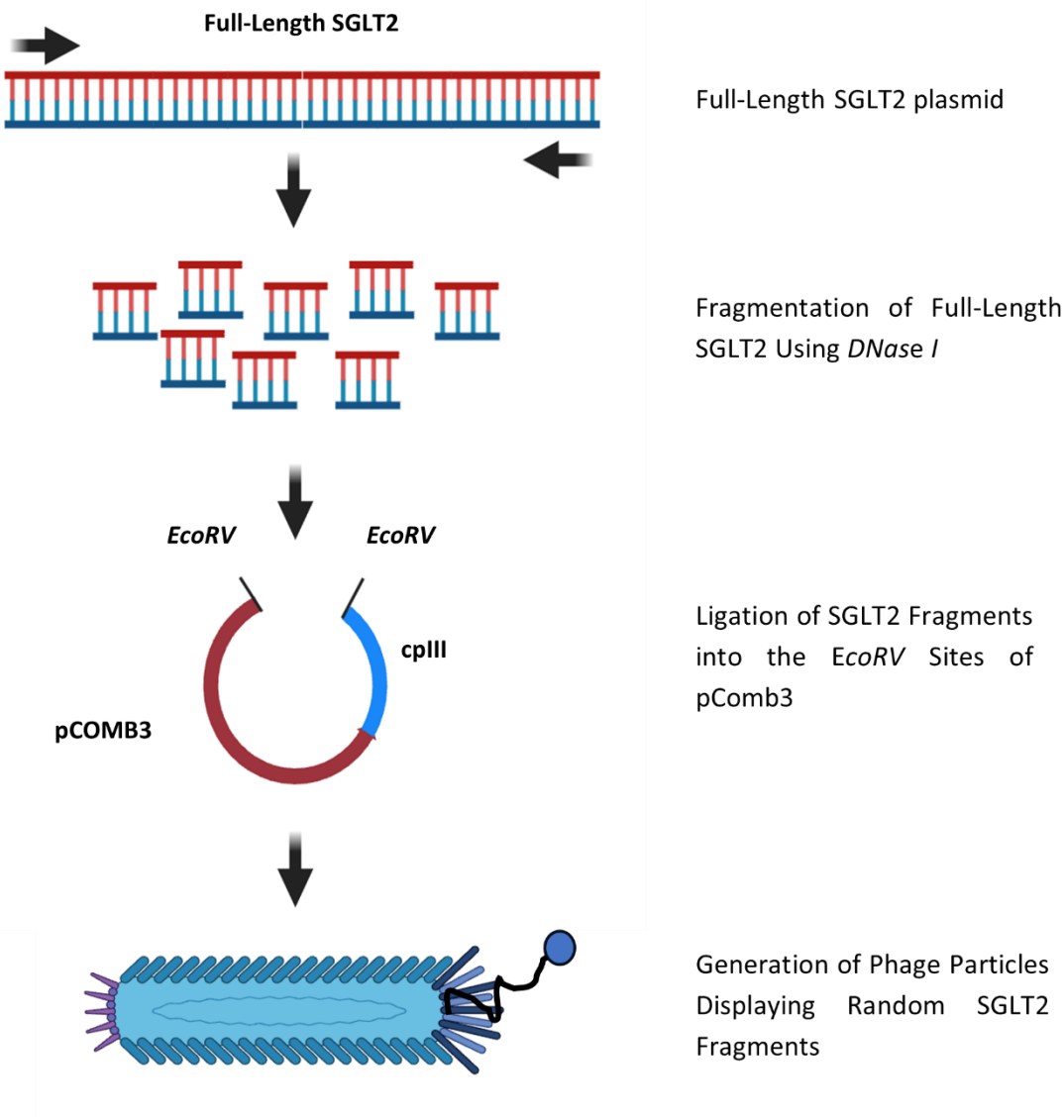

Figure 6.5: Schematic Representation of Phage Display Library Construction Using SGLT2 Fragments.

The figure shows the process of generating phage particles displaying random SGLT2 fragments. Full-length SGLT2 DNA was fragmented, ligated into the *EcoR*V sites of the pComb3 vector, and introduced into *E. coli* XL1-Blue cells. After electroporation, cells were superinfected with VCSM13 helper phage to produce phage particles displaying SGLT2 fragments for epitope mapping.

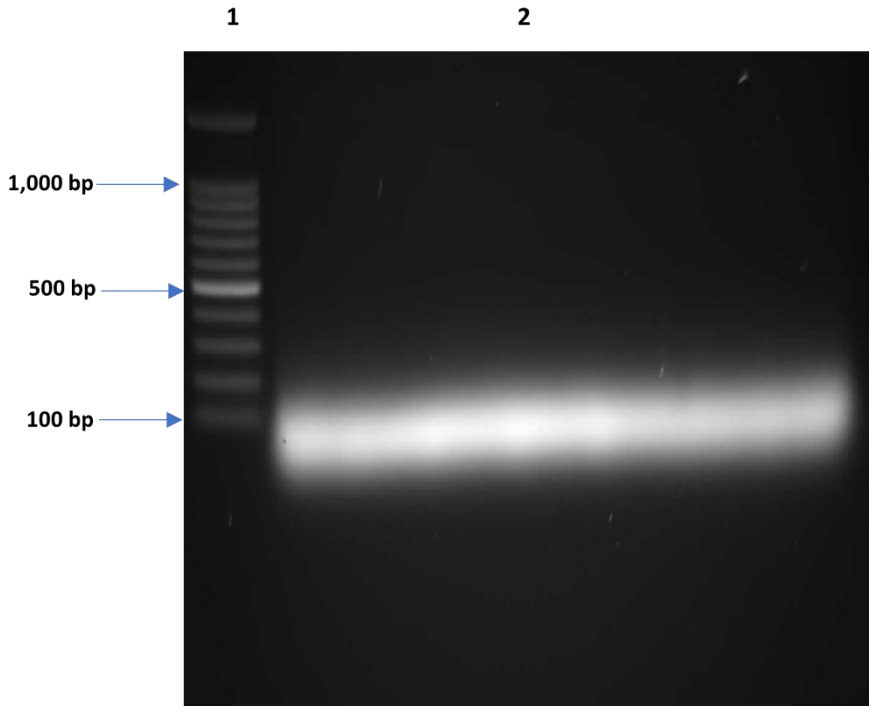

Figure 6.6: Agarose Gel Electrophoresis of Fragmented SGLT2 DNA.

This figure displays the agarose gel electrophoresis results used to assess the fragmentation of full-length SGLT2 DNA following digestion with *DNase*I. The smear observed on the gel represents a range of DNA fragment sizes, primarily between 100 and 200 base pairs, which were targeted for subsequent use in epitope mapping. The ladder on the left indicates the molecular weight markers, providing a reference for the approximate size of the DNA fragments.

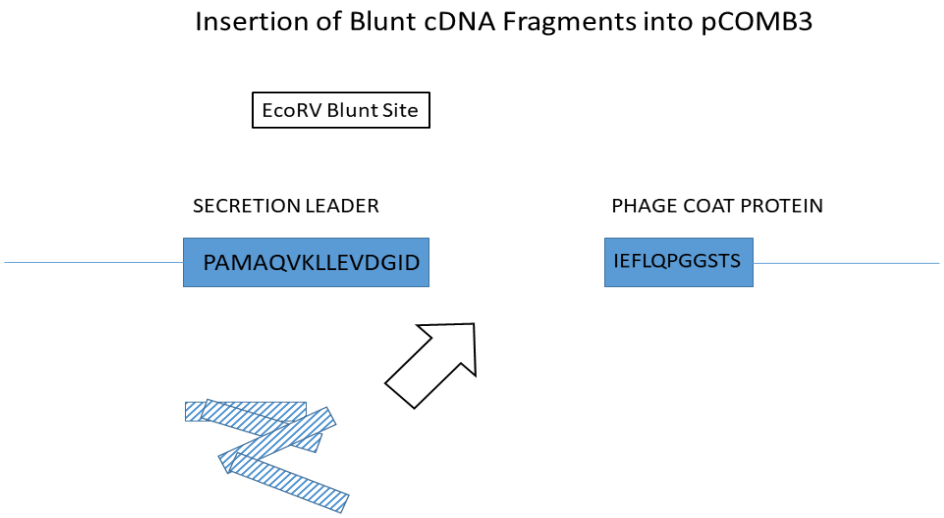

Figure 6.7: Construction of random cDNA fragment in pComb3.

Random cDNA fragments were ligated into the blunt *EcoR*V site of pComb3. For Inserts to be expressed on the phage surface, they must be in-frame with both the secretion leader and the coat protein coding sequence (overall probability of 1:18).

6.3.1.5 Preparation of pComb3 for Fab Library Construction

To generate a fragment library for epitope mapping, the pComb3 phagemid vector was carefully prepared to accommodate the fragmented SGLT2 DNA. The preparation began by digesting the pComb3 vector with the restriction enzyme *EcoRV*, which creates blunt-ended DNA fragments. The digestion reaction was performed by incubating 10 µl of 0.6 µg/µl of pComb3 vector with 3 µl *EcoRV* in a suitable reaction buffer (r3.1) under optimal conditions. The reaction was maintained at 37°C for 4 hours to ensure complete digestion of the vector.

Then, the vector was treated with 1 µl of alkaline phosphatase to remove the 5'-phosphate groups from the cut DNA ends and prevent the vector from self-ligating during the subsequent ligation process (Fig 6.8).

The digested and dephosphorylated vector was then subjected to gel electrophoresis, and the linearised pComb3 vector was purified using a gel extraction method. This purification step is essential to eliminate any residual enzymes and small DNA fragments that could interfere with the ligation process.

The purified, blunt-ended pComb3 vector was mixed with the fragmented SGLT2 DNA in a ligation reaction. T4 DNA ligase was employed to create a recombinant plasmid library. The ligation reaction was conducted overnight at 15°C.

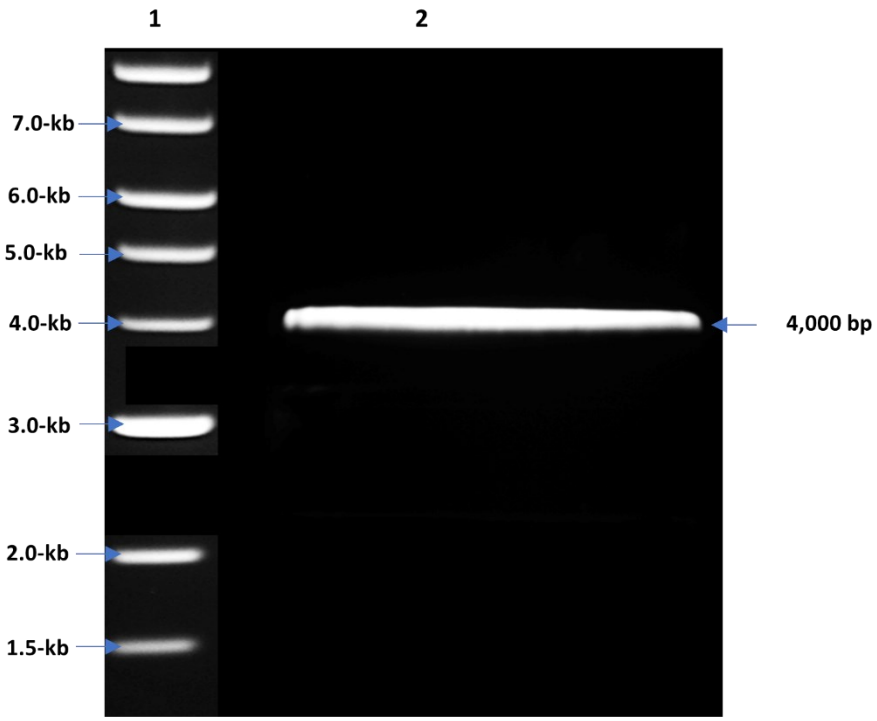

Figure 6.8: Preparation of pComb3 Vector for SGLT2 Fragment Library Construction via EcoRV Digestion.

The pComb3 phagemid vector (approximately 4000 bp) was digested with *EcoR*V to create blunt ends suitable for ligation with SGLT2 DNA fragments. The digested vector was treated with alkaline phosphatase to prevent self-ligation, and the resulting linearised vector was purified via gel electrophoresis. The image shows the electrophoretic analysis of the *EcoR*V-digested pComb3 vector, with a clear band at 4000 bp, indicating successful digestion and preparation for subsequent ligation with SGLT2 DNA fragments.

6.3.1.6 Transformation of SGLT Fragment Library and Phage Rescue

Following the ligation of the SGLT2 DNA fragments into the pComb3 vector, the recombinant plasmid was introduced into *E. coli* XL1-Blue cells via electroporation (2.2.2.2). The transformed cells were cultured on LB agar plates containing ampicillin to select for colonies that had successfully incorporated the plasmid.

The entire library of transformed colonies was subsequently amplified in an SB medium supplemented with 100 µg/ml ampicillin and 1% glucose to maintain the plasmid. To initiate phage rescue, the amplified bacterial culture containing the library was superinfected with VCSM13 helper phage and incubated overnight. This step facilitated the production of phage particles displaying the SGLT2 DNA fragments as fusion proteins on their surface. The phage particles were harvested from the culture supernatant via NaCl/PEG precipitation for subsequent use in panning and library screening. This process ensured the entire library, not individual selected colonies, was converted into phage format for downstream epitope mapping.

To confirm the success of the ligation and ensure the integrity of the constructed library, five bacterial colonies were randomly picked for mini-prep plasmid isolation. The isolated plasmids were then sequenced to verify the presence and correct orientation of the SGLT2 DNA fragments within the pComb3 vector. The sequencing results confirmed the successful generation of the SGLT2 fragment library, demonstrating that the SGLT2 DNA fragments were correctly inserted into the pComb3 vector, making the library suitable for subsequent epitope mapping studies.

6.3.1.7 Library Enrichment (Epitope Mapping)

To enrich the SGLT2 fragment library, biopanning was performed using ELISA wells coated with specific antigens. The phage library used in this process was a recombinant library derived from *E. coli* XL1-Blue cells transformed with the SGLT2 fragment-containing pComb3 vector. This library consisted of phage particles displaying the SGLT2 DNA fragments as fusion proteins, generated via VCSM13 helper phage rescue. The library represented the diversity of DNA fragments ligated into the pComb3 vector, allowing for the selection of phage displaying high-affinity binders to the target antigens.

One well was coated with purified Fab 19.2 at a concentration of 10 µg/ml in carbonate coating buffer. As a positive control, another well was coated with 10 µg/ml of anti-SGLT2/SLC5A2 Antibody Picoband (rabbit) (Boster, A03748). Both wells were incubated overnight at 4°C to ensure optimal antigen binding.

The next day, the wells were thoroughly washed five times with 1X TBST to remove unbound antigens, followed by blocking with 3% BSA in 1X TBST for 1 hour at room temperature to prevent non-specific binding. Subsequently, 100 µl of the fragment phage library, containing approximately 10^{11} pfu, was added to each well and incubated at room temperature for 1 hour. This allowed the phage displaying SGLT2 fragments with specific binding affinity to interact with the immobilised antigens.

After incubation, the wells were washed five times with 1X TBST to remove non-specifically bound phage during the first round of bio-panning. In subsequent rounds of bio-panning, the washing stringency was increased to ten washes to progressively enrich for phage particles displaying high-affinity binders. The enriched phage pools were recovered and amplified after each round for further selection and analysis.

To elute the adherent phage, 100 µl of glycine buffer (pH 2.7) was added to each well, and the plate was incubated for 10 min at room temperature. The elution buffer was carefully pipetted up and down to ensure complete recovery of the bound phage, which was then neutralised with 6 µl of 2 M Tris-HCl. The eluted phage was used to infect 1 ml of freshly prepared XL1-Blue host cells, which were then plated onto LB agar plates containing 100 µg/ml ampicillin and incubated overnight at 37°C.

The same procedure was followed in parallel for both the Fab 19.2 and the rabbit SGLT2-coated wells, allowing for the enrichment of phage. This process was repeated for three rounds, progressively enriching the phage library for high-affinity binders.

After each round, the resulting colonies were counted to quantify the number of phages selected from the library. The culture from each round was transferred to 10 ml SB medium supplemented with 100 µg/ml ampicillin and 1% glucose and incubated for 6 hours at 37°C until the OD_{600}nm was approximately 0.4. The culture was then transferred to 100 ml SB containing 100 µg/ml ampicillin, VCSM13 helper phage and 1 mM IPTG and incubated

overnight at 37°C with shaking. The culture was centrifuged, and the phage particles were precipitated using 40% PEG/5 M NaCl, then resuspended in 3% BSA in 1X TBST.

After the final round of bio-panning, enriched phage pools were amplified, and the phage particles were used to infect *E. coli* XL1-Blue cells. The infected cells were then plated onto LB agar plates containing 100 µg/ml ampicillin to select for bacterial colonies harboring the recombinant pComb3 plasmid encoding high-affinity SGLT2 binders.

From these plates, 10 individual bacterial colonies were randomly picked from both the SGLT2-Loops antigen selection and the rabbit SGLT2 antibody selection groups. These colonies represent individual clones, each potentially encoding a unique SGLT2 fragment identified during the enrichment process. The selected colonies were cultured overnight in an SB medium containing 100 µg/m ampicillin to amplify the plasmids for miniprep. Plasmid DNA was extracted from these cultures using a miniprep procedure (2.2.2.4). The extracted DNA was then sent to Azenta for sequencing to verify the presence and correct insertion of SGLT2 DNA fragments into the pComb3 vector.

6.3.1.8 Epitope Mapping Results

From the 10 random clones selected for sequencing, 3 contained in-frame fragments of SGLT2 cDNA. The sequences are shown in Appendix IV. The remaining clones contained random fragments of the digested plasmid with broken reading frames, inverted sequences, and/or sections of the cloning vector. Translation of the 3 productive clones showed peptide sequences that were all contained within a region of SGLT2 corresponding to the first large extracellular loop (Table 6.2).

Table 6.2: BLASTP Analysis of Reading Frames from Clones 4, 7, and 8.

All three reading frames were contained within a region of SGLT2 from positions 243-276, corresponding to the first large extracellular loop. Clone 4 terminates at position 267, Clone 7 terminates at position 270, and Clone 8 terminates at position 270.

Clone 4

```
Query  5    DPSVGNISSTCYQPRPDSYHLLRDP  29
            DPSVGNISSTCYQPRPDSYHLLRDP
SGLT2  243  DPSVGNISSTCYQPRPDSYHLLRDP  267
```

Clone 7

```
Query  1    NISSTCYQPRPDSYHLLRDPVTGDLPWPA  29
            NISSTCYQPRPDSYHLLRDPVTGDLPWPA
SGLT2  248  NISSTCYQPRPDSYHLLRDPVTGDLPWPA  276
```

Clone 8

```
Query  1    NISSTCYQPRPDSYHLLRDPVTG  23
            NISSTCYQPRPDSYHLLRDPVTG
SGLT2  248  NISSTCYQPRPDSYHLLRDPVTG  270
```

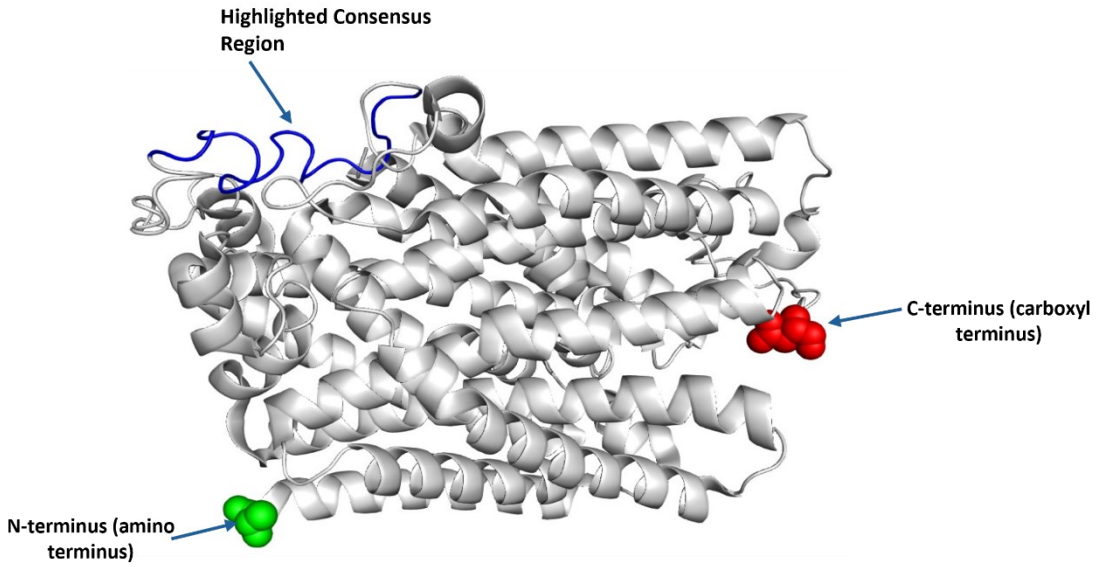

Figure 6.9: Structural Mapping of SGLT2 Epitopes.

The three-dimensional structure of SGLT2 was analysed using PyMOL to identify potential antibody-binding regions. The highlighted blue loops represent the consensus sequence identified in the study, which satisfies the criteria of being in frame with both the secretion leader and the phage coat protein (cpIII) and corresponds to a region of SGLT2 targeted during immunisation. The green sphere indicates the N-terminal (amino terminus), while the red region highlights the carboxt terminus of the protein. This visualisation provides insights into the structural context of the SGLT2-targeted antibody.

6.3.2 Western Blot Experiment

6.3.2.1 Preparation of Full-Length SGLT2 Insert and pcDNA3.1 Vector

The full-length SGLT2 DNA was excised from the pUC-full-Length-SGLT2 plasmid by digesting the plasmid with *Hind*III and *Nhe*I restriction enzymes. Similarly, the pcDNA3.1 vector, which serves as the backbone for high-level expression in mammalian systems, was also digested with *Hind*III and *Nhe*I to create compatible ends for ligation (2.2.2.5) (Figs. 6.9 and 6.10).

The digested SGLT2 insert and pcDNA3.1 vector were separated by electrophoresis on a 0.8% agarose gel (2.2.2.6). The appropriate DNA bands were carefully excised from the gel and purified using a DNA extraction kit, ensuring the recovery of high-purity DNA fragments (2.2.2.7).

6.3.2.2 Cloning of Full-Length SGLT2 insert into the pcDNA3.1 Plasmid

The SGLT2-Full-Length insert was successfully ligated into the pcDNA3.1 vector, using T4 DNA Ligase in 10X buffer, and allowed to proceed overnight at 15˚C. Then, the ligation product was transformed into JM109 *E. coli* via heat shock at 42°C for 40 seconds (2.2.2.1). Following overnight incubation at 37˚C, five colonies were picked from the ligation plate for mini preps analysis. The pcDNA3.1 SGLT2-full-length plasmid mini preps were conducted, and the recovered plasmids were digested with restriction enzymes *Hind*III and *Nhe*I to validate successful incorporation (Fig. 6.11). Sequencing was subsequently performed to confirm that the insert remained in the correct frame and orientation.

The validated pcDNA3.1-SGLT2 plasmid mini prep 3 was amplified in *E. coli*, followed by a maxi prep using a maxi-prep kit (Qiagen) to obtain sufficient DNA (2.2.2.4). The concentration of the purified plasmid DNA was measured using a Nanodrop.

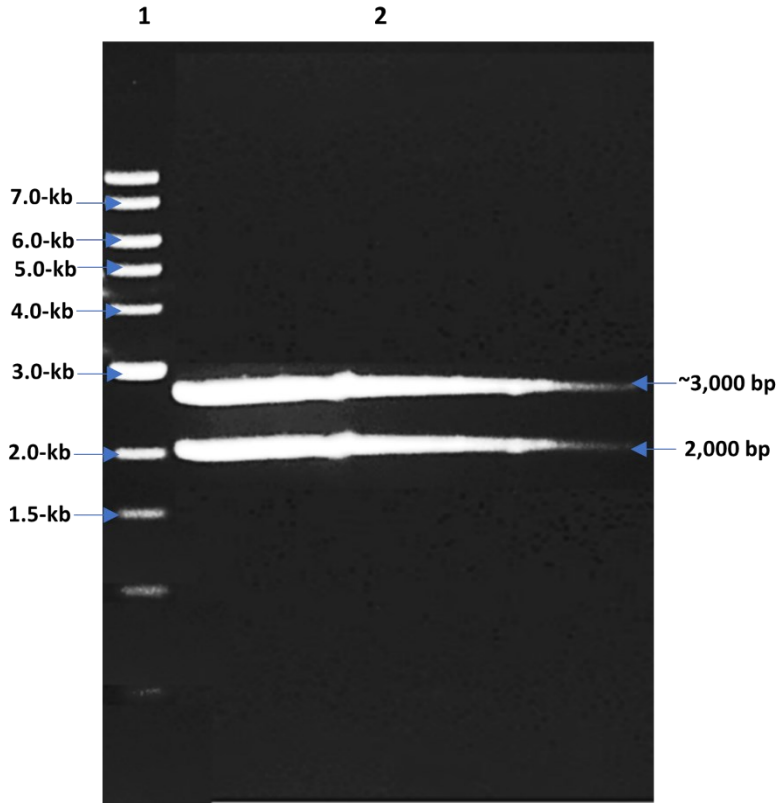

Figure 6.10: Restriction Digest of SGLT2 Full-Length from pUC-SGLT2 Plasmid.

The figure displays the results of a restriction digest of the pUC-SGLT2 full-length plasmid. The digestion with *Hind*III and *Nhe*I yielded two distinct bands: a 2,000-bp fragment corresponding to the full-length SGLT2 gene and a ~3,000-bp fragment representing the remaining pUC vector backbone. The separation of these fragments was confirmed by agarose gel electrophoresis.

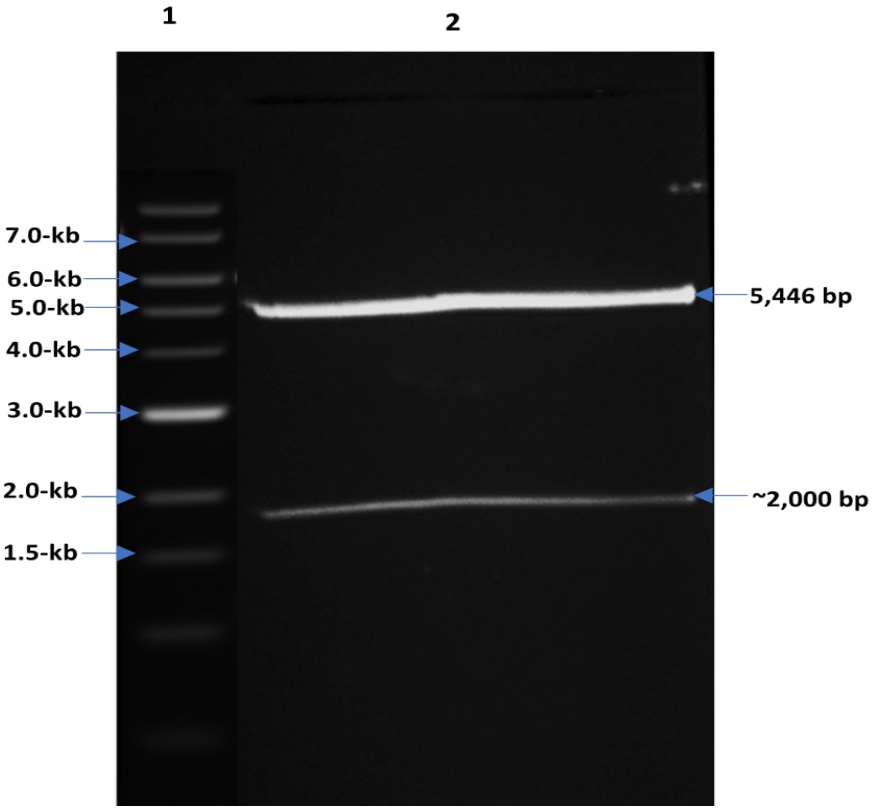

Figure 6.9: Restriction Digest of pcDNA3.1 Vector.

The figure shows the results of a restriction digest of the provided plasmid, which consisted of the pcDNA3.1 vector already containing a 2,000 bp insert. Digestion with *Hind*III and *Nhe*I resulted in two bands: a single band of approximately 5,446 bp, corresponding to the vector backbone, and a 2,000 bp band representing the insert. This indicates that the plasmid provided was pre-constructed and not an empty pcDNA3.1 vector.

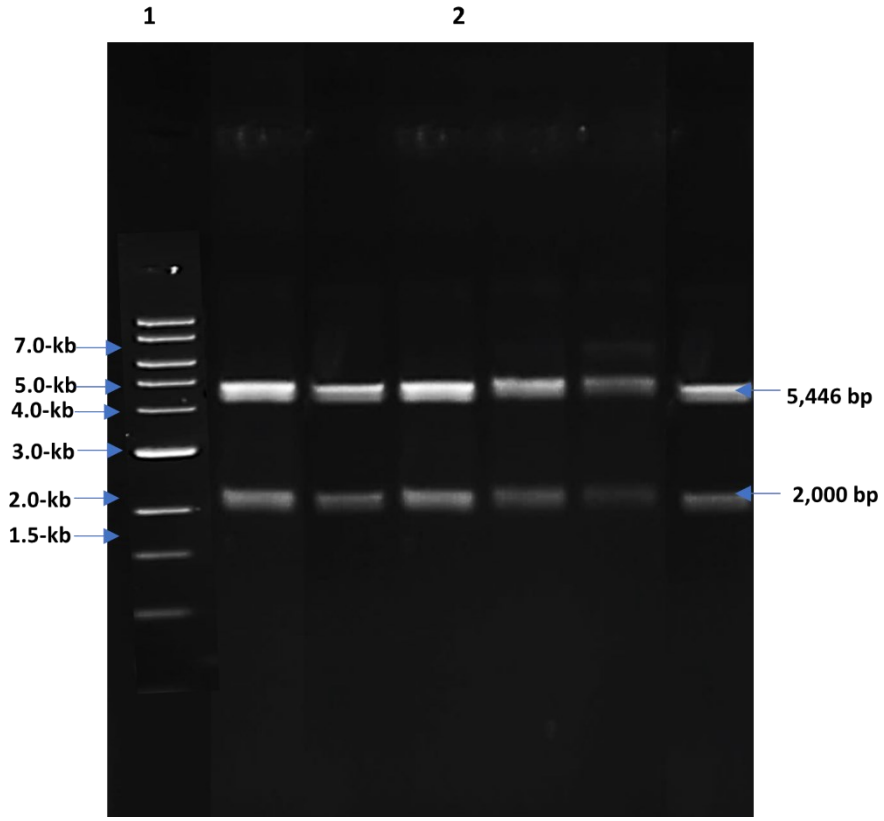

Figure 6.10: Screening of Minipreps From pcDNA3.1 SGLT2-Full-Length Ligation.

This figure displays the results of restriction enzyme digestion using *Hind*III and *Nhe*I to confirm the successful ligation of the full-length SGLT2 gene into the pcDNA3.1 vector. The digestion released two distinct bands: one corresponding to the pcDNA3.1 vector backbone (~5,446 bp) and the other to the SGLT2 insert (~2,000 bp).

6.3.2.3 Transient Transfection of Full-Length SGLT2 in CHO-K1 Cells

Transient transfection was performed in a 6-well plate format to express the full-length SGLT2 protein along with a GFP (green fluorescent protein) marker in CHO-K1 cells effectively (2.2.2.5). GFP was used as a transfection efficiency indicator, allowing visualisation and confirmation of successful transfection under a fluorescence microscope.

CHO-K1 cells were seeded in 6-well plates at a density of 1×10^6 cells/well in 2 ml of DMEM-F12 medium to achieve 50–60% confluence by the time of transfection. This ensured optimal conditions for transfection, as higher confluence can reduce transfection efficiency.

On the day of transfection, the growth medium was removed, and the cells were gently washed with 1X PBS. Fresh 2 ml of DMEM-F12 medium was added to each well to prepare the cells for transfection. Lipofectamine 2000 reagent was prepared by diluting 12 µl in 150 µl of Opti-MEM Medium. Concurrently, 14 µg of the pcDNA3.1-SGLT2 plasmid DNA and 14 µg of pMAX-eGFP plasmid DNA were each diluted in 700 µl of Opti-MEM Medium. For the transfection, 75 µl of the pcDNA3.1-SGLT2 DNA and 75 µl of the pMAX-eGFP DNA solutions were combined to make a total volume of 150 µl of DNA mix. This combined DNA mix was added to the 150 µl of diluted Lipofectamine 2000 reagent in a 1:1 ratio to form the DNA-lipid complexes. The DNA-lipid mixture was incubated at room temperature for 10 min. 250 µl of the DNA-lipid complex was added dropwise to one well-containing cells, resulting in a final concentration of 2500 ng of DNA and 12 µl of Lipofectamine 2000 Reagent per well. The cells were then incubated at 37°C for 48 hours to allow for the expression of the transfected genes. A negative control well (non-transfected cells) and a positive control well (cells transfected with pMAX-eGFP alone) were included to ensure the specificity and effectiveness of the transfection.

After 48 hours of incubation, transfection efficiency was assessed using a Zeiss Cell Discoverer 7 Automated Microscope. The microscope allowed for the visualisation of GFP expression in the cells, confirming successful transfection.

The results confirmed the successful transfection of CHO-K1 cells with the SGLT2 and GFP plasmids (Fig. 6.12). A strong GFP signal was observed in the transfected wells, indicating efficient transfection. The cells exhibited bright green fluorescence, demonstrating that the

GFP plasmid was effectively expressed within the cells, which means overall transfection efficiency.

In contrast, the control wells containing un-transfected cells displayed no GFP fluorescence, confirming the specificity of the transfection procedure. GFP fluorescence in the experimental wells verifies that the transfection method was effective and that the cells were successfully expressing the introduced SGLT2. These findings provide a solid foundation for further analysis with a western blot to confirm the expression of the SGLT2 protein in the transfected cells.

Post-visualisation, the transfected cells were lysed using RIPA buffer to prepare samples for the western blot analysis. This methodical approach ensured that the transfection was effective and that the experimental results were reliable.

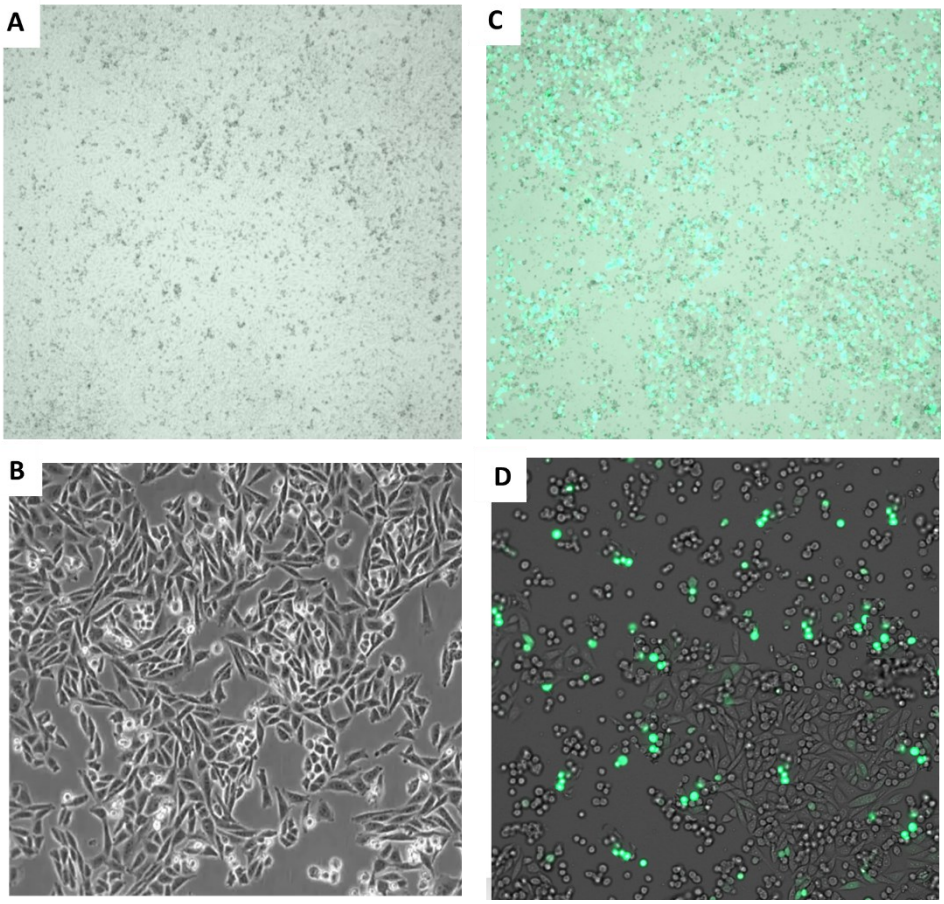

Figure 6.11: Transient Transfection of CHO-K1 Cells with Full-Length SGLT2 and GFP.

These images compare the morphology and GFP expression between untransfected CHO-K1 cells and CHO-K1 cells transiently transfected with full-length SGLT2 and GFP. The left column displays untransfected CHO-K1 cells under brightfield (A) and phase contrast microscopy (B), showing typical cell morphology with no GFP expression. The right column shows CHO-K1 cells transfected with pcDNA3.1-SGLT2 and pMAX-eGFP plasmids. Panel (C), captured under brightfield with fluorescence overlay, demonstrates successful transfection, as indicated by GFP-positive cells (green fluorescence) at a relatively low frequency. Panel (D), captured under phase contrast with fluorescence overlay, further confirms the presence of GFP-positive cells in the same field.

6.3.2.4 Analysis of SGLT2 by Western Blot

A western blot was employed to assess the specificity and binding efficiency of biotinylated Fab 19.2 in detecting SGLT2 expression across different sample types (2.2.4.11). Lysates from un-transfected CHO-K1 and CHO-K1 cells transiently transfected with full-length SGLT2, as well as mouse kidney tissue, were analysed alongside appropriate controls to validate the antibody's performance.

Electrophoresis was conducted on 2X 12% SDS-PAGE gels at 50 V for stacking gel and 100 V for resolving gel for 3 hours. Each gel lane was loaded with 50 µg of protein sample under reducing conditions. The lanes were assigned as follows: Lane 1 contained the molecular weight marker, Lane 2 held lysates from un-transfected CHO-K1 cells, Lane 3 contained lysates from CHO-K1 cells transfected with the SGLT2 construct, Lane 4 was loaded with mouse kidney tissue lysates, Lane 5 contained lysates from CHO-K1 cells transfected with SGLT2 but treated only with the secondary antibody as a control, and Lane 6 was loaded with mouse kidney tissue lysates treated only with the secondary antibody for control purposes.

After electrophoresis, the separated proteins were transferred onto a PVDF membrane using the Trans-Blot Turbo System, following the Turbo protocol for 7 min. At room temperature, the membranes were blocked with 3% BSA in 1X TBST for 1.5 hours. Then, membrane one was cut, and lanes 1-4 were incubated with Biotinylated Fab 19.2 overnight at 4°C. Similarly, membrane two was cut, and lanes 1-4 were incubated with rabbit anti-SGLT2/SLC5A2 Antibody Picoband (A03748, Elabscience) at 0.5 µg/ml concentration under the same conditions. The remaining sections of membranes 1 and 2, containing lanes 5 and 6, continued to be incubated in the blocking buffer at 4°C overnight.

All membrane sections were washed thrice with 1X TBST the following day, each lasting 5 min. Membrane one and its remaining section were probed with Streptavidin (peroxidase/HRP conjugated) (E-AB-1043, Elabscience). Meanwhile, membrane two and its remaining section were probed with goat anti-rabbit IgG-HRP secondary antibody at a dilution 1:10,000. The signal was detected using an Enhanced Chemiluminescent detection substrate (ECL Western Blotting Substrate, W1015, Promega).

No detectable signal was observed in the analysis of un-transfected CHO-K1 cells, which served as a negative control. In contrast, CHO-K1 cells transiently transfected with full-length

SGLT2 exhibited a distinct band corresponding to the expected molecular weight of 73 kDa, consistent with the SGLT2 protein. This result confirms the successful transfection and expression of the SGLT2 protein, underscoring the effectiveness of biotinylated Fab 19.2 in recognising SGLT2 within transfected cells (Figs. 6.13 and 6.14).

Further validation was provided by the mouse kidney tissue lysate analysis, which detected a strong band at the expected molecular weight of 73 kDa. This observation aligns with the known expression of SGLT2 in kidney tissue, demonstrating that Fab 19.2 can successfully bind to the endogenous SGLT2 protein in native tissue.

Control samples were included to ensure the specificity of the observed signals. No bands were detected in the transfected CHO-K1 cells where only the secondary antibody was used. This result confirms that the signal observed in the transfected lysate was due to the specific interaction between Fab 19.2 and the SGLT2 protein rather than the non-specific binding of the Streptavidin-HRP conjugate. Similarly, no signal was observed in the mouse kidney tissue control with secondary antibody only, further reinforcing the specificity of biotinylated Fab 19.2 for its target antigen.

The western blot results prove that biotinylated Fab 19.2 specifically and effectively binds to the SGLT2 protein in transfected CHO-K1 cells and mouse kidney tissue lysates. The absence of non-specific binding in the control samples further validates the specificity of this antibody. These findings support the use of Fab 19.2 in subsequent assays, confirming its utility in detecting SGLT2 in both overexpression systems and native tissues.

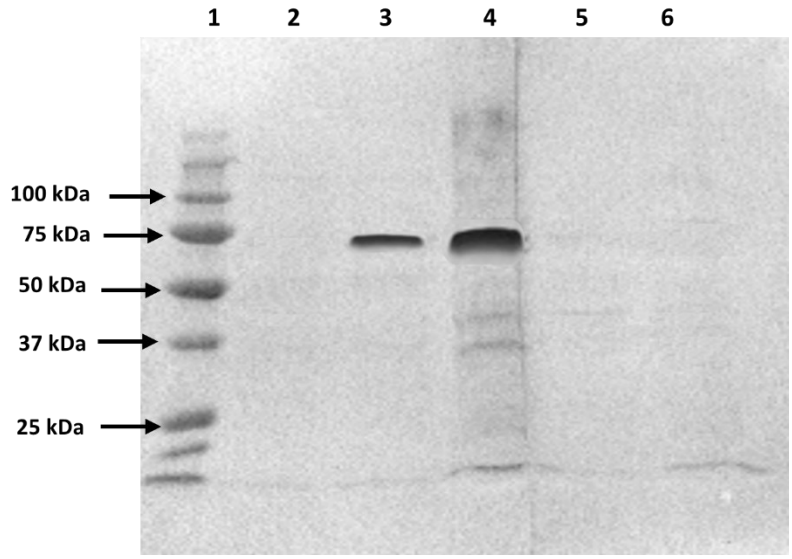

Figure 6.12: Western Blot Analysis of SGLT2 Expression in Transfected CHO-K1 Cells and Mouse Kidney Tissue.

Western blot analysis demonstrating the expression of SGLT2 across various samples. The lanes are Lane 1: Protein Precision All Blue marker for molecular weight reference. Lane 2: Un-transfected CHO-K1 cell lysates (negative control); Lane 3: CHO-K1 cells transfected with SGLT2 in pcDNA3.1 lysates, showing SGLT2 expression at 73 kDa; Lane 4: Mouse kidney tissue lysates, showing native SGLT2 expression at 73 kDa; Lane 5: CHO-K1 cells transfected lysates probed with the secondary antibody (Streptavidin-HRP), which controls non-specific binding; Lane 6: Mouse kidney tissue lysates probed with the secondary antibody only (Streptavidin-HRP), further controlling for non-specific binding. The antibodies used for detection in this experiment include biotinylated Fab 19.2.

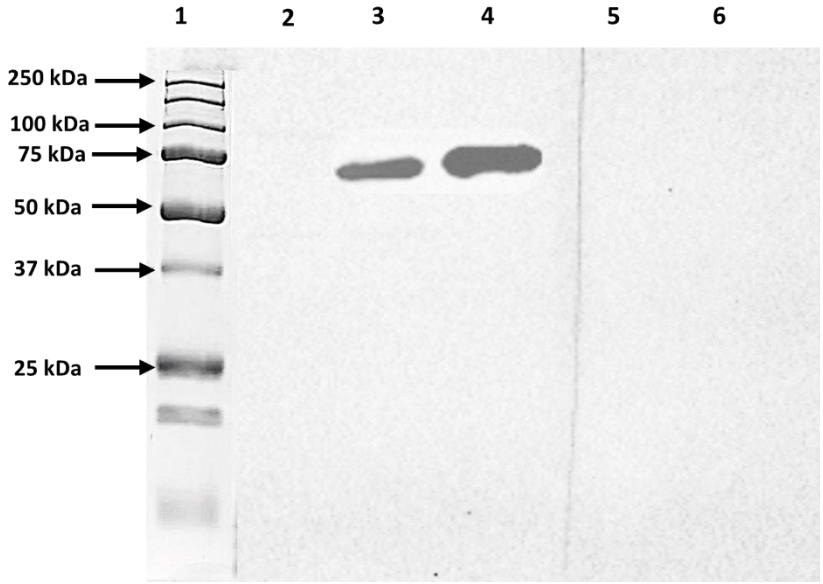

Figure 6.13: Western Blot Analysis of SGLT2 Detection Using Rabbit Anti-SGLT2/SLC5A2 Antibody in Transfected CHO-K1 Cells and Mouse Kidney Tissue.

This figure presents the results of a WB assessing the specificity and binding efficiency of rabbit anti-SGLT2/SLC5A2 antibodies in detecting SGLT2 expression across various sample types. Samples were separated on 12% SDS-PAGE gels under reducing conditions. The proteins were detected using a chemiluminescent substrate. The lanes in the blot are assigned as follows: Lane 1: Protein Precision All Blue marker for molecular weight reference; Lane 2: un-transfected CHO-K1 cell Lysates (negative control); Lane 3: CHO-K1 cells transiently transfected with full-length SGLT2 Lysates, showing a distinct band at 73 kDa, corresponding to the expected molecular weight of SGLT2; Lane 4: Mouse kidney tissue lysates, displaying a strong band at 73 kDa, consistent with endogenous SGLT2 expression; Lane 5: Lysates from CHO-K1 cells transfected with the SGLT2 construct but treated only with the secondary antibody, acting as a control for non-specific binding; Lane 6: Mouse kidney tissue lysates treated only with the secondary antibody, further controlling for non-specific binding. No signal was detected in un-transfected CHO-K1 cells, or the lanes treated only with the secondary antibody.

6.3.3 Immunohistochemistry Experiment

6.3.3.1 Analysis of SGLT2 Expression in Mouse Kidney Tissue

Following the successful detection of SGLT2 protein in transfected CHO-K1 cells and mouse kidney tissue lysates using western blotting, we attempted to validate the spatial distribution and expression of SGLT2 within intact tissue architecture. IHC could directly visualise SGLT2 expression within mouse kidney tissue sections, taking advantage of the specificity of biotinylated Fab 19.2. This technique enables the examination of SGLT2 localisation at the cellular level, providing insights into its physiological role within kidney tissue.

IHC was carried out using formalin-fixed, paraffin-embedded mouse kidney sections (2.2.10). The sections were initially dewaxed, rehydrated, and subjected to antigen retrieval to enhance antibody binding. Endogenous peroxidase activity and non-specific binding were blocked before the sections were incubated with biotinylated Fab 19.2, the primary antibody. The biotinylated Fab 19.2 facilitates precise detection of SGLT2 through the subsequent application of streptavidin conjugated to horseradish peroxidase (HRP), followed by chromogenic detection.

For blocking, the slides were incubated with Fab 19.2, and the negative control slides were treated with 10% streptavidin in 1 ml of 1% BSA in 1X PBS. The positive control slides were blocked using 10% goat serum in 1 ml of 1% BSA in 1X PBS. As the secondary reagent for the Fab and negative control sections, streptavidin conjugated to peroxidase (HRP) (Elabscience, E-AB-1043) was used to detect the biotinylated Fab 19.2.

Control sections were included to ensure the specificity of the staining. These controls consisted of sections incubated with only the secondary reagent to confirm that any observed staining was due to the specific interaction between Fab 19.2 and SGLT2. For the positive control, rabbit anti-SGLT2/SLC5A2 antibody (Picoband) was used as the primary antibody, followed by detection with Goat Anti-Rabbit IgG (H+L) (FITC) (Abcam, ab6717).

The IHC results determine the binding specificity of Fab 19.2 to SGLT2 in mouse kidney sections. The images show DAPI staining (blue) to label cell nuclei and Fab 19.2 staining (green) to localise SGLT2 expression.

6.3.3.2 The Immunohistochemistry Results

Fab 19.2 IHC Results

- **DAPI Nuclear Staining**

The nuclei in the tissue sections are stained with DAPI, offering a well-defined counterstain to highlight cellular architecture. The distinct nuclear blue staining allows for the precise identification of cell boundaries and provides a reference for localising SGLT2 expression within the tissue.

- **SGLT2 Staining with Fab 19.2**

The green fluorescence indicates specific binding of the biotinylated Fab 19.2 to SGLT2 within the renal tubular structures. Strong and localised fluorescence is observed along the brush border of the renal proximal tubules, where SGLT2 is highly expressed. The intensity and distribution of the staining suggest robust and specific detection of the SGLT2 protein by Fab 19.2.

- **Merged Image**

The merged image (DAPI + Fab 19.2) clearly shows that SGLT2 expression is localised to the proximal tubular regions, with the green staining corresponding to regions adjacent to the nuclei in the renal tubules. The strong overlap between the tubular structures and the SGLT2 signal supports the specificity of Fab 19.2 in detecting SGLT2 in situ.

Control Comparisons

Positive Control IHC Results

The positive control, employing rabbit anti-SGLT2/SLC5A2 antibody for SGLT2 detection, further validates the specificity of Fab 19.2. DAPI staining was used to label nuclei, while anti-SGLT2 was visualised through a Goat Anti-Rabbit IgG H&L (FITC) secondary antibody.

- **DAPI Nuclear Staining**

As observed with the Fab 19.2 staining, DAPI (blue) effectively presented the nuclear architecture, providing a consistent baseline for evaluating SGLT2 localisation.

- **SGLT2 Detection**

The green fluorescence generated by the primary anti-SGLT2 antibody demonstrated intense and specific binding along the renal proximal tubules, which aligns with SGLT2's expected localisation in kidney tissue. The high-intensity fluorescence and its apical confinement confirm the successful and specific binding of the anti-SGLT2 antibody.

- **Merged Image**

The merged image clearly illustrates that the green fluorescence corresponds to the proximal tubular regions, with co-localisation of nuclear and protein markers. The overlap between anti-SGLT2 staining and the tubules validates the antibody's specificity for SGLT2, reinforcing the expected expression pattern.

- **Control Validation**

These positive control results confirm the reliability of the IHC protocol and provide a reference for comparison with Fab 19.2 experimental results. The localised and specific expression of SGLT2 in the renal proximal tubules confirms the efficacy of the staining approach, further validating the use of Fab 19.2 in similar assays.

Negative Control IHC Results

The negative control experiments were conducted to ensure the absence of non-specific binding in the absence of the primary antibody. Only the secondary antibody (streptavidin-HRP) was applied to the mouse kidney tissue in these sections.

- **DAPI Nuclear Staining**

The DAPI staining (blue) remained visible throughout the tissue sections, providing consistent and reliable nuclear staining across all samples. This reference allowed for a clear comparison with experimental and positive control sections.

- **Absence of Non-Specific Green Fluorescence**

No detectable fluorescence was observed in the green fluorescence channel (associated with the secondary antibody). The absence of a green signal confirms that the secondary antibody alone does not produce non-specific background staining. This further supports the specificity of Fab 19.2 and anti-SGLT2 staining in the experimental and positive control sections.

- **Merged Image**

The merged image (DAPI + green fluorescence) showed only the blue nuclear staining, with no evidence of green fluorescence. This finding confirms that the green fluorescence in the experimental and positive control sections was due to specific interactions between the antibodies and SGLT2 rather than non-specific binding of the secondary antibody or other reagents.

The IHC results successfully demonstrate the specific binding of Fab 19.2 to SGLT2 in mouse kidney tissue, particularly within the proximal tubules where SGLT2 is predominantly expressed. The positive control, using rabbit anti-SGLT2/SLC5A2 antibody, further validated the IHC protocol and provided an apparent reference for SGLT2 localisation. The absence of non-specific staining in the negative control confirms the specificity of the experimental and control antibodies. Overall, these findings support Fab 19.2 as a reliable and specific tool for detecting SGLT2 in its native tissue context, with potential applications in diagnostic and therapeutic studies targeting renal SGLT2.

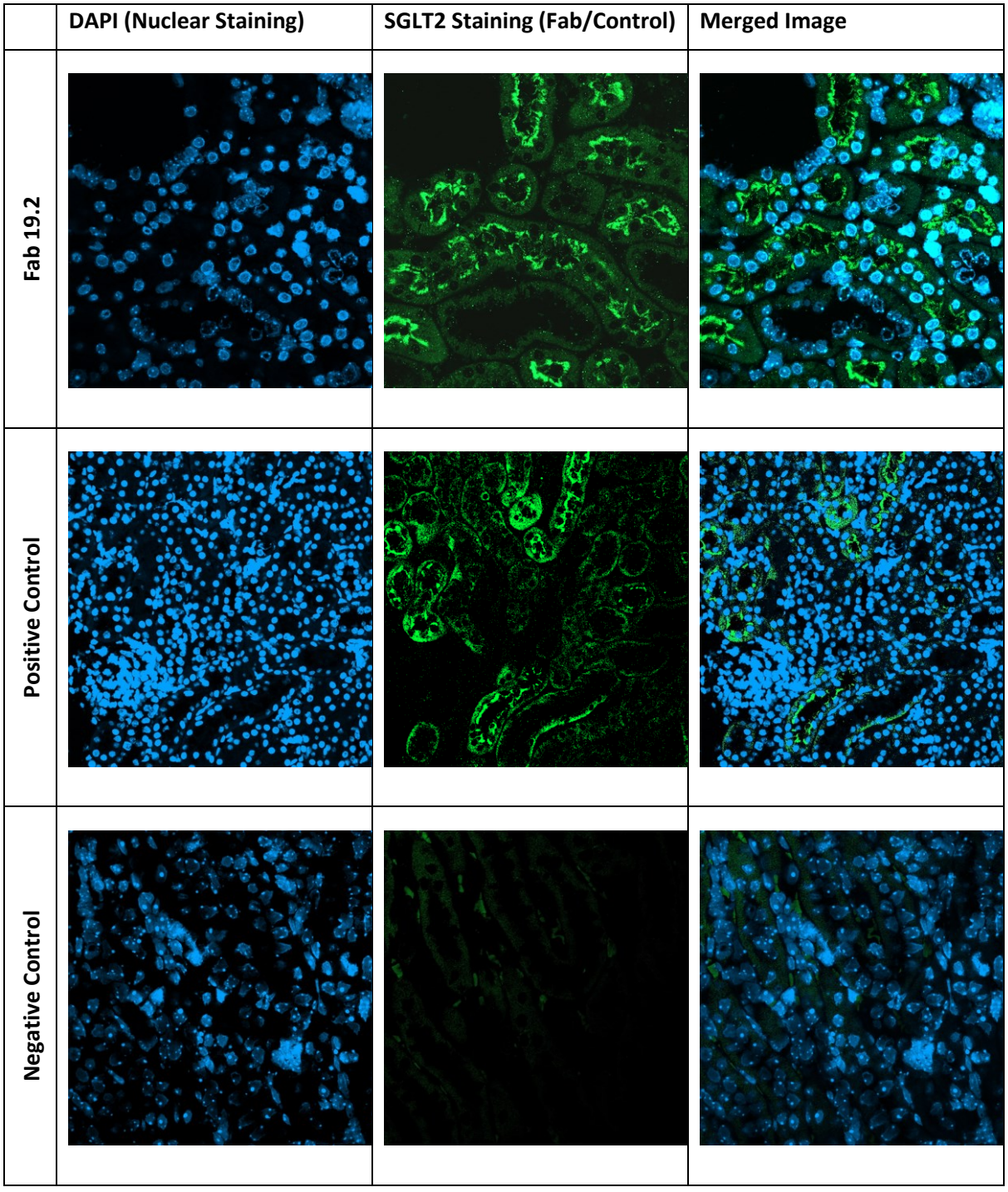

Figure 6.14: Comparative Immunohistochemistry Analysis of Fab 19.2 and Controls for SGLT2 Detection in Mouse Kidney Tissue.

These images represent the IHC results for SGLT2 detection in mouse kidney tissue, with each experiment repeated three times to ensure reproducibility and reliability. Top Row) Fab 19.2 staining showing DAPI nuclear staining, SGLT2 detection with Fab 19.2, and the merged image. Middle Row) Positive control with anti-SGLT2/SLC5A2 antibody showing DAPI, SGLT2 detection, and merged image. Bottom Row) Negative control with only the secondary antibody shows non-specific binding absence.

6.4 Discussion

This chapter detailed the characterisation process of Fab 19.2, a monoclonal antibody fragment targeting the SGLT2-Loops domain, through different advanced technologies such as epitope mapping, western blotting, and Immunohistochemistry. Several methods, such as biotinylation of Fab, competitive ELISA, and phage display, were explored to identify the specific epitopes on the SGLT2 protein recognised by Fab 19.2.

The biotinylation of Fab 19.2 was a crucial step in enabling its use in various assays, such as western blotting and immunohistochemistry. The process was optimised to ensure that biotinylation did not interfere with the antibody's ability to bind SGLT2, confirmed by the competitive ELISA results. However, the partial competition observed in the competitive ELISA suggests that the concentration of the unbiotinylated Fab in the supernatant may have been too low to fully inhibit the biotinylated Fab's binding. The partial inhibition observed in the competitive ELISA suggests that while biotinylated Fab 19.2 can compete effectively, the concentration of unbiotinylated Fab in the supernatant may have been insufficient to fully compete with its biotinylated counterpart. This observation is consistent with the known relationship between antibody concentration and competitive binding in ELISA assays (Meyer, 2010, Fack et al., 1997).

Determining the optimal concentration of biotinylated Fab 19.2 through a dilution series provided valuable insights into the antibody's binding efficiency. The results indicated that even at high dilutions (up to 1:20,000), Fab 19.2 maintained detectable binding activity with reduced signal intensity.

The biopanning and enrichment of the random cDNA fragment library against Fab 19.2 demonstrated the effectiveness of the phage display technique in isolating high-affinity binders. The sequencing of phage from the final round confirmed the presence of SGLT2 fragments, indicating successful enrichment of potential epitopes. The epitope mapping experiments were partially successful and suggested that the target epitope of Fab 19.2 was found within the first large extracellular loop of mouse SGLT2. Out of 10 random clones sequenced, 3 possessed in-frame inserts and corresponded to this region of the SGLT2 sequence. The results indicated that the phage selection experiment had not utilised sufficient rounds of enrichment in order to confidently determine a consensus sequence

derived from a larger number of samples. Nevertheless, the results are suggestive and future work could extend this study.

The western blot analysis demonstrated that Fab 19.2 could detect SGLT2 in both overexpressed and native protein contexts. The distinct band at approximately 73 kDa, corresponding to the molecular weight of SGLT2, was consistently observed in CHO-K1 cells transfected with the SGLT2 construct and mouse kidney tissue. These findings confirm the ability of Fab 19.2 to bind specifically to SGLT2, supporting its potential utility as a tool for SGLT2 detection in future studies.

The IHC results further confirmed the specificity of Fab 19.2 in detecting SGLT2 within mouse kidney tissue. The strong and localised green fluorescence observed along the brush border of the renal proximal tubules, where SGLT2 is highly expressed, aligns with the expected localisation of this protein. The absence of non-specific staining in the negative control sections and the consistency with the positive control using the anti-SGLT2/SLC5A2 antibody further validated the specificity of Fab 19.2 for its target antigen. These findings suggest that Fab 19.2 can be reliably used in future diagnostic or therapeutic applications targeting SGLT2.

Chapter 7: General Discussion and Future Work

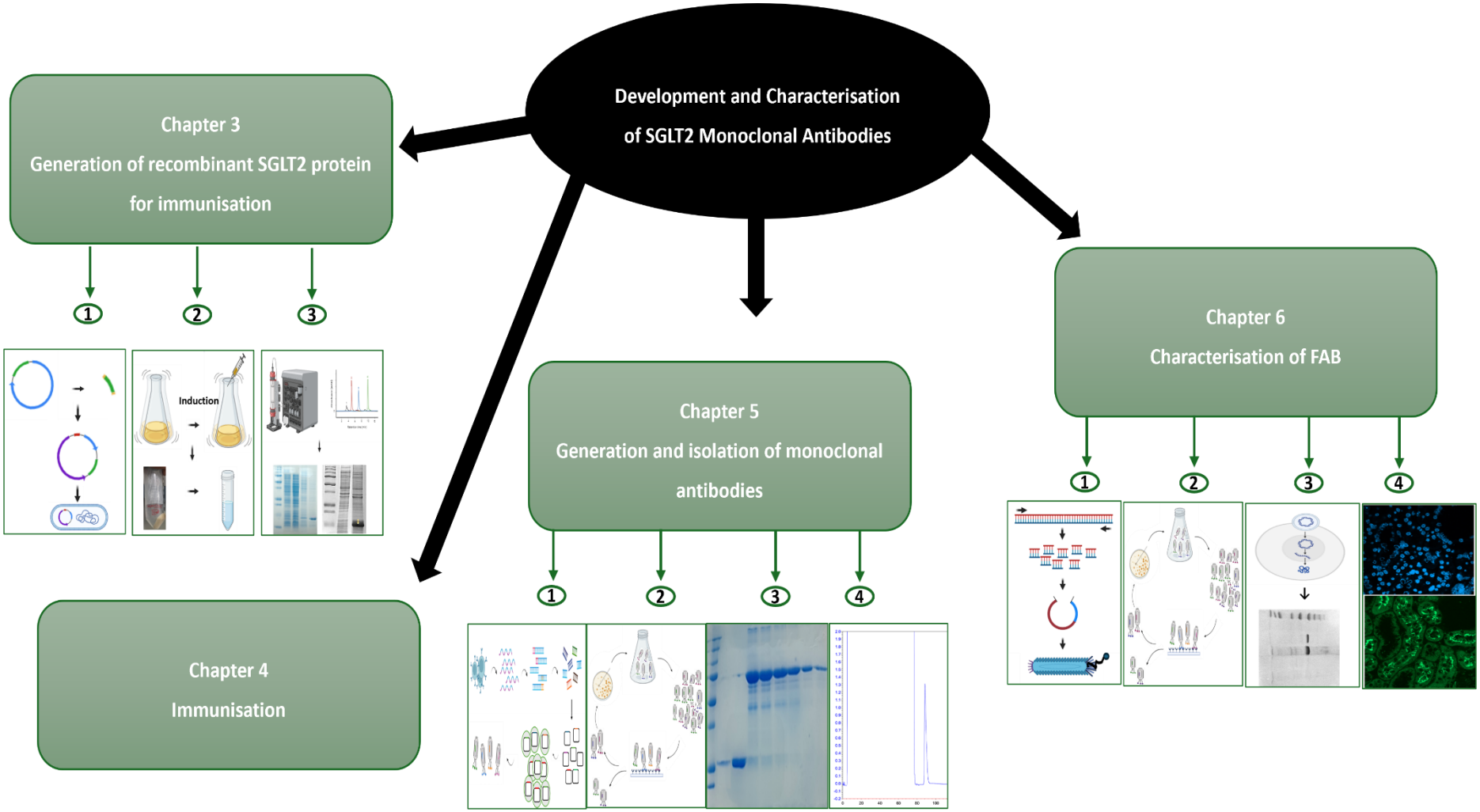

Figure 7.1: Schematic Overview of the Methodological Approach for the Generation and Characterisation of a Monoclonal Antibody Targeting SGLT2 in this Study.

7.1 The Burden of Chronic Kidney Disease

Chronic kidney disease represents one of the most significant public health challenges. Its multifactorial aetiology includes genetic, environmental, pharmacological, autoimmune, and dietary determinants. Despite these diverse origins, the hallmark pathology of CKD feature is the chronic scarring of renal structures, which progressively impairs kidney function and often leads to end-stage renal disease. This condition requires either dialysis or kidney transplantation to sustain life (Levey et al., 2005). The burden of CKD on healthcare systems is enormous, particularly in developed countries. In the United States alone, CKD affects approximately 35.5 million people (CDC, 2023), while in the UK, in 2009, CKD-related healthcare costs were estimated at £1.45 billion annually (Kerr et al., 2012). These alarming statistics underscore the urgent need for novel therapies that can effectively target the underlying mechanisms of renal fibrosis.

Therapeutic strategies for CKD have focused mainly on slowing disease progression rather than reversing fibrosis. They aim primarily to slow the disease progression and manage its complications rather than completely reversing fibrosis, considered an advanced and largely irreversible stage of CKD (Hewitson, 2009). The available treatments, such as blood pressure control, blood glucose management (in diabetic patients), and use of renin-angiotensin-aldosterone system inhibitors, are designed to reduce proteinuria, lower blood pressure, control blood sugar levels, and slow the decline in kidney function over time (Campanholle et al., 2013). Although these interventions can delay the progression of CKD, reversing fibrosis—the excessive deposition of extracellular matrix components such as collagen in the kidneys, which leads to structural changes and scarring—remains a significant challenge. Once fibrosis has developed, it is generally considered irreversible with current treatments. Research is ongoing to develop anti-fibrotic therapies that could potentially target and reverse fibrosis, but such treatments are not yet widely available.

One of the more recent advancements in CKD treatment is the development of anti-SGLT2 antibodies, which have demonstrated some success in slowing the advances of CKD, particularly in diabetic patients (Heerspink et al., 2016). However, these agents are primarily protective, delaying CKD progression without reversing fibrosis or addressing the underlying pathological processes.

To address these limitations, my research focuses on developing a novel anti-SGLT2 monoclonal antibody conjugated with specific anti-fibrotic agents, such as TG2 inhibitors. This innovative approach is designed to precisely target key drivers of fibrosis in CKD. Unlike existing therapies, which are not curative, this strategy aims not only to delay disease progression but also to mitigate fibrosis and potentially restore renal function. By focusing on both renal protection and anti-fibrotic activity, this work offers a therapeutic strategy that goes beyond the current paradigm.

Developing novel therapies that directly target fibrogenic pathways in the kidney may transform the clinical management of CKD (Duffield, 2014). This project explores the potential of targeting SGLT2 with monoclonal antibodies to reduce renal fibrosis and preserve renal function. By leveraging the high expression of SGLT2 in renal proximal tubules (Ghezzi and Wright, 2012), it aimed to develop a therapeutic strategy that localises treatment to the kidney, thereby minimising systemic side effects while addressing the critical need for effective anti-fibrotic interventions.

7.2 Mechanisms of Fibrosis in CKD: Insights from Experimental Models

The pathological basis of renal fibrosis involves an imbalance in the deposition and degradation of the extracellular matrix. This imbalance results in the progressive accumulation of ECM components, such as collagen, within the structural framework of the kidney, ultimately disrupting nephron function and accelerating tissue scarring (Farris and Colvin, 2012). While these processes have been extensively studied, particularly in experimental models, the complexity of the fibrotic pathways continues to pose challenges for therapeutic targeting.

Researchers have developed several experimental models to simulate the fibrotic mechanisms underlying CKD. Among these, scientists frequently use the subtotal nephrectomy rat model to mimic the progressive scarring observed in humans with CKD. By surgically removing 5/6ths of renal mass, researchers induce histological and physiological features similar to those seen in CKD patients, providing a valuable tool for studying disease progression and evaluating potential therapies (Johnson et al., 2007). Studies of fibrosis-associated proteins, such as TG2 and collagen, have demonstrated the model's utility by identifying these proteins as crucial mediators of ECM deposition (Johnson et al., 2007).

While the subtotal nephrectomy model is primarily utilised in rats, mouse models are also widely used for CKD research, particularly for studying fibrosis and testing therapeutic agents, such as monoclonal antibodies. Models like the unilateral ureteral obstruction (UUO) mouse model or adenine-induced nephropathy offer well-established systems for evaluating fibrosis progression and therapeutic interventions. These mouse models align with my research, as they allow for testing of the anti-SGLT2 monoclonal antibody developed in this study, providing an avenue for translational relevance. However, despite the insights gained from both rat and mouse models, translating these findings into clinical treatments remains a significant challenge (Kramann and Menzel, 2021, Jia et al., 2013).

This project focused on the therapeutic potential of targeting SGLT2 with Fab constructs. By localising therapy to the kidney, it was hypothesised that SGLT2-targeted antibodies could deliver anti-fibrotic agents directly to fibrotic tissues, reducing scarring and preserving renal function. This approach was designed to overcome the limitations of systemic treatments, which often produce off-target effects and are less effective in halting fibrosis.

7.3 Project Justification

Given the critical role of SGLT2 in kidney function and its therapeutic significance, the high expression of SGLT2 in the kidney could make it a prominent target for drug delivery, especially for diseases affecting kidney function, such as renal fibrosis. Targeting SGLT2 allows for localised therapeutic intervention in the kidney, minimising the impact on other organs and reducing systemic side effects. This is particularly important in chronic kidney disease, where off-target effects from systemic treatments pose significant challenges. By focusing drug delivery on the fibrotic tissue within the kidneys, SGLT2-targeted therapies hold promise to alleviate kidney scarring while preserving the function of unaffected tissues, providing a more precise and safer therapeutic approach. This makes SGLT2 an attractive candidate for drug conjugation aimed at treating renal fibrosis while avoiding broader systemic effects.

While pharmacological SGLT2 inhibitors have demonstrated success in treating diabetic kidney disease, monoclonal antibodies may offer an alternative or complementary therapeutic approach with potential advantages, including higher specificity, longer half-life, and the ability to be conjugated to other therapeutic agents. Monoclonal antibodies targeting

SGLT2 could be designed to localise to the kidney selectively and, when conjugated with anti-fibrotic drugs, could help reduce scarring while minimising off-target effects.

Thus, this project was conceived to develop and characterise SGLT2-specific monoclonal antibodies, focusing exclusively on Fab fragments. The ultimate goal was to generate a Fab construct that could be used for diagnostic purposes (to detect SGLT2 expression) and therapeutic applications (in conjunction with anti-fibrotic agents). A Fab construct was chosen instead of a full monoclonal antibody due to its smaller size, which allows better tissue penetration and reduces potential Fc-mediated off-target effects. This makes it particularly suitable for targeted therapy and diagnostic applications in the kidney, where precision and reduced immunogenicity are critical.

7.4 Generation of Recombinant SGLT2 Protein

Generating recombinant proteins is foundational in producing monoclonal antibodies, as they act as antigens during immunisation. In this study, we generated recombinant SGLT2 protein using *E. coli* as the expression system. This choice is due to the well-documented efficiency and cost-effectiveness of *E. coli* for producing recombinant proteins (Rosano and Ceccarelli, 2014).

In contrast, other researchers have relied on eukaryotic expression systems such as *Pichia pastoris* to produce recombinant proteins that require more complex post-translational modifications. For instance, Leonard (2015) successfully expressed SGLT2 in *Pichia pastoris*, leveraging glycosylation to enhance protein folding and functionality. This modification is vital for maintaining structural integrity and biological activity, especially in membrane proteins like SGLT2. However, while *Pichia pastoris* can yield high-quality proteins, it tends to be more expensive and time-consuming than bacterial systems like *E. coli*. These increased demands may limit its usefulness for large-scale antibody production, particularly in situations requiring rapid, cost-effective expression.

In our study, while *E. coli* was effective in producing sufficient quantities of recombinant SGLT2 for immunisation; the absence of glycosylation and other post-translational modifications likely affected the native structure of the protein. This may have contributed to the inconsistent results observed during epitope mapping. The SGLT2-targeted antibody developed in this study likely recognizes conformational epitopes that depend on the native

three-dimensional structure of the protein (Amit et al., 1986). The use of prokaryotic expression systems to produce SGLT2 may have resulted in non-native folding and a lack of post-translational modifications, such as glycosylation, which are critical for maintaining the protein's native conformation. Future studies may benefit from employing eukaryotic expression systems to produce glycosylated SGLT2, providing a more accurate representation of the native protein and enhancing the precision of epitope mapping experiments.

To address the structural context of antibody binding, the observed consensus sequence was analysed and mapped onto the SGLT2 structure using PyMOL. This sequence satisfied the criteria of being in frame with both the secretion leader and the phage coat protein (cpIII) and corresponded to a region of SGLT2 targeted during immunisation. Highlighting this consensus sequence on the SGLT2 structure provides insight into the likely binding region of the antibody and offers a basis for understanding its specificity. This analysis represents a preliminary effort to map the epitopes recognised by the antibody, with future work needed to explore this in greater detail using a glycosylated SGLT2 model for confirmation.

7.5 Breaking Tolerance and Immunisation Strategy

At the outset of the project, one important goal was to isolate antibodies that could be used in mouse models of renal scarring. Generating antibodies in other species would have been a simpler task, as tolerance would not have been an issue. However, using non-autologous antibodies over a long-term experiment would pose problems with immune responses against the antibody itself as a non-self protein. Immune tolerance mechanisms protect the body from mounting an immune response against its own proteins, making it challenging to generate high-affinity antibodies against self-antigens. In this study, we both immunised mice with recombinant protein and overcame immune tolerance. The basis for this strategy is that the resultant monoclonal should be helpful for tissue targeting in mouse models of renal scarring. Even though mouse, rat, and human SGLT2 exhibit a degree of structural conservation, immunisation of mice with SGLT2 from a different species would result in a high probability of obtaining antibodies selected for the most divergent epitopes and thus unlikely to react with mouse SGLT2.

Recent studies have shown that using fusion proteins can overcome immune tolerance in the mouse and produce a range of self-reactive antibodies (Percival-Alwyn et al., 2015). The

fusion partners are selected from highly immunogenic polypeptides such as tetanus toxin or diphtheria toxin, which stimulate a robust immune response in immunised mice. Here, we used a region of diphtheria toxin containing several immunogenic T cell epitopes, which was fused to the carboxy terminus of mSGLT2. These T-cell epitopes play a crucial role in augmenting the humoral response by activating helper T cells, which in turn provide essential signals (such as cytokine secretion and co-stimulation) to B cells. This interaction promotes B-cell activation, proliferation, and differentiation into antibody-secreting plasma cells, thereby enhancing the production of high-affinity antibodies against SGLT2.

The coding sequence was synthesised commercially and designed to include a C-terminal 6-histidine tag. Although the pET21a expression vector includes a built-in His-tag feature, the additional His-tag was incorporated into the coding sequence to ensure consistent placement, enhance protein recovery, and retain flexibility for downstream applications. This design choice also ensured compatibility with the experimental setup and expression requirements.

This approach has been successfully used in other studies to break tolerance and generate high-affinity antibodies against self-antigens. For instance, Percival-Alwyn et al. (2015) demonstrated that Diphtheria toxin conjugates could effectively break tolerance against self-antigens, leading to robust immune responses and the production of high-affinity antibodies.

In immunology, adjuvants play a crucial role in enhancing self-antigen immunogenicity. Carter and Reed (2010) highlight that adjuvant, such as Freund's complete adjuvant, can significantly boost the immune response by promoting antigen presentation and activating various immune pathways. However, using Freund's complete adjuvant and similar adjuvants can sometimes lead to non-specific immune responses, complicating the interpretation of results and potentially causing unwanted side effects.

In comparison, our strategy of using Diphtheria toxin conjugates with SGLT2 allowed us to elicit a more robust and targeted immune response, successfully isolating SGLT2-specific monoclonal antibodies. By utilising DTA, we could stimulate the immune system effectively without the pitfalls associated with broader-spectrum adjuvants like Freund's complete adjuvant.

7.6 Phage Display and Antibody Isolation

Phage display is a widely used technique for isolating high-affinity monoclonal antibodies from immunised animals. Conventional monoclonal antibody isolation depends upon the serial dilution of fused splenocytes. This can be problematic if the frequency of the desired antibody-producing cells is low. The number of recovered mAbs may be limited, which could hinder the availability of suitable candidates; there is a risk that the recovered mAbs will be dominated by those targeting the DTA fusion partner rather than the desired target, SGLT2. Screening for autoreactive mAbs, which react against the body's own tissues, may require a large-scale operation, complicating the process further.

In this study, we employed phage display to isolate Fab fragments specific to SGLT2 following the immunisation of mice. The Fab fragment Fab 19.2 was initially selected based on its strong binding affinity to SGLT2 observed during the phage display panning and screening process. This preliminary selection was further validated by its high specificity for SGLT2, as demonstrated by subsequent western blotting and immunohistochemistry experiments. Phage display provided several advantages, including the ability to screen large antibody libraries and rapidly identify antigen-specific clones (Barbas 3rd et al., 1991).

To address these challenges, we adopted the recombinant antibody approach using phage display recovery. This method allows us to recover the entire repertoire of antibodies generated from the immunised mice and preserve them in a library format, providing access to a broader range of potential antibodies.

Comparatively, other researchers have used hybridoma technology for monoclonal antibody isolation, which, while effective, is more labour-intensive and time-consuming. Hybridoma technology involves fusing B cells from immunised animals with myeloma cells to produce hybrid cell lines that continuously secrete antibodies. While this method has been the gold standard for monoclonal antibody production (Köhler and Milstein, 1975), compared to phage display, it is less amenable to high-throughput screening. The phage display technique allows for the rapid selection of antigen-specific clones and the generation of antibody libraries with diverse affinities and specificities (Smith, 1985).

However, it is essential to consider the limitations of phage display in the context of Fab fragment selection. While Fab fragments are smaller and have better tissue penetration, they

lack the Fc region, contributing to antibody stability and effector functions such as antibody-dependent cellular cytotoxicity (Frenzel et al., 2013). Future studies may explore generating full-length monoclonal antibodies instead of Fab fragments to enhance therapeutic efficacy. Given that the sequences of the variable regions of Fab 19.2 are now known, a full-length monoclonal antibody could be constructed using recombinant DNA techniques. This would involve cloning the variable regions into expression vectors containing constant regions for the heavy and light chains, followed by co-expression in a eukaryotic system to ensure proper folding and post-translational modifications. Such an approach could combine the specificity of the variable regions with the effector functions of the Fc region, potentially improving therapeutic applications.

By utilising phage display recovery, we effectively overcame the limitations of conventional monoclonal antibody generation, enhancing our ability to generate antibodies targeting SGLT2. This innovative strategy streamlines the discovery process and maximises our potential to develop practical therapeutic tools for CKD.

7.7 Epitope Mapping

Epitope mapping is essential in characterising monoclonal antibodies, as it identifies the specific regions of the antigen that the antibody binds to. In this study, we achieved success in epitope mapping for Fab 19.2. Data suggested a possible epitope within the first extracellular loop of SGLT2, which would be consistent with the immunohistochemical results. Further enrichment of the SGLT2 cDNA fragment library would clarify this question and enable us to clearly define a consensus sequence for the epitope recognised by Fab 19.2.

7.8 Limitations

Several limitations were encountered during this study. One major limitation is the absence of *in vivo* validation. While the *in vitro* analyses of Fab 19.2's binding to SGLT2 provided valuable insights into its specificity and potential, these findings alone are insufficient to determine the antibody's therapeutic applicability in renal fibrosis. Further studies using *in vivo* models are necessary to evaluate the efficacy, safety, and potential side effects of Fab 19.2 as a treatment option for renal fibrosis. Without such studies, how the antibody will perform in a complex biological environment remains unclear.

Conducting these *in vivo* studies was not feasible within the project's current scope due to logistical and licensing constraints, which prevented the use of animal models. Logistical and licensing challenges prevented the completion of *in vivo* validation studies, leaving a gap in assessing the antibody's behaviour in a complex biological environment and highlighting the importance of including such studies in future research.

7.9 Future Work

Several research areas should be pursued to address these limitations and enhance the utility of Fab 19.2. One of the critical areas for improvement is the optimisation of epitope mapping techniques. Future studies should employ advanced structural analysis methods, such as cryo-electron microscopy or X-ray crystallography, to preserve the native conformational epitopes of SGLT2. These techniques would allow for more precise identification of Fab 19.2's binding regions, overcoming the current challenges posed by protein fragmentation and ensuring that the structural integrity of the target antigen is maintained throughout the analysis (Amit et al., 1986). Optimising these methods is essential for obtaining consistent and reliable results in future epitope mapping studies.

Another important direction for future research is the evaluation of the full-length monoclonal antibodies targeting SGLT2. While Fab fragments offer several advantages, including smaller size and improved tissue penetration, they lack the Fc region, affecting their stability and half-life *in vivo*. Due to their enhanced structural stability, full-length antibodies may offer greater binding affinity and therapeutic potential. A comparative analysis between Fab fragments and full-length monoclonal antibodies could provide valuable insights into which form of antibody is more effective for targeting SGLT2 in therapeutic applications.

As part of my ongoing research, I conducted preliminary qPCR experiments to investigate the expression of essential proteins involved in renal fibrosis, including LOXL2, LOXL4, TG2, Collagen I, and Collagen III. These proteins play significant roles in the progression of fibrosis and scarring in various kidney diseases. Using a UUO model, I compared their gene expression between normal and diseased kidney tissues at two critical time points: 7 days and 21 days post-obstruction.

Although the analysis provides exciting insights into the early and late stages of fibrosis development, due to time constraints, I could not fully correlate these findings with other

experimental methods, such as IHC. In the future, I aim to integrate these qPCR data with IHC results to understand better the spatial and temporal distribution of these proteins in kidney tissues. This will allow me to characterise the structural changes and protein expression patterns during the fibrotic process (Appendices VII-XI).

To extend this work, I also plan to develop a targeted therapeutic strategy by conjugating an inhibitor of one of these fibrotic proteins (e.g., LOXL2) to our SGLT2-targeting antibody. This conjugation would enable the precise delivery of the inhibitor to the kidneys, specifically targeting the areas most affected by fibrosis, thereby minimising off-target effects. By utilising SGLT2's high expression in the renal proximal tubules, this targeted approach can potentially reduce fibrosis more effectively than systemic administration.

Furthermore, I will investigate the efficacy of this targeted treatment in relevant kidney disease models, using both functional assays and histological analyses to assess improvements in kidney function and reduction in fibrosis. This future work aims to establish a novel therapeutic strategy that could improve outcomes for patients with chronic kidney disease and other fibrotic kidney disorders.

Finally, future work must include the preclinical validation of these antibody-drug conjugates in animal models of kidney disease. Testing conjugated antibodies, such as Fab 19.2 linked to anti-fibrotic agents, in appropriate preclinical models will be essential for assessing their therapeutic efficacy, safety, and potential in mitigating renal scarring. This step will be crucial for advancing these targeted therapies toward clinical applications and evaluating their impact on renal fibrosis in a more complex biological system.

7.10 Final Conclusion

In summary, this research successfully demonstrated the development and characterisation of Fab 19.2, a monoclonal antibody specific to SGLT2. The antibody showed excellent specificity in both western blot and IHC assays, confirming its utility for detecting SGLT2 in native kidney tissues. While challenges were encountered in the epitope mapping experiments, these limitations can be addressed in future studies. Overall, Fab 19.2 represents a promising tool for advancing the diagnosis and treatment of SGLT2-related kidney pathologies, particularly renal fibrosis. Through continued optimisation and future *in*

vivo validation, Fab 19.2 could pave the way for new therapeutic strategies targeting chronic kidney disease.

References

ABBAS, A., LICHTMAN, A. & POBER, J. 2002. *Antibodies and Antigens in Cellular and Molecular Immunology.* Philadelphia: WB Saunders.

ABBAS, A. K., LICHTMAN, A. H. & PILLAI, S. 2021. *Cellular and Molecular Immunology, 10e, South Asia Edition-E-Book*, New Delhi: Elsevier Health Sciences.

ALLEN, T. M. & CULLIS, P. R. 2013. Liposomal drug delivery systems: from concept to clinical applications. *Advanced Drug Delivery Reviews,* 65**,** 36-48.

ALMAGRO, J. C. & FRANSSON, J. 2008. Humanization of antibodies. *Frontiers in Bioscience,* 13**,** 1619-1633.

ALMAGRO, J. C., PEDRAZA-ESCALONA, M., ARRIETA, H. I. & PéREZ-TAPIA, S. M. 2019. Phage display libraries for antibody therapeutic discovery and development. *Antibodies,* 8**,** 44.

ALTSHULER, E. á., SEREBRYANAYA, D. & KATRUKHA, A. 2010. Generation of recombinant antibodies and means for increasing their affinity. *Biochemistry (Moscow),* 75**,** 1584-1605.

AMIT, A., MARIUZZA, R., PHILLIPS, S. & POLJAK, R. 1986. Three-dimensional structure of an antigen-antibody complex at 2.8 Å resolution. *Science,* 233**,** 747-753.

APWEILER, R., HERMJAKOB, H. & SHARON, N. 1999. On the frequency of protein glycosylation, as deduced from analysis of the SWISS-PROT database. *Biochimica et Biophysica Acta (BBA)-General Subjects,* 1473**,** 4-8.

BAKER, M. 2015. Blame it on the antibodies. *Nature,* 521**,** 274.

BANEYX, F. 1999. Recombinant protein expression in Escherichia coli. *Current Opinion in Biotechnology,* 10**,** 411-421.

BARBAS 3RD, C., KANG, A. S., LERNER, R. A. & BENKOVIC, S. J. 1991. Assembly of combinatorial antibody libraries on phage surfaces: the gene III site. *Proceedings of the National Academy of Sciences USA,* 88**,** 7978-7982.

BARBAS, C. F. 2001. *Phage display: a laboratory manual*. New York: Cold Spring Harbor Laboratory Press.

BARDIA, A., MAYER, I.A., VAHDAT, L.T., TOLANEY, S.M., ISAKOFF, S.J., DIAMOND, J.R., O'SHAUGHNESSY, J., MOROOSE, R.L., SANTIN, A.D., ABRAMSON, V.G. & SHAH, N.C., 2019. Sacituzumab govitecan-hziy in refractory metastatic triple-negative breast cancer. *New England Journal of Medicine*, *380*(8), 741-751.

BARKER, H. E., COX, T. R. & ERLER, J. T. 2012. The rationale for targeting the LOX family in cancer. *Nature Reviews Cancer,* 12**,** 540-552.

BARRY-HAMILTON, V., SPANGLER, R., MARSHALL, D., MCCAULEY, S., RODRIGUEZ, H. M., OYASU, M., MIKELS, A., VAYSBERG, M., GHERMAZIEN, H. & WAI, C. 2010. Allosteric inhibition of lysyl oxidase–like-2 impedes the development of a pathologic microenvironment. *Nature Medicine,* 16**,** 1009-1017.

BECK, A., GOETSCH, L., DUMONTET, C. & CORVAïA, N. 2017. Strategies and challenges for the next generation of antibody–drug conjugates. *Nature Reviews Drug Discovery,* 16**,** 315-337.

BELYAYEVA, M. & JEONG, J. M. 2023. *Acute Pyelonephritis*, StatPearls [Internet]. Treasure Island (FL): StatPearls Publishing. [2 August 2024].

BERGMANN, C., GUAY-WOODFORD, L. M., HARRIS, P. C., HORIE, S., PETERS, D. J. M. & TORRES, V. E. 2018. Polycystic kidney disease. *Nature Reviews Disease Primers,* 4**,** 50.

BETTER, M., CHANG, C. P., ROBINSON, R. R. & HORWITZ, A. H. 1988. Escherichia coli secretion of an active chimeric antibody fragment. *Science,* 240**,** 1041-1043.

BIKBOV, B., PURCELL, C. A., LEVEY, A. S., SMITH, M., ABDOLI, A., ABEBE, M., ADEBAYO, O. M., AFARIDEH, M., AGARWAL, S. K. & AGUDELO-BOTERO, M. 2020. Global, regional, and national burden of chronic kidney disease, 1990–2017: a systematic analysis for the Global Burden of Disease Study 2017. *The Lancet,* 395**,** 709-733.

BORDEAUX, J., WELSH, A. W., AGARWAL, S., KILLIAM, E., BAQUERO, M. T., HANNA, J. A., ANAGNOSTOU, V. K. & RIMM, D. L. 2010. Antibody validation. *Biotechniques,* 48**,** 197-209.

BRADFORD, M. M. (1976). A rapid and sensitive method for the quantitation of microgram quantities of protein utilizing the principle of protein-dye binding. *Analytical biochemistry*, 72(1-2), 248-254.

BRAMLAGE, P., LANZINGER, S., HESS, E., FAHRNER, S., HEYER, C. H., FRIEBE, M., BUSCHMANN, I., DANNE, T., HOLL, R. W. & SEUFERT, J. 2020. Renal function deterioration in adult patients with type-2 diabetes. *BMC Nephrology,* 21**,** 1-10.

CABILLY, S., RIGGS, A. D., PANDE, H., SHIVELY, J. E., HOLMES, W. E., REY, M. A., PERRY, L. J., WETZEL, R. & HEYNEKER, H. L. 1984. Generation of antibody activity from immunoglobulin polypeptide chains produced in Escherichia coli. *Proceedings of the National Academy of Sciences USA,* 81**,** 3273-3277.

CAMPANHOLLE, G., LIGRESTI, G., GHARIB, S. A. & DUFFIELD, J. S. 2013. Cellular mechanisms of tissue fibrosis. 3. Novel mechanisms of kidney fibrosis. *American Journal of Physiology-Cell Physiology,* 304**,** C591-C603.

CAO, Q., HARRIS, D. C. & WANG, Y. 2015. Macrophages in kidney injury, inflammation, and fibrosis. *Physiology,* 30**,** 183-194.

CARDOSO, M. M., PEçA, I. N. & ROQUE, A. C. 2012. Antibody-conjugated nanoparticles for therapeutic applications. *Current Medicinal Chemistry,* 19**,** 3103-3127.

CARRIO, M. M. & VILLAVERDE, A. 2002. Construction and deconstruction of bacterial inclusion bodies. *Journal of Biotechnology,* 96**,** 3-12.

CARTER, D. & REED, S. G. 2010. Role of adjuvants in modeling the immune response. *Current Opinion in HIV and AIDS,* 5**,** 409-413.

CARTER, P. J. 2006. Potent antibody therapeutics by design. *Nature Reviews Immunology,* 6**,** 343-357.

CARTER, P. J. & LAZAR, G. A. 2018. Next generation antibody drugs: pursuit of the'high-hanging fruit'. *Nature Reviews Drug Discovery,* 17**,** 197-223.

CDC, C. F. D. C. A. P. 2023. *Chronic Kidney Disease in the United States, 2023* [Online]. Available: https://www.cdc.gov/kidneydisease/publications-resources/ckd-national-facts.html [14 September 2024].

CHEN, W., YANG, A., JIA, J., POPOV, Y. V., SCHUPPAN, D. & YOU, H. 2020. Lysyl oxidase (LOX) family members: rationale and their potential as therapeutic targets for liver fibrosis. *Hepatology,* 72**,** 729-741.

CHEVALIER, R. L. 2016. The proximal tubule is the primary target of injury and progression of kidney disease: Role of the glomerulotubular junction. *American Journal of Physiology - Renal Physiology*, 310(10), F1105–F1115.

CHEVALIER, R. L., FORBES, M. S. & THORNHILL, B. A. 2009. Ureteral obstruction as a model of renal interstitial fibrosis and obstructive nephropathy. *Kidney International,* 75**,** 1145-1152.

CHITTY, J. L., SETARGEW, Y. F. I. & COX, T. R. 2019. Targeting the lysyl oxidases in tumour desmoplasia. *Biochemical Society Transactions,* 47**,** 1661-1678.

CHUANG, P. Y., MENON, M. C. & HE, J. C. 2013. Molecular targets for treatment of kidney fibrosis. *Journal of Molecular Medicine (Berl),* 91**,** 549-559.

CMS, C. F. M. M. S. 2020. *CMS Announces Transformative New Model of Care for Medicare Beneficiaries with Chronic Kidney Disease* [Online]. Available: https://www.cms.gov/newsroom/press-releases/cms-announces-transformative-new-model-care-medicare-beneficiaries-chronic-kidney-disease [1 October 2024].

COLLIGHAN, R. & GRIFFIN, M. 2009. Transglutaminase 2 cross-linking of matrix proteins: biological significance and medical applications. *Amino Acids,* 36**,** 659-670.

COPIN, R., BAUM, A., WLOGA, E., PASCAL, K.E., GIORDANO, S., FULTON, B.O., ZHOU, A., NEGRON, N., LANZA, K., CHAN, N. & COPPOLA, A., 2021. The monoclonal antibody combination REGEN-COV protects against SARS-CoV-2 mutational escape in preclinical and human studies. *Cell*, *184*(15), 3949-3961.

COSGROVE, D., DUFEK, B., MEEHAN, D. T., DELIMONT, D., HARTNETT, M., SAMUELSON, G., GRATTON, M. A., PHILLIPS, G., MACKENNA, D. A. & BAIN, G. 2018. Lysyl oxidase like-2 contributes to renal fibrosis in Col4α3/Alport mice. *Kidney International,* 94**,** 303-314.

DEBIE, P., LAFONT, C., DEFRISE, M., HANSEN, I., VAN WILLIGEN, D.M., VAN LEEUWEN, F.W., GIJSBERS, R., D'HUYVETTER, M., DEVOOGDT, N., LAHOUTTE, T. & MOLLARD, P., 2020. Size and affinity kinetics of nanobodies influence targeting and penetration of solid tumours. *Journal of Controlled Release*, *317*, 34-42.

DUFFIELD, J. S. 2014. Cellular and molecular mechanisms in kidney fibrosis. *The Journal of Clinical Investigation,* 124**,** 2299-2306.

ECKER, D. M., JONES, S. D. & LEVINE, H. L. 2015. The therapeutic monoclonal antibody market. *MAbs*, Taylor & Francis, 9-14.

EJERBLAD, E., FORED, C. M., LINDBLAD, P., FRYZEK, J., MCLAUGHLIN, J. K. & NYRéN, O. 2006. Obesity and risk for chronic renal failure. *Journal of the American Society of Nephrology,* 17**,** 1695-1702.

FACK, F., HüGLE-DöRR, B., SONG, D., QUEITSCH, I., PETERSEN, G. & BAUTZ, E. K. 1997. Epitope mapping by phage display: random versus gene-fragment libraries. *Journal of Immunological Methods,* 206**,** 43-52.

FARRIS, A. B. & COLVIN, R. B. 2012. Renal interstitial fibrosis: mechanisms and evaluation. *Current Opinion in Nephrology and Hypertension,* 21**,** 289-300.

FENTON, R. & PRAETORIUS, J. 2016. Anatomy of the kidney. *Brenner and Rector's the kidney,* 1**,** 42-82.

FLYGARE, J. A., PILLOW, T. H. & ARISTOFF, P. 2013. Antibody-drug conjugates for the treatment of cancer. *Chemical Biology & Drug Design,* 81**,** 113-121.

FRENZEL, A., HUST, M. & SCHIRRMANN, T. 2013. Expression of recombinant antibodies. *Frontiers in Immunology,* 4**,** 217.

FURINI, G., SCHROEDER, N., HUANG, L., BOOCOCK, D., SCARPELLINI, A., COVENEY, C., TONOLI, E., RAMASWAMY, R., BALL, G. & VERDERIO, C. 2018. Proteomic profiling reveals the transglutaminase-2 externalization pathway in kidneys after unilateral ureteric obstruction. *Journal of the American Society of Nephrology,* 29**,** 880-905.

GELSE, K., PöSCHL, E. & AIGNER, T. 2003. Collagens—structure, function, and biosynthesis. *Advanced Drug Delivery Reviews,* 55**,** 1531-1546.

GEORGE, J. A. & GOUNDEN, V. 2019. Novel glomerular filtration markers. *Advances in Clinical Chemistry,* 88**,** 91-119.

GHEZZI, C. & WRIGHT, E. M. 2012. Regulation of the human Na+-dependent glucose cotransporter hSGLT2. *American Journal of Physiology-Cell Physiology,* 303**,** C348-C354.

GRENARD, P., BRESSON-HADNI, S., EL ALAOUI, S. D., CHEVALLIER, M., VUITTON, D. A. & RICARD-BLUM, S. 2001. Transglutaminase-mediated cross-linking is involved in the stabilization of extracellular matrix in human liver fibrosis. *Journal of Hepatology,* 35**,** 367-375.

GRIFFIN, M., CASADIO, R. & BERGAMINI, C. M. 2002. Transglutaminases: nature's biological glues. *Biochemical Journal,* 368**,** 377-396.

GROENEN, P. J., SMULDERS, R. H., PETERS, R. F., GROOTJANS, J. J., VAN DEN IJSSEL, P. R., BLOEMENDAL, H. & DE JONG, W. W. 1994. The amine-donor substrate specificity of tissue-type transglutaminase: Influence of amino acid residues flanking the amine-donor lysine residue. *European Journal of Biochemistry,* 220**,** 795-799.

GU, C., ZHANG, J., NOBLE, N. A., PENG, X. R. & HUANG, Y. 2016. An additive effect of anti-PAI-1 antibody to ACE inhibitor on slowing the progression of diabetic kidney disease. *American Journal of Physiology-Renal Physiology,* 311**,** F852-F863.

HE, Y., WANG, Y., STRUBLE, E. B., ZHANG, P., CHOWDHURY, S., REED, J. L., KENNEDY, M., SCOTT, D. E. & FISHER, R. W. 2012. Epitope mapping by random peptide phage display reveals essential residues for vaccinia extracellular enveloped virion spread. *Virology Journal,* 9**,** 1-11.

HEERSPINK, H. J., PERKINS, B. A., FITCHETT, D. H., HUSAIN, M. & CHERNEY, D. Z. 2016. Sodium-glucose cotransporter 2 inhibitors in the treatment of diabetes mellitus: cardiovascular and kidney effects, potential mechanisms, and clinical applications. *Circulation,* 134**,** 752-772.

HEIER, J.S., KHANANI, A.M., RUIZ, C.Q., BASU, K., FERRONE, P.J., BRITTAIN, C., FIGUEROA, M.S., LIN, H., HOLZ, F.G., PATEL, V. & LAI, T.Y., 2022. Efficacy, durability, and safety of intravitreal faricimab up to every 16 weeks for neovascular age-related macular degeneration (TENAYA and LUCERNE): two randomised, double-masked, phase 3, non-inferiority trials. *The Lancet*, *399*(10326), 729-740.

HENRY, K. A. & MACKENZIE, C. R. 2018. Antigen recognition by single-domain antibodies: structural latitudes and constraints. *MAbs*, Taylor & Francis, 815-826.

HEROLD, K.C., BUNDY, B.N., LONG, S.A., BLUESTONE, J.A., DIMEGLIO, L.A., DUFORT, M.J., GITELMAN, S.E., GOTTLIEB, P.A., KRISCHER, J.P., LINSLEY, P.S. & MARKS, J.B., 2019. An anti-CD3 antibody, teplizumab, in relatives at risk for type 1 diabetes. *New England Journal of Medicine*, *381*(7), 603-613.

HEWITSON, T. D. 2009. Renal tubulointerstitial fibrosis: common but never simple. *American Journal of Physiology-Renal Physiology,* 296**,** F1239-F1244.

HOOGENBOOM, H. R. 2005. Selecting and screening recombinant antibody libraries. *Nature Biotechnology,* 23**,** 1105-1116.

HOOGENBOOM, H. R., DE BRUıNE, A. P., HUFTON, S. E., HOET, R. M., ARENDS, J.-W. & ROOVERS, R. C. 1998. Antibody phage display technology and its applications. *Immunotechnology,* 4**,** 1-20.

HOOGENBOOM, H. R., GRIFFITHS, A. D., JOHNSON, K. S., CHISWELL, D. J., HUDSON, P. & WINTER, G. 1991. Multi-subunit proteins on the surface of filamentous phage: methodologies for displaying antibody (Fab) heavy and light chains. *Nucleic Acids Research,* 19**,** 4133-4137.

HOWARD, J.F., BRIL, V., VU, T., KARAM, C., PERIC, S., MARGANIA, T., MURAI, H., BILINSKA, M., SHAKARISHVILI, R., SMILOWSKI, M. & GUGLIETTA, A., 2021. Safety, efficacy, and tolerability of efgartigimod in patients with generalised myasthenia gravis (ADAPT): a multicentre, randomised, placebo-controlled, phase 3 trial. *The Lancet Neurology*, *20*(7), 526-536.

HUANG, L., BON, H., MAAMRA, M., HOLMES, T., ATKINSON, J., CAIN, K., KENNEDY, J., KETTLEBOROUGH, C., MATTHEWS, D. & TWOMEY, B. 2024. The effect of TG2-inhibitory monoclonal antibody zampilimab on tissue fibrosis in human in vitro and primate in vivo models of chronic kidney disease. *PloS One,* 19**,** e0298864.

IKEE, R., KOBAYASHI, S., HEMMI, N., SAIGUSA, T., NAMIKOSHI, T., YAMADA, M., IMAKIIRE, T., KIKUCHI, Y., SUZUKI, S. & MIURA, S. 2007. Involvement of transglutaminase-2 in pathological changes in renal disease. *Nephron Clinical Practice,* 105**,** c139-c146.

ISAKA, Y. 2018. Targeting TGF-β signaling in kidney fibrosis. *International Journal of Molecular Sciences,* 19**,** 2532.

ISEKI, K., IKEMIYA, Y., KINJO, K., INOUE, T., ISEKI, C. & TAKISHITA, S. 2004. Body mass index and the risk of development of end-stage renal disease in a screened cohort. *Kidney International,* 65**,** 1870-1876.

JAIN, K. K. 2008. Drug delivery systems-an overview. *Drug Delivery Systems***,** 1-50.

JANEWAY, C., TRAVERS, P., WALPORT, M. & SHLOMCHIK, M. 2001. *Immunobiology: the Immune System in Health and Disease*. New York: Garland Pub.

JIA, T., OLAUSON, H., LINDBERG, K., AMIN, R., EDVARDSSON, K., LINDHOLM, B., ANDERSSON, G., WERNERSON, A., SABBAGH, Y., SCHIAVI, S. & LARSSON, T.E., 2013. A novel model of adenine-induced tubulointerstitial nephropathy in mice. *BMC nephrology*, *14*, 1-8.

JOHNSON, T. S., EL-KORAIE, A. F., SKILL, N. J., BADDOUR, N. M., EL NAHAS, A. M., NJLOMA, M., ADAM, A. G. & GRIFFIN, M. 2003. Tissue transglutaminase and the progression of human renal scarring. *Journal of the American Society of Nephrology,* 14**,** 2052-2062.

JOHNSON, T. S., FISHER, M., HAYLOR, J. L., HAU, Z., SKILL, N. J., JONES, R., SAINT, R., COUTTS, I., VICKERS, M. E. & EL NAHAS, A. M. 2007. Transglutaminase inhibition reduces fibrosis and preserves function in experimental chronic kidney disease. *Journal of the American Society of Nephrology,* 18**,** 3078-3088.

JOHNSON, T. S., GRIFFIN, M., THOMAS, G. L., SKILL, J., COX, A., YANG, B., NICHOLAS, B., BIRCKBICHLER, P. J., MUCHANETA-KUBARA, C. & EL NAHAS, A. M. 1997. The role of transglutaminase in the rat subtotal nephrectomy model of renal fibrosis. *The Journal of Clinical Investigation,* 99**,** 2950-2960.

JOHNSTON, C., MARTIN, B., FICHANT, G., POLARD, P. & CLAVERYS, J.-P. 2014. Bacterial transformation: distribution, shared mechanisms and divergent control. *Nature Reviews Microbiology,* 12**,** 181-196.

JONES, P. T., DEAR, P. H., FOOTE, J., NEUBERGER, M. S. & WINTER, G. 1986. Replacing the complementarity-determining regions in a human antibody with those from a mouse. *Nature,* 321**,** 522-525.

JOO, Y. S., LEE, C., KIM, H. W., JHEE, J., YUN, H.-R., PARK, J. T., CHANG, T. I., YOO, T.-H., KANG, S.-W. & HAN, S. H. 2020. Association of longitudinal trajectories of systolic BP with risk of incident CKD: results from the Korean Genome and Epidemiology Study. *Journal of the American Society of Nephrology,* 31**,** 2133-2144.

JOVČEVSKA, I. & MUYLDERMANS, S., 2020. The therapeutic potential of nanobodies. *BioDrugs*, *34*(1), 11-26.

JOYCE, E., GLASNER, P., RANGANATHAN, S. & SWIATECKA-URBAN, A. 2017. Tubulointerstitial nephritis: diagnosis, treatment, and monitoring. *Pediatric Nephrology,* 32**,** 577-587.

JUNG, D., GIALLOURAKIS, C., MOSTOSLAVSKY, R. & ALT, F. W. 2006. Mechanism and control of V (D) J recombination at the immunoglobulin heavy chain locus. *Annual Review of Immunology,* 24**,** 541-570.

KAGAN, H. M. & TRACKMAN, P. C. 1991. Properties and function of lysyl oxidase. *American Journal of Respiratory Cell and Molecular Biology,* 5**,** 206-210.

KRAMANN, R. & MENZEL, S., 2021. Mouse models of kidney fibrosis. In *Myofibroblasts: Methods and Protocols*, 323-338. New York, NY: Springer US.

KATSURADA, K., NANDI, S. S., SHARMA, N. M. & PATEL, K. P. 2021. Enhanced Expression and Function of Renal SGLT2 (Sodium-Glucose Cotransporter 2) in Heart Failure: Role of Renal Nerves. *Circulation: Heart Failure,* 14**,** e008365.

KAZI, A. M. & HASHMI, M. F. 2023. *Glomerulonephritis*. Treasure Island (FL): StatPearls Publishing.

KERR, M., BRAY, B., MEDCALF, J., O'DONOGHUE, D. J. & MATTHEWS, B. 2012b. Estimating the financial cost of chronic kidney disease to the NHS in England. *Nephrology Dialysis Transplantation,* 27**,** iii73-iii80.

KIM, S.S., KIROU, K.A. & ERKAN, D., 2012. Belimumab in systemic lupus erythematosus: an update for clinicians. *Therapeutic Advances in Chronic Disease*, *3*(1), 11-23.

KINOSHITA, K. & HONJO, T. 2001. Linking class-switch recombination with somatic hypermutation. *Nature Reviews Molecular Cell Biology,* 2**,** 493-503.

KDIGO, 2012. Clinical Practice Guideline for the Evaluation and Management of Chronic Kidney Disease. *Kidney International Supplements*. 3(1), 1-150.

CMS, C. F. M. M. S. 2020. *CMS Announces Transformative New Model of Care for Medicare Beneficiaries with Chronic Kidney Disease* [Online]. Available: https://www.cms.gov/newsroom/press-releases/cms-announces-transformative-new-model-care-medicare-beneficiaries-chronic-kidney-disease [1 October 2024].

KLINKHAMMER, B. M., FLOEGE, J. & BOOR, P. 2018. PDGF in organ fibrosis. *Molecular Aspects of Medicine,* 62**,** 44-62.

KOEPPEN, B. M. & STANTON, B. A. 2018. *Renal Physiology E-Book*, Elsevier Health Sciences.

KöHLER, G. & MILSTEIN, C. 1975. Continuous cultures of fused cells secreting antibody of predefined specificity. *Nature,* 256**,** 495-497.

KOMOHARA, Y. & TAKEYA, M. 2017. CAFs and TAMs: maestros of the tumour microenvironment. *The Journal of Pathology,* 241**,** 313-315.

LABRIJN, A.F., JANMAAT, M.L., REICHERT, J.M. & PARREN, P.W., 2019. Bispecific antibodies: a mechanistic review of the pipeline. *Nature Reviews Drug Discovery*, *18*(8), 585-608.

LAFAYETTE, R. A., MAYER, G., PARK, S. K. & MEYER, T. W. 1992. Angiotensin II receptor blockade limits glomerular injury in rats with reduced renal mass. *The Journal of Clinical Investigation,* 90**,** 766-771.

LEONARD, S. 2015. *Therapeutic Approaches to Insulin Resistance and Type 2 Diabetes.* Doctor of Philosophy, National University of Ireland, Maynooth (Ireland).

LEVEY, A. S., ECKARDT, K.-U., TSUKAMOTO, Y., LEVIN, A., CORESH, J., ROSSERT, J., ZEEUW, D. D., HOSTETTER, T. H., LAMEIRE, N. & EKNOYAN, G. 2005. Definition and classification of chronic kidney disease: a position statement from Kidney Disease: Improving Global Outcomes (KDIGO). *Kidney International,* 67**,** 2089-2100.

LEVIN, M.J., USTIANOWSKI, A., DE WIT, S., LAUNAY, O., AVILA, M., TEMPLETON, A., YUAN, Y., SEEGOBIN, S., ELLERY, A., LEVINSON, D.J. & AMBERY, P., 2022. Intramuscular AZD7442 (tixagevimab–cilgavimab) for prevention of Covid-19. *New England Journal of Medicine*, *386*(23), 2188-2200.

LI, J.F., HE, L., DENG, Y.Q., QI, S.H., CHEN, Y.H., ZHANG, X.L., HU, S.X., FAN, R.W., ZHAO, G.Y. & QIN, C.F., 2021. Generation and characterization of a nanobody against SARS-CoV. *Virologica Sinica*, 36(6), 1484-1491.

LIBURKIN-DAN, T., TOLEDANO, S. & NEUFELD, G. 2022. Lysyl oxidase family enzymes and their role in tumor progression. *International Journal of Molecular Sciences,* 23**,** 6249.

LóPEZ-NOVOA, J. M., MARTíNEZ-SALGADO, C., RODRíGUEZ-PEñA, A. B. & LóPEZ-HERNáNDEZ, F. J. 2010. Common pathophysiological mechanisms of chronic kidney disease: therapeutic perspectives. *Pharmacology & Therapeutics,* 128**,** 61-81.

LINGE, C., RICHARDSON, J., VIGOR, C., CLAYTON, E., HARDAS, B. & ROLFE, K. J. 2005. Hypertrophic scar cells fail to undergo a form of apoptosis specific to contractile collagen—the role of tissue transglutaminase. *Journal of Investigative Dermatology*, 125, 72-82.

LOTE, C. 2000. The loop of Henle, distal tubule and collecting duct. *Principles of Renal Physiology***,** 70-85.

LOTE, C. J. 1994. *Principles of renal physiology*. London: Chapman & Hall.

LU, L. L., SUSCOVICH, T. J., FORTUNE, S. M. & ALTER, G. 2018. Beyond binding: antibody effector functions in infectious diseases. *Nature Reviews Immunology,* 18**,** 46-61.

LUCERO, H. & KAGAN, H. 2006. Lysyl oxidase: an oxidative enzyme and effector of cell function. *Cellular and Molecular Life Sciences CMLS,* 63**,** 2304-2316.

LYON, R.P., BOVEE, T.D., DORONINA, S.O., BURKE, P.J., HUNTER, J.H., NEFF-LAFORD, H.D., JONAS, M., ANDERSON, M.E., SETTER, J.R. & SENTER, P.D., 2015. Reducing hydrophobicity of homogeneous antibody-drug conjugates improves pharmacokinetics and therapeutic index. *Nature Biotechnology*, *33*(7), 733-735.

MA, Y., CAI, F., LI, Y., CHEN, J., HAN, F. & LIN, W. 2020. A review of the application of nanoparticles in the diagnosis and treatment of chronic kidney disease. *Bioactive Materials,* 5**,** 732-743.

MAIBOM-THOMSEN, S. L., TRIER, N. H., HOLM, B. E., HANSEN, K. B., RASMUSSEN, M. I., CHAILYAN, A., MARCATILI, P., HøJRUP, P. & HOUEN, G. 2019. Immunoglobulin G structure and rheumatoid factor epitopes. *PLoS One,* 14**,** e0217624.

MÄKI, J. M., RÄSÄNEN, J., TIKKANEN, H., SORMUNEN, R., MÄKIKALLIO, K., KIVIRIKKO, K. I. & SOININEN, R. 2002. Inactivation of the lysyl oxidase gene Lox leads to aortic aneurysms, cardiovascular dysfunction, and perinatal death in mice. *Circulation,* 106**,** 2503-2509.

MAKRIDES, S. C. 1996. Strategies for achieving high-level expression of genes in Escherichia coli. *Microbiological Reviews,* 60**,** 512-38.

MATSUO, S., LóPEZ-GUISA, J. M., CAI, X., OKAMURA, D. M., ALPERS, C. E., BUMGARNER, R. E., PETERS, M. A., ZHANG, G. & EDDY, A. A. 2005. Multifunctionality of PAI-1 in fibrogenesis: evidence from obstructive nephropathy in PAI-1-overexpressing mice. *Kidney International,* 67**,** 2221-2238.

MCCAFFERTY, J., GRIFFITHS, A. D., WINTER, G. & CHISWELL, D. J. 1990. Phage antibodies: filamentous phage displaying antibody variable domains. *Nature,* 348**,** 552-554.

MCCONOUGHEY, S. J., BASSO, M., NIATSETSKAYA, Z. V., SLEIMAN, S. F., SMIRNOVA, N. A., LANGLEY, B. C., MAHISHI, L., COOPER, A. J., ANTONYAK, M. A. & CERIONE, R. A. 2010.

Inhibition of transglutaminase 2 mitigates transcriptional dysregulation in models of Huntington disease. *EMBO Molecular Medicine,* 2**,** 349-370.

MENG, X. M., NIKOLIC-PATERSON, D. J. & LAN, H. Y. 2014. Inflammatory processes in renal fibrosis. *Nature Reviews Nephrology,* 10**,** 493-503.

MEYER, T. 2010. Competitive ELISA. *Antibody engineering***,** 739-742.

MIRZA, A., LIU, S., FRIZELL, E., ZHU, J., MADDUKURI, S., MARTINEZ, J., DAVIES, P., SCHWARTING, R., NORTON, P. & ZERN, M. 1997. A role for tissue transglutaminase in hepatic injury and fibrogenesis, and its regulation by NF-kappaB. *American Journal of Physiology-Gastrointestinal and Liver Physiology,* 272**,** G281-G288.

MITCHELL, M. J., BILLINGSLEY, M. M., HALEY, R. M., WECHSLER, M. E., PEPPAS, N. A. & LANGER, R. 2021. Engineering precision nanoparticles for drug delivery. *Nature Reviews Drug Discovery,* 20**,** 101-124.

MODI, S., SAURA, C., YAMASHITA, T., PARK, Y.H., KIM, S.B., TAMURA, K., ANDRE, F., IWATA, H., ITO, Y., TSURUTANI, J. & SOHN, J., 2020. Trastuzumab deruxtecan in previously treated HER2-positive breast cancer. *New England Journal of Medicine*, *382*(7), 610-621.

MOE, S. M., DRüEKE, T., LAMEIRE, N. & EKNOYAN, G. 2007. Chronic kidney disease–mineral-bone disorder: a new paradigm. *Advances in Chronic Kidney Disease,* 14**,** 3-12.

MORISHITA, Y., IMAI, T., YOSHIZAWA, H., WATANABE, M., ISHIBASHI, K., MUTO, S. & NAGATA, D. 2015. Delivery of microRNA-146a with polyethylenimine nanoparticles inhibits renal fibrosis in vivo. *International Journal of Nanomedicine***,** 3475-3488.

MURAMATSU, M., KINOSHITA, K., FAGARASAN, S., YAMADA, S., SHINKAI, Y. & HONJO, T. 2000. Class switch recombination and hypermutation require activation-induced cytidine deaminase (AID), a potential RNA editing enzyme. *Cell,* 102**,** 553-563.

MURPHY, K. & WEAVER, C. 2017. *Janeway's immunobiology,* New York: Garland Science.

MURUGAPOOPATHY, V., MCCUSKER, C. & GUPTA, I. R. 2020. The pathogenesis and management of renal scarring in children with vesicoureteric reflux and pyelonephritis. *Pediatric Nephrology,* 35**,** 349-357.

MUSSO, C. G., ÁLVAREZ-GREGORI, J., JAUREGUI, J. & MACíAS-NúñEZ, J. F. 2016. Glomerular filtration rate equations: a comprehensive review. *International Urology and Nephrology,* 48**,** 1105-1110.

MYCEK, M., CLARKE, D., NEIDLE, A. & WAELSCH, H. 1959. Amine incorporation into insulin as catalyzed by transglutaminase. *Archives of Biochemistry and Biophysics,* 84**,** 528-540.

NARDACCI, R., CICCOSANTI, F., FALASCA, L., LO IACONO, O., AMENDOLA, A., ANTONUCCI, G. & PIACENTINI, M. 2003. Tissue transglutaminase in HCV infection. *Cell Death & Differentiation,* 10**,** S79-S80.

NELSON, A. L., DHIMOLEA, E. & REICHERT, J. M. 2010. Development trends for human monoclonal antibody therapeutics. *Nature Reviews Drug Discovery,* 9**,** 767-774.

NEUBERGER, M. S. 1983. Expression and regulation of immunoglobulin heavy chain gene transfected into lymphoid cells. *The EMBO Journal,* 2**,** 1373-1378.

NILVEBRANT, J. & ROCKBERG, J. 2018. An introduction to epitope mapping. *Epitope Mapping Protocols***,** 1-10.

NIU, Y., LIU, R., GUAN, C., ZHANG, Y., CHEN, Z., HOERER, S., NAR, H. & CHEN, L. 2022. Structural basis of inhibition of the human SGLT2-MAP17 glucose transporter. *Nature,* 601**,** 280-284.

NOGUEIRA, A., PIRES, M. J. & OLIVEIRA, P. A. 2017. Pathophysiological Mechanisms of Renal Fibrosis: A Review of Animal Models and Therapeutic Strategies. *In Vivo,* 31**,** 1-22.

ORLANDI, R., GüSSOW, D. H., JONES, P. T. & WINTER, G. 1989. Cloning immunoglobulin variable domains for expression by the polymerase chain reaction. *Proceedings of the National Academy of Sciences,* 86**,** 3833-3837.

OSTENDORF, T., EITNER, F. & FLOEGE, J. 2012. The PDGF family in renal fibrosis. *Pediatric Nephrology,* 27**,** 1041-1050.

PAN, S.-H. & MALCOLM, B. A. 2000. Reduced background expression and improved plasmid stability with pET vectors in BL21 (DE3). *Biotechniques,* 29**,** 1234-1238.

PEINADO, H., MORENO-BUENO, G., HARDISSON, D., PéREZ-GóMEZ, E., SANTOS, V., MENDIOLA, M., DE DIEGO, J. I., NISTAL, M., QUINTANILLA, M. & PORTILLO, F. 2008. Lysyl oxidase-like 2 as a new poor prognosis marker of squamous cell carcinomas. *Cancer Research,* 68**,** 4541-4550.

PERCIVAL-ALWYN, J. L., ENGLAND, E., KEMP, B., RAPLEY, L., DAVIS, N. H., MCCARTHY, G. R., MAJITHIYA, J. B., CORKILL, D. J., WELSTED, S., MINTON, K., COHEN, E. S., ROBINSON, M. J., DOBSON, C., WILKINSON, T. C., VAUGHAN, T. J., GROVES, M. A. & TIGUE, N. J. 2015. Generation of potent mouse monoclonal antibodies to self-proteins using T-cell epitope "tags". *MAbs,* 7**,** 129-137.

PINNELL, S. R. & MARTIN, G. R. 1968. The cross-linking of collagen and elastin: enzymatic conversion of lysine in peptide linkage to alpha-aminoadipic-delta-semialdehyde (allysine) by an extract from bone. *Proceedings of the National Academy of Sciences USA,* 61**,** 708-716.

PISANO, J., FINLAYSON, J. & PEYTON, M. P. 1968. Cross-link in fibrin polymerized by factor XIII: ε-(γ-glutamyl) lysine. *Science,* 160**,** 892-893.

PROVENZANO, M., ANDREUCCI, M., GAROFALO, C., FAGA, T., MICHAEL, A., IELAPI, N., GRANDE, R., SAPIENZA, P., FRANCISCIS, S., MASTROROBERTO, P. & SERRA, R. 2020. The Association of Matrix Metalloproteinases with Chronic Kidney Disease and Peripheral Vascular Disease: A Light at the End of the Tunnel? *Biomolecules,* 10.

PUENTE, A., FORTEA, J. I., CABEZAS, J., ARIAS LOSTE, M. T., IRUZUBIETA, P., LLERENA, S., HUELIN, P., FáBREGA, E. & CRESPO, J. 2019. LOXL2—A new target in antifibrogenic therapy? *International Journal of Molecular Sciences,* 20**,** 1634.

RAEESZADEH-SARMAZDEH, M. & BODER, E. T. 2022. Yeast surface display: new opportunities for a time-tested protein engineering system. *Yeast Surface Display.* New York: Springer.

RAHMOUNE, H., THOMPSON, P. W., WARD, J. M., SMITH, C. D., HONG, G. & BROWN, J. 2005. Glucose transporters in human renal proximal tubular cells isolated from the urine of patients with non-insulin-dependent diabetes. *Diabetes,* 54**,** 3427-3434.

RAJASEKERAN, H., CHERNEY, D. Z. & LOVSHIN, J. A. 2017. Do the effects of sodium-glucose cotransporter-2 inhibitors in patients with diabetes give insight into potential use in non-diabetic kidney disease? *Current Opinion in Nephrology and Hypertension,* 26**,** 358-367.

RANI, K. & PALIWAL, S. 2014. A review on targeted drug delivery: Its entire focus on advanced therapeutics and diagnostics. *Scholars Journal of Applied Medical Sciences (SJAMS),* 2**,** 328-31.

RAPPU, P., SALO, A. M., MYLLYHARJU, J. & HEINO, J. 2019. Role of prolyl hydroxylation in the molecular interactions of collagens. *Essays in Biochemistry,* 63**,** 325-335.

REISS, A. B., JACOB, B., ZUBAIR, A., SRIVASTAVA, A., JOHNSON, M. & DE LEON, J. 2024. Fibrosis in Chronic Kidney Disease: Pathophysiology and Therapeutic Targets. *Journal of Clinical Medicine,* 13**,** 1881.

REROLLE, J.-P., HERTIG, A., NGUYEN, G., SRAER, J.-D. & RONDEAU, E. P. 2000. Plasminogen activator inhibitor type 1 is a potential target in renal fibrogenesis. *Kidney International,* 58**,** 1841-1850.

RICARD-BLUM, S. 2011. The collagen family. Cold Spring Harbor Perspect. *Biology,* 3**,** a004978.

RICHARDS, D. A., MARUANI, A. & CHUDASAMA, V. 2017. Antibody fragments as nanoparticle targeting ligands: a step in the right direction. *Chemical Science Journal,* 8**,** 63-77.

RODRIGUEZ, H. M., VAYSBERG, M., MIKELS, A., MCCAULEY, S., VELAYO, A. C., GARCIA, C. & SMITH, V. 2010. Modulation of lysyl oxidase-like 2 enzymatic activity by an allosteric antibody inhibitor. *Journal of Biological Chemistry,* 285**,** 20964-20974.

ROMAGNANI, P., REMUZZI, G., GLASSOCK, R., LEVIN, A., JAGER, K. J., TONELLI, M., MASSY, Z., WANNER, C. & ANDERS, H. J. 2017. Chronic kidney disease. *Nature Reviews Disease Primers,* 3**,** 17088.

ROSANO, G. L. & CECCARELLI, E. A. 2014. Recombinant protein expression in Escherichia coli: advances and challenges. *Frontiers in Microbiology,* 5**,** 172.

ROSE, B. D. 2001. *Clinical Physiology of Acid-Base and Electrolyte Disorders* (5th ed.). McGraw-Hill.

RUIZ-ORTEGA, M., RAYEGO-MATEOS, S., LAMAS, S., ORTIZ, A. & RODRIGUES-DIEZ, R. R. 2020. Targeting the progression of chronic kidney disease. *Nature Reviews Nephrology,* 16**,** 269-288.

RUSSEL, M. 1991. Filamentous phage assembly. *Molecular Microbiology,* 5**,** 1607-1613.

SATOSKAR, A. A., PARIKH, S. V. & NADASDY, T. 2020. Epidemiology, pathogenesis, treatment and outcomes of infection-associated glomerulonephritis. *Nature Reviews Nephrology,* 16**,** 32-50.

SCHAERTL, S., PRIME, M., WITYAK, J., DOMINGUEZ, C., MUNOZ-SANJUAN, I., PACIFICI, R. E., COURTNEY, S., SCHEEL, A. & MACDONALD, D. 2010. A profiling platform for the characterization of transglutaminase 2 (TG2) inhibitors. *Journal of Biomolecular Screening,* 15**,** 478-487.

SCHATZ, D. G. & SWANSON, P. C. 2011. V (D) J recombination: mechanisms of initiation. *Annual Review of Genetics,* 45**,** 167-202.

SCHELLING, J. R. 2009. Tissue transglutaminase inhibition as a treatment for diabetic glomerular scarring: it's good to be glueless. *Kidney International,* 76**,** 363-365.

SCHILTER, H., FINDLAY, A. D., PERRYMAN, L., YOW, T. T., MOSES, J., ZAHOOR, A., TURNER, C. I., DEODHAR, M., FOOT, J. S. & ZHOU, W. 2019. The lysyl oxidase-like 2/3 enzymatic inhibitor, PXS-5153A, reduces crosslinks and ameliorates fibrosis. *Journal of Cellular and Molecular Medicine,* 23**,** 1759-1770.

SCHROEDER JR, H. W. & CAVACINI, L. 2010. Structure and function of immunoglobulins. *Journal of Allergy and Clinical Immunology,* 125**,** S41-S52.

SEHN, L.H., CHUA, N., MAYER, J., DUECK, G., TRNĚNÝ, M., BOUABDALLAH, K., FOWLER, N., DELWAIL, V., PRESS, O., SALLES, G. & GRIBBEN, J., 2016. Obinutuzumab plus bendamustine versus bendamustine monotherapy in patients with rituximab-refractory indolent non-Hodgkin lymphoma (GADOLIN): a randomised, controlled, open-label, multicentre, phase 3 trial. *The Lancet Oncology*, *17*(8), 1081-1093.

SERCOMBE, L., VEERATI, T., MOHEIMANI, F., WU, S. Y., SOOD, A. K. & HUA, S. 2015. Advances and challenges of liposome assisted drug delivery. *Frontiers in Pharmacology,* 6**,** 286.

SGANGA, S., RIONDINO, S., IANNANTUONO, G. M., ROSENFELD, R., ROSELLI, M. & TORINO, F. 2023. Antibody-drug conjugates for the treatment of renal cancer: a scoping review

on current evidence and clinical perspectives. *Journal of Personalized Medicine,* 13**,** 1339.

SHARGH, V. H., HONDERMARCK, H. & LIANG, M. 2016. Antibody-targeted biodegradable nanoparticles for cancer therapy. *Nanomedicine (Lond),* 11**,** 63-79.

SHEN, B.Q., XU, K., LIU, L., RAAB, H., BHAKTA, S., KENRICK, M., PARSONS-REPONTE, K.L., TIEN, J., YU, S.F., MAI, E. & LI, D., 2012. Conjugation site modulates the in vivo stability and therapeutic activity of antibody-drug conjugates. *Nature Biotechnology*, *30*(2), 184-189.

SHWEKE, N., BOULOS, N., JOUANNEAU, C., VANDERMEERSCH, S., MELINO, G., DUSSAULE, J.-C., CHATZIANTONIOU, C., RONCO, P. & BOFFA, J.-J. 2008. Tissue transglutaminase contributes to interstitial renal fibrosis by favoring accumulation of fibrillar collagen through TGF-β activation and cell infiltration. *The American Journal of Pathology,* 173**,** 631-642.

SIEGEL, M. & KHOSLA, C. 2007. Transglutaminase 2 inhibitors and their therapeutic role in disease states. *Pharmacology & Therapeutics,* 115**,** 232-245.

SKERRA, A. & PLüCKTHUN, A. 1988. Assembly of a functional immunoglobulin Fv fragment in Escherichia coli. *Science,* 240**,** 1038-1041.

SKILL, N. J., GRIFFIN, M., EL NAHAS, A. M., SANAI, T., HAYLOR, J. L., FISHER, M., JAMIE, M. F., MOULD, N. N. & JOHNSON, T. S. 2001. Increases in renal ε-(γ-glutamyl)-lysine crosslinks result from compartment-specific changes in tissue transglutaminase in early experimental diabetic nephropathy: Pathologic implications. *Laboratory Investigation,* 81**,** 705-716.

SMITH, G. P. 1985. Filamentous fusion phage: novel expression vectors that display cloned antigens on the virion surface. *Science,* 228**,** 1315-1317.

SMITH, G. P. & PETRENKO, V. A. 1997. Phage display. *Chemical Reviews,* 97**,** 391-410.

SMITH, H. W. 1951. *The kidney: Structure and Function in Health and Disease*, Oxford University Press.

SPICER, C. D., JUMEAUX, C., GUPTA, B. & STEVENS, M. M. 2018. Peptide and protein nanoparticle conjugates: versatile platforms for biomedical applications. *Chemical Society Reviews,* 47**,** 3574-3620.

STANFIELD, R. L., GORNY, M. K., WILLIAMS, C., ZOLLA-PAZNER, S. & WILSON, I. A. 2004. Structural rationale for the broad neutralization of HIV-1 by human monoclonal antibody 447-52D. *Structure,* 12**,** 193-204.

STAVNEZER, J., GUIKEMA, J. E. & SCHRADER, C. E. 2008. Mechanism and regulation of class switch recombination. *Annual Review of Immunology,* 26**,** 261-292.

STUDIER, F. W. & MOFFATT, B. A. 1986. Use of bacteriophage T7 RNA polymerase to direct selective high-level expression of cloned genes. *Journal of Molecular Biology,* 189**,** 113-130.

SZONDY, Z., KORPONAY-SZABó, I., KIRáLY, R., SARANG, Z. & TSAY, G. J. 2017. Transglutaminase 2 in human diseases. *Biomedicine (Taipei),* 7**,** 15.

TALREJA, S., PANDEY, S. & KUMAR, S. 2020. A review on Monoclonal antibody and its application in biotechnology. *Journal of Pharmaceutical Sciences and Research,* 12**,** 49-53.

THEOCHARIS, A. D., SKANDALIS, S. S., GIALELI, C. & KARAMANOS, N. K. 2016. Extracellular matrix structure. *Advanced Drug Delivery Reviews,* 97**,** 4-27.

TILLY, H., MORSCHHAUSER, F., SEHN, L.H., FRIEDBERG, J.W., TRNĚNÝ, M., SHARMAN, J.P., HERBAUX, C., BURKE, J.M., MATASAR, M., RAI, S. & IZUTSU, K., 2022. Polatuzumab

vedotin in previously untreated diffuse large B-cell lymphoma. *New England Journal of Medicine*, *386*(4), 351-363.

TJIN, G., WHITE, E. S., FAIZ, A., SICARD, D., TSCHUMPERLIN, D. J., MAHAR, A., KABLE, E. P. & BURGESS, J. K. 2017. Lysyl oxidases regulate fibrillar collagen remodelling in idiopathic pulmonary fibrosis. *Disease Models & Mechanisms,* 10**,** 1301-1312.

TONEGAWA, S. 1983. Somatic generation of antibody diversity. *Nature,* 302**,** 575-581.

TRACKMAN, P. C. 2016. Lysyl oxidase isoforms and potential therapeutic opportunities for fibrosis and cancer. *Expert Opinion on Therapeutic Targets,* 20**,** 935-945.

TSURUDA, T., COSTELLO-BOERRIGTER, L. C. & BURNETT, J. C., JR. 2004. Matrix metalloproteinases: pathways of induction by bioactive molecules. *Heart Failure Reviews,* 9**,** 53-61.

TUTTLE, K. R., BAKRIS, G. L., BILOUS, R. W., CHIANG, J. L., DE BOER, I. H., GOLDSTEIN-FUCHS, J., HIRSCH, I. B., KALANTAR-ZADEH, K., NARVA, A. S. & NAVANEETHAN, S. D. 2014. Diabetic kidney disease: a report from an ADA Consensus Conference. *Diabetes Care,* 37**,** 2864-2883.

UHLEN, M., BANDROWSKI, A., CARR, S., EDWARDS, A., ELLENBERG, J., LUNDBERG, E., RIMM, D. L., RODRIGUEZ, H., HILTKE, T. & SNYDER, M. 2016. A proposal for validation of antibodies. *Nature Methods,* 13**,** 823-827.

ULINSKI, T., SELLIER-LECLERC, A. L., TUDORACHE, E., BENSMAN, A. & AOUN, B. 2012. Acute tubulointerstitial nephritis. *Pediatric Nephrology,* 27**,** 1051-1057.

VALLON, V. & THOMSON, S.C., 2017. Targeting renal glucose reabsorption to treat hyperglycaemia: the pleiotropic effects of SGLT2 inhibition. *Diabetologia*, *60*(2), 215-225.

VAN AUDENHOVE, I. & GETTEMANS, J., 2016. Nanobodies as versatile tools to understand, diagnose, visualize and treat cancer. *EBioMedicine*, *8*, 40-48.

VAN BUREN, P. N. & TOTO, R. 2011. Hypertension in diabetic nephropathy: epidemiology, mechanisms, and management. *Advances in Chronic Kidney Disease,* 18**,** 28-41.

VAUGHAN, T.J., OSBOURN, J.K. & TEMPEST, P.R., 1998. Human antibodies by design. *Nature biotechnology*, *16*(6), 535-539.

VERDERIO, E. A., JOHNSON, T. S. & GRIFFIN, M. 2005. Transglutaminases in wound healing and inflammation. *Transglutaminases,* 38**,** 89-114.

VERMA, R., BOLETI, E. & GEORGE, A. J. 1998. Antibody engineering: comparison of bacterial, yeast, insect and mammalian expression systems. *Journal of Immunological Methods,* 216**,** 165-81.

VILLAVERDE, A. & CARRIO, M. M. 2003. Protein aggregation in recombinant bacteria: biological role of inclusion bodies. *Biotechnology Letters,* 25**,** 1385-95.

VOULGARI, P.V. & DROSOS, A.A., 2014. Adalimumab in the treatment of rheumatoid arthritis. *Expert Opinion on Biological Therapy*, *14*(4), 549-561.

WANG, H., POE, A., PAK, L., NANDAKUMAR, K., JANDU, S., STEPPAN, J., LöSER, R. & SANTHANAM, L. 2021. An in situ activity assay for lysyl oxidases. *Communications Biology,* 4**,** 840.

WANG, X., ZHOU, Y., TAN, R., XIONG, M., HE, W., FANG, L., WEN, P., JIANG, L. & YANG, J. 2010. Mice lacking the matrix metalloproteinase-9 gene reduce renal interstitial fibrosis in obstructive nephropathy. *American Journal of Physiology-Renal Physiology,* 299**,** F973-F982.

WEBSTER, A. C., NAGLER, E. V., MORTON, R. L. & MASSON, P. 2017. Chronic Kidney Disease. *Lancet,* 389**,** 1238-1252.

WICIK, Z., NOWAK, A., JAROSZ-POPEK, J., WOLSKA, M., EYILETEN, C., SILLER-MATULA, J. M., VON LEWINSKI, D., SOURIJ, H., FILIPIAK, K. J. & POSTULA, M. 2022. Characterization of the SGLT2 Interaction Network and Its Regulation by SGLT2 Inhibitors: A Bioinformatic Analysis. *Frontiers in Pharmacology,* 13**,** 901340.

WILCZEWSKA, A. Z., NIEMIROWICZ, K., MARKIEWICZ, K. H. & CAR, H. 2012. Nanoparticles as drug delivery systems. *Pharmacological Reports,* 64**,** 1020-1037.

WINTER, G., GRIFFITHS, A. D., HAWKINS, R. E. & HOOGENBOOM, H. R. 1994. Making antibodies by phage display technology. *Annual Review of Immunology,* 12**,** 433-455.

WRIGHT, E. M., LOO, D. D. & HIRAYAMA, B. A. 2011. Biology of human sodium glucose transporters. *Physiological Reviews,* 91**,** 733-794.

WU, D., CONG, J., WEI, J., HU, J., SUN, W., RAN, W., LIAO, C., ZHENG, H. & YE, L., 2023. A Naïve Phage Display Library-Derived Nanobody Neutralizes SARS-CoV-2 and Three Variants of Concern. *International Journal of Nanomedicine*, 5781-5795.

YAMAUCHI, M., BARKER, T. H., GIBBONS, D. L. & KURIE, J. M. 2018. The fibrotic tumor stroma. J*ournal of Clinical Investigation,* 128**,** 16-25.

YAMAZAKI, D., HITOMI, H. & NISHIYAMA, A. 2018. Hypertension with diabetes mellitus complications. *Hypertension Research,* 41**,** 147-156.

YANG, C. W., HARRIS, D. C. H., LUYCKX, V. A., NANGAKU, M., HOU, F. F., GARCIA GARCIA, G., ABU-AISHA, H., NIANG, A., SOLA, L., BUNNAG, S., EIAM-ONG, S., TUNGSANGA, K., RICHARDS, M., RICHARDS, N., GOH, B. L., DREYER, G., EVANS, R., MZINGAJIRA, H., TWAHIR, A., MCCULLOCH, M. I., AHN, C., OSAFO, C., HSU, H. H., BARNIEH, L., DONNER, J. A. & TONELLI, M. 2020. Global case studies for chronic kidney disease/end-stage kidney disease care. *Kidney International Supplements (2011),* 10**,** e24-e48.

YANG, J., DAI, C. & LIU, Y. 2005. A novel mechanism by which hepatocyte growth factor blocks tubular epithelial to mesenchymal transition. *Journal of the American Society of Nephrology,* 16**,** 68-78.

YU, H., LIN, T., CHEN, W., CAO, W., ZHANG, C., WANG, T., DING, M., ZHAO, S., WEI, H., GUO, H. & ZHAO, X. 2019. Size and temporal-dependent efficacy of oltipraz-loaded PLGA nanoparticles for treatment of acute kidney injury and fibrosis. *Biomaterials,* 219**,** 119368.

ZAKIYANOV, O., KALOUSOVá, M., ZIMA, T. & TESAř, V. 2019. Matrix Metalloproteinases in Renal Diseases: A Critical Appraisal. *Kidney and Blood Pressure Research,* 44**,** 298-330.

ZHANG, W. 1996. *Epitope Mapping and Functional Analysis of Monoclonal Antibodies to DnaA Protein.* Doctor of Philosophy, Michigan State University, Michigan (USA).

ZHANG, Y. & KOMPA, A. R. 2014. A practical guide to subtotal nephrectomy in the rat with subsequent methodology for assessing renal and cardiac function. *Nephrology,* 19**,** 552-561.

ZHOU, P., SUN, X. & ZHANG, Z. 2014. Kidney-targeted drug delivery systems. *Acta Pharmaceutica Sinica B,* 4**,** 37-42.

ZUCKERMAN, J. E., GALE, A., WU, P., MA, R. & DAVIS, M. E. 2015. siRNA delivery to the glomerular mesangium using polycationic cyclodextrin nanoparticles containing siRNA. *Nucleic Acid Therapeutics,* 25**,** 53-64.

Appendix

Appendix I: Fab Heavy Chain Sequencing Data

>Fab-1.3
QVKLLEQSGAELVRPGASVKLSCKASGYIFTSYWINWVKQRPGQGLEWIGNIYPSDSYTNYNQKFKDKATLTVDKSSSTAYMQLSSPTSEDSAV
YYCTRDGNYGNFDVWGAGTTVTVSSAKTTPPSVYPLAPGSAAQTNSMVTLGCLVKGYFPEPVTVTWNSGSLSSGVHTFPAVLQSDLYTLSSSVT
VPSSTWPSETVTCNVAHPASSTKVDKKIVPRDCTS

>FAB-2.3
QVKLLEQSGAELVRPGASVKLSCKASGYTFTNFWINWVKQGPGQGLEWIGNIYPSDSYSNYNQKFKDKVTLTVDKSSSTAFMQLSSPTSEDSAV
YYCTRDDNYGAMDYWGQGTSVTVSSAKTTPPSVYPLAPGSAAQTNSMVTLGCLVKGYFPEPVTVTWNSGSLSSGVHTFPAVLQSDLYTLSSSVT
VPSSTWPSETVTCNVAHPASSTKVDKKIVPRDCT

>Fab-3.2
QVKLLEQPGAELVRPGASVKLSCKASGYIFTSYWINWVKQRPGQGLEWIGNIYPSDSYTNYNQKFKDKATLTVDKSSSTAYMQLSSPTSEDSAV
YYCTRDGNYGNFDVWGAGTTVTVSSAKTTPPSVYPLAPGSAAQTNSMVTLGCLVKGYFPEPVTVTWNSGSLSSGVHTFPAVLQSDLYTLSSSVT
VPSSTWPSETVTCNVAHPASSTKVDKKIVPRDCTS

>Fab-3.3
QVKLLEQPGSELVRPGASVELSCKASGYTFTNFWINWVKQGPGQGLEWIGNIYPSDSYSNYNQKFKDKVTLTVDKSSSTAFMQLSSPTSEDSAV
YYCTRDDNYGAMDYWGQGTSVTVSSAKTTPPSVYPLAPGSAAQTNSMVTLGCLVKGYFPEPVTVTWNSGSLSSGVHTFPAVLQSDLYTLSSSVT
VPSSTWPSETVTCNVAHPASSTKVDKKIVPRDCTS

>Fab-5.2
QVKLLEQSGSELVRPGTSVKLSCKASGYIFTSYWINWVKQRPGQGLEWIGNIYPSDSYTNYNQKFKDRATLTVDKSSSTAYMQLSSPTSEDSAV
YYCTRDGNYGNFDVWGAGTTVTVSSAKTTPPSVYPLAPGSAAQTNSMVTLGCLVKGYFPEPVTVTWNSGSLSSGVHTFPAVLQSDLYTLSSSVT
VPSSTWPSETVTCNVAHPASSTKVDKKIVPRDCTS

>Fab-5.3
QVKLLEQSGSELVRPGASVKLSCKASGYIFTSYWINWVKQRPGQGLEWIGNIYPSDSYTNYNQKFKDKATLTVDKSSSTAYMQLSSPTSEDSAV
YYCTRDGNYGNFDVWGAGTTVTVSSAKTTPPSVFPLAPGSAAQTNSMVTLGCLVKGYFPEPVTVTWNSGSLSSGVHTFPAVLQSDLYTLSSSVT
VPSSTWPSETVTCNVAHPASSTKVDKKIVPRDCTS

>Fab-7.2
QVKLLEQSGSELVRPGASVKLSCKASGYTFTNYWINWVKQRPGQGLEWIGNIYPSDNYINYNQKFKDKATLTVDKSSSTAYMQLSSPTSEDSAV
YYCTRDDNYGAMDYWGQGTSVTVSSAKTTPPSVYPLAPGSAAQTNSMVTLGCLVKGYFPEPVTVTWNSGSLSSGVHTFPAVLQSDLYTLSSSVT
VPSSTWPSETVTCNVAHPASSTKVDKKIVPRDCTS

>Fab-7.3
QVKLLEQSGSELVRPGASVKLSCKASGYIFTSYWINWVKQRPGQGLEWIGNIYPSDSYTNYNQKFKDKATLTVDKSSSTAYMQLSSPTSEDSAV
YYCTRDGNYGNFDVWGAGTTVTVSSAKTTPPSVYPLAPGSAAQTNSMVTLGCLVKGYFPEPVTVTWNSGSLSSGVHTFPAVLQSDLYTLSSSVT
VPSSTWPSETVTCNVAHPASSTKVDKKIVPRDCTS

>Fab-9.2
QVKLLEQSGAEVVRPGASVKLSCKASGYTFTSYWINWVKQRPGQGLEWIGNIYPSDSYTNYNQKFKGKATLTVDKSSSTAYMQLSSPTSEDSAV
YYCTRDGNYGAMDYWGQGTSVTVSSAKTTPPSVYPLAPGSAAQTNSMVTLGCLVKGYFPEPVTVTWNSGSLSSGVHTFPAVLQSDLYTLSSSVT
VPSSTWPSETVTCNVAHPASSTKVDKKIVPRDCTS

>Fab-19.2
QVKLLEQSGSEVVRPGASVKLSCKASGYTFTSYWINWVRQRPGQGLEWIGNIYPSDSYTNYNQKFKGKATLTVDKSSSTAYMQLSSPTSEDSAV
YYCTRDGNYGAMDYWGQGTSVTVSSAKTTPPSVYPLAPGSAAQTNSMVTLGCLVKGYFPEPVTVTWNSGSLSSGVHTFPAVLQSDLYTLSSSVT
VPSSTWPSETVTCKVAHPASSTKVDKKIVPRDCTS

Appendix II: CLUSTAL 2.1 Multiple Sequence Alignment

```
Fab-1.3         QVKLLEQSGAELVRPGASVKLSCKASGYIFTSYWINWVKQRPGQGLEWIGNIYPSDSYTN
Fab-3.2         QVKLLEQPGAELVRPGASVKLSCKASGYIFTSYWINWVKQRPGQGLEWIGNIYPSDSYTN
Fab-5.2         QVKLLEQSGSELVRPGTSVKLSCKASGYIFTSYWINWVKQRPGQGLEWIGNIYPSDSYTN
Fab-5.3         QVKLLEQSGSELVRPGASVKLSCKASGYIFTSYWINWVKQRPGQGLEWIGNIYPSDSYTN
Fab-7.3         QVKLLEQSGSELVRPGASVKLSCKASGYIFTSYWINWVKQRPGQGLEWIGNIYPSDSYTN
Fab-9.2         QVKLLEQSGAEVVRPGASVKLSCKASGYTFTSYWINWVKQRPGQGLEWIGNIYPSDSYTN
Fab-19.2        QVKLLEQSGSEVVRPGASVKLSCKASGYTFTSYWINWVRQRPGQGLEWIGNIYPSDSYTN
FAB-2.3         QVKLLEQSGAELVRPGASVKLSCKASGYTFTNFWINWVKQGPGQGLEWIGNIYPSDSYSN
Fab-3.3         QVKLLEQPGSELVRPGASVELSCKASGYTFTNFWINWVKQGPGQGLEWIGNIYPSDSYSN
Fab-7.2         QVKLLEQSGSELVRPGASVKLSCKASGYTFTNYWINWVKQRPGQGLEWIGNIYPSDNYIN
                *******.*:*:****:**:******** **.:*****:* ***************.* *

Fab-1.3         YNQKFKDKATLTVDKSSSTAYMQLSSPTSEDSAVYYCTRDGNYGNFDVWGAGTTVTVSSA
Fab-3.2         YNQKFKDKATLTVDKSSSTAYMQLSSPTSEDSAVYYCTRDGNYGNFDVWGAGTTVTVSSA
Fab-5.2         YNQKFKDRATLTVDKSSSTAYMQLSSPTSEDSAVYYCTRDGNYGNFDVWGAGTTVTVSSA
Fab-5.3         YNQKFKDKATLTVDKSSSTAYMQLSSPTSEDSAVYYCTRDGNYGNFDVWGAGTTVTVSSA
Fab-7.3         YNQKFKDKATLTVDKSSSTAYMQLSSPTSEDSAVYYCTRDGNYGNFDVWGAGTTVTVSSA
Fab-9.2         YNQKFKGKATLTVDKSSSTAYMQLSSPTSEDSAVYYCTRDGNYGAMDYWGQGTSVTVSSA
Fab-19.2        YNQKFKGKATLTVDKSSSTAYMQLSSPTSEDSAVYYCTRDGNYGAMDYWGQGTSVTVSSA
FAB-2.3         YNQKFKDKVTLTVDKSSSTAFMQLSSPTSEDSAVYYCTRDDNYGAMDYWGQGTSVTVSSA
Fab-3.3         YNQKFKDKVTLTVDKSSSTAFMQLSSPTSEDSAVYYCTRDDNYGAMDYWGQGTSVTVSSA
Fab-7.2         YNQKFKDKATLTVDKSSSTAYMQLSSPTSEDSAVYYCTRDDNYGAMDYWGQGTSVTVSSA
                ******.:.***********:******************.*** :* ** **:******

Fab-1.3         KTTPPSVYPLAPGSAAQTNSMVTLGCLVKGYFPEPVTVTWNSGSLSSGVHTFPAVLQSDL
Fab-3.2         KTTPPSVYPLAPGSAAQTNSMVTLGCLVKGYFPEPVTVTWNSGSLSSGVHTFPAVLQSDL
Fab-5.2         KTTPPSVYPLAPGSAAQTNSMVTLGCLVKGYFPEPVTVTWNSGSLSSGVHTFPAVLQSDL
Fab-5.3         KTTPPSVFPLAPGSAAQTNSMVTLGCLVKGYFPEPVTVTWNSGSLSSGVHTFPAVLQSDL
Fab-7.3         KTTPPSVYPLAPGSAAQTNSMVTLGCLVKGYFPEPVTVTWNSGSLSSGVHTFPAVLQSDL
Fab-9.2         KTTPPSVYPLAPGSAAQTNSMVTLGCLVKGYFPEPVTVTWNSGSLSSGVHTFPAVLQSDL
Fab-19.2        KTTPPSVYPLAPGSAAQTNSMVTLGCLVKGYFPEPVTVTWNSGSLSSGVHTFPAVLQSDL
FAB-2.3         KTTPPSVYPLAPGSAAQTNSMVTLGCLVKGYFPEPVTVTWNSGSLSSGVHTFPAVLQSDL
Fab-3.3         KTTPPSVYPLAPGSAAQTNSMVTLGCLVKGYFPEPVTVTWNSGSLSSGVHTFPAVLQSDL
Fab-7.2         KTTPPSVYPLAPGSAAQTNSMVTLGCLVKGYFPEPVTVTWNSGSLSSGVHTFPAVLQSDL
                *******:**************************************************

Fab-1.3         YTLSSSVTVPSSTWPSETVTCNVAHPASSTKVDKKIVPRDCTS
Fab-3.2         YTLSSSVTVPSSTWPSETVTCNVAHPASSTKVDKKIVPRDCTS
Fab-5.2         YTLSSSVTVPSSTWPSETVTCNVAHPASSTKVDKKIVPRDCTS
Fab-5.3         YTLSSSVTVPSSTWPSETVTCNVAHPASSTKVDKKIVPRDCTS
Fab-7.3         YTLSSSVTVPSSTWPSETVTCNVAHPASSTKVDKKIVPRDCTS
Fab-9.2         YTLSSSVTVPSSTWPSETVTCNVAHPASSTKVDKKIVPRDCTS
Fab-19.2        YTLSSSVTVPSSTWPSETVTCKVAHPASSTKVDKKIVPRDCTS
FAB-2.3         YTLSSSVTVPSSTWPSETVTCNVAHPASSTKVDKKIVPRDCT-
Fab-3.3         YTLSSSVTVPSSTWPSETVTCNVAHPASSTKVDKKIVPRDCTS
Fab-7.2         YTLSSSVTVPSSTWPSETVTCNVAHPASSTKVDKKIVPRDCTS
                **********************:********************
```

Multiple alignments of amino acid sequences of cloned Fab VH regions.

Appendix III: Fab Light Chain Sequencing Data

>VK-1.3
ELQMTQSPSYLAASPGETITINCRASKSISKYLAWYQEKPGKTNKLLIYSGSTLQSGIPSRFSGSGSGTDFTLTISSLEPEDF
AMYYCQQHNIYPYTFGGGTKLEIKRADAAPTVSIFPPSSEQLTSGGASVVCFLNNFYPKDINVKWKIDGSERQNGVLNSWTDQ
DGKDSTYSMSSTLTLTKDEYERHNSYTCEATHKTSTSPIVKSFNRNEC

>VK-2.3
ELQMTQSPSYLAASPGETITINCRASKSISKYLAWYQEKPGKTNKLLIYSGSTLQSGIPSRFSGSGSGTDFTLTISSLEPEDS
AMYYCQQHNEYPYTFGGGTRLEIKRANAAPTVSIFPPSSEQLTSGGASVVCFLNNFYPKDINVKWKIDGSERQNGVLNSWTDQ
DSKDSTYSMSSTLTLTKDEYERHNSYTCEATHKTSTSPIVKSFNRNEC

>VK-3.2
ELQMTQSPSYLAASPGETITINCRASKSISKYLAWYQEKPGKTNKLLIYSGSTLQSGIPSRFSGSGSGTDFTLTISSLEPEDF
AMYYCQQHNEYPYTFGGGTKLEIKRADAAPTVSIFPPSSEQLTSGGASVVCFLNNFYPKDINVKWKIDGSERQNGVLNSWTDQ
DSKDSTYSMSSTLTLTKDEYERHNSYTCEATHKTSTSPIVKSFNRNEC

>VK-3.3
ELQMTQSPSYLAASPGETITINCRASKSISKYLAWYQEKPGKTNKLLIYSGSTLQSGIPSRFSGSGSGTDFTLTISSLEPEDF
AMYYCQQHNIYPYTFGGGTKLEIKRADAAPTVSIFPPSSEQLTSGGASVVCFLNNFYPKDINVKWKIDGSERQNGVLNSWTDQ
DSKDSTYSMSSTLTLTKDEYERHNSYTCEATHKTSTSPIVKSFNRNEC

>VK-5.2
ELQMTQSPSYLAASPGETITINCRASKSISKYLAWYQEKPGKTNKLLIYSGSTLQSGIPSRFSGSGSGTDFTLTISSLEPEDF
AMYYCQQHNIYPYTFGGGTKLEIKRADAAPTVSIFPPSSEQLTSGGASVVCFLNNFYPKDINVKWKIDGSERQNGVLNSWTDQ
DSKDSTYSMSSTLTLTKDEYERHNSYTCEATHKTSTSPIVKSFNRNEC

>VK-5.3
ELQMTQSPSYLAASPGETITINCRASKSISKYLAWYQEKPGKTNKLLIYSGSTLQSGIPSRFSGSGSGTDFTLTISSLEPEDF
AMYYCQQHNEYPYTFGGGTKLEIKRADAAPTVSIFPPSSEQLTSGGASVVCFLNNFYPKDINVKWKIDGSERQNGVLNSWTDQ
DSKDSTYSMSSTLTLTKDEYERHNSYTCEATHKTSTSPIVKSFNRNEC

>VK-7.2
ELQMTQSPSYLAASPGESITINCTASKSFSKYLAWYQEKPGKTNKLLIYSGSTLQSGIPSRFSGSGSGTDFTLTISSLEPEDF
AMYYCQQHYEYPYTFGSGTKLDIKRADAAPTVSIFPPSSEQLTSGGASVVCFLNNFYPKDINVKWKIDGSERQNGVLNSWTDQ
DSKDSTYSMSSTLTLTKDEYERHNSYACEATHKTSTSPIVKSFNRNEC

>VK-7.3
ELQMTQSPSYLAASPGETITINCRASKSISKYLAWYQEKPGKTNKLLIYSGSTLQSGIPSRFSGSGSGTDFTLTISSLEPEDF
AMYYCQQHNEYPYTFGGGTKLEIKRADAAPTVSIFPPSSEQLTSGGASVVCFLNNFYPKDINVKWKIDGSERQNGVLNSWTDQ
DSKDSTYSMSSTLTLTKDEYERHNSYTCEATHKTSTSPIVKSFNRNEC

>VK-9.2
ELQMTQSPSYLAASPGETITINCRASKSISKYLAWYQEKPGKTNKLLIYSGSTLQSGIPSRFSGSGSGTDFTLTISSLEPEDF
AMYYCQQHNEYPYTFGGGTKLEIKRADAAPTVSIFPPSSEQLTSGGASVVCFLNNFYPKDINVKWKIDGSERQNGVLNSWTDQ
DSKDSTYSMSSTLTLTKDEYERHNSYTCEATHKTSTSPIVKSFNRNEC

>VK-19.2
ELQMTQSPSYLAASPGETITINCRASKSISKYLAWYQEKPGKTNKLLIYSGSTLQSGIPSRFSGSGSGTDFTLTISSLEPEDF
AMYYCQQHNEYPYTFGGGTKLEIKRADAAPTVSIFPPSSEQLTSGGASVVCFLNNFYPKDINVKWKVDGSERQNGVLNSWTDQ
DSKDSTYSMSSTLTLTKDEYERHNSYTCEATHKTSTSPIVKSFNRNEC

Appendix IV: CLUSTAL 2.1 Multiple Sequence Alignment

```
VK-1.3          RFSGSGSGTDFTLTISSLEPEDFAMYYCQQHNIYPYTFGGGTKLEIKRADAAPTVSIFPP
VK-3.3          RFSGSGSGTDFTLTISSLEPEDFAMYYCQQHNIYPYTFGGGTKLEIKRADAAPTVSIFPP
VK-5.2          RFSGSGSGTDFTLTISSLEPEDFAMYYCQQHNIYPYTFGGGTKLEIKRADAAPTVSIFPP
VK-2.3          RFSGSGSGTDFTLTISSLEPEDSAMYYCQQHNEYPYTFGGGTRLEIKRANAAPTVSIFPP
VK-3.2          RFSGSGSGTDFTLTISSLEPEDFAMYYCQQHNEYPYTFGGGTKLEIKRADAAPTVSIFPP
VK-7.3          RFSGSGSGTDFTLTISSLEPEDFAMYYCQQHNEYPYTFGGGTKLEIKRADAAPTVSIFPP
VK-5.3          RFSGSGSGTDFTLTISSLEPEDFAMYYCQQHNEYPYTFGGGTKLEIKRADAAPTVSIFPP
VK-9.2          RFSGSGSGTDFTLTISSLEPEDFAMYYCQQHNEYPYTFGGGTKLEIKRADAAPTVSIFPP
VK-19.2         RFSGSGSGTDFTLTISSLEPEDFAMYYCQQHNEYPYTFGGGTKLEIKRADAAPTVSIFPP
VK-7.2          RFSGSGSGTDFTLTISSLEPEDFAMYYCQQHYEYPYTFGSGTKLDIKRADAAPTVSIFPP
                ********************** ********  ******.**:*:****:**********

VK-1.3          SSEQLTSGGASVVCFLNNFYPKDINVKWKIDGSERQNGVLNSWTDQDGKDSTYSMSSTLT
VK-3.3          SSEQLTSGGASVVCFLNNFYPKDINVKWKIDGSERQNGVLNSWTDQDSKDSTYSMSSTLT
VK-5.2          SSEQLTSGGASVVCFLNNFYPKDINVKWKIDGSERQNGVLNSWTDQDSKDSTYSMSSTLT
VK-2.3          SSEQLTSGGASVVCFLNNFYPKDINVKWKIDGSERQNGVLNSWTDQDSKDSTYSMSSTLT
VK-3.2          SSEQLTSGGASVVCFLNNFYPKDINVKWKIDGSERQNGVLNSWTDQDSKDSTYSMSSTLT
VK-7.3          SSEQLTSGGASVVCFLNNFYPKDINVKWKIDGSERQNGVLNSWTDQDSKDSTYSMSSTLT
VK-5.3          SSEQLTSGGASVVCFLNNFYPKDINVKWKIDGSERQNGVLNSWTDQDSKDSTYSMSSTLT
VK-9.2          SSEQLTSGGASVVCFLNNFYPKDINVKWKIDGSERQNGVLNSWTDQDSKDSTYSMSSTLT
VK-19.2         SSEQLTSGGASVVCFLNNFYPKDINVKWKVDGSERQNGVLNSWTDQDSKDSTYSMSSTLT
VK-7.2          SSEQLTSGGASVVCFLNNFYPKDINVKWKIDGSERQNGVLNSWTDQDSKDSTYSMSSTLT
                ****************************:*****************.************

VK-1.3          LTKDEYERHNSYTCEATHKTSTSPIVKSFNRNEC
VK-3.3          LTKDEYERHNSYTCEATHKTSTSPIVKSFNRNEC
VK-5.2          LTKDEYERHNSYTCEATHKTSTSPIVKSFNRNEC
VK-2.3          LTKDEYERHNSYTCEATHKTSTSPIVKSFNRNEC
VK-3.2          LTKDEYERHNSYTCEATHKTSTSPIVKSFNRNEC
VK-7.3          LTKDEYERHNSYTCEATHKTSTSPIVKSFNRNEC
VK-5.3          LTKDEYERHNSYTCEATHKTSTSPIVKSFNRNEC
VK-9.2          LTKDEYERHNSYTCEATHKTSTSPIVKSFNRNEC
VK-19.2         LTKDEYERHNSYTCEATHKTSTSPIVKSFNRNEC
VK-7.2          LTKDEYERHNSYACEATHKTSTSPIVKSFNRNEC
                ************:**********************
```

Multiple alignments of the amino acid sequences of cloned Fab VK regions.

Appendix V: Epitope Mapping Sequence Data

Clone 1

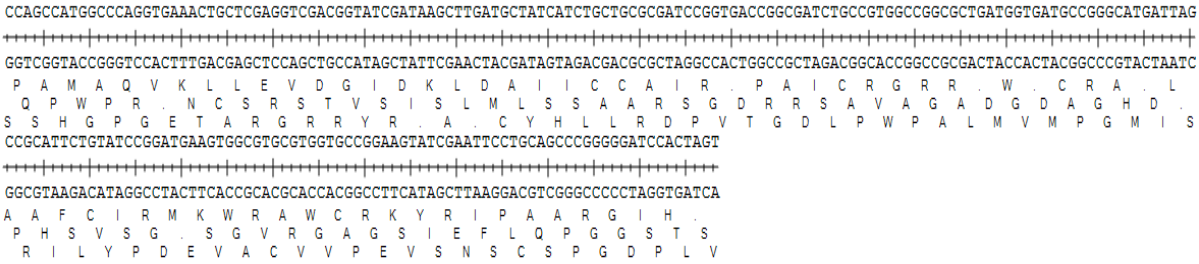

Clone 2

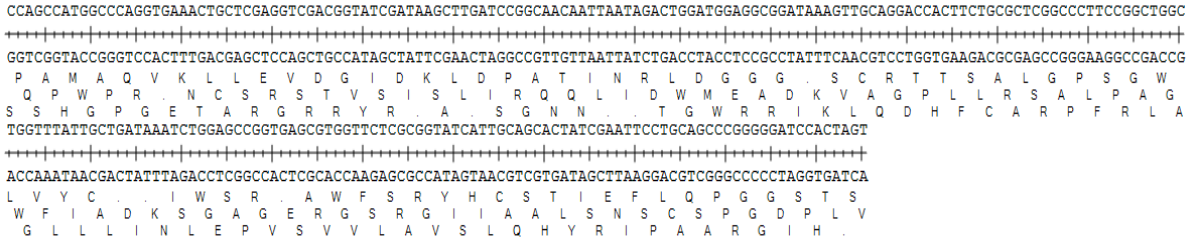

Clone 3

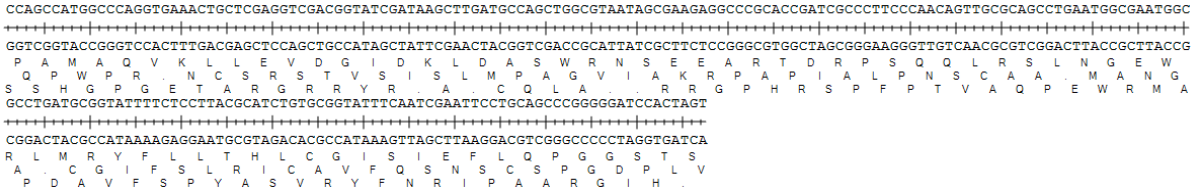

Clone 4

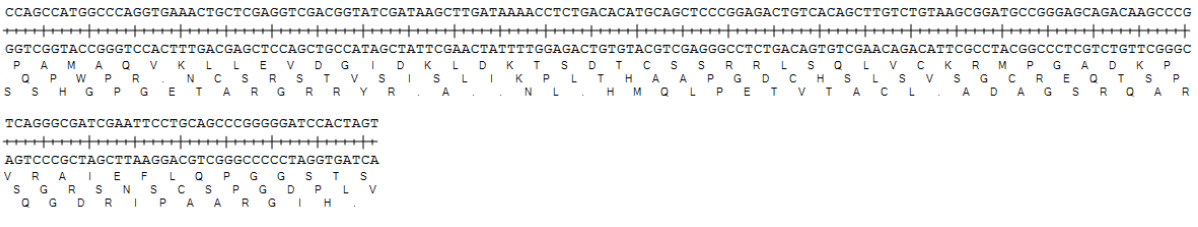

Clone 5

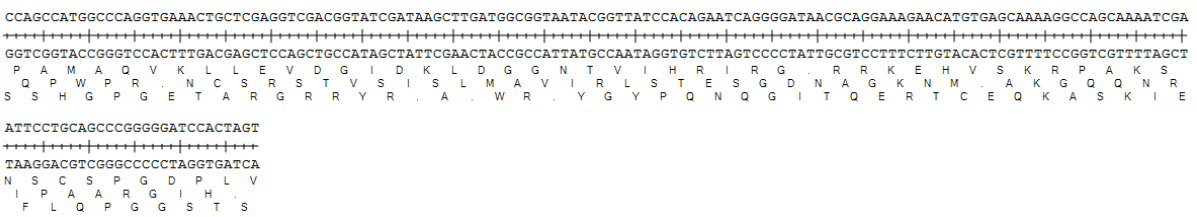

Clone 6

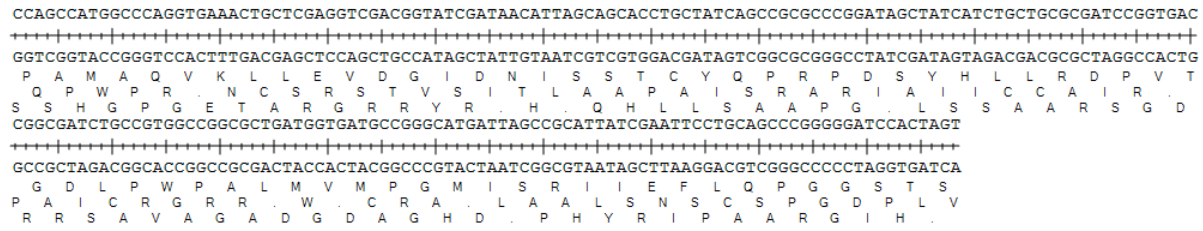

Clone 7

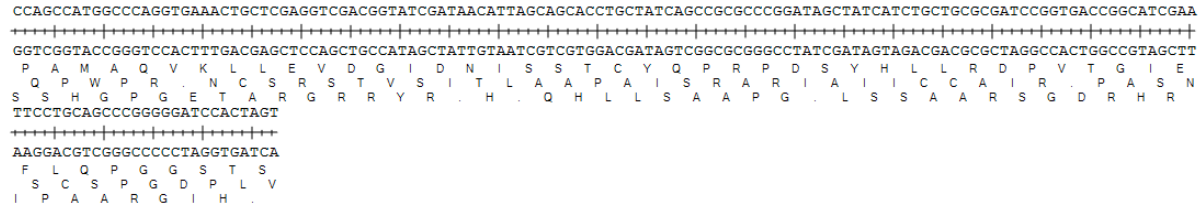

Clone 8

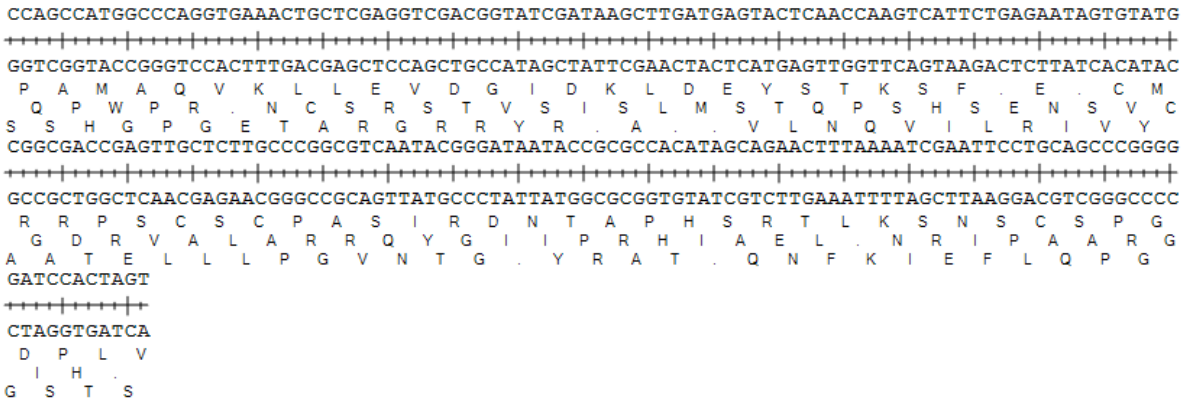

Clone 9

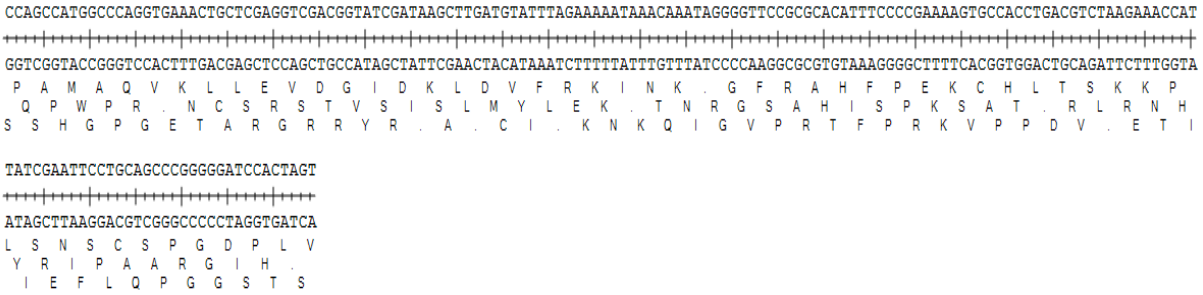

Clone 10

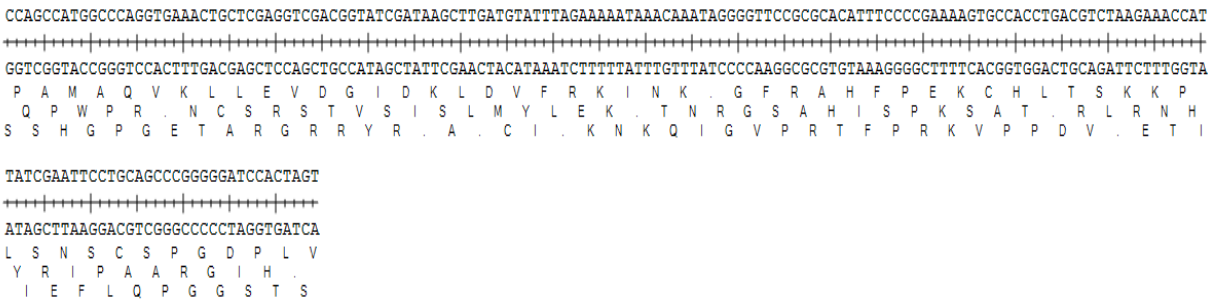

Appendix VI: Reading Frames of 10 Random Epitope Mapping Clones

Clone 1	AIICCAIR.PAICRGRR.W.CRA.LAAFCIRMKWRAWCRK
Clone 2	PATINRLDGGG.SCRTTSALGPSGWLVYC..IWSR.AWFSRYHCST
Clone 3	KLDASWRNSEEARTDRPSQQLRSLNGEWRLMRYFLLTHLCGIS
Clone 4	DPSVGNISSTCYQPRPDSYHLLRDPV
Clone 5	KTSDTCSSRRLSQLVCKRMPGADKPVRA
Clone 6	GGNTVIHRIRG.RRKEHVSKRPA
Clone 7	NISSTCYQPRPDSYHLLRDPVTGDLPWPA
Clone 8	NISSTCYQPRPDSYHLLRDPVTG
Clone 9	EYSTKSF.E.CMRRPSCSCPASIRDNTAPHSRTL
Clone 10	VFRKINK.GFRAHFPEKCHLTSKKP

Appendix VII: RT-qPCR Mouse Primers

	Name	Sense Primer	Antisense Primer
Mouse	**LOXL-2**	TCTGCCTGGAGGACACTGAGT	TCGGTGATGTCTATCCACTGGC
	LOXL-4	TTCTCGGCTGGCGTTGCTTGTA	GACTTGGAGAGGCAGTTTTCC
	TG2	GGGCCTTCTCATCGAACCAG	CAGGACCCGGATCTTGATTTC
	Collagen I	ATGGATTCCCGTTCGAGTACG	TCAGCTGGATAGCGACATCG
	Collagen III	CACCCTTCTTCATCCCACTCTTA	ACCAAGGTGGCTGCATCC
	GAPDH	CATCACTGCCACCCAGAAGACTG	TGCCAGTGAGCTTCCCGTTCAG

This table lists the specific sense and antisense primers used for RT-qPCR amplification of fibrosis-related genes in mouse models. The genes targeted include lysyl oxidase-like proteins (LOXL-2 and LOXL-4), transglutaminase 2 (TG2), collagen types I and III, and the housekeeping gene glyceraldehyde-3-phosphate dehydrogenase (GAPDH). These primers were designed to amplify the respective gene sequences to assess gene expression levels in experiments related to kidney fibrosis.

Appendix VIII: LOXL-2 Expression in UUO Model at Different Time Points.

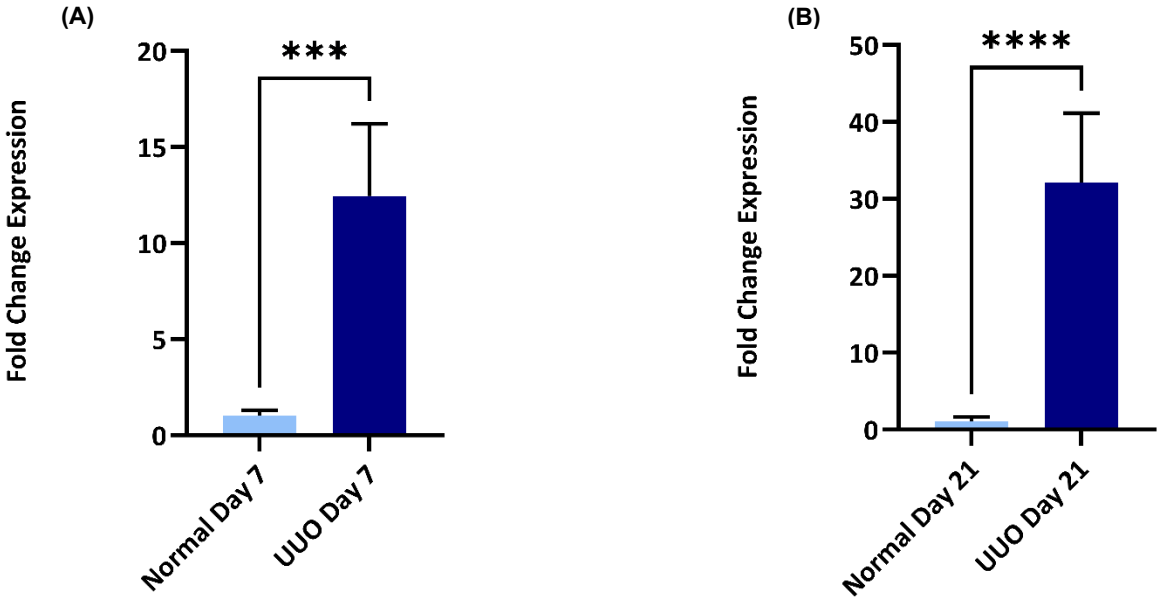

(A) Relative fold change in LOXL-2 expression in UUO Day 7 versus Normal Day 7 kidneys, showing significant upregulation in UUO ($p = 0.0001$). (B) LOXL-2 expression at Day 21 in UUO kidneys compared to normal controls, showing a further increase ($p < 0.0001$).

Appendix VIII: LOXL-4 Expression in UUO Models at Different Time Points.

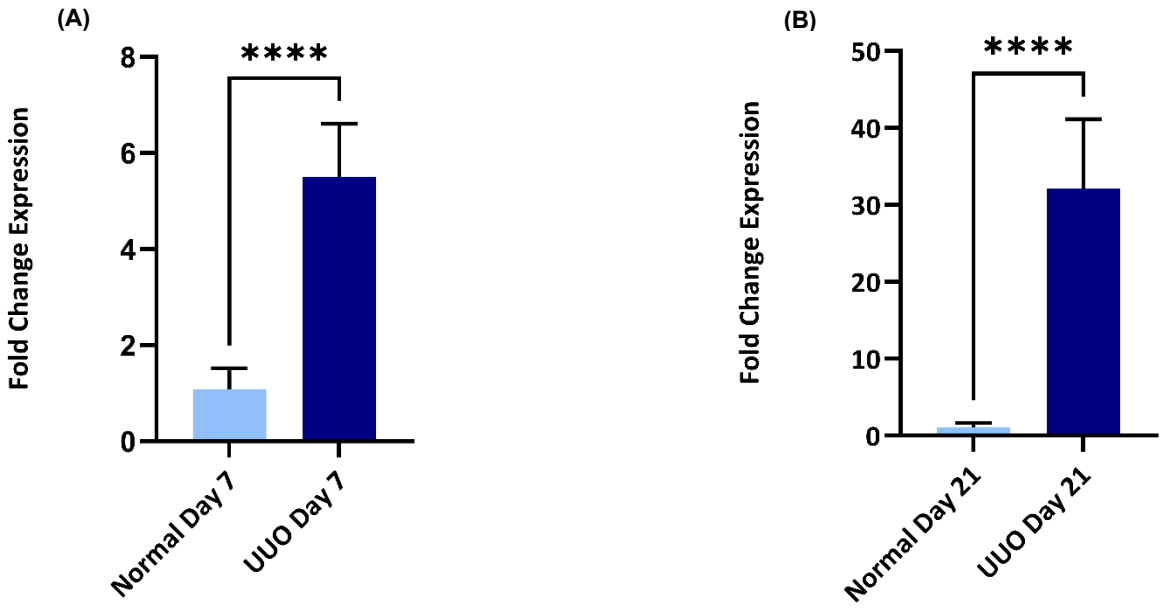

(A) Relative fold change in LOXL-4 expression in UUO Day 7 versus Normal Day 7 kidneys show significant upregulation ($p < 0.0001$). (B) LOXL-4 expression at Day 21 in UUO kidneys compared to normal controls, showing a further increase ($p < 0.0001$).

Appendix IX: TG2 Expression in UUO Models at Different Time Points.

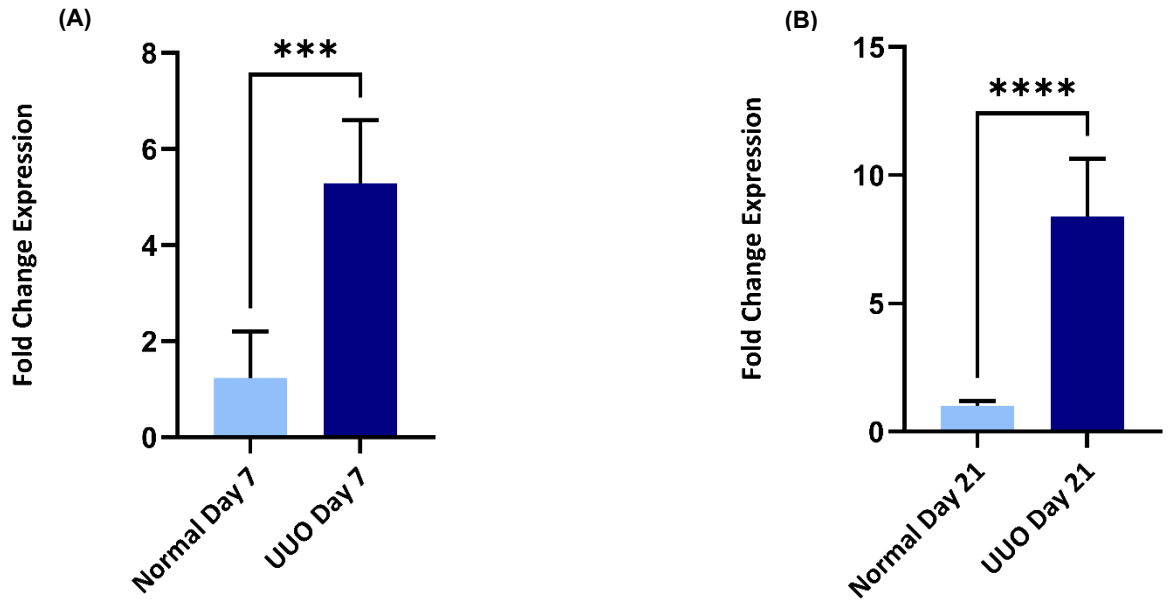

(A) TG2 expression in UUO Day 7 compared to Normal Day 7 kidneys showed significant upregulation ($p < 0.001$). (B) TG2 expression in UUO Day 21 versus Normal Day 21 kidneys, with sustained upregulation ($p < 0.001$).

Appendix X: Collagen I Expression in UUO Models at Different Time Points.

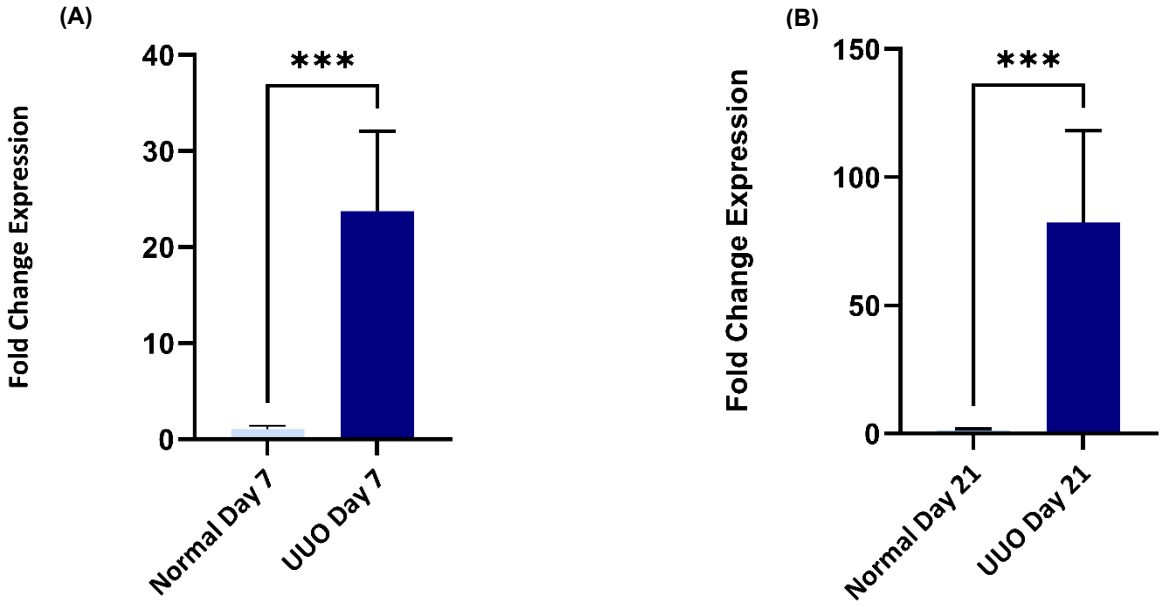

(A) Collagen I expression in UUO Day 7 versus Normal Day 7 kidneys, demonstrating significant upregulation ($p < 0.001$). (B) Collagen I expression in UUO Day 21 compared to Normal Day 21 kidneys showed a significant increase ($p < 0.001$).

Appendix XI: Collagen III Expression in UUO Models at Different Time Points.

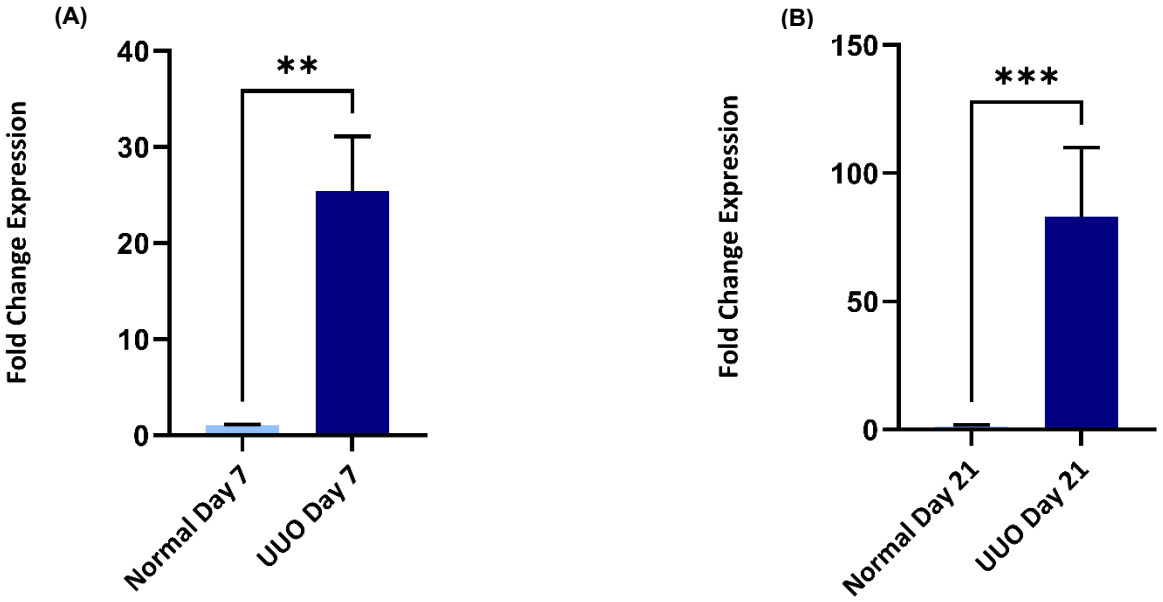

(A) Collagen III expression in UUO Day 7 compared to Normal Day 7 kidneys, demonstrating significant upregulation ($p = 0.0027$). (B) Collagen III expression in UUO Day 21 versus Normal Day 21 kidneys, showing sustained significant upregulation ($p = 0.0001$).